

2013

Characterization of Parametric Internal Structures for Components Built by Fused Deposition Modeling

Luis Fernando Villalpando Rosas

Follow this and additional works at: <http://scholar.uwindsor.ca/etd>

 Part of the [Engineering Commons](#)

Recommended Citation

Villalpando Rosas, Luis Fernando, "Characterization of Parametric Internal Structures for Components Built by Fused Deposition Modeling" (2013). *Electronic Theses and Dissertations*. Paper 4763.

This online database contains the full-text of PhD dissertations and Masters' theses of University of Windsor students from 1954 forward. These documents are made available for personal study and research purposes only, in accordance with the Canadian Copyright Act and the Creative Commons license—CC BY-NC-ND (Attribution, Non-Commercial, No Derivative Works). Under this license, works must always be attributed to the copyright holder (original author), cannot be used for any commercial purposes, and may not be altered. Any other use would require the permission of the copyright holder. Students may inquire about withdrawing their dissertation and/or thesis from this database. For additional inquiries, please contact the repository administrator via email (scholarship@uwindsor.ca) or by telephone at 519-253-3000ext. 3208.

**Characterization of Parametric Internal Structures for Components Built by Fused
Deposition Modeling**

By

Luis Fernando Villalpando Rosas

A Thesis
Submitted to the Faculty of Graduate Studies
through the Department of Industrial and Manufacturing Systems Engineering
in Partial Fulfillment of the Requirements for
the Degree of Master of Applied Science
at the University of Windsor

Windsor, Ontario, Canada

2013

© 2013 Luis Fernando Villalpando Rosas

Characterization of Parametric Internal Structures for Components Built by Fused
Deposition Modeling

by

Luis Fernando Villalpando Rosas

APPROVED BY:

Dr. Nader Zamani, Department of Mechanical, Automotive and Materials Engineering

Dr. Ahmed Azab, Department of Industrial and Manufacturing Systems Engineering

Dr. Jill Urbanic, Advisor, Department of Industrial and Manufacturing Systems
Engineering

Dr. Rashid Rashidzadeh, Chair of Defense, Department of Electrical and Computer
Engineering

1/10/2013

DECLARATION OF CO-AUTHORSHIP / PREVIOUS PUBLICATION

I. Co-Authorship Declaration

I hereby declare that this thesis incorporates material that is result of joint research, as follows:

This thesis incorporates the outcome of a joint research undertaken in collaboration with Dr. Ruth Jill Urbanic and Luis Fernando Villalpando Rosas. The collaboration is covered in Chapter VII of the thesis. In all cases, the key ideas, primary contributions, experimental designs, data analysis and interpretation, were performed by the author, and the contribution of coauthors was primarily through the provision of comments, thoughts and suggestions that led to the successful completion of the present work.

I am aware of the University of Windsor Senate Policy on Authorship and I certify that I have properly acknowledged the contribution of other researchers to my thesis, and have obtained written permission from each of the co-author(s) to include the above material(s) in my thesis.

I certify that, with the above qualification, this thesis, and the research to which it refers, is the product of my own work.

II. Declaration of Previous Publication

This thesis includes one original paper that has been previously submitted for publication in peer reviewed conference proceedings, as follows:

Thesis Chapter	Publication Title / Full Citation	Publication Status
Chapter 7	Villalpando, L. and Urbanic, J. (2010) “Parametric Internal Matrix Structures for Components Built by Fused Deposition Modeling”, Proceedings of the 4 th International Conference on Changeable, Agile, Reconfigurable and Virtual Production (CARV2011), Montreal, Canada, October 2-5.	Published

I certify that I have obtained a written permission from the copyright owner(s) to include the above published materials in my thesis. I certify that the above material describes work completed during my registration as a graduate student at University of Windsor.

I declare that, to the best of my knowledge, my thesis does not infringe upon anyone’s copyright nor violate any proprietary rights and that any ideas, techniques, quotations or any other material from the work of other people in my thesis, published or otherwise, are fully acknowledged in accordance with the standard referencing practices.

Furthermore, to the extent that I have included copyrighted material that surpasses the bounds of fair dealing within the meaning of the Canada Copyright Act, I have obtained a written permission from the copyright owner(s) to include such material(s) in my thesis.

I declare that this is a true copy of my thesis, including any final revisions, as approved by my thesis committee and the Graduate Studies office, and that this thesis has not been submitted for a higher degree to any other University or Institution.

ABSTRACT

Parametric internal structures based on basic geometries present an easy and reliable way to reduce the internal solid volume fraction of the fused deposition modeling (FDM) rapid prototype (RP) part while guaranteeing the structural integrity of the physical model. This would reduce the material costs, which may be significant for large components. The present research proposes a novel method that, based on multidisciplinary and experimental approach, characterizes the mechanical behavior and predicts the material use and build time with the intention of optimizing the strength while reducing costs. The proposed approach comprises a set of physical and virtual experimentation techniques that merge to provide a comprehensive analytical resource. Results indicate that the FEA method represents accurately the mechanical behavior of the RP parts whereas the statistical analysis provides insight. This unique approach serves as a basis to understand the work performed in similar studies and leaves a number of possible topics that, once explored, will have a strong impact on the optimization of not only the FDM process, but the entire Rapid Prototyping industry.

DEDICATION

To all the people that have given me their support, understanding, and love throughout all the good and bad moments that life brings.

ACKNOWLEDGEMENTS

I thank the thesis committee members. I thank Dr. Nader Zamani for honouring me being part of this committee and for all the support throughout my years as a University scholar. I thank Dr. Ahmed Azab for allocating valuable time and accepting being part of this committee and valuable contributions during the realization of this thesis. I thank Dr. Jill Urbanic for providing me with her expertise and for accepting to be my thesis supervisor.

This research was partially funded by the AUTO21 Network of Centres of Excellence. In this regard, I would like to thank Dr. Jerry Sokolowski for the confidence and the resources in the early stages of this research. Thank you to Dr. Waguih ElMaraghy and Dr. Hoda ElMaraghy for the use of the FDM machine at the University of Windsor Intelligent Manufacturing Systems Centre at the initial stages of this research.

I would like to thank the people that have been involved, voluntarily and involuntarily, with the present research. Please bear in mind that the present work would not have been as enjoyable as it was without all of you. In this respect, I would like to thank Lucian Pop for his availability and support in performing the tensile tests in the initial stages. Similarly, I would like to thank Matthew St. Louis for his support in performing the tensile and compressive tests in the last stage of the research.

Additionally, I thank Mario and Stephane Boucher for their continuous support at the intermediate and last stage of this process. I thank Shawn Mckinlay for the expertise advice with regards to the refinement of the modeling done in the present research. I thank Amir Hassannejadasi for all the support and valuable comments in the last stages of the present study.

I extend my sincere thankfulness to Dr. Jill Urbanic for accepting me to be part of this unique research group, which has been motivational due to the many factors including the uniqueness of it and the visionary perspective to see the research procedure. Dr. Jill Urbanic has given me the support, the time, the guidance, and the comprehension needed to achieve the goal of finalizing the thesis successfully. Thank you to Robert Hedrick for the time and knowledge provided to the realization of this research. I extend a special thank you to the Rapid Prototyping Research Group that has provided their support and kind understanding.

Thank you to my family who has always given me their support, confidence, and advice in many ways, my Dad, my Mom, my brother Jesus, and to Marzieh.

TABLE OF CONTENTS

DECLARATION OF CO-AUTHORSHIP / PREVIOUS PUBLICATION.....	iii
ABSTRACT.....	v
DEDICATION.....	vi
ACKNOWLEDGEMENTS.....	vii
LIST OF TABLES.....	xi
LIST OF FIGURES.....	xiii
CHAPTER I INTRODUCTION.....	1
1.1 INTRODUCTION TO RAPID PROTOTYPING.....	1
1.1.1 INDUSTRIAL RAPID PROTOTYPING SYSTEMS.....	4
1.1.2 THE RAPID PROTOTYPING PROCESS.....	5
1.1.3 CAD SYSTEMS.....	7
1.1.4 RP MACHINE SOFTWARE.....	9
1.1.5 LAYARED MANUFACTURING TECHNOLOGIES.....	10
1.1.6 FUSED DEPOSITION MODELING.....	12
1.2 MOTIVATION, THESIS OBJECTIVES, AND SCOPE OF THE RESEARCH.....	14
1.2.1 MOTIVATION.....	14
1.2.2 THESIS OBJECTIVES.....	16
1.2.3 SCOPE OF THE RESEARCH.....	17
1.3 BACKGROUND.....	18
1.3.1 POLYMERIC MATERIALS.....	19
1.3.2 COMPOSITE MATERIALS.....	20
1.3.3 ABS PLASTIC.....	21
1.3.4 CHARACTERIZATION OF FDM-ABS.....	22
1.4 THESIS OVERVIEW.....	25
CHAPTER II DESIGN OF EXPERIMENTS.....	28
2.1 BACKGROUND.....	28
2.1.1 FDM-ABS MANUFACTURING PARAMETERS.....	30
2.1.2 DESIGN OF EXPERIMENTS AND DATA ANALYSIS.....	33
2.1.3 PARAMETRIC OPTIMIZATION OF FDM PARTS.....	35
2.2 DISCUSSION.....	43
2.3 SELECTION OF PARAMETERS.....	45
CHAPTER III COMPUTER-AIDED DESIGN FOR RAPID PROTOTYPING.....	49
3.1 INTRODUCTION TO CAD FOR RAPID PROTOTYPING.....	49
3.1.1 DESIGN FOR OPTIMIZATION.....	50
3.1.2 DESIGN FOR STRENGTH.....	60
3.2 DISCUSSION.....	76

3.3 RESULTS	79
CHAPTER IV RAPID PROTOTYPING OF PARAMETRICAL MODELS	81
4.1 INTRODUCTION TO 3D MODELING	81
4.1.1 METHODOLOGY	81
4.1.2 PARAMETRIC ELEMENT GENERATION	82
4.1.3 PARAMETRIC MATRIX WEB STRUCTURES	84
4.1.4 INTERNAL STRUCTURE INTEGRATION	87
4.2 PREPARATION OF TEST SAMPLES	88
4.3 FDM MACHINE SOFTWARE SIMULATION	89
4.4 RESULTS	91
4.4.1 LAYERED TENSILE SPECIMENS' MORPHOLOGY	94
4.4.2 LAYERED COMPRESSIVE SPECIMENS' MORPHOLOGY	97
4.5 ANALYSIS OF VARIANCE FOR THE MATERIAL, SUPPORT, AND TIME	102
4.5.1 ANOVA – MATERIAL USAGE FROM VIRTUAL RP	103
4.5.2 ANOVA – BUILD TIME FROM VIRTUAL RP	106
CHAPTER V CHARACTERIZATION OF THE MECHANICAL BEHAVIOR OF THE FDM PARTS	
EXPERIMENTAL INVESTIGATION	109
5.1 INTRODUCTION	109
5.1.1 TENSILE STRENGTH	110
5.1.2 COMPRESSIVE STRENGTH	111
5.2 THE BEHAVIOR OF THERMOPLASTICS	112
5.2.1 THE STRAIN-STRESS CURVE	114
5.2.2 TRUE STRAIN-STRESS	115
5.3 MATERIAL TESTING	116
5.3.1 THE TENSILE TEST	117
5.3.1.1 TEST PREPARATION	117
5.3.1.2 TESTING PROCEDURE	118
5.3.1.3 RESULTS OF THE TENSILE TESTS	118
5.3.2 THE COMPRESSION TEST	120
5.3.2.1 TEST PREPARATION	120
5.3.2.2 TESTING PROCEDURE	121
5.3.2.3 RESULTS OF THE COMPRESSIVE TESTS	121
5.4 SIMULATION OF THE MECHANICAL BEHAVIOR OF THE INTERNALLY MODIFIED	
STRUCTURES	123
5.4.1 BACKGROUND	123
5.4.2 ELEMENT TYPE AND MESH	126
5.4.3 BOUNDARY CONDITIONS	126

5.4.4 INPUT DATA.....	127
5.4.5 RESULTS.....	128
5.5 ANALYSIS OF VARIANCE FOR THE MECHANICAL PROPERTIES.....	138
5.5.1 ANOVA – MECHANICAL PROPERTIES – INTERNAL STRUCTURES.....	139
5.5.2 ANOVA – MECHANICAL PROPERTIES – SOLID AND HOLLOW.....	141
5.6 CASE STUDY: PLASTIC BOTTLE BLOW MOLD.....	142
5.6.1 INTRODUCTION.....	142
5.6.2 DESIGN PROCESS.....	143
5.6.3 RESULTS.....	144
CHAPTER VI DISCUSSION.....	147
6.1 DISCUSSION AND COMPARISON.....	147
6.1.1 FDM RP RESULTS.....	147
6.1.2 PHYSICAL TESTING RESULTS.....	150
6.1.3 FEA SIMULATION RESULTS.....	152
6.1.4 COMPARISON OF RESULTS.....	155
6.2 STATISTICAL RESULTS REFINEMENT.....	166
CHAPTER VII CONCLUDING REMARKS AND FUTURE WORK.....	169
7.1 CONCLUSIONS.....	169
7.2 RECOMMENDATIONS.....	170
7.3 FUTURE WORK.....	171
REFERENCES.....	173
APPENDIX.....	177
VITA AUCTORIS.....	207

LIST OF TABLES

Table 1.1: Materials utilized in their respective AM technology.....	4
Table 1.2: Standardized interfaces used in practice.....	7
Table 1.3: Characteristics of currently available RP technologies.....	11
Table 1.4: Values for the different variables for the FDM Prodigy 1000®.....	14
Table 1.5: Properties of common polymers	20
Table 2.1: FDM manufacturing parameters.....	29
Table 2.2: Specific parameters and their description.....	32
Table 2.3: Parameters and levels describing the optimization of the FDM process.....	34
Table 2.4: Filament micrographs of different raster orientations.....	37
Table 2.5: Average tensile strength at different build planes and raster angles.....	40
Table 2.6: Yield stress for different samples at different parameter values.....	41
Table 2.7: Compressive samples micrographs with different raster gap.....	42
Table 2.8: Summary of FDM manufacturing parameters and researchers cited in this thesis	45
Table 2.9 Summary of the overall parameters and their levels of the present study	47
Table 2.10: Selected parameters and their levels for the present study.....	48
Table 3.1: Schematics for the different specimens with internal voids.....	61
Table 3.2: Strength, time, and material use values for parts in different void angles.....	64
Table 3.3: Build parameters for the compressive inside porous parts	67
Table 3.4: Values from the tensile test at different angle orientations.....	69
Table 3.5: Mechanical properties of the upright specimens at different angle orientations.....	69
Table 4.1: Steps to construct the basic parametric element.....	82
Table 4.2: Dimension differences between the loose and the compact mode specimens.....	84
Table 4.3. Orthogonal, hexagonal, and pyramid geometrical elements studied in the present research.....	85
Table 4.4: Study and machine-related parameters involved in the present research.....	90
Table 4.5: Level descriptions and correspondence for the factors studied.....	91
Table 4.6: RP software results at the moment of rapid prototyping the tensile specimens.....	92
Table 4.7: RP software results at the moment of rapid prototyping the compressive specimens.....	93
Table 4.8: Layered tensile CAD models obtained from the RP software oriented in the XY planes.....	94
Table 4.9: Layered tensile CAD models obtained from the RP software oriented in the YZ planes	96
Table 4.10: Layered compressive CAD models obtained from the RP software oriented in the XY	

planes	97
Table 4.11: Layered compressive CAD models obtained from the RP software oriented in the YZ planes	99
Table 4.12: Variable description and respective abbreviation	103
Table 5. 1 ASTM D-638 Type I specimen dimensions [ASTM]	110
Table 5.2: Compressive properties and respective description	111
Table 5.3: ASTM D-695 specimens dimensions [ASTM]	112
Table 5.4: Load values obtained from the physical tensile testing (3 samples per exp. = 96 reps.)	119
Table 5.5: Advantages and disadvantages of compression testing	120
Table 5.6: Load values obtained from the physical compressive testing (3 samples per exp. = 96 reps.)	122
Table 5.7: Abaqus/CAE® FEA simulation parameters, mechanical properties, and mesh schematics	126
Table 5.8: FEA simulation of the solid/hollow specimens' deformation and stress distribution	129
Table 5.9: FEA simulation of the loose/compact orthogonal specimens' deformation	131
Table 5.10: FEA simulation of the loose/compact hexagonal specimens' deformation	132
Table 5.11: FEA simulation of the solid/hollow specimens' deformation and stress distribution	133
Table 5.12: FEA simulation of the loose/compact orthogonal specimens' deformation and stress	135
Table 5.13: FEA simulation of the loose/compact hexagonal specimens' deformation and stress	136
Table 5.14: FEA simulation of the loose/compact pyramid specimens' deformation and stress	138
Table 5.15: Variable description and corresponding abbreviation	139
Table 5.16: Comparison between the internally enhanced blow mold half and the solid blow mold half	146
Table 5.17: Potential savings when adopting the internally modified blow mold	146
Table 6.1: Experiment number and complete description for tensile and compressive specimens	148
Table 6.2: Material/Load ratio x 100 for tensile specimens	164
Table 6.3: Material/Load ratio x 100 for compressive specimens	165
Table 6.4: Summary of the RA models for the orthogonal, hexagonal, and pyramid structures and load	167
Table 6.5: General model of the main interactions from the RA for the tested specimens	168

LIST OF FIGURES

Figure 1.1.1: Final part obtained from the material removal RP process.....	1
Figure 1.1.2: Number of responses of the RP models based on their industrial application	2
Figure 1.1.3: Situation of the LM process with respect to conventional manufacturing technologies depending upon complexity and quantity.....	3
Figure 1.1.4: End use of Additive Manufacturing prototypes.....	5
Figure 1.1.5: Additive Manufacturing process from the virtual CAD model to the physical RP model	6
Figure 1.1.6: STL representation of a sphere in two different facet sizes	8
Figure 1.1.7: Data acquisition source variation and the common process path among them.....	9
Figure 1.1.8: Schematic of the FDM machine	13
Figure 1.2.1: Comparison of a normal and a distorted FDM part.....	15
Figure 1.3.1: Atomic and molecular arrangement of isotropic and anisotropic materials.....	19
Figure 1.3.2: RP ABS scaled differential support for a 1977 GMC Corvette.....	21
Figure 1.3.3: Tensile strength for parts RP in different raster angle orientations.....	24
Figure 1.3.4: Compressive strength for parts RP in different part orientations.....	25
Figure 2.1.1: Schematic of the FDM feeding head assembly and build platform.....	30
Figure 2.1.2: Difference in the raster fill approach.....	31
Figure 2.1.3: Bond formation between deposited FDM rasters.....	32
Figure 2.1.4: Two-section cantilevered geometry.....	36
Figure 2.1.5: Strength variation depending upon the raster orientation.....	36
Figure 2.1.6: Failure paths of tensile specimens upon the raster orientation	38
Figure 2.1.7: Level values for a set of different manufacturing parameters.....	39
Figure 2.1.8: Tensile specimens oriented in different positions in the build chamber.....	40
Figure 2.1.9: Compressive strength, raster gap, and porosity comparison	43
Figure 2.3.1: INSIGHT® user interface.....	47
Figure 2.3.2: Methodology followed in the present study.....	48
Figure 3.1.1: Skeleton extension of the octree elements.....	51
Figure 3.1.2: Sub-boundary octree distribution inside the bounding cube.....	51
Figure 3.1.3: RP part with internal sub-boundary octree structures.....	52
Figure 3.1.4: Raster path optimization for the internal fill.....	53
Figure 3.1.5: Free form geometry with the optimization algorithm.....	53
Figure 3.1.6: ABS RP part with the free form geometry optimization algorithm.....	54

Figure 3.1.7: Hollowing process based on the 3D surface geometry	54
Figure 3.1.8: Swept volume obtained based on the 3D surface geometry.....	55
Figure 3.1.9: Schematic of the force acting on the investment casting inner walls.....	56
Figure 3.1.10: Investment casting internal structures.....	57
Figure 3.1.11: Hoop stresses on the ceramic casting walls for different structures	58
Figure 3.1.12: Truss structural geometries before and after RP.....	59
Figure 3.1.13: Node bonding truss morphology.....	59
Figure 3.1.14: Simple and complex geometrical structures obtained by truss bonding.....	60
Figure 3.1.15: Von Mises stress distribution for the specimens with internal voids.....	62
Figure 3.1.16: Material use, maximum stresses, and build time for the void specimens	63
Figure 3.1.17: Double narrow-waisted specimen.....	65
Figure 3.1.18: Cylinder orientation affecting the topology of the RP part.....	66
Figure 3.1.19: Compressive test part with inside porous parts.....	66
Figure 3.1.20: Mono filament tensile stress equations.....	68
Figure 3.1.21: Internal node approximation for different geometries.....	71
Figure 3.1.22: Mesh approximation to different strut geometries.....	71
Figure 3.1.23: Mesh refinement based on the resulting strut filleting.....	72
Figure 3.1.24: SLA RP parts constructed via truss bonding.....	72
Figure 3.1.25: 2.5D and 3D SLA RP parts with the proposed truss approach.....	73
Figure 3.1.26: 2.5D and 3D structures constructed by inside geometry warping functions.....	74
Figure 3.1.27: Gaps and overlaps refinement at the node level.....	75
Figure 3.1.28: Internal structures allocated inside a hollow part based on trusses and struts	76
Figure 4.1.1: Process for modeling the basic parametric element.....	83
Figure 4.1.2: SolidWorks® interface for setting up or modifying the parametric relations	83
Figure 4.1.3: Basic CAD modeling process to construct the geometrical elements.....	85
Figure 4.1.4. CAD modeling process for assembling the parametric matrix-type structure.....	86
Figure 4.1.5. CAD process flow for modeling the specimen parts with internal parametric structures.....	87
Figure 4.2.1: CAD models for the tensile samples with different internal structures.....	88
Figure 4.2.2: CAD models for the compressive samples with different internal structures.....	89
Figure 5.1.1: ASTM D-638 Type I specimen characteristics.....	110
Figure 5.1.2: ASTM D-695 cylinder and rectangle specimen characteristics.....	112
Figure 5.2.1:Engineering stress-strain diagram for common thermoplastics.....	113

Figure 5.2.2: Tensile specimen evidencing necking behavior.....	113
Figure 5.2.3: Difference of the mechanical behavior for tension and compression.....	114
Figure 5.2.4: Stress-strain diagram for plastic materials.....	115
Figure 5.2.5: Engineering stress-strain and true stress-strain diagrams.....	116
Figure 5.3.1: Tinius Olsen® tensile/compressive equipment setup.....	117
Figure 5.3.2: Tensile test setup while testing.....	117
Figure 5.3.3: Force effect in the a tensile specimen.....	118
Figure 5.3.4: Compressive test setup while testing.....	120
Figure 5.3.5: Load effect in a compressive specimen.....	121
Figure 5.4.1: Fiber-to-fiber interface strength model.....	124
Figure 5.4.2: Load and displacement of physical and simulation experiments.....	125
Figure 5.4.3: Necking FEA simulation of a tensile specimen via ANSYS®.....	125
Figure 5.4.4: Constraints location for the compressive and tensile specimens.....	127
Figure 5.4.5: True stress-strain diagram from the average solid tensile specimens tests.....	128
Figure 5.4.6: Load and displacement diagram for the solid and hollow tensile specimens.....	129
Figure 5.4.7: Load and displacement diagram for the loose and compact orthogonal tensile specimens.....	130
Figure 5.4.8: Load and displacement diagram for the loose and compact hexagonal tensile specimens.....	131
Figure 5.4.9: Load and displacement diagram for the solid and hollow compressive specimens.....	133
Figure 5.4.10: Load and displacement diagram for the loose and compact orthogonal compressive specimens.....	134
Figure 5.4.11: Load and displacement diagram for the loose and compact hexagonal compressive specimens.....	136
Figure 5.4.12: Load and displacement diagram for the loose and compact pyramid compressive specimens.....	137
Figure 5.6.1: Plastic bottle blow mold design process.....	144
Figure 5.6.2: Internally enhanced hollowed blow mold half and solid blow mold half.....	145
Figure 6.1.1: Material use results for the tensile specimens.....	149
Figure 6.1.2: Material use results for the compressive specimens.....	150
Figure 6.1.3: Maximum load results for the tensile specimens.....	151
Figure 6.1.4: Maximum load results for the compressive specimens.....	152
Figure 6.1.5: Mechanical behavior of the tensile specimens from the FEA simulation.....	153
Figure 6.1.6: Detail of the behavior of specific tensile specimens from the FEA simulation.....	153

Figure 6.1.7: Mechanical behavior of the compressive specimens from the FEA simulation	154
Figure 6.1.8: Detail of the behavior of specific compressive specimens from the FEA simulation	155
Figure 6.1.9: Similitude between the FEA and physical tensile testing	156
Figure 6.1.10: Similitude between the FEA and physical compressive testing	157
Figure 6.1.11: Data range values from the physical tests for the tensile specimens	158
Figure 6.1.12: Data range values from the physical tests for the compressive specimens	159
Figure 6.1.13: Physical load and model material comparison for all the tensile specimens	160
Figure 6.1.14: Physical load and model material comparison for all the compressive specimens	161
Figure 6.1.15: Physical load and build time comparison for all the tensile specimens	162
Figure 6.1.16: Physical load and build time comparison for all the compressive specimens	163
Figure 6.1.17: Physical load, model material, and build time comparison for all the tensile specimens	164
Figure 6.1.18: Physical load, model material, and build time comparison for all the compressive specimens	165

CHAPTER 1

INTRODUCTION

1.1 INTRODUCTION TO RAPID PROTOTYPING

Rapid Prototyping (RP) is a manufacturing term that pertains to the automatic creation of tangible models - prototypes - from three-dimensional (3D) computer-aided design (CAD) math data. The term “*rapid*” refers to the quick creation of physical models compared to traditional methods. These traditional methods pertain to manufacturing processes such as, but not limited to, turning, milling, drilling, grinding, eroding, etcetera [Gebhardt, 2003]. RP can be performed by either material removal or material addition. In the material-removal RP process [Santos, 2005], the machine extracts the part out from a block of the desired material using computer-numeric controlled (CNC) machining centers as depicted by Figure 1.1.1 [Santos, 2005]. In the material-addition RP process, the prototype is made by the addition of layers of material. Bak et al. refer to “*true*” rapid manufacturing systems to the ones that use additive processes to deliver finished parts directly from the math data eliminating all tooling [Bak, 2003].

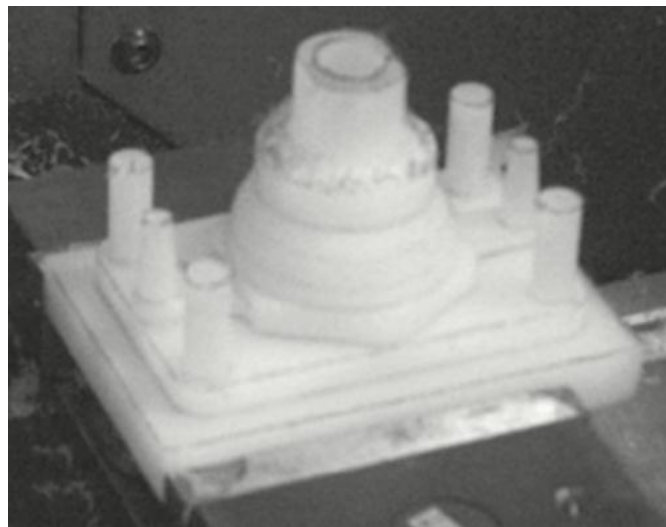


Figure 1.1.1: Final part obtained from the material removal RP process [Santos, 2005]

Prototypes have been extensively used in many fields of the industry and at any design phase of any given product. The conceptualization and preparation of physical tangible models is of special importance in the education and in the research fields. Prototypes allow a far better 3D visualization of parts leading to enhance the geometric interpretation and spatial analysis. As a

result, prototypes heighten the optimization of manufacturing resources by reducing the trial-and-error in manufacturing. Allowing a better analysis of the interference with other parts and the kinematic behavior of the product within a system reduces the risk of failure and enhances the productivity [Santos, 2005]. Figure 1.1.2 [Bak, 2003] depicts a chart that shows the response in number of prototype models based on the use for all the industrial applications that can be found. As it can be seen, the three main applications of prototype models are: as functional models, as visual aids for engineering, and for the verification of the fit and final assembly of the part. In other words, prototypes provide a way to demonstrate form, function, and the visual aspect of the design intent in an efficient way.

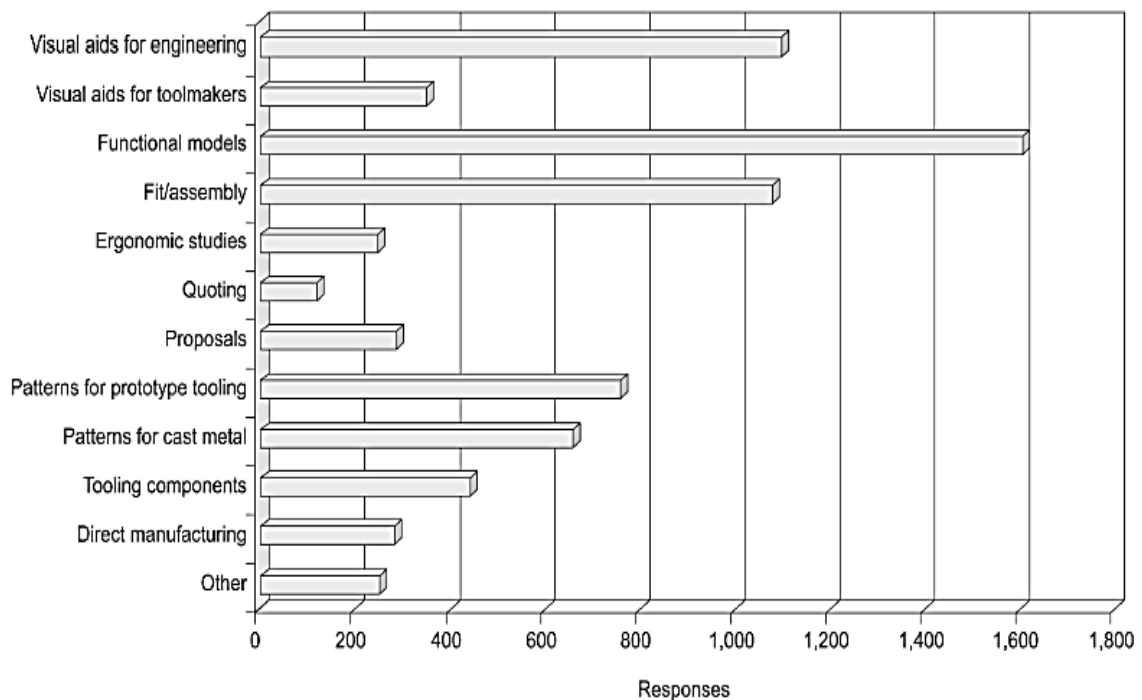


Figure 1.1. 2: Number of responses of the RP models based on their industrial application [Bak, 2003]

The present study focuses on the material-addition RP, also known as Layered Manufacturing (LM). Rapid prototyping allows designers and engineers to make prototypes faster and cheaper. As mentioned before, it avoids the use of tooling equipment and reduces the level of complexity in the manufacturing phases. LM has its own specific niche within the manufacturing industry and has proven that is commercially sustainable. According to Levy et al., in terms of competitiveness with other manufacturing processes regarding geometrical complexity and required quantities, LM has found its own market share and has even been able to provide parts from medium to high geometrical complexity at relatively low quantities [Levy, 2003]. As it can be seen in Figure 1.1.3 [Levy, 2003], the direct metal-type LM situates in a privileged place

and its borders (complexity and quantity) float within the chart and depend on a case-to-case basis. However, in principle, more productive and better performing LM processes and machines will shift the corresponding upper quantity-capability limit upwards.

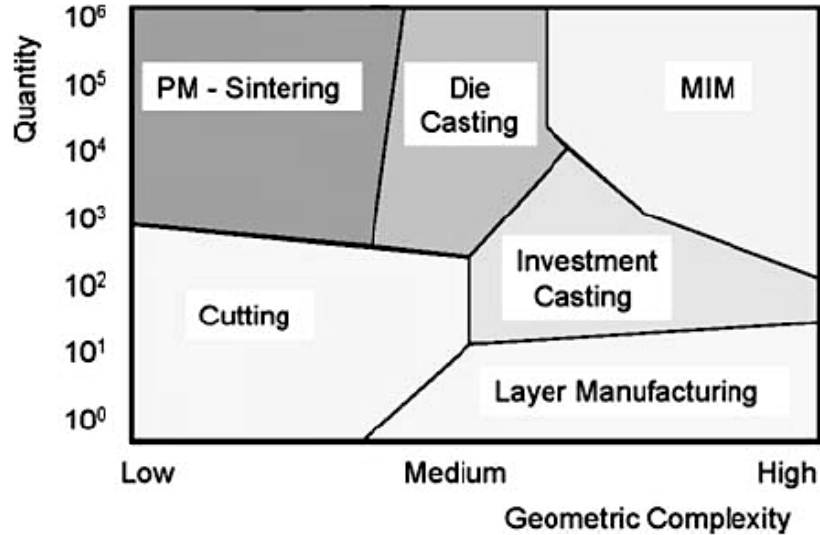


Figure 1.1. 3: Situation of the LM process with respect to conventional manufacturing technologies depending upon complexity and quantity [Levy, 2003]

Generally, for small production runs and more complex parts, LM has been considered as the best manufacturing strategy according to Saravanan et al. [Saravanan, 2010]. In this regard, the LM technologies described in Section 1.1.5 of this chapter have been successfully applied to produce low-volume end-use parts. Nevertheless, LM is a term that does not exactly mean the fabrication of “instant” prototypes. Depending on the size, the math data complexity, and the LM technology used, prototypes may require from two to twenty-four hours for completion. Comparatively, this time is less than the time (sometimes weeks or months) required to building a part by means of traditional techniques – subtractive and/or removal [Bak, 2003].

It would be ideal to merge LM capabilities with the high-volume throughput traditionally associated with conventional manufacturing technologies. Terry Wohlers, from The Wohler Report [<http://www.wohlersassociates.com>, 2012], states: “*for RP to better penetrate new markets, a number of changes must occur. Machines must become less expensive to buy and easier to use and maintain. System prices and the overall cost of ownership must drop further and materials must improve*” [Bak, 2003]. Meeting this challenge involves the proper implementation of manufacturing paradigms such as mass customization and agile manufacturing, which are possible in the LM domain.

1.1.1 INDUSTRIAL RAPID PROTOTYPING SYSTEMS

Layered Manufacturing systems use cross-sectional data from a computer source to build 3D objects layer after layer. Section 1.1.5 of this chapter briefly describes the basics of LM technologies whereas Section 1.1.6 comprises a detailed review of a kind of LM technology known as Fused Deposition Modeling (FDM) - the subject of study in the present research.

At this point, it is important to express that the term Additive Manufacturing (AM) is also used, indistinctively, to refer to Layered Manufacturing (LM). As mentioned before, the prototypes' applications vary from concept visualization to functional analysis. The most utilized additive/layered/rapid manufacturing and/or prototyping technologies in the industry and in the academia are: stereolithography (SLA), selective laser sintering (SLS), fused layer modeling (FLM) or fused deposition modeling (FDM), 3D printing (3DP), laminate object manufacturing (LOM), and ballistic particle modeling (BPM) [Gebhardt, 2003]. Each of these technologies has its own advantages and disadvantages; however, all of them share the same principle: material addition. In fact, the materials used from one to the other may differ considerably. Table 1.1 comprises some of the materials used by these AM technologies.

Table 1. 1: Materials utilized in their respective AM technology [Gebhardt, 2003]

AM Technology	Material used
Selective Laser Sintering (SLS)	Thermoplastics, metal powders
Laminated Object Manufacturing (LOM)	Paper
3D Printing (3DP)	Powder, various
Stereolithography (SLA)	Photopolymer
Solid Ground Curing (SGC)	Photopolymer
Fused Deposition Modeling (FDM)	Thermoplastics, eutectic metals

As it can be seen in Figure 1.1.4 [Bak, 2003], the industrial use of AM parts according to their end application has an extensive scope. The use of AM models as consumer products and in the automotive industry has the most extensive partition. In addition, the aerospace industry, business machines, and the medical applications have the second largest portion of the market. In third place, the government/military, academic institutions and other uses are located at the bottom of the chart [Bak, 2003].

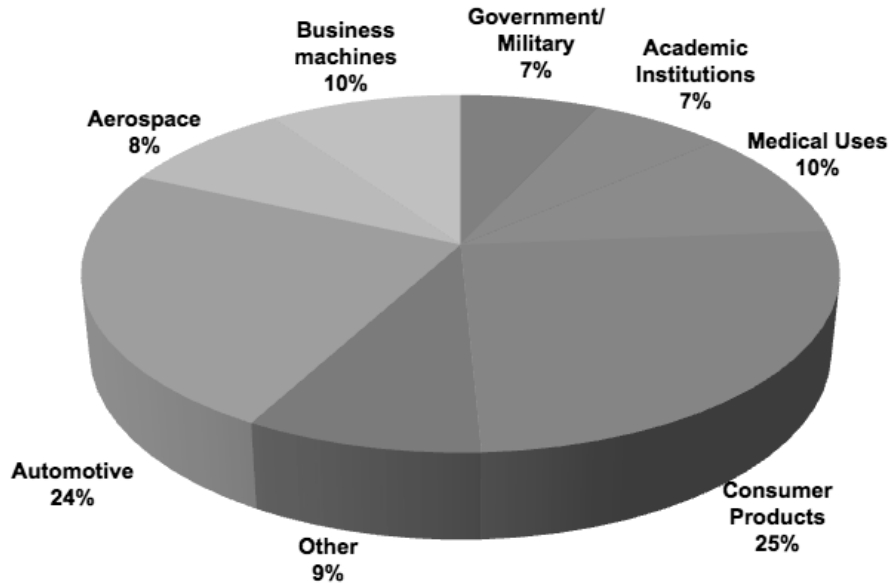


Figure 1.1. 4 End use of Additive Manufacturing prototypes [Bak, 2003]

Some years ago, companies did weigh whether their technology was used as a generic term or not. Due to the increasing demand for such systems, companies have intellectually protected and trademarked the generic term to advertise and sell their own products. Stratasys®, for example, owns the trademark of the technology known as Fused Deposition Modeling (FDM). Nowadays, many competitors have entered into the market with similar or somehow related technologies. Trademark owners observe accurately if their brand name is not used for advertising the competitor's own products [Bakar, 2010]. It is well known that rapid prototyping has positioned in the interest of people over the past twenty years. It was estimated, as in 2001, that the production of models and prototypes reached around 3.55 million and the numbers kept growing steadily at a rate of twenty percent per year. According to estimates, about 1000 machines were sold from 1998 to 2003 and about 400 RP service centers were established worldwide [Levy, 2003].

1.1.2 THE RAPID PROTOTYPING PROCESS

Once the designer has opted for the AM manufacturing process, there are certain necessary steps to be performed. Independently from which AM technology was chosen to be used, all the known AM processes share specific steps. These basic steps are classified into two fundamental process steps: (i) the generation of the mathematical information (math data) and (ii) the generation of the physical layered model. Likewise, these two processes are decomposed into the following: (a) the creation of a computer-aided design (CAD) model, (b) the conversion of the CAD file to a suitable RP format, (c) the slicing of the converted file into two-dimensional (2D) cross-sectional

layers, (d) the construction of the model, and (e) the finishing and post-processing of the model. The generation of the mathematical information is based on a purely computer-oriented CAD model. The CAD model is cut into layers by mathematical methods. This layer information is used for the generation of physical single layers in the RP machine. The total sum of the single layers stacked one on top the other builds the physical model. Figure 1.1.5[Gebhardt, 2003] depicts the aforementioned process.

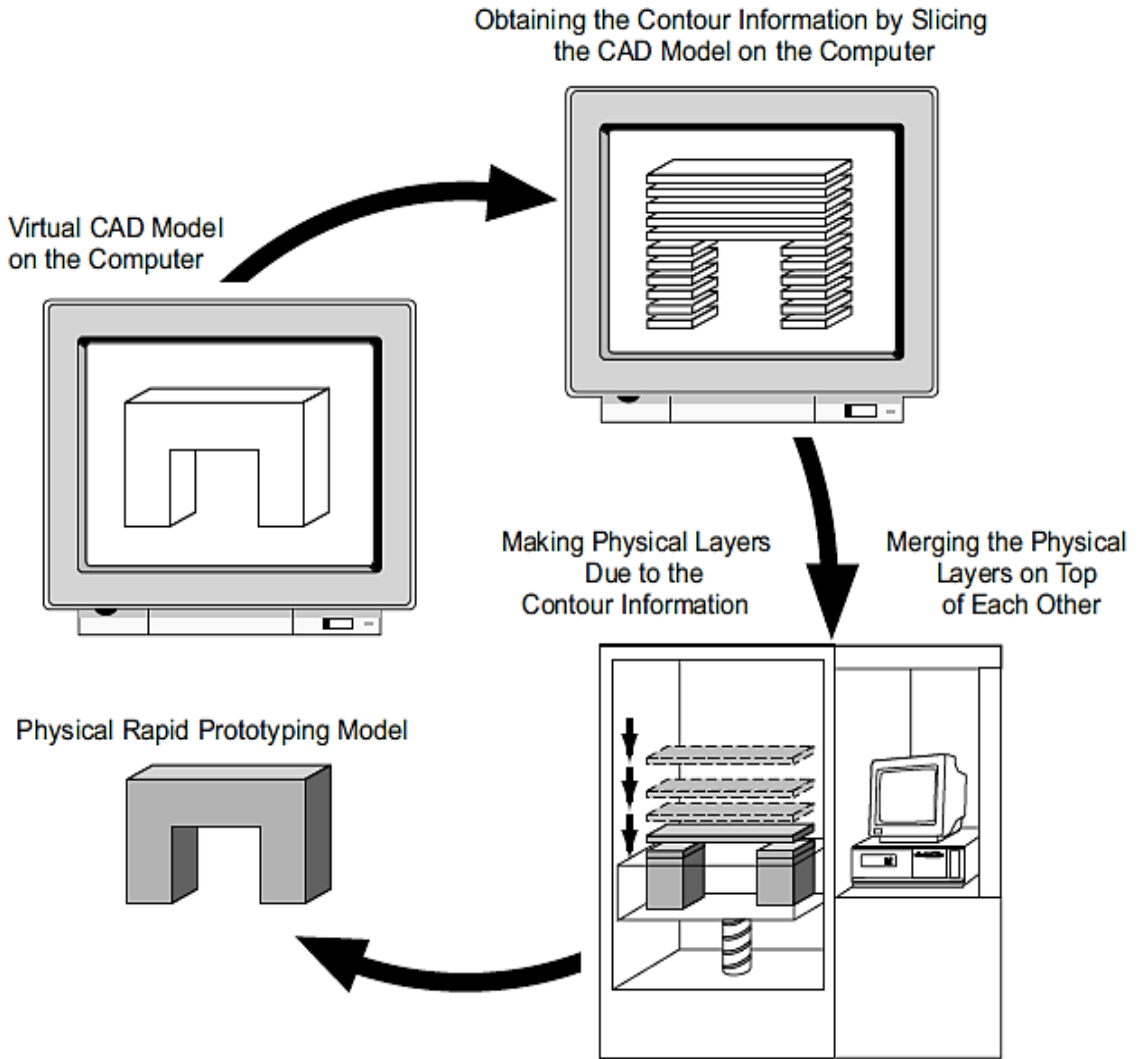


Figure 1.1. 5 Additive Manufacturing process from the virtual CAD model to the physical RP model [Gebhardt, 2003]

1.1.3 CAD SYSTEMS

A complete three-dimensional (3D) math data set (3D solid model) is produced in a 3D CAD system. CAD modeling software such as SOLIDWORKS®, CATIA®, NX®, INVENTOR®, and AUTOCAD® represent 3D solid models via a number of different algorithms and mathematical representations. Regardless of their operating platform, it is desirable to transmit the math data via standardized interfaces – standard formats. Interfaces have grown with CAD systems. Today, a large number of different interfaces exist. Table 1.2 comprises the most popular interfaces for the majority of today’s CAD systems. For rapid processing, only geometric data is required and none of the additional information or CAD attributes (all-level constraints, associativity, parametrics, and materials’ properties) usually included in complete CAD data. Once the 3D model is designed, the file is usually converted into the Standard Tessellation Language (STL) format. Depending on the complexity, the size of the 3D math data (file), and on the CAD system, the processing time varies.

Table 1.2: Standardized interfaces used in practice [Gebhardt, 2003]

Standardized Interfaces	Definition
IGES	Initial Graphics Exchange Specification
VDA	Verband der Automobilhersteller
DXF	Drawing Exchange Format
SET	Standard d’Echange et de Transfer
STEP	Standard for the Exchange of Product Model Data
STL	Standard Tessellation Language

Math data transfer is possible with the use of the STL file standard format. The STL format provides a method of representing a closed boundary model – a method to represent triangles. These are described by the X-Y-Z coordinates at the three vertex points and a surface normal vector indicating the facet orientation and defining which side faces out. An STL file only contains a list of facet data without any topological information [Urbanic, 2004]. This mathematical type of representation (binary and/or ASCII) makes the model math data more compact, hence more manageable. As a consequence, this format has become the industry’s standard. Nevertheless, common errors in the STL data set such as interrupted surfaces, overlapping faces, and missing edges need correction. A common mistake in STL data derives from the incorrect orientation of surfaces. That is to say, a normal vector pointing to the inside of the component could lead to problems when generating machine data, best described in Section

1.1.4 of this chapter, as the interior and the exterior of the component to be produced may not always be differentiated. Often, surfaces that are not exactly partitioned may result in gaps in the STL data. Figure 1.1.6 [Gebhardt, 2003] shows the errors resulting from the translation of 3D math data into the STL faceted math data. It is evident that there is a loss of math data which misrepresents the 3D model.

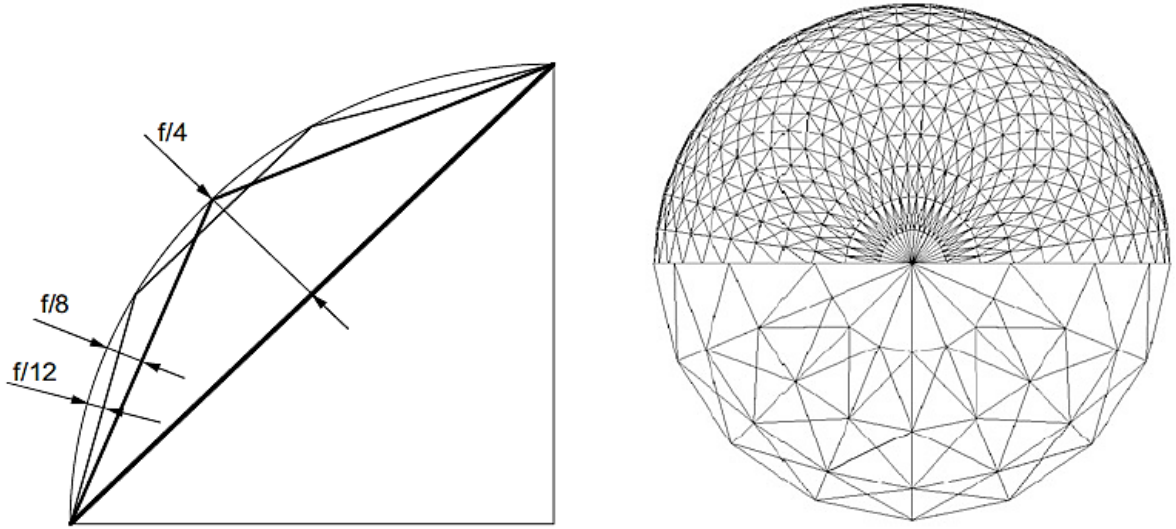


Figure 1.1. 6: STL representation of a sphere in two different facet sizes [Gebhardt, 2003]

In addition to the common sources of 3D data generation explained above (CAD modeling software), there are several other possibilities for obtaining data for model making as it can be seen in Figure 1.1.7, where examples of possible data acquisition sources and processing flows are depicted [Gebhardt, 2003].

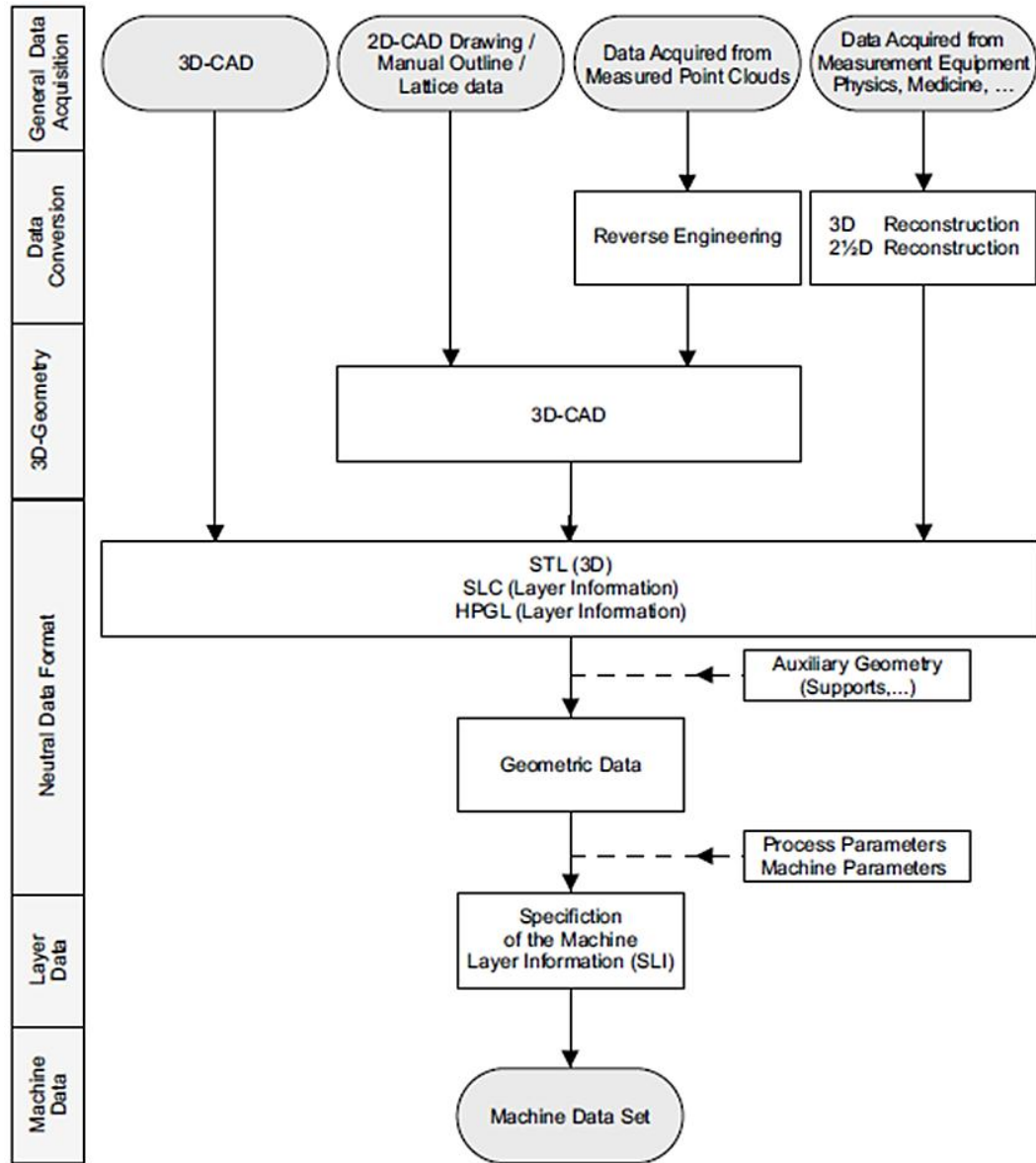


Figure 1.1. 7 Data acquisition source variation and the common process path among them [Gebhardt, 2003]

1.1.4 RP MACHINE SOFTWARE

There is a number of RP software packages that processes the STL, or any similar file such as SLC, file obtained from 3D CAD systems. Most of the RP software such as CATALYST®, QUICKSLICE®, INSIGHT®, and ZPRINT® repair, orient, re-orient, scale, color, engrave, mirror, partition, and “*print*” the 3D model file. Nevertheless, the most important function is to “*slice*” horizontally, into thin sections, the 3D model.

The second most important feature of the RP software is to determine the parameters pertaining to layer resolution, interior fill, and the type of support, whenever those apply. The level of complexity of the RP software varies depending on the LM technology utilized. Regarding to the fundamental function of the software, the obtained 2D sections represent the 3D model's two-dimensional cross-sections from top to bottom or vice versa. These 2D sections, when stacked upon one another, correspond to the original 3D part. The greater the number of 2D sections - "*slices*" - the more refined the 3D model the higher layer resolution.

Once all the manufacturing parameters have been entered, best described (for the fused deposition modeling technology) in Section 2.1.1 in Chapter II of this thesis, the software creates layers made of boundary polygons and lines where the material will or will not be deposited. If needed, the software will generate an auxiliary structure to provide support during the construction of the model. The generation of auxiliary geometries such as supports and similar, which may not be necessary in every LM technology, is done by either with the generation of geometrical data or separately with the aid of embedded algorithms in the RP software [Gebhardt, 2003]. A build file will be created and translated into the LM machine's internal language where X-Y coordinates determine the travel paths of the extrusion (material depositing) head [Urbanic, 2003].

1.1.5 LAYERED MANUFACTURING TECHNOLOGIES

As previously mentioned, Layer Manufacturing (LM) technologies are often referred to as Rapid Prototyping (RP) technologies. A universally agreed terminology does not exist and depends on the context of use. LM technologies have some generic and exclusive common features, as described in previous Section 1.1.2, which encompass a number of processes between them. However, those technologies differ in terms of physical processes, geometry, and materials that can be processed and, thus, their performance [Levy, 2003].

Once a particular process is selected the next step is to generate a process plan. Designers still face difficulties in making decisions regarding the selection of methods, materials, and machines out from the different RP technologies available. Table 1.3 [Pande, 2008] discloses a comparison of the RP technologies currently available and their specific features. As it can be seen, LM technologies still have wide deficiencies with respect to accuracy and repeatability, which are typically in the range of 0.1 to 0.2 mm.

Table 1. 3: Characteristics of currently available RP technologies [Pande, 2008]

Technology	Stereo-lithography	Wide area inkjet	Selective laser sintering	Fused deposition modeling	Single jet inkjet	Three dimensional printing	Laminated object manufacturing
Representative vendor	3D Systems			Stratasys	Solidscape	Z Corp.	Cubic technologies
General qualitative features							
Maximum part size (inches)	20×20×24	10×8×8	15×13×18	24×20×24	12×6×9	20×24×16	32×22×20
Speed	Average	Good	Average to fair	Poor	Poor	Excellent	Good
Accuracy	Very good	Good	Good	Fair	Excellent	Fair	Fair
Surface finish	Very good	Fair	Fair	Fair	Excellent	Fair	Fair to poor (depending on application)
Strengths	Market leader, large part size, accuracy, wide product line	Market leader, office okay	Market leader, accuracy, materials	Office okay, price, materials	Accuracy, finish, office okay	Speed, office okay, price, color, price	Large part size, good for large castings, material cost
Weaknesses	Post processing, messy liquids	Size and weight, fragile parts, limited materials, part size	Size and weight, system price, surface finish	Speed	Speed, limited materials, part size	Limited materials, fragile parts, finish	Part stability, smoke finish and accuracy
System price	\$75-800 K	\$50 K	\$300K	\$30-300K	\$70-80 K	\$30-70 K	\$120-240 K
Material costs \$/pound							
Plastics	\$75-110	\$100	\$30-60	\$115-185	\$100		\$9
Metal			\$25-30				
Other			\$5 (foundry sand)			Starch: \$0.35/cu.in., Plaster: \$0.60/cu.in.	\$5-8 (paper)

Once a build file has been created, the next step is to manufacture the part. The LM machine performs this phase automatically. Most of the LM technologies generate the cross-section in the X-Y plane and join the layers with the preceding one. This arrangement in the Z-direction with one another is achieved in the same way as joining them in the X-Y direction. A number of layered manufacturing process, specific parameters, and constraints are to be considered while deciding the part deposition orientation. Determination of an optimal part deposition orientation is a difficult and time-consuming task as disclosed by Pandey et al. [Pandey, 2007]. Likewise, a considerable number of researchers have studied the effects of the layer deposition topology in terms of the mechanical properties of the finished product. A brief review of these studies on one type of LM technologies (fused deposition modeling also known as FDM) is disclosed in Section 1.3.4 of this chapter.

1.1.6 FUSED DEPOSITION MODELING

The fused deposition modeling (FDM) process builds a model from layers of molten thermoplastic filaments. The FDM technology was established in the late 1980s while the model FDM Prodigy Plus® was developed during several series of models (such as FDM Vantage®, FDM Maxum®, and FDM 3000®) in the late 1990s [Bakar, 2010].

The filament is fed through a heating element (controlled head) where it is semi melted. Then, the filament is pushed through a nozzle and deposited exactly on the build chamber's substrate. The deposited material fuses with the already deposited material around it. The extrusion head is mounted on a computer X-Y positioning system and moved around the X-Y plane depositing material according to the STL file characteristics and the build file instructions (obtained from the RP software). The extrusion head repeats this same procedure depositing material layer after layer to produce the 3D model.

Initially, the substrate lies on a table that can be moved up and down in the Z plane. After one layer has been deposited, the table indexes lower in order to deposit another layer; the distance depends on the desired layer thickness. Finite length roads of fibers compose the layers, and their dimensions are controlled by the material's flow rate and the translation of the extrusion head. The bonding between individual roads and layers is done by molecular diffusion bonding enhanced by the thermal energy of the extruded fiber in molten state [Rodriguez, 1999]. Layer thicknesses can vary between 0.002 inches to 0.030 inches (0.050 – 0.76 mm) for the Prodigy FDM 1000® from Stratasys® [Urbanic, 2004]. After a number of layers have been deposited, the

part is finally represented such as the model imported from the CAD math data. The FDM process requires a support structure beneath the build material. If any of the layers overhangs the one below, such will fall to the substrate when the extrusion head deposits it. The support material is similar to the model material, but it is more brittle so that it may be easily removed after the model is completed. The FDM machine builds support for any structure that has an overhang angle of less than 45° from the horizontal as by default [Montero, 2001] Nevertheless, newer machines (Stratasys® FORTUS 400mc®) are able to modify the overhang angle as the designer's will until specific limits. As it can be seen in Figure 1.1.8, the FDM machine possesses a primary and a secondary nozzle that extrudes building material and support material, respectively. Figure 1.1.8 [http://www.custompartnet.com/wu/fused-deposition-modeling, 2012] depicts a schematic of the FDM machine's composition.

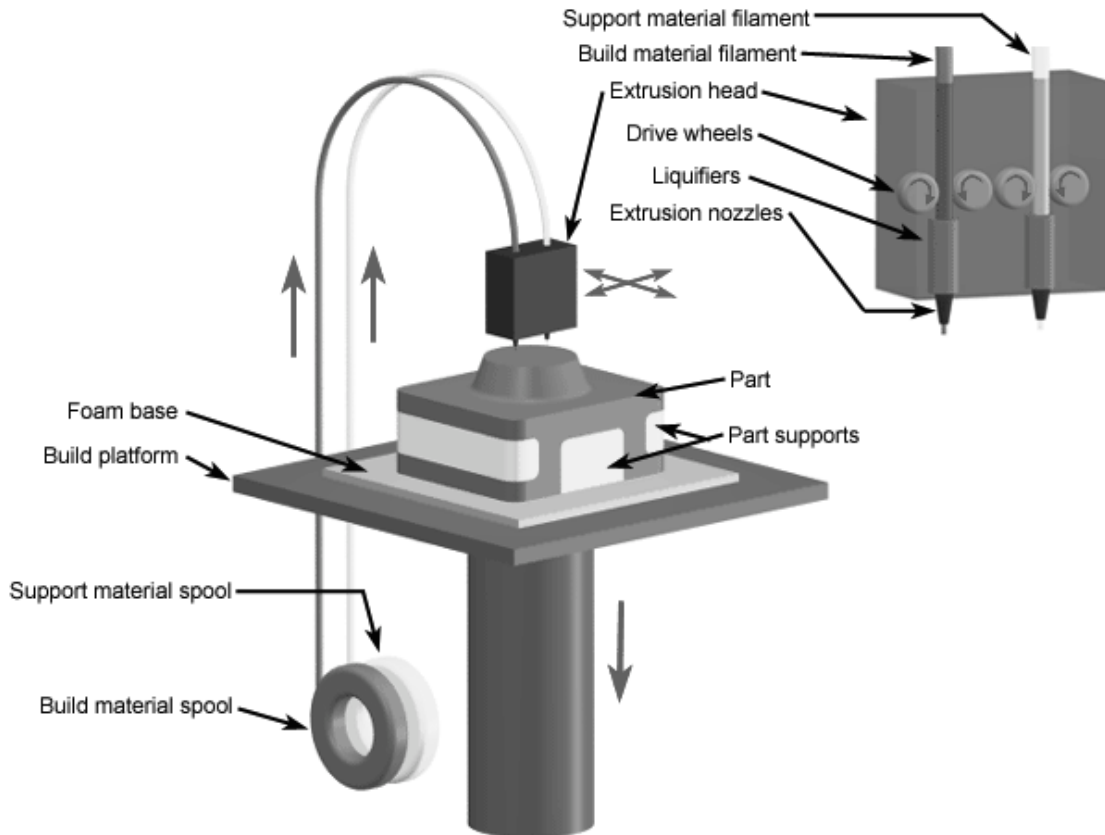


Figure 1.1. 8 Schematic of the FDM machine [www.custompartnet.com/wu/fused-deposition-modeling]

Several materials are available with different trade-offs between strength and temperature properties. As well as acrylonitrile butadiene styrene (ABS) (better described in Section 1.3.3) FDM can be used with polycarbonates, polycaprolactone, polyphenylsulfones, waxes, and newer materials such as ULTEM 9085®. For example, a "water-soluble" material can be used for

making temporary supports while the model material is being deposited. Marketed under the name of Waterworks® by Stratasys®, this soluble support material is quickly dissolved with specialized mechanical agitation equipment utilizing a heated sodium hydroxide solution [Chaturvedi, 2009]. On the other hand, there are two filling styles for the Stratasys FDM® machines: solid and sparse. For the solid build style, there is no air gap; for the sparse build style, there is a large positive air gap and a system defined wall thickness, which is based on three offset perimeter contours. In example, key process data for the FDM Prodigy 1000® machine for the solid and sparse build types is summarized in Table 1.4 [Urbanic, 2004] for the three build modes and their fabrication characteristics [Urbanic, 2004].

Table 1. 4: Values for the different variables for the FDM Prodigy 1000® [Urbanic, 2004]

Variable	Draft	Normal	Fine	Solid	Sparse
Bead Width (mm)	0.026	0.020	0.014	x	x
Layer Height (mm)	0.013	0.010	0.007	x	x
# of Contours - Solid	1	1	1	x	
# of Contours - Sparse	3	3	3		x
# of Solid Bottom Layers - Sparse	3	3	3		x
# of Solid Top Layers – Sparse	3	3	3		x
# of Solid Layers (vertical normal)-Sparse	1	2	4		x
# of Support Layers - loose	3	4	6	x	x
# of Support Layers - solid	1	1	1	x	x
Support Bead Width (mm)	0.018	0.018	0.014	x	x
Support Air Gap (step over) – loose (mm)	0.065	0.05	0.035	x	x
Support Air Gap (step over)- solid (mm)	-0.0018	-0.0018	-0.0014	x	x
Sparse Raster Width (mm)	0.015	0.015	0.014		x
Sparse Raster Air Gap (step over) (mm)	0.150	0.150	0.150		x
Raster Angle 1 (deg)	45	45	45	x	x
Raster Angle 2 (deg)	135	135	135	x	x

1.2 MOTIVATION, THESIS OBJECTIVES, AND SCOPE OF THE RESEARCH

1.2.1 MOTIVATION

As disclosed in Section 1.1.6, FDM is an additive fabrication process that builds a product from thin layers of extruded filaments of a thermoplastic. In the particular case of the FDM – ABS and ABS derivative materials; the part’s mechanical properties depend on the material’s depositing

orientation, flow rate, fiber separation, and extrusion temperatures. These parameters control the meso-structure (extruded fibers' scale approximate to 0.1 mm) characteristics and influence the fiber-to-fiber bonding. The dependence of the material's properties on the manufacturing parameters provides the FDM technology the ability to optimize the mechanical performance. This is accomplished by modifying the meso-structure [Rodriguez, 1999].

There are two main manufacturing strategies for the body of a part built by FDM: solid and shell. There are applications when the solid build strategy may not be necessary and even problematic when there is a thick wall – thin wall condition, which leads to distortion; likewise, a shelled component is too weak. Figure 1.2.1 [<http://electecnik.blogspot.ca/>] depicts a comparison between two finished models of the same part obtained from a FDM machine exhibiting (a) distortion and (b) without distortion.

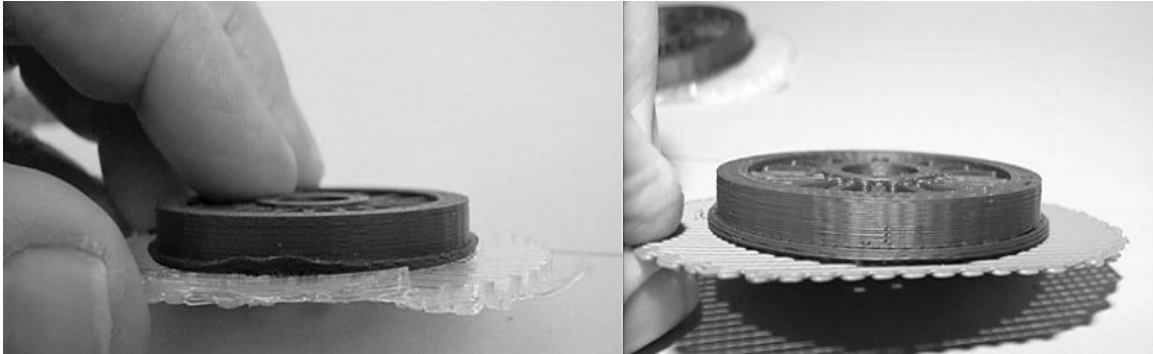


Figure 1.2. 1Comparison of a normal and a distorted FDM part [<http://electecnik.blogspot.ca/>]

Time use and material waste are greatly increased when a part with thick wall conditions needs to be prototyped. Research has shown that when thick and thin wall conditions configure a FDM part, such tends to deform substantially. This phenomenon has not been fully explained yet. For some specific uses, thin wall parts are not desirable since there may be stability and structure mishaps due to the weak composition of the prototypes. Evidently, it is desirable to include supporting structures with specific characteristic that provide the support needed while reducing the manufacturing time and reducing, in some cases balancing, the amount of material used (model and support material). The aforementioned action will decrease the impact on the environment by reducing the material used and by reducing the time the FDM machine is on. At the same time, it is desirable to characterize and ensure the mechanical behavior of the part.

The mechanical properties of the FDM-ABS are governed by the manufacturing parameters; thus, it is important to characterize the material's meso-structure and the mechanical properties as a function of the built parameters which include, among others, the topology of the deposited layers

of the part (which refers to the internal structure arrangement or cross-sectional morphology), the raster orientation, and the part orientation.

1.2.2 THESIS OBJECTIVES

It is the intention to develop a mechanical/material - based understanding that helps designers to optimize the design for strength, optimize the material usage, and balance the component wall thickness by utilizing parametrical internal fill strategies. This will minimize material costs, reduce build times, and improve quality, as some research has shown that the thick wall - thin wall conditions may lead to distortion.

Different internal geometric structures in a web-like array are to be designed using primitive parametric elements. Each of these basic 3D geometric structures (trusses) will be composed by a set of parametrical primitive elements which have the capability to be configurable. This level of flexibility promotes the agile modification of the virtual production component with internal web-like structures. Moreover, it is the intention that this proposed method will reduce the material used which will have a positive impact in the economy and in the environment. Parametric 3D web-like geometries proposed in this research will enable the improvement of the rapid prototyping process in terms of flexibility and modifiability. The modeling approach followed in the present research may be identified in the CAD domain. That is to say, any CAD system, such as the ones referred to in Section 1.1.3 of this chapter, may be used to model the proposed internal web-like structures. In the present research, SolidWorks® from Dessault Systems® is utilized as the CAD modeling system and the modeling methodology is described in Section 4.1 of Chapter IV of this thesis.

Once the parts are modeled in the CAD software, the RP is carried out using the Stratasys® FORTUS 400mc® and the model material utilized was ABS. Based on previous research and considering the novel approach on this study, it was determined that the material is to be characterized by the internal structure type, the internal structure's density, and the raster orientation. The three aforementioned manufacturing parameters are the ones chosen to have the most influence on the part's material meso-structure and macro-structure. The results obtained from the experimental physical testing yield in providing the extreme, lower and upper, values for the computational simulation that characterizes the part's mechanical strength and stiffness. Thereafter, tensile/compressive experiments are conducted on modified specimens (with the proposed internal structures) under identical testing conditions to validate the

analytical/computational experimental simulation. The experimental simulation is carried out by a finite element analysis (FEA) software to make stress, deformation, strain, and strength predictions of the FDM – ABS parts with modified internal web-like structures. The FEA simulation is carried out in the Abaqus® FEA solver from Dessault Systems®. This research intends to identify and characterize the web-like internal structures and their effect on hollow modified FDM produced parts. It is the intention of this study to serve as the basis in the creation of a model that will function as a predictive tool in order to: (i) estimate the mechanical properties of the part, and (ii) calculate the build time and materials utilized based on various internal structural configurations depending upon the part's application.

1.2.3 SCOPE OF THE RESEARCH

To achieve the thesis objectives, the mechanical behavior of the modified FDM parts must be understood and documented. Hence, the investigation requires a comprehensive literature review in order to identify and distinguish the significant research pertaining to this research subject matter. Several sources have been cited in the present job and a comparison of different research areas has been made (encompassed throughout Chapters I to V). Those areas include CAD design, mathematical algorithms for representing CAD math data, polymers and their material properties, rapid prototyping technologies and their impact in the industry and science, design of experiments, analysis of variance and regression analysis, fused deposition modeling, part design for optimization of strength, finite element analysis and simulation, and material testing.

After several sources were identified, discerning yielded the selection of key parameters subject to be studied and explained. However, design of experiments approach is to be followed in order to understand the relationship between the selected parameters since there is a vast number of combinations possible when applying the parameters chosen.

When the relevant information was found, three manufacturing variables were selected as the parameters to be studied. Two of those parameters deal with the experimental characterization of the web-like internal structures, while the last parameter deal with the raster orientation of the prototyped part. Each of said parameters has two levels (as described in Section 2.3 in Chapter II of this thesis) accounting for a total of 16 test specimens. Half of those pertain to the tensile and half to the compressive type of samples.

Once the parameters were chosen, the 3D model representation is to be followed. The 3D model was designed using commercial software. The design allowed for rapid and flexible manipulation

of design parameters within the sketch-constraint level. Thanks to this approach, the parts were easy to modify and to produce two types of internal packing for all the structure: loose and compact. Three geometrical entities were chosen: orthogonal, pyramid, and hexagonal. Based on previous studies, it is desirable to understand the effects of different geometries acting as internal truss structures within the modeled part.

After the modeled parts were cleaned and saved in an appropriate STL format, the specimens were prototyped in the Stratasys® FORTUS 400mc®. The specimens were “*printed*” according to specifications of the selected parameter (in example, raster orientation). Hence, specimens with the same type of structure were printed at different raster orientation and specimens with different level of internal packing were prototyped with the same raster orientation. This would allow identifying the influence of the manufacturing parameters on the mechanical properties of the part.

As part of the goal to characterize the internal structures, physical experiments were carried based on industry standards. Data was recorded for the end values (upper and lower). Also, the same was done for all of the rest of the specimens. However, it must be mentioned that there is not test that considers testing polymers with the topology this novel approach proposed. Hence, the obtained values from all the rest samples are to be considered as experimental and its purpose is to compare them with the results obtained from the FEA simulation.

Finally, analysis of variance is to be performed in order to give meaning to the results obtained from the physical experiments and to obtain an equation that predicts the allowable load based on the structure type as well as the material usage and the build time based on all of the parameters involved in the present research. The virtual experiments will help to set the baseline for a mathematical model that will relate the mechanical properties and build parameters of the prototyped parts.

1.3 BACKGROUND

Engineering materials are typically classified into four classes: metals, ceramics and glasses, polymers, and composite materials. Materials of all types can be used for rapid prototyping; however, for the sake of simplicity, the present research has only considered the subject matter pertaining to polymers and composites, which are used in commercial FDM machines.

The structure of the materials affects their properties and their mechanical behavior. According to their structural arrangement, materials can be classified as crystalline or amorphous. Crystalline

structures are organized structures in which atoms and molecules arrange themselves in a regular and repeating order - lattice. Conversely, amorphous structures show local order, but they do not have a globally ordered structure. Likewise, these materials exhibit different physical properties, such as thermal expansion. Figure 1.3.1 depicts the different atomic and molecular arrangements of materials. Amorphous structures are generally observed in glass and plastic materials; nevertheless, some plastics have a semi-crystalline structure (a combination of both) [Kridli, 2006]. At this point, it is important to define the term isotropic and anisotropic. Isotropic materials' properties are not dependent on the direction whereas anisotropic materials' properties depend on the direction of the structural array of the molecules.

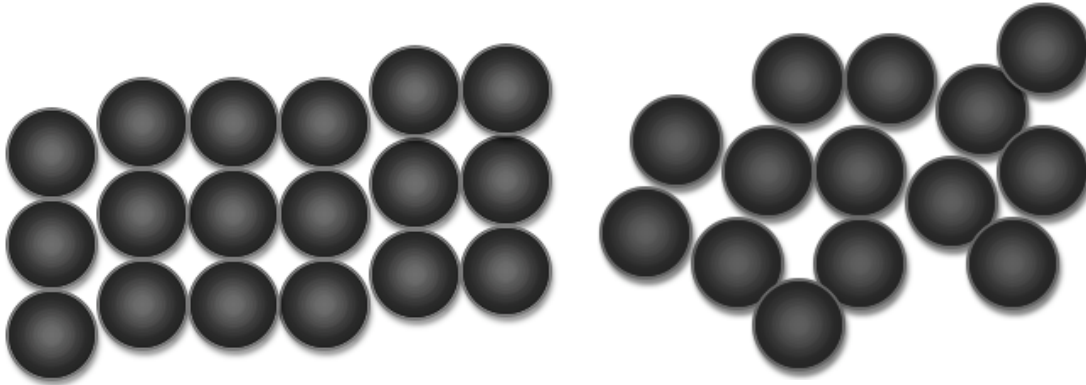


Figure1.3. 1Atomic and molecular arrangement of isotropic and anisotropic materials

1.3.1 POLYMERIC MATERIALS

A polymer is made of multiple repeating molecular structures and has an amorphous or a semi-crystalline structure. Polymers have lower density, strength, and stiffness than metals. They also have very low electrical conductivities, which makes them suitable as insulation materials. Polymers are classified into three groups:

1. Thermoplastics: have a linear or branched structure and can be re-softened by heating and then reshaped.
2. Thermosets: have cross-linked structures that develop upon curing (controlled heating to promote cross linking). Once cured, they cannot be reshaped.
3. Elastomers: have a cross-linked structure. They possess elastic behavior similar to that of natural rubber [Gebhardt, 2003].

Table 1.5 [Kridli, 2006] discloses the mechanical properties of important polymers commonly used in the RP processes.

Table 1. 5: Properties of common polymers [Kridli, 2006]

Material	Structure	Specific Gravity	Rockwell Hardness	UTS MPa	Modulus			Impact Notched Izod J/cm	Temperature (°C)		
					Elongation to Fracture	Tensile GPa	Flexure GPa		Deflection at 460 kPa	Glass	Melting
ABS	A	1.05	110 R	42.0	27%	2.40	2.40	2.50	68-140	107-115	
Acrylics	A	1.18	91 M	68.7	6%	3.10	3.30	0.16	80-103	100-105	130
Nylon	S	1.12	110 R	73.1	83%	2.10	2.40	1.50	85-245		250
Polycarbonate	A	1.21	120 R	69.4	96%	2.60	2.40	6.80	128-174	145-148	
Polyester											
PBT	A,S	1.42	120 R	57.1	36%	2.70	2.90	2.10	95-225		220
PET	A,S	1.32	110 R	55.0	130%	2.70		1.40	68-72	73-78	250
Polyethylene											
LDPE	S(55 % C)	0.92	60 R	11.0	190%	0.21	0.27	3.90	40-67		110
HDPE	S(90 % C)	0.96	63 R	20.3	380%	0.91	1.10	1.90	60-104		130
Polypropylene	S	0.94	96 R	38.8	120%	1.90	1.40	0.98	13-238		160
Polyvinylchloride											
Rigid	A	1.40		40.0	60%		3.00	2.75	62	75-105	200
Flexible	A			13.0	320%				62	75-105	

*A=Amorphous S=Semicrystalline C=Crystalline

1.3.2 COMPOSITE MATERIALS

The term composite material refers to a solid material made by combining two or more different materials, by mechanical and/or metallurgical means, to produce a material with enhanced properties compared to each of its constituents. Composite materials consist of a matrix material and the reinforcing material that is imbedded in the matrix material. In addition to holding the reinforcing material, the matrix provides means for supporting and transferring applied loads. The

properties of the composite materials are affected by the volume fraction and size of the reinforcing material [Gebhardt, 2003].

1.3.3 ABS PLASTIC

Acrylonitrile butadiene styrene (ABS) is a thermoplastic polymer that has an amorphous structure and is composed by three monomers: acrylonitrile (C_3H_3N), butadiene (C_4H_6), and styrene (C_8H_8). The combination of these monomers leads to the formation of two different co-polymer phases to make up the ABS polymer. The first phase is a hard styrene-butadiene copolymer and the second is a rubbery styrene acrylonitrile co-polymer [Kridli, 2006]. ABS polymers are used in several applications including automotive, consumer electronics, and applications as depicted in Figure 1.3.2.

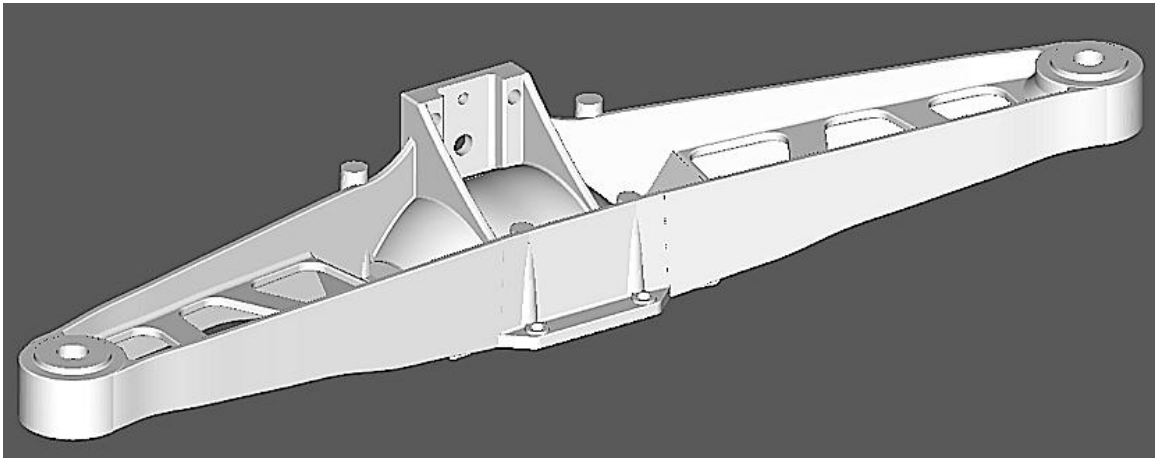


Figure 1.3. 2 RP ABS scaled differential support for a 1977 GMC Corvette

The advantage of ABS is that this material combines the strength and rigidity of the acrylonitrile and styrene polymers with the toughness of the polybutadiene rubber. The most important mechanical properties of ABS are resistance and toughness. A variety of modifications can be made to ABS to improve impact resistance, toughness, and heat resistance. Even though ABS plastics are used largely for mechanical purposes, they also have good electrical properties that are fairly constant over a wide range of frequencies. ABS polymers are resistant to aqueous acids, alkalis, concentrated hydrochloric and phosphoric acids, alcohols and animal, vegetable and mineral oils, but they tend to yield under the presence of acetic acid, carbon tetrachloride and aromatic hydrocarbons and are attacked by concentrated sulfuric and nitric acids.

As like other material composites, mechanical testing is used to determine a material property or a set of properties. The most common types of tests performed on this material and its derivatives are the uniaxial tension test, impact toughness test, flexure test, hardness tests, and creep tests.

1.3.4 CHARACTERIZATION OF FDM-ABS

The mechanical properties of polymers are characterized as in metals using stress strain curves and the parameters derived are from those curves. Polymeric materials display brittle and ductile behavior observed in metals, as well as a highly elastic behavior.

All forms of mechanical stress have components of tensile loading which makes the tensile strength the most common property due to its wide influence when considering the strength of materials. Tension occurs in bending, in shear, in torsion, and in compression. There can be one or two phases during the failure of a polymer when in tension. The material may yield first, which results in a reduction of its load carrying capacity, but continues to elongate. The second phase is the brittle and rapid failure. Yielding occurs when the load to overcome the intermolecular secondary forces is less than that required to break primary molecular bonds.

Within the yielding phenomena, the long chain-like molecules begin to uncoil and slip past each other. If the load persists, the material will continue to elongate along the continued molecular orientation. Further loading results in considerable molecular re-orientation in which the molecules are almost completely aligned in an anisotropic fashion in the direction of loading. At this point, the load begins to be withstood by primary molecular bonds. The load carrying capacity may then increase until the primary bond strength within the molecular chains is exceeded and the material undergoes rapid brittle failure [Fodran, 1996].

Research has shown that the approach for modeling heterogeneous composite materials is to transform them into a one-material approach. Being the homogeneous material the one with the “*known*” properties such that it depends on its constituent material and its geometries. The aforementioned is accomplished by a mathematical homogenization. Likewise, traditional mechanics of materials approaches express the average macroscopic stress and strain states in terms of constituent stress-strain states using displacement continuity and force equilibrium conditions. Basic assumptions in modeling unidirectional composites include: homogeneous (isotropic linear elastic constituent behavior) and homogeneous (orthotropic or transversely isotropic linear elastic composite behavior).

There have been significant experimental studies to comprehend the effect of the parameters of the FDM parts in terms of the modeled part characteristics such as surface finish, accuracy and material reduction. In this sense, Bakar et al. [Bakar, 2010] have studied the effects of fabricated FDM parts by modifying three parameters: layer thickness, contour width, and internal raster. They measured the dimensional accuracy using a touch-probe type coordinate measuring machine (CMM) and the surface roughness was measured using a portable surface tester at the horizontal and vertical corners of the modeled parts. Results showed that the surface of the prototyped cylinders became rougher and worse when the part sizes were smaller. That meant that the residual stress is severe on smaller features (prototypes). This can be explained by stating that the surface condition prevails more when the diameter of the feature is about 2 mm. Error on the cylinder formation or part distortion has been described by Zhang [Zhang, 2008] and it is identified as residual stress. In this sense, there are three factors of the residual stress: thermal gradient, speed of deposition and part geometry [Sun, 2008]. As it can be seen, from the work of Bakar et al., geometry plays an important role as a major factor of residual stress.

Similarly, Anitha et al. [Anitha, 2001] have studied the effect of process variables on the surface roughness of the components produced by FDM and had the objective to reduce it in prototyped parts. The variables comprised in this study were layer thickness, road width, and speed of deposition, each with a set of three levels. Results from the analysis of variance (ANOVA) showed that only the layer thickness is effective to 49.37% at a significance level of 95%. In combination, however, the layer thickness effectiveness is of 51.57% at a significance level of 99%. Road width and speed contributed to the 15.57% and 15.83% at 99% of significance level, respectively. Finally, the significance of layer thickness is strengthened by the correlation analysis that indicates an inverse relationship with surface roughness. This means that other factors, such as speed of deposition and road width, have no effect on surface finish.

On the other hand, Ahn et al. [Ahn, 2002] performed research on the manufacturing variables affecting the anisotropic material properties of FDM parts. It should be noted that the FDM process produces parts with unique characteristics. That is to say, the machine deposits material in a directional way that results in parts with anisotropic behavior. Their work focuses on the characterization of the mechanical properties of ABS parts fabricated by the Stratasys FDM 1650®. Experiments, based on the ASTM D-638, were performed in which the effect of several process parameters on the mechanical behavior of FDM parts was examined. The five variables (building parameters) selected came from three different classifications: unprocessed ABS material, FDM build specifications, and FDM environment. The five variables were air gap, bead

(road) width, model temperature, ABS color, and raster orientation. Among the five variables, one variable is qualitative (ABS color) whereas the remaining four are quantitative parameters. Each of the variables was independently tested and the tensile strength was calculated. It is important to mention that the parameters herein mentioned have been fully described in Chapter II, Section 2.1.1 of this thesis.

For setting up the reference strength of the ABS material, tensile and compressive specimens were fabricated by injection molding since this process yields a more stable isotropic condition than that of the FDM. Their results evidenced that the air gap and raster orientation affect the tensile strength of a FDM part greatly. Bead width, model temperature, and color have little effect. The aforementioned information will be of particular interest for the parameter selection in the present study disclosed in Chapter II, Section 2.3. The measured material properties showed that parts made by FDM exhibited anisotropic characteristics. Measured tensile strengths of the typical criss-cross raster $[45^\circ/-45^\circ]$ and raster $[0^\circ/90^\circ]$ with -0.003 air gap were between 65 and 72 percent of the measured strength of injection molded FDM ABS as it can be seen in Figure 1.3.3 [Ahn, 2002].

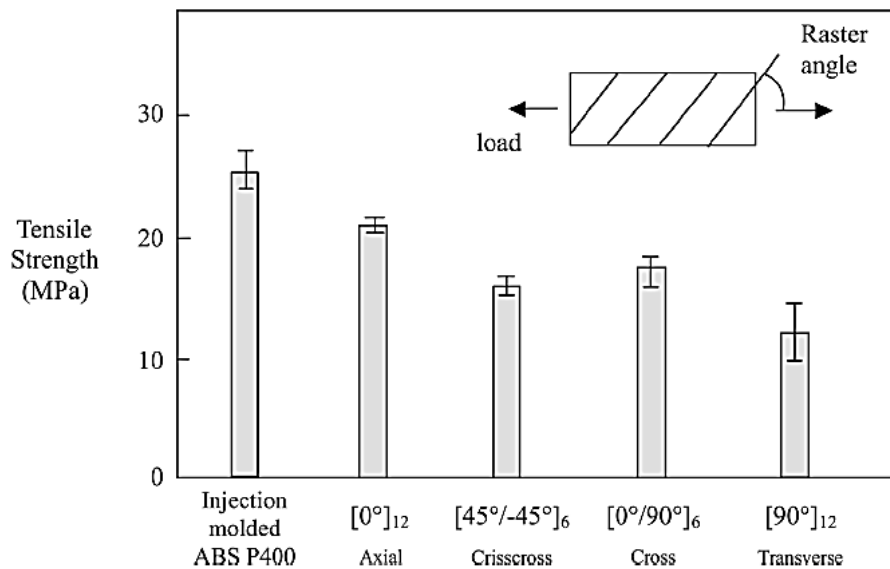


Figure 1.3. 3: Tensile strength for parts RP in different raster angle orientations [Ahn, 2002]

The compressive strength of the FDM material was higher than the tensile strength and was not affected significantly by the raster orientation as shown in Figure 1.3.4 [Ahn, 2002]. Because of the anisotropic behavior of the parts made by the FDM process, the strength of a local area in the part depends on the raster direction.

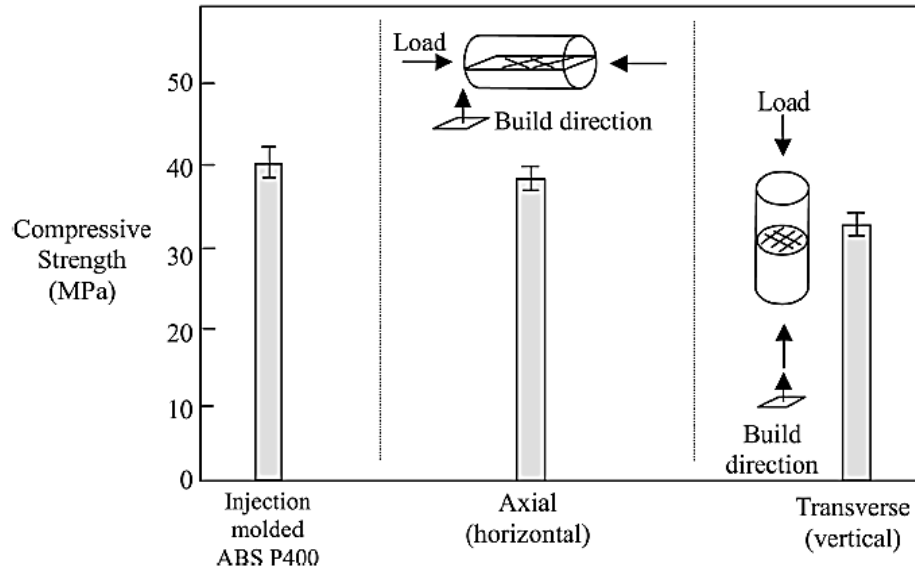


Figure 1.3. 4 Compressive strength for parts RP in different part orientations [Ahn, 2002]

As it can be seen from the aforementioned research, the manufacturing parameters that have had the greatest influence on the surface quality and accuracy are the layer thickness and the part's geometry itself. With respect to the mechanical characteristics of the finished parts, raster orientation exhibited the major influence on the tensile strength on the prototyped part. Conversely, the relevant manufacturing parameters for Bakar et al. and Anitha et al. were of more influence on the mechanical behavior of the part. Likewise, the compressive strength was not influenced by the raster orientation, but the build direction of the part within the building chamber.

A comparison of the published work regarding designing for optimization of the mechanical properties of ABS modeled parts is presented in Chapter III, Section 3.1.2 of this thesis. However, there has not been a complete research that characterizes the relation of the FDM manufacturing parameters to meso-structures and mechanical properties when the processed parts are made with different internal topology such as internal structures in an anisotropic arrangement.

1.4 THESIS OVERVIEW

The present work is organized in seven chapters where each of them comprises an introduction and a background in order to introduce the reader to the subject. The thesis was organized in this way due to the fact that the topics covered in it, although related, differ in terms of the subject matter with respect to each other.

Chapter I introduces the topic to the reader from the general definitions of RP to the particular matter of the present study. It explains the motivation, the thesis objectives and the scope of the research. Also, it gives a brief background of relevant terms and comprises related literature review that will serve as an easy-to-understand guide for subsequent sections in the thesis.

Chapter II summarizes an extensive literature review of work in the realm of FDM in terms of design for manufacturing parameter optimization for specific purposes. It also describes the selection criteria followed to choose the parameters relevant for the present research that will have the most impact on the results and are meaningful according to the proposed novel approach.

Chapter III encompasses an extensive literature review of similar work in the realm of CAD modeling in terms of design for optimization and design for strength. It explains how the research developed methods and/or algorithms in the light of optimizing the RP process. At the end of the chapter, the reader can find a discussion of the selected information that has influenced some decision regarding the direction of this research.

Chapter IV reports the RP process since the conception of the CAD models with parametric structures up to the completion of the STL file and the subsequent cleaning and post-processing of the finished part. A statistical analysis is presented based on the obtained results from the RP software simulation.

Chapter V comprises two parts. The first part relates to the characterization of the mechanical behavior of the experimental FDM parts by means of the physical testing. This part describes how the physical process was carried out, the data acquisition, formulas and calculations made, and it provides important definitions. The second part relates to the characterization of the mechanical behavior of the experimental FDM parts by means of the virtual simulation. This part states the process followed to simulate the FDM tensile and compressive specimens via a FEA solver and shows the results obtained from such simulation. It explains the considerations and conditions considered for simulating the tests, the input data used, and it gives meaning to the results obtained from the FEA. Finally, it discloses a brief analysis of variance study to study the interactions of all the parameters chosen in the present study, which will serve as a baseline for further analysis and study.

Chapter VI discloses the discussion of several topics from the present work. First, it discusses and compares the results obtained from the physical and virtual experiments for the tensile and compressive samples. Second, it discusses the validity of the FEA model and expands into the

correlation between the proposed FEA model with the data obtained from the tensile and compressive tests. Finally, it presents and discusses the refinement of the statistical model so that it becomes a functional and simpler model and its implication as a hands-on tool for designers.

Chapter VII encompasses the concluding remarks of the research. It provides the main thoughts regarding the outcome of this research. It presents the limitations and provides justification to the unknowns in this subject matter. All these thoughts add up to provide an insight of what is desired to be done in a future work. It also addresses the challenges faced during the realization of the present work and hints in order to success in case a fellow researcher opts for embarking in the world of rapid prototyping.

CHAPTER II

DESIGN OF EXPERIMENTS

2.1 BACKGROUND

The present research has the intention to understand specific process parameters and their interacting effects on response variables, such as the mechanical properties of the FDM built part. The methodology of the present study is defined in Section 2.3 of this chapter. The following two sub-sections (Section 2.1.1 and 2.1.2) will explain and define the parameters that best adapt to the manufacturing conditions in the present study. Once all the manufacturing parameters have been described, the main selection criterion is presented. It should be noted that the present approach is experimental and the selected parameters are believed to be the ones that will positively contribute with a meaningful use of this approach in the later research.

Several researchers have shown that process parameters/variables (also named as manufacturing parameters) of the FDM technology affect the manufactured part significantly. Additionally, the FDM RP technology has the attribute of being able to fabricate parts with localized material properties, namely: density, porosity, surface finish, and specific mechanical properties. Similarly, these local properties may be varied according to their practical usage. According to Gu et al. [Gu, 2002], FDM can produce a composite structure with locally controlled properties (LCP) by changing deposition density and deposition strategy. For example, with the appropriate material and process parameter selection, RP technology can create distinct regions within a part with properties similar to natural bone and model the non-homogenous variations within a region and material density distribution. Often, researchers focus on optimizing build time while reducing material amount without affecting the intrinsic structural quality of the parts.

According to Agarwala et al. [Agarwala, 1996], the manufacturing parameters that affect the FDM prototyped parts may be divided into four categories, as shown in Table 2.1 [Agarwala, 1996]. These parameters are operation specific, machine specific, materials specific, and geometry specific. From Table 2.1, the materials specific parameters are optimized in order to develop better RP systems. This task is often associated with the development of the fabricator's new technology. As previously commented in Chapter I, Section 1.1, once a specific technology or manufacturing parameter has been improved; proper optimization of other process variables may be determinant to affect others positively. These last ones are the ones related to end user

decisions.

The operative parameters (machine and operation specific), as their own names imply, are modifiable providing extended flexibility in the light of fabricating high quality FDM processed parts. Regardless of the complete optimization of existing FDM processes, day-to-day practice has shown that defects can result when using the FDM process to manufacture parts. This is caused by the nature of the process itself. As there are heat gradients due to the melting, solidification, air flow, slicing, orientation and form of the component being built, each processed part is unique. The elimination of these defects requires development and implementation of novel processing strategies in existing FDM systems [Agarwala, 1996]. The strategies followed respond to the research subject matter and seek the complete explanation of the interaction between the non-modifiable and the modifiable processing variables.

Table 2. 1 FDM manufacturing parameters [Agarwala, 1996]

Operation specific	Machine specific	Materials specific	Geometry specific
Slice thickness	Nozzle diameter	Powder characteristics	Fill vector length
Road width	Filament feed rate	Binder characteristics	Support structure
Head speed	Roller speed	Viscosity	
Extrusion temperature	Flow rate	Stiffness (column strength)	
Envelope temperature	Filament diameter	Flexibility	
Fill pattern		Thermal conductivity	

In section 2.1.1, specific modifiable parameters are described and the ones that may form the primary core set of manufacturing parameters are emphasized. Previous research with similar scope is analyzed and then reviewed in Section 2.1.3 of this chapter. The results from this selection along with the review of Section 3.1.1 and Section 3.1.2 of Chapter III, will serve as the baseline for designing the 3D model for all the set of specimens. It should be noted that this is an important step since limiting the vast number of interactions will help to reduce the complexity of the present study. Section 2.1.2 will reveal the strategy followed in order to assess the impact of the interactions by the parameters involved in the research. Similarly, Section 2.3 of this chapter will express the approach followed to statistically claim the significance of the physical experiments performed to the designed FDM processed parts.

2.1.1 FDM-ABS MANUFACTURING PARAMETERS

It is important to recall the FDM manufacturing process and discuss key elements in more detail. Having understood the generalities of the process (described in Section 1.1.6 of Chapter I), the material extruded from the head is deposited in the form of a fine bead of material, usually referred to as a “road” or “raster” in a feeding process that utilizes a constant volumetric displacement. The dimensions of the deposited rasters are, therefore, controlled by the material flow rate, which is itself controlled by the speed of the rotating rollers in the extrusion head, as described in Figure 2.1.1 [Sun, 2008]. The dimensions of the raster (width and thickness) along with the liquefier head speed determine the flow rate of the material to be extruded out of the nozzle tip [Agarwala, 1996].

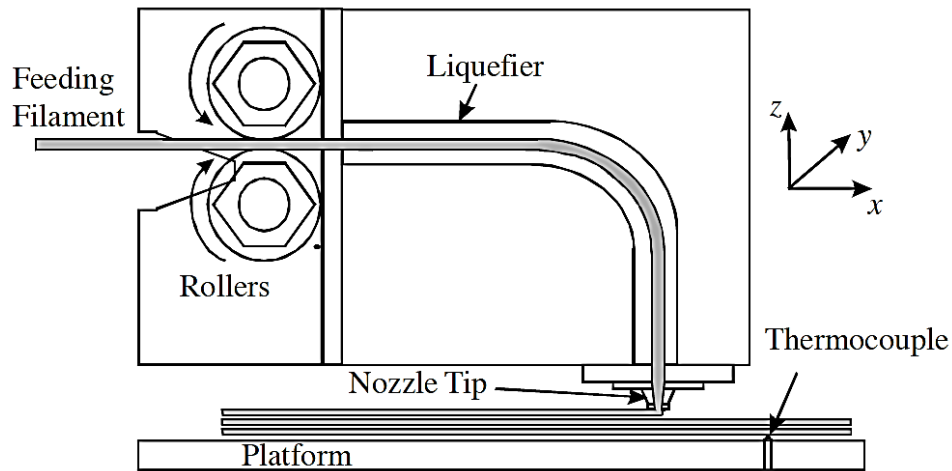


Figure 2.1. 1 Schematic of the FDM feeding head assembly and build platform [Sun, 2008]

As described in Section 1.1.2 of Chapter I, AM systems build a 3D object layer-by-layer. Specifically for the FDM technology, the process of depositing material in each layer starts with a road of material, where the user, usually, defines width and thickness. The raster is deposited in order to define the perimeter (s) or boundary (ies) of the given part layer. Each perimeter is a closed loop with a start and end point. Once the perimeters are defined, the internal portion of the layer is filled by roads of defined width and thickness in one of three ways. These three ways are depicted in Figure 2.1.2 [Agarwala, 1996]. The (a) raster fill approach is the most used due to its speed and the ability to change the direction of raster motion thru neighboring layers. In FDM, adjacent layers are built with raster directions at 90° to one another. Similarly, Figure 2.1.2 [Agarwala, 1996] depicts the (b) contour fill pattern and the (c) contour plus raster fill pattern bead depositing methods. In raster fill, the whole path can usually be laid in one single motion of the nozzle. However, raster paths suffer inaccuracies in the deposition; hence, they exhibit poor

surface quality.

In the (b) contour fill pattern, the boundary of a slice is successively offset until it fills the entire area. The method fits boundaries of prototypes well and has good surface quality, but it yields a set of distinct paths that need to be traversed to deposit all the material. The (c) contour plus raster fill pattern process deposits contours to fit the boundary and raster to fill the inside of the deposition region. It yields good surface quality with relatively short build time. In addition to different deposition strategies, gap sizes between the adjacent paths can also change the material deposition density. The bigger the gap, the lower the material density [Gu, 2002].

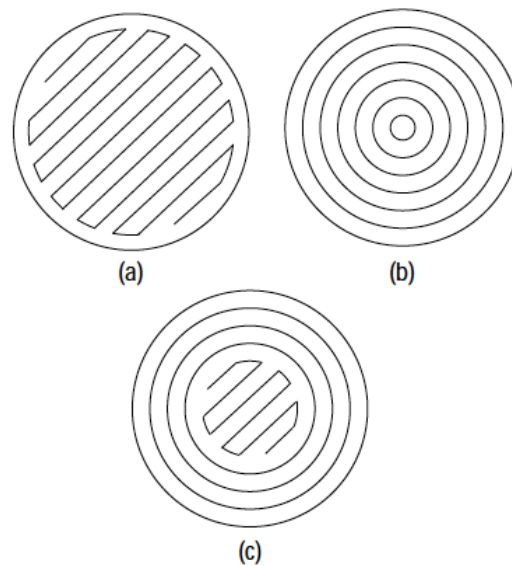


Figure 2.1. 2 Difference in the raster fill approach [Agarwala, 1996]

As described by Agarwala et al. [Agarwala, 1996], the (a) raster fill pattern results in maximum packing of material and a minimum of voids between roads and layers. As shown Figure 2.1.3 [Sun, 2008], the bond formation process, generally, comprises three steps: the surface contacting, the neck growth, and the molecular diffusion at the beads' interfaces. Whether the bead (raster) is deposited along a relative long segment or not, poor optimization of material flow and liquefier head motion parameters (at the beginning and end of a perimeter or raster segment) can result in defects detrimental to structural properties of the parts [Agarwala, 1996]. In addition to raster width, thickness, extrusion head speed, and fill pattern, several other build parameters require optimization for a given material in the intent to output an error-free part.

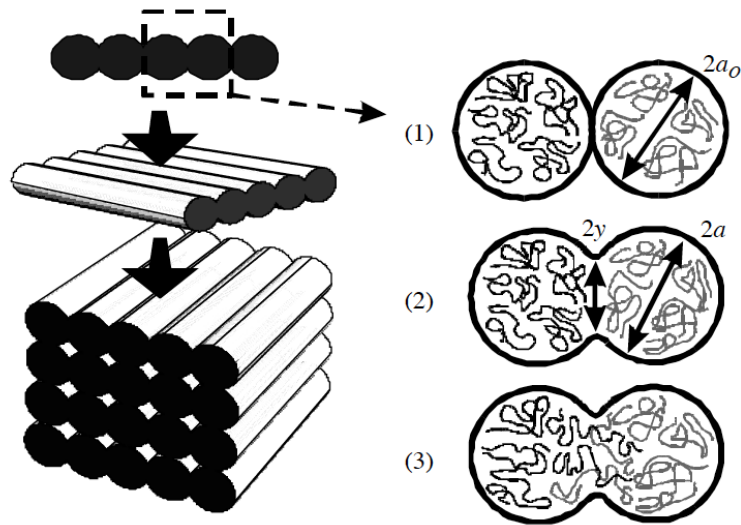


Figure 2.1. 3 Bond formation between deposited FDM rasters [Sun, 2008]

In addition to the parameters described in Table 2.1, relevant process parameters involved in part manufacturing, which some are of great importance in the present study and will be referenced in previous researches, are disclosed in Table 2.2.

Table 2. 2 Specific parameters and their description

Parameters	Description
Part Interior Fill	It refers to how the interior volume in each layer is filled. There are two methods: Solid normal and Sparse. The sparse has a semi-hollow interior with a predefined honeycomb structure.
Depositing Raster Angle	It refers to the direction of the raster relative to the X-axis of the build platform.
Raster-to-raster Air Gap	It refers to the gap between the adjacent rasters on the same layer.
Part Orientation	It refers to the position of the part inside the building envelop with respect to the X, Y, and Z-axis. X and Y-axis are considered to be laying on the building platform and the Z-axis projects along the building direction.

Since the mechanical properties are the preponderant factors for functional parts, it is absolutely essential to understand the influence of process parameters on the mechanical properties so that improvement can be made through the selection of best FDM machine settings.

As described by Sun et al. [Sun, 2008], FDM manufacturing process planning research has included the consideration of processing parameters in optimizing processing time, mechanical properties and surface accuracy of the final product [Sun, 2008]. In this regard, a number of improvements are essential: the mechanical properties of the parts produced should be enhanced so that they can maintain their integrity during service, the variety of polymeric materials

available for use in these technologies should increase, the process improvements should result in greater dimensional control and better tolerances, and functional parts require improvements in surface finish.

2.1.2 DESIGN OF EXPERIMENTS AND DATA ANALYSIS

As previously mentioned in Section 2.1, it is desirable to optimize the material usage and building time without affecting the mechanical properties of the FDM processed prototype by means of a novel alternative that involves the addition of parametrically defined internal web-like structures within the inside volume of processed parts. In order to achieve the aforementioned, a new approach would have to emerge in the light of giving significance to the findings reached in the present study. In this sense, it was important to research on similar approaches in order to acquire meaningful guidance on how to overcome the challenge of understanding and characterizing a novel path without any previous direct background. Influenced by what was found in the literature, design of experiments (DOE) and analysis of variance (ANOVA) are two important techniques that aid in the direction and comprehension of an experimental claim and the results yielded from it.

In this regard, Chockalingman et al. [Chockalingman, 2006] define optimization as the selection of the best course of action for specific objectives among the many possible choices that depend on resource availability specified as constraints. The objective for the optimization problem is the relationship between the part strength and process parameters that could be used for the selection of optimal settings, which differ with environments, applications, and specific requirements. Evidently, the optimization depends on the RP machine and in the RP processing software, explained in Section 1.1.4 of Chapter I, and most important, the functional objective of the RP processed part.

Also, Chockalingman et al. [Chockalingman, 2006] define DOE as the optimizing tool to optimize the influencing parameters. In other words, DOE is a series of ordered tests in which purposeful changes are made to the input variables of a process or system to identify the corresponding changes in the output response variable. Finally, Chockalingman et al. [Chockalingman, 2006] claimed that DOE is a powerful statistical technique used to study the effect on the outcome of multi variables simultaneously. Apparently, this approach may be the ultimate option for the manufacturing variables that are involved in the FDM process. According to their research, a process or system is usually influenced by two sets of process variables

namely controllable variables and uncontrollable variables (noise factor). In this case, all the uncontrollable variables have been neglected, as it will be discussed in the next Section 2.3, since such did not affect the data obtained in the physical testing.

Similarly, Lee et al. [Lee, 2005] studied the optimization of FDM process parameters for optimum performance of a model of a catapult that can be used in a sling shot toy. They utilized the Taguchi method, which is a technique that provides a systematic and efficient methodology for design optimization and has been widely used for product design and process optimization due to the advantages of the design of experiment. Those advantages include the simplification of the experimental plan and the feasibility to study the interaction between different parameters; hence, a lesser number of experiments means time and costs are reduced [Lee, 2005]. They chose four parameters to study: air gap, raster angle, raster width, and layer thickness. Each of those parameters comprises three levels (the term level will be defined in the next Section 2.2 of this chapter). Table 2.3 comprises the parameters and the levels that describe the optimization of the FDM process for the study performed by Lee et al. [Lee, 2005].

Table 2. 3 Parameters and levels describing the optimization of the FDM process [Lee, 2005]

FDM Parameter	Level 1	Level 2	Level 3
Air gap (mm)	Solid	Sparse	Double
Raster angle (degree angle)	0°/90°	45°/-45°	30°/60°
Raster width (mm)	0.305	0.655	0.980
Layer Thickness (mm)	0.178	0.254	0.305

Likewise, Sood et al. [Sood, 2009] adopted the previously described Taguchi method since the method not only reduces the number of experiments, but also identifies the influencing factors and their interactions. However, with the conventional Taguchi method, when multiple performance characteristics with conflicting goals are considered, the approach becomes unsuitable. Therefore, Sood et al. [Sood, 2009] used the grey Taguchi method to generate a single response from different performance characteristics.

They studied five parameters, namely: layer thickness, part build orientation, raster angle, raster to raster gap (air gap), and raster width each at three levels. The goal of the research was to study the interaction of part build orientation with all the other factors on the dimensional accuracy of FDM build part. Taguchi's design of experiment is used to find the optimum factor levels and significant factors and interactions. The results yielded that shrinkage is dominant along the length, width, and diameter of the test part, whereas thickness is always more than the desired

value [Sood, 2009]. As part of the objectives of the experiment include the determination of the most influencing (controllable) variable on the output response, the significant setting of these influential variables so as to minimize the variability in the output, the percentage of contribution of variables, and the relationship between performance parameters and response variables. It should be mentioned that as the FDM part increases in size, time, material, labor costs, and energy consumption increase as well. The time factor affects these last two considerably. Evidently, time is reduced when the FDM machine has less model material to deposit when a prototype CAD design does not involve complex geometries.

2.1.3 PARAMETRIC OPTIMIZATION OF FDM PARTS

In addition to what was expressed in Section 1.3.4 of Chapter I, the following section adds, in addition to the research carried up by Bakar et al., Zhang et al., Anitha et al., and Ahn et al., a more profound explanation of the parameters that affect the micro and meso-structures of the processed FDM parts. As mentioned before, the mechanical properties of FDM materials exhibit anisotropy and are sensitive to the processing parameters that affect its meso-structure. According to Rodriguez et al. [Rodriguez, 2003], the important FDM processing parameters are: the orientation of the layering plane relative to the part, the raster orientation (angle), the fiber-to-fiber gap, the road width, and the extrusion and envelope temperatures. Their research explains that there are other additional parameters (perimeter/contour gap and contour fill gap) affecting the layer structure in FDM parts; however, these parameters affect the material behavior at the bounding surfaces of the part and do not interact with the meso-structure. In this regard, they assume that the material meso-structure in the interior of the part governs the overall mechanical behavior of the part. Their research yielded a mathematical model of a FDM ABS structural system (cantilever structure) linked to an optimization algorithm to find the FDM parameter settings resulting in the optimal mechanical performance for the component. They employed a two section cantilevered geometry for finding two optimal values for θ and θ_2 in terms of the maximum loading capacity F , as it can be seen in Figure 2.1.4 [Rodriguez, 2003].

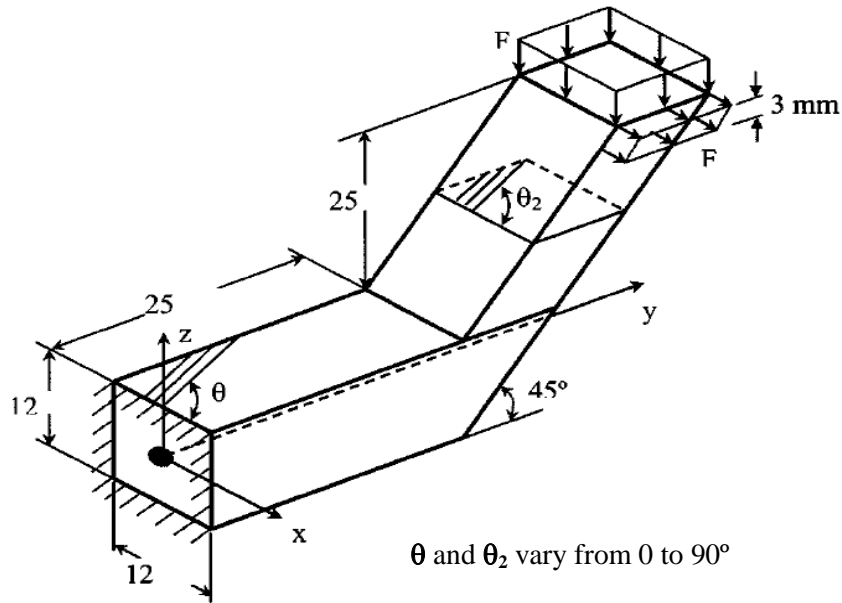


Figure 2.1. 4 Two-section cantilevered geometry [Rodriguez, 2003]

The results, from experiments and theory, that arose from the formula proposed by Azzi and Tsai [Azzi, V. D., and Tsai, S. W., 1965, “*Anisotropic Strength of Composites,*” *Exp. Mech.*, 5 (9), pp. 283–288.] and fitted for the geometry under study yielded that orientation plays a major role in determining the normal and shear stresses in a particular geometry. As it can be seen from Figure 2.1.5 [Rodriguez, 2003], the raster orientation for any of the two θ s that exhibited highest stress is at 0° . Evidently, as the angle was increased, the strength diminished due to the raster orientation layout and the strength needed to break those bonds. The aforementioned subject matter will be fully explained in Section 5.1 of Chapter V. The experiment and the theoretical results relate close to each other and concur with the research made by Ahn et al. [Ahn, 2002].

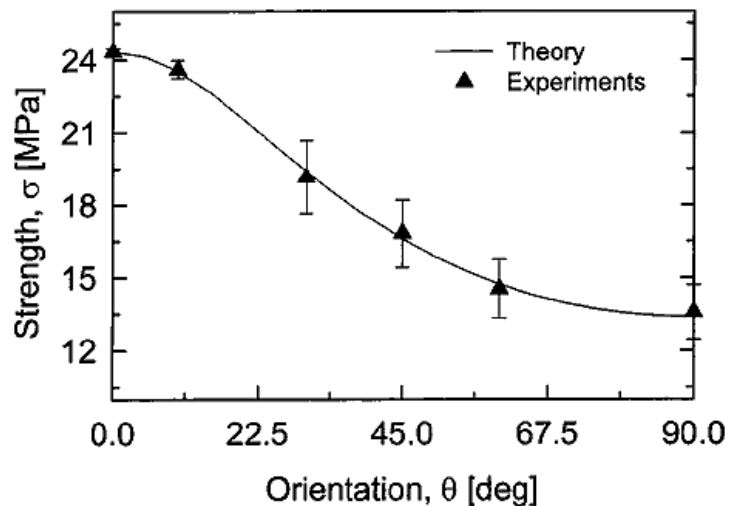
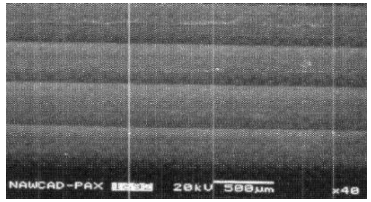
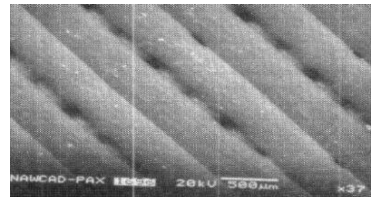
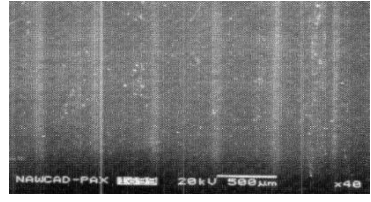


Figure 2.1. 5 Strength variation depending upon the raster orientation [Rodriguez, 2003]

According to Es-Said et al. [Es-Said, 2000], FDM parts experience volume changes as the ABS thermoplastic transforms from the semi-liquid to the solid state. Evidently, the prototype created is slightly smaller than its design dimensions. Although very small differences from the CAD model, these are sufficient enough to cause the 2-D layers to have directional properties. A precise definition of this anisotropy is not well established; however, according to Es-Said et al. [Es-Said, 2000], this anisotropy can be caused by the polymer molecules aligning themselves with the direction of the flow when they are extruded and by the formation of pores in preferred orientations and weak interlayer bonding.

They examined the effect of layer orientation on the mechanical properties of RP FDM samples by performing tensile tests. Table 2.4 encompasses the parameters subjected to study in Es-Said et al. [Es-Said, 2000] research along with the parameter description and a scanning electron microscope (SEM) micrograph of the respective parameter. Results from their work evidence the effect on layer orientation on the mechanical properties of the tested FDM specimen.

Table 2. 4 Filament micrographs of different raster orientations [Es-Said, 2000]

Parameter	Description	Micrograph (SEM)
0° orientation	The layers are at a 0° angle with respect to the sample length	 SEM micrograph showing horizontal layers at 0 degrees orientation. The image displays a series of parallel, slightly wavy horizontal lines representing the layers of the FDM filament. The background is dark, and the layers are light gray. A scale bar at the bottom right indicates 500 μm. Technical details at the bottom left include 'NAWCAD-PAX 10000 20kV 500μm x40'.
45/-45° orientation	The two diagonal layers intersect at ±45° to the sample length	 SEM micrograph showing diagonal layers intersecting at 45 degrees. The image displays two sets of parallel lines intersecting at a 45-degree angle. The lines are light gray against a dark background. A scale bar at the bottom right indicates 500 μm. Technical details at the bottom left include 'NAWCAD-PAX 10000 20kV 500μm x37'.
90° orientation	The layers are at a 90° angle along the to the sample length	 SEM micrograph showing vertical layers at 90 degrees orientation. The image displays a series of parallel, slightly wavy vertical lines representing the layers of the FDM filament. The background is dark, and the layers are light gray. A scale bar at the bottom right indicates 500 μm. Technical details at the bottom left include 'NAWCAD-PAX 10000 20kV 500μm x40'.

The results arose from the work of Es-Said et al. [Es-Said, 2000] yielded similar trends in terms of what was explained in Section 1.3.4 in Chapter I by Ahn et al. [Ahn, 2002] and by Rodriguez et al. [Rodriguez, 2003] in this section. They found that raster orientation significantly affects the

mechanical properties of the FDM prototyped parts. In their results, the ultimate and yield (0.2% offset) strengths were the highest for the 0° orientation, 20.6 and 16.3 MPa, respectively. The $45/0^\circ$ was second (14.0 and 13.6 MPa), followed by the standard orientation, $45/-45^\circ$, (13.7 and 10.4MPa). The weakest orientations were the 90° and 45° angles.

Nevertheless, one of the most significant results obtained from the tests was the observation, from the topographic analysis, of the fracturing surfaces. The analysis illustrated the weakest path for crack propagation. It was observed that the fracture path of all the samples depended on the 2-D layer orientation, always occurring along the layer interface. Figure 2.1.6 [Es-Said, 2000] shows a schematic representation of the failure paths.

In the 0° orientation (a), the samples broke at the layer interfaces parallel to the stress direction and eventually at weak points within the layers perpendicular to the stress direction. In the 90° orientation (b), the samples broke at the raster boundary perpendicular to the tensile axis. In the 45° orientation (c), the samples broke at a 45° angle. In the $45/-45^\circ$ orientation (d), two interlayer fracture paths initiated and intersected at $\pm 45^\circ$ (zigzag). Finally, in the $45/0^\circ$ orientation (e), the samples broke at a 45° angle.

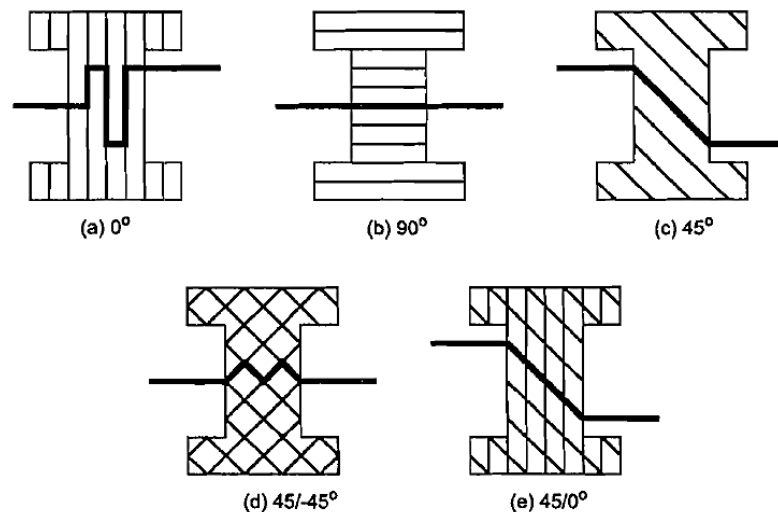


Figure 2.1. 6 Failure paths of tensile specimens upon the raster orientation [Es-Said, 2000]

In a similar way, Montero et al. [Montero, 2001] experimented to understand the effect of design and process parameters on the tensile strength in FDM tensile specimens. The five parameters involved are: air gap, bead width, model temperature, ABS color, and raster orientation. Among the five variables, one variable is qualitative (ABS color) whereas the remaining four are quantitative parameters. The DOE method was selected to minimizing the number of tests and providing clear estimations of the effects of such process parameters. The tensile strength

evidenced a linear behavior as response as a function of the 5 parameters, each with two levels set at a high (+1) and a low (-1). A visual representation of the main effects observed in the tests can be seen in Figure 2.1.7 [Montero, 2001].

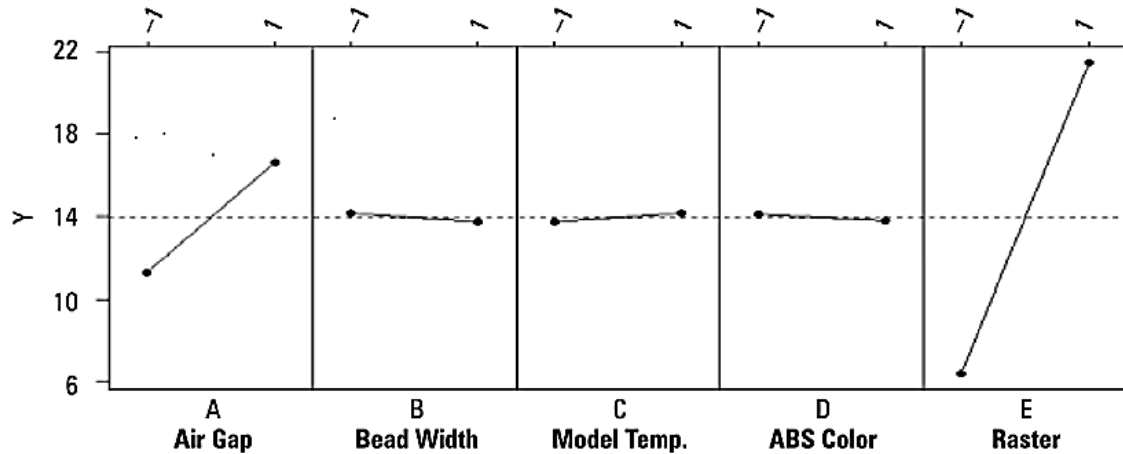


Figure 2.1. 7 Level values for a set of different manufacturing parameters [Montero, 2001]

From Figure 2.1.7, the air gap and the raster orientation (when set from low to high levels) demonstrated to have a significant effect on the tensile strength (Y intercept). The results evidenced that when the tensile specimen was oriented in a 90° angle from the tensile direction (-1), the air gap would influence the tensile strength greatly. Conversely, when the roads were oriented in a 0° angle from the tensile direction (+1) the air gap effect is less. Another relevant conclusion from Montero et al. [Montero, 2001] was that the parts built with an axial raster orientation were significantly stiffer than those built with transverse raster orientation. Also, the crisscross raster FDM parts with a negative air gap were stiffer than those built with zero air gaps. In conclusion, the air gap did not have a significant effect on the elastic modulus for the axial or transverse parts.

On the other hand, Bertoldi et al. [Bertoldi, 1998] focused their research on the orientation and the tool path of FDM ABS specimens in order to determine the stiffness matrix and the thermal expansion coefficients for an equivalent orthotropic material. They oriented the specimens in six different ways as seen in Figure 2.1.8 [Bertoldi, 1998]. As it can be seen, the vertical and the 45° oriented bars in the XY and ZY planes were built with aid of the support material [Bertoldi, 1998].

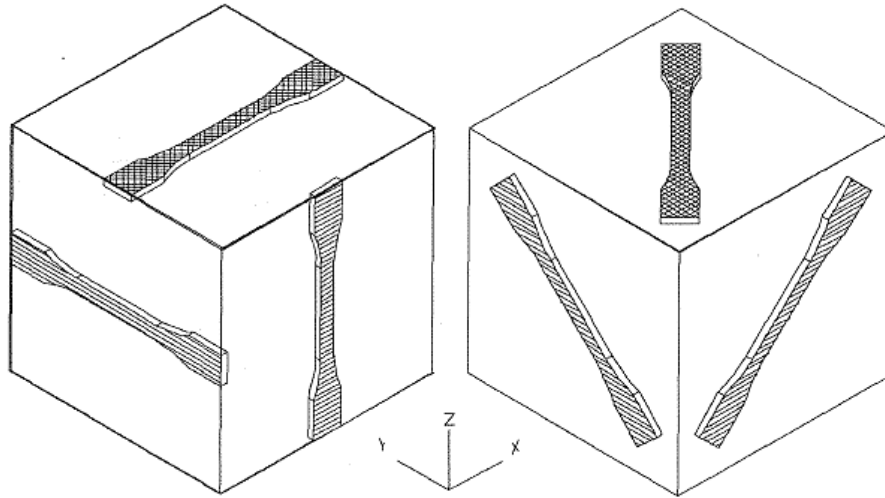


Figure 2.1. 8 Tensile specimens oriented in different positions in the build chamber [Bertoldi, 1998]

The experiments carried out by Bertoldi et al. [Bertoldi, 1998] yielded important conclusions. The specimens oriented in the vertical XZ planes exhibited brittle failure. The specimens oriented in the XY and YZ planes exhibited a common elastic behavior; where the specimens in the XY planes had the highest elastic module and tensile strength. Conversely, the XZ plane-oriented specimens have the lowest tensile strength. Table 2.5 summarizes the results obtained from Bertoldi et al. [Bertoldi, 1998]. The results concur with what Es-Said et al. [Es-Said, 2000] found where the specimens oriented in a 0° angle with respect to the tensile direction showed the highest strengths. According to Bertoldi et al. [Bertoldi, 1998], they refer to orientation in the XY, YZ, and XZ as what Es-Said et al. [Es-Said, 2000], Montero et al. [Montero, 2001], and Rodríguez et al. [Rodríguez, 2003] to the $-45^\circ/45^\circ$, 0° , and 0° angle degree orientation with respect to the axial load of the test specimens, respectively.

Table 2. 5 Average tensile strength at different build planes and raster angles [Bertoldi, 1998]

Build Plane	Orientation (Raster angle axis)	Average Tensile Strength [MPa]
XY	X + 0°	11.7
YZ	Y + 0°	15.9
XZ	Z + 0°	7.6
XY	X + 45°	10.8
YZ	Y + 45°	13.4
XZ	Z + 45°	14.7

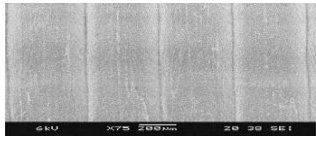
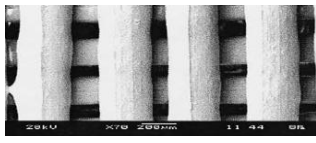
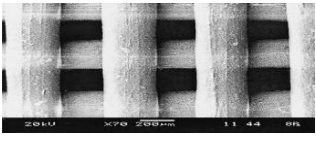
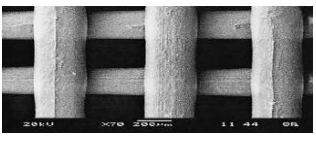
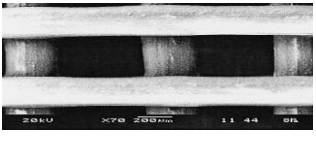

Fodran et al. [Fodran, 1996] studied the effects of processing parameters such as fill gap (air gap), line (raster) width, and slice thickness (layer thickness) on the mechanical properties of FDM samples. The parameters and their respective values are comprised in Table 2.6 [Fodran, 1996]. They conducted dimensional analysis by magnifying the tested samples utilizing the SEM in order to characterize the failure of those specimens. From Table 2.6 [Fodran, 1996], it can be seen that the difference in stress between samples was not significant when keeping the air gap and the layer width constant. Even more, the difference (in stress [MPa]) of the highest value when prototyped at a 45°/45° with the value when prototyped at a 0° angle (contour) with a difference in road fill of just 0.005 in (0.127 mm) was of just less than 4 MPa. Hence, their results evidence that layer width and air gap are not significant parameters that may modify the results in terms of mechanical properties for this set of samples.

Table 2. 6 Yield stress for different samples at different parameter values [Fodran, 1996]

Sample No.	Layer width (in)	Raster angle	Air Gap (in)	Raster Width (in)	Yield Stress (MPa)
1	0.010	45°/45°	0	0.020	17.3
2	0.010	45°/45°	0	0.015	19.4
3	0.010	0°	0	0.20	21.1

On the other hand, Too et al. [Too, 2002] centralized their work on the feasibility of using FDM to construct bio-scaffolds. Their work focused on the microstructure of the FDM parts to determine their conformity to scaffold requirements in terms of its porosity, pore sizes, and mechanical strength. They built test specimens in cube shapes of 10 mm per side in a perpendicular raster angle of 0°/90°, which were subjected to compressive loading. The compressive stresses were calculated based on the apparent cross-sectional area of the specimen and do not account for the open void area of the pores, since it is desirable to evaluate the structure of the specimens as a whole [Too, 2002]. The parameters that were used to assess the compressive strength of the samples are slice thickness, raster gap, and road width. They based these parameters based on the usage of the RP FDM part and found that the 3D interconnectivity of open voids or pores is capable of producing a matrix-like structure or scaffold that is consistently controllable, with reproducible porosity and uniform pore arrangement. This is disclosed in Table 2.7.

Table 2. 7 Compressive samples micrographs with different raster gap [Too, 2002]

Raster Gap (mm)	Road Width (mm)	Slice Thickness (mm)	SEM Micrograph
0.0	0.315	0.254	
0.1	0.315	0.254	
0.2	0.315	0.254	
0.3	0.315	0.254	
0.4	0.315	0.254	
0.5	0.315	0.254	

As it can be seen, the aforementioned micrographs obtained from SEM observations represent a consistent interconnected microstructure. Table 2.7 micrographic representations of the FDM samples evidence a series of surface morphologies with different raster gap settings. From these micrographs, the raster gap parameter has the most significant influence on the microstructure of the specimen. Since a pore or void is the space created between successive roads within a layer by increasing the value of the raster gap. It can be observed that the pore increases in size (calculated porosity) [Too, 2002].

Finally, the research from Too et al. [Too, 2002] yielded that the compressive strength of the specimen decreases with increasing the raster gap (air gap). This is due to the decrease in the number of raster lines, within each layer, owing to the use of high raster gap, resulting in a decrease in the amount of load-carrying material. That is to say, the compressive strength of the

porous structure depends on micro-structural factors such as porosity or relative density [Too, 2002]. Figure 2.1.9 [Too, 2002] depicts the (a) compressive strength versus the raster gap and (b) the (b) compressive strength versus the calculated porosity for the samples tested in their research: the more the porosity the less compressive strength in the FDM ABS parts.

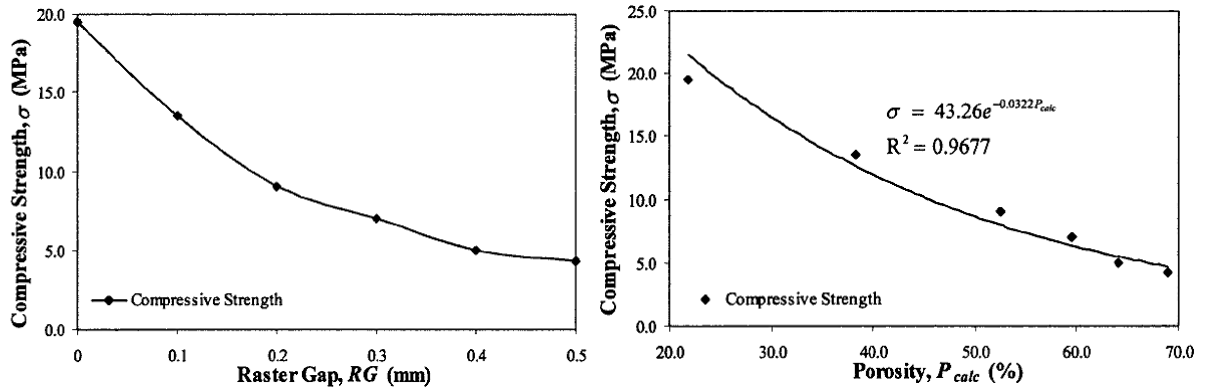


Figure 2.1. 9 Compressive strength, raster gap, and porosity comparison [Too, 2002]

2.2 DISCUSSION

The process parameters for the FDM RP process number more than a dozen. However, not all of the parameters influence the strength characteristics as previously described. Sections 2.1.1 and 2.1.2 summarized the relevant parameters according to a wide variety of research carried out. Some of them seek for the optimization of surface finish, dimensional accuracy, and the strength optimization. It should be pointed out that the approach followed in the present research has not been totally described in the literature. As it will be discussed in Section 3.1.1 and 3.1.2, there are some approaches that have followed a similar approach and have had a similar objective.

Now then, it is important to define the terms degrees of freedoms and levels. As commented in previous sections, researchers have centralized the importance in the number of levels and their ability to manipulate such in order to obtain inclusive results. In this sense, degrees of freedom (DOF) are defined as the number of comparisons between process parameters that need to be made to determine which level is better, and specifically, how much better it is. For example, a three-level process parameter counts for two degrees of freedom. The total degrees of freedom are obtained by multiplying the degrees of freedom of each process parameter to the number of parameters [Lee, 2005]. Again, the parameters selected on each of the approaches described in the previous section depend on the objective of the research in terms of the optimization of FDM properties including accuracy, surface finish, material optimization, and strength optimization and

characterization.

In this regard, Lee et al. [Lee, 2005] examined the process parameters for optimum performance of a model where four parameters were modified: air gap, raster angle, raster width, and layer thickness. Sood et al. [Sood, 2009] studied five parameters: layer thickness, part build orientation, raster angle, raster to raster gap, and raster width each at three levels in order to study the interaction of part build orientation with all the other factors on the dimensional accuracy of the build part. Rodriguez et al. [Rodriguez, 2003] focused on: part orientation, raster orientation, the fiber-to-fiber gap, the road width, and the extrusion and envelope temperatures so as to explain the material behavior at the meso-structure. Es-Said et al. [Es-Said, 2000] just centralized on the effect of layer orientation on the mechanical properties of RP FDM parts.

Bakar et al. [Bakar, 2010] studied three parameters: layer thickness, contour width, and internal raster to comprehend their effects on the dimensional accuracy and the surface roughness. Agarwala et al. [Agarwala, 1996] based their analysis on these parameters: fill vector length; fill pattern, road diameter, extrusion temperature, and envelope temperature. They studied the defects to structural properties of the parts. Anitha et al. [Anitha, 2001] aimed to reduce the surface roughness of FDM components by analyzing the effect of the layer thickness, road width, and speed of deposition. They found that the speed of deposition and road width have no effect on surface finish.

Ahn et al. [Ahn, 2002] performed research on five variables: air gap, road width, model temperature, ABS color, and raster orientation. They desired to assess the effect on tensile strength of a FDM part. Similarly, Montero et al. [Montero, 2001] wanted to understand the effect of air gap, bead width, model temperature, ABS color, and raster orientation on the tensile strength in FDM tensile specimens. Bertoldi et al. [Bertoldi, 1998] focused on these two parameters: orientation and tool path of FDM ABS parts. They intended to determine the stiffness matrix and the thermal expansion coefficients for an equivalent orthotropic material. Fodran et al. [Fodran, 1996] studied the effects of fill gap, raster width, and slice thickness on the mechanical properties of FDM samples. Evidencing that layer width and air gap are not significant parameters that may modify the results in terms of mechanical properties for this set of samples. Unlike the previously mentioned researchers, Too et al. [Too, 2002] studied the porosity and mechanical strength (compressive) of scaffold micro-parts by modifying the slice thickness, raster gap, and road width.

Different parameters and levels have been previously disclosed. It can be seen that some researches have shared similar sets of parameters. Again, these parameters depend on the final

application or what it is intended to optimize. Table 2.8 summarizes the selected FDM manufacturing parameters by all the researchers disclosed herein. It should be noted that air gap, road width, raster orientation, and layer thickness had more than six incidences. This means that these parameters are the ones that play a relevant role in mechanical properties' optimization.

Table 2. 8 Summary of FDM manufacturing parameters and researchers cited in this thesis

Researcher	FDM Manufacturing Parameters										
	Air Gap	Road Width	Envelope Temperature	ABS Color	Raster Angle Orientation	Contour Fill	Fill Vector Length	Extrusion Temperature	Layer Thickness	Deposition Speed	Build Plane
Agarwala et al.		✓	✓			✓	✓	✓			
Ahn et al.	✓	✓		✓	✓			✓			
Anitha et al.		✓							✓	✓	
Bakar et al.					✓	✓			✓		
Bertoldi et al.					✓						✓
Es-Said et al.					✓						
Fodran et al.	✓	✓							✓		
Lee et al.	✓	✓			✓				✓		
Montero et al.	✓	✓		✓	✓			✓			
Rodriguez et al.	✓	✓	✓		✓			✓			✓
Sood et al.	✓	✓			✓				✓		✓
Too et al.	✓	✓							✓		

2.3 SELECTION OF PARAMETERS

By testing RP samples, the properties of the component can be evaluated without actually manufacturing it in full scale, which would be more expensive. By using ABS, the mechanical properties of the design can be measured, and the design can be modified in the early development stage, as described in Section 1.2.1 of Chapter I, when it is less costly to make design changes. The FDM RP machine can be programmed to create solid models with various manufacturing parameter settings. Processing or manufacturing parameters of the FDM technology number a different variety according to their use, time optimization, material optimization, strength optimization, etc. as it can be seen from previous sections of this chapter.

However, the fabrication parameters considered in this research focus their optimization in terms of strength and reduction in time for RP prototypes that exceed the micro-scale. In other words, the study centralizes on the effect of internal web-like structures for meso and macro structures (within the FDM limits). As mentioned before, the mechanical properties of FDM materials exhibit anisotropy and are sensitive to the processing parameters that affect its meso-structure.

According to what it was described in Section 2.2 of this chapter, the results obtained from the experiments were usually influenced by a set of process variables, namely: controllable variables and uncontrollable variables. In the previously disclosed researches dealing with optimizing the mechanical properties, all the uncontrollable variables have been neglected. Results demonstrated that the uncontrollable variables did not affect the data obtained in the physical testing. Also, none of the research comprised in Table 2.8 studied the effect on form or geometry of the tested parts.

The purpose of this research is not to find the optimum factor levels and significant factors and interactions. Nevertheless, this research's objective includes the determination of the most influencing parameter on the output response, the percentage of contribution of variables, and the relationship between performance parameters and response variables. For this reason, design of experiments (DOE) will be utilized as the optimizing tool to find the influencing parameters and to study the effect on the outcome of multi variables simultaneously. Chockalingman et al. [Chockalingman, 2006], Lee et al. [Lee, 2001], and Sood et al. [Sood, 2009] employed the Taguchi and grey Taguchi methods. These methods generate a single response from different performance characteristics of different parameters. However, a simpler method will be utilized in the present research, which is described in Figure 2.3.2.

Considering the above mentioned, the following parameters and levels, identified as the most significant with respect to strength, are comprised in Table 2.9. The number of levels of each factor depends on the behavior of the response variables (strength, material usage, and build time) to the factor under consideration. Two levels, minimum and maximum limits of the factor, were set for a linear pattern. These levels depend on the machine and material specifications. In this study, the Stratasys® FORTUS 400mc® was used to perform the RP. The LM machine was operated by INSIGHT®: the RP Software (Section 1.1.4 of Chapter I). INSIGHT® has the ability to let the user modify the manufacturing parameters such as: layer resolution (thickness), model interior, support fill, number of copies, STL units, STL scale, etc., as described in Figure 2.3.1.

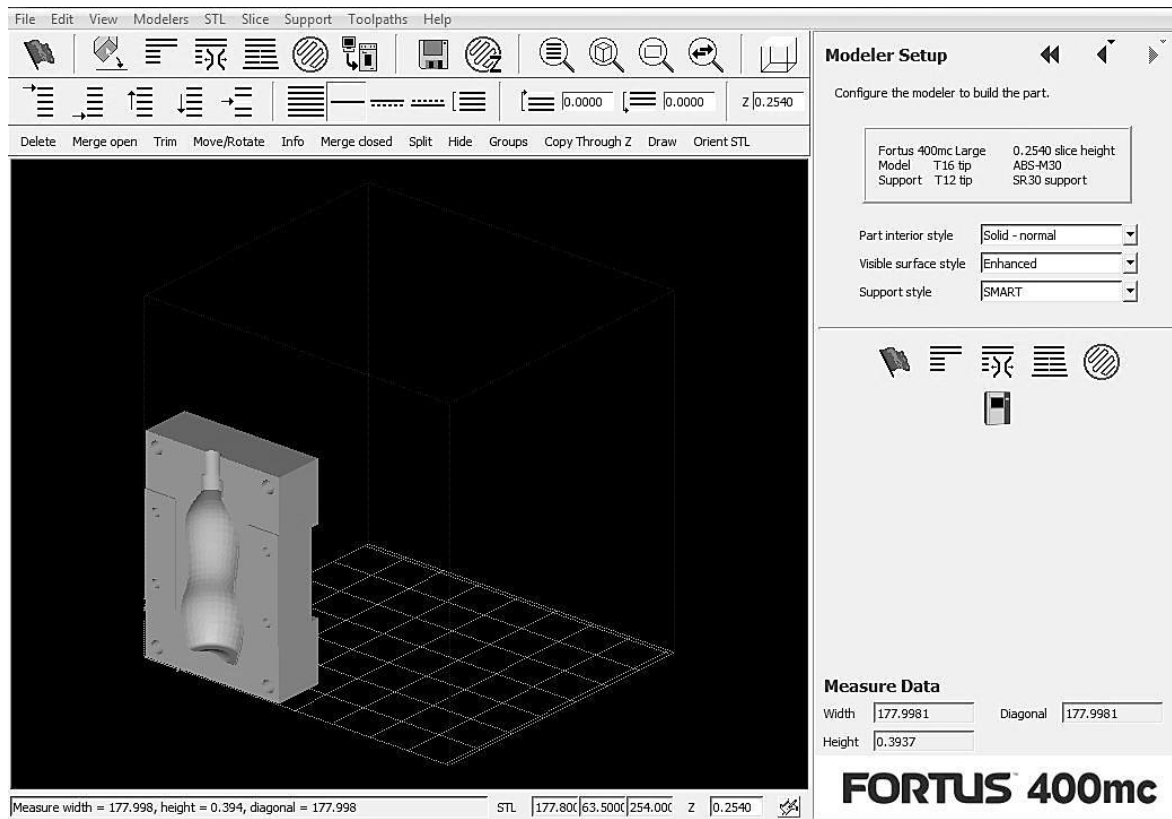


Figure 2.3. 1 INSIGHT® user interface

Table 2. 9 Summary of the overall parameters and their levels of the present study

Parameters	Low / High	Low / High	Low / High	Low / High	Low / High
Layer Thickness	0.254 mm	0.254mm	0.254mm	0.254mm	0.254mm
Support Fill	SMART	SMART	SMART	SMART	SMART
Raster Orientation	0°/90° / 45°/-45°	0°/90° / 45°/-45°	0°/90° / 45°/-45°	0°/90° / 45°/-45°	0°/90° / 45°/-45°
Build Plane	XY / XZ	XY / XZ	XY / XZ	XY / XZ	XY / XZ
Internal Structure	Solid	Hollow	Orthogonal	Hexagonal	Pyramid
Internal Density	NA	NA	Compact/Loose	Compact/Loose	Compact/Loose

Six parameters were chosen for the present study. Two of those parameters (layer width and support fill) were kept constant in order to maintain the scope of the research in plausible research extent. Also, it was disclosed that raster orientation was disclosed to have the highest impact on mechanical properties. In this regard, the two novel parameters subjected to characterization in this study are: internal structure and internal density. The internal structure and internal density parameters are described in Section 4.1.3 of Chapter IV. Hence, the final modifiable parameters (raster orientation, build plane, and internal density), each at two levels, selected for this study are

encompassed in Table 2.10.

Table 2. 10 Selected parameters and their level correspondence for the present study

Factors	Solid		Hollow		Orthogonal		Hexagonal		Pyramid	
	Raster Orientation	45°/-45°	-1	45°/-45°	-1	45°/-45°	-1	45°/-45°	-1	45°/-45°
0°/90°		+1	0°/90°	+1	0°/90°	+1	0°/90°	+1	0°/90°	+1
Build Plane	XY	-1	XY	-1	XY	-1	XY	-1	XY	-1
	XZ	+1	XZ	+1	XZ	+1	XZ	+1	XZ	+1
Internal Density	NA	NA	NA	NA	Loose	-1	Loose	-1	Loose	-1
					Compact	+1	Compact	+1	Compact	+1

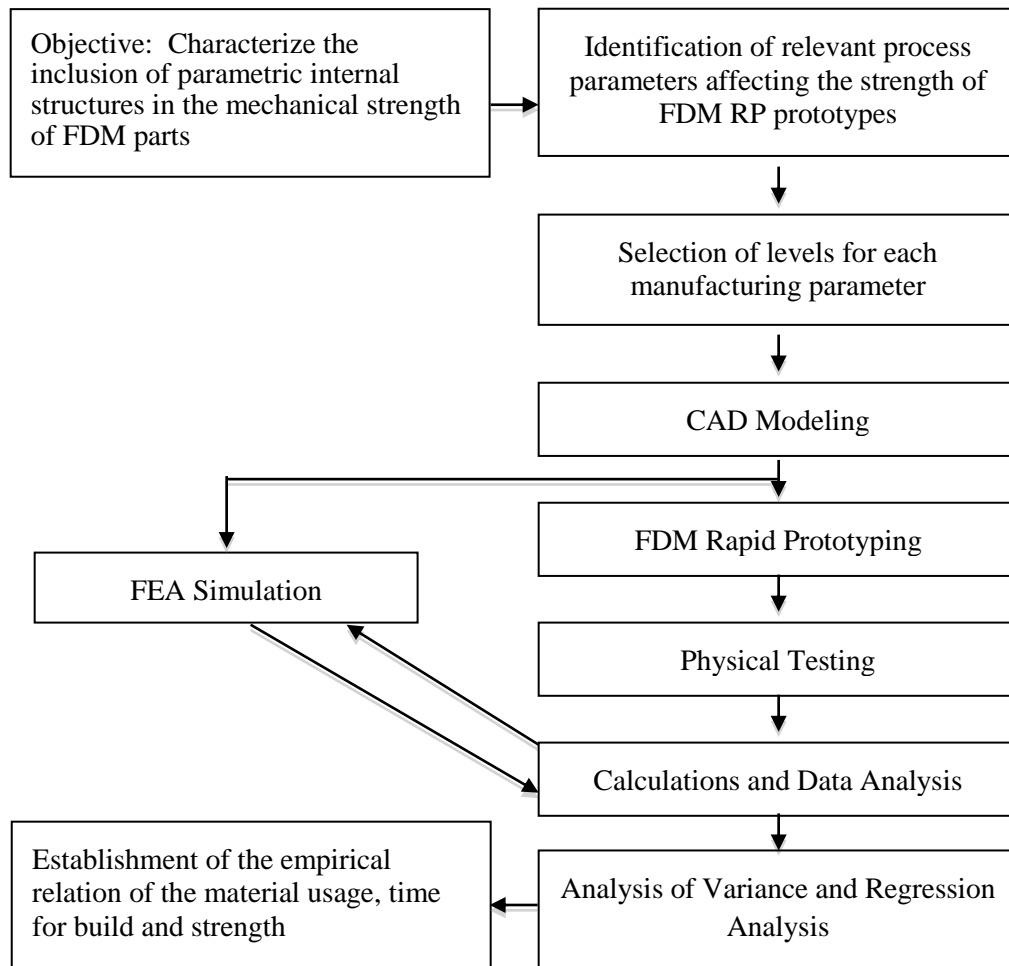


Figure 2.3. 2 Methodology followed in the present study

CHAPTER III

COMPUTER-AIDED DESIGN FOR RAPID PROTOTYPING

3.1 INTRODUCTION TO CAD MODELING

In order to build parts with enhanced capabilities, it is necessary to model and test FDM parts relative to the mechanical characteristics of the material. The mechanical properties of the FDM ABS thermoplastic have to be characterized experimentally according to the scope and characteristics of the present research. In view of the scope and purpose of this research, CAD models with internal web-like structures should be representative of the macro-mechanical properties from the results obtained from test samples under standard test conditions. As previously described in Section 2.1.3 of Chapter II, meso-structure affects the mechanical properties of the FDM ABS material. Primarily, the mechanical strength is influenced by the part orientation - anisotropy of the monofilament deposition. Similarly, the fiber-to-fiber bonding (the bonding density) affects the strength and the material degradation since the air gap controls the quality of the material at high stress values.

As described in Section 1.3.4 of Chapter I, when characterization of FDM-ABS was introduced, the internal structure of FDM parts is analogous to the fiber layout in composite materials. As such, various researchers have attempted a number of methods to characterize this condition. El-Gizawy et al. [El-Gizawy, 2010] discloses that classical lamination theory (CLT) has been used to predict the failure criteria of FDM parts. Other approaches described by Rodriguez [Rodriguez, 1999] include the definition of a representative volume element, which is statically representative of the infinitesimal material neighborhood of that material point. As it is described, once the volume element is defined, homogenization theory is used to transform the constitutive characteristics of a heterogeneous composite material to that of a homogeneous material with properties resulting in an average macroscopic response. Now then, there are some approaches to solve the homogenization theory and are: netting analysis, mechanics of materials, and elasticity based methods. This last one includes a number of approaches such as: self-consistent models, variational methods, and elasticity approaches for solid with periodic structures. When the solid comprises periodic structures (micro or meso), two elasticity-based homogenization procedures are used. The first one expresses the displacement as an expansion in Fourier series in the period of the micro/meso structure while the second one expresses the displacement as a perturbed

solution in the period of the micro/meso structure, which is assumed to tend to zero [Rodriguez, 1999].

Nevertheless, these methods do not reflect what the present study requires as a viable approach in order to characterize the macro/mega structure of the novel FDM parts studied in this research. It is important to mention that, unlike such methods and mathematical techniques, the present approach is semi-empiric. However, these does not downgrade the merit of the novel approach herein followed. For this reason, a different method is to be followed in order to give a meaning to the characterization of the FDM ABS parts of this study. Evidently, a suitable method is to be chosen, such as the one described by El-Gizawy et al. [El-Gizawy, 2010] of Section 3.1.2 of this chapter, where they mention that the three-dimensional finite element analysis (FEA) is a suitable method for predicting the mechanical behavior of FDM parts.

The purpose of this chapter is to introduce similar approaches from a wide variety of studies that have shown meaningful development in the understanding of RP optimization. Specifically, parts with optimized load-supporting characteristics, which demanded preparing models that reflect strength and stiffness in the RP material in relation to meso and macro-structural parameters. In this regard, Section 3.1.1 (Design for Optimization) encompasses a brief summary of the research that shares evidences points in common with the present work in terms of the optimization in the CAD domain. These points may be related to optimization of the math algorithms and other mathematical operations embedded in a variety of software applications or CAD modeling instructions developed to perform accordingly. Similarly, Section 3.1.2 (Design for Strength) comprises a brief review of some of the research that exhibits similar characteristics with the present study in terms of the optimization of strength based on specific characteristics of the modeled parts such as voids, reinforced structures, and shelling operations. At the end of this chapter, the results and the approach to obtain the final FDM sample parts is disclosed.

3.1.1 DESIGN FOR OPTIMIZATION

As many other approaches, computer software eases the achievement of complicated mathematical operations. This is evident in the research performed by Lam et al. [Lam, 1998] where they incorporated internal structures to act like reinforced thin-shell elements. Their main objective was to prove that the RP process could be accelerated if the tracing volume (solid material) is reduced. They proposed reducing this volume by extracting empty volumes from the original solid based on a theory, which offsets negative solids. They investigated on producing a

sub-boundary octree approach for producing a thin-shell RP with reinforced interior structures. The algorithm produced sub-boundary octree elements. Octants are created from proceeding part subdivisions and are stored inside the object. Once these are classified, they are aligned in a skeleton-type extraction procedure and the skeleton is extended. It is important to mention that the algorithm is a recursive procedure, which was implemented in C++ language. Once the skeleton is extended, the skeleton-extraction algorithm is then used to multiply the octree elements in all three directions, X, Y, and Z, as shown in Figure 3.1.1 [Lam, 1998].

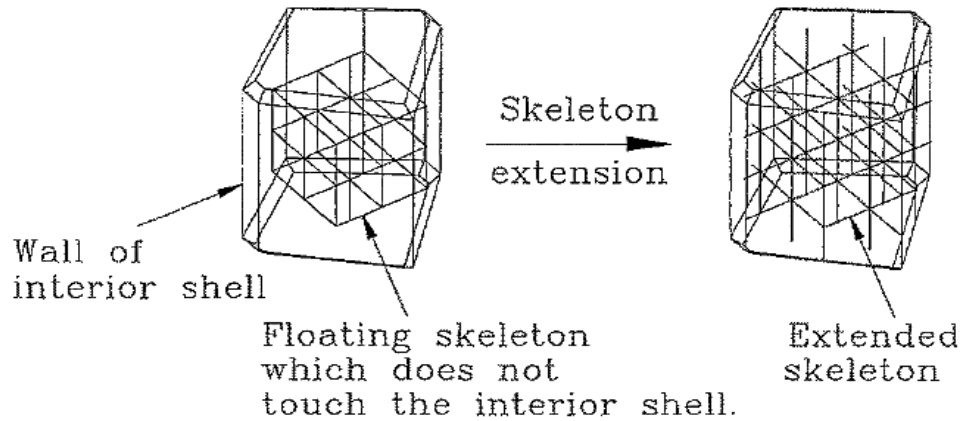


Figure 3.1. 1 Skeleton extension of the octree elements [Lam, 1998]

An octree consists on mimicking the external shape of the solid and duplicating that shape n-times in a reduced scale. Once the duplication is achieved, the sub-boundary octree solids are used to offset negatively the solid main element. The result is a hollow solid with shelled mini-structures that adapt perfectly to the original shape and size as shown in Figure 3.1.2 [Lam, 1998].

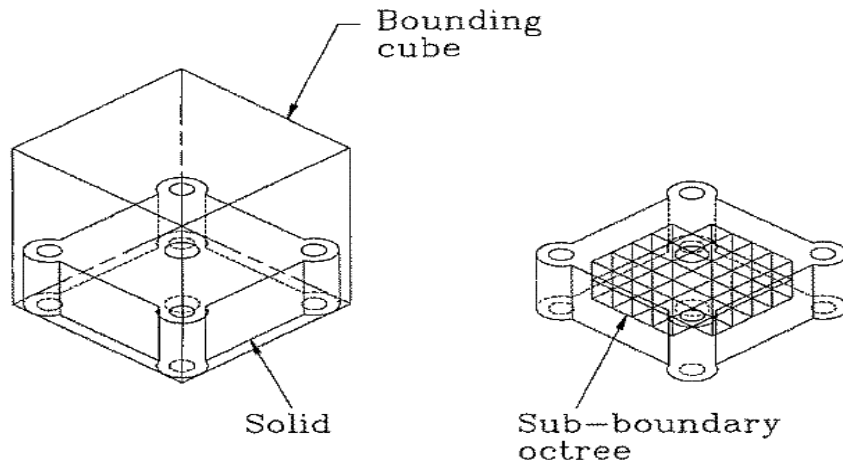


Figure 3.1. 2 Sub-boundary octree distribution inside the bounding cube [Lam, 1998]

Boolean operations are used in order to reduce the number of operations to be performed and avoiding overlapping. The research checked the capability of the Stratasys® FDM system to produce octree reinforced thin shell parts. They observed acceptable accuracy in the produced part as depicted in Figure 3.1.3 [Lam, 1998]. However, they observed that the filaments dropped more significantly in large area spans. They concluded that the wall thickness of the thin shell must be kept between the ranges of 3 to 5% of the longest side of the model part. Once the first two “*weak layers*” have been deposited, the filaments return to normal once the third layer is drawn. Dimensional accuracy was verified and compared. They found an average deviation of 0.18mm compared to the modeled part. From the results, a considerable material saving of 65% and a lead production time reduction of 44% was observed.

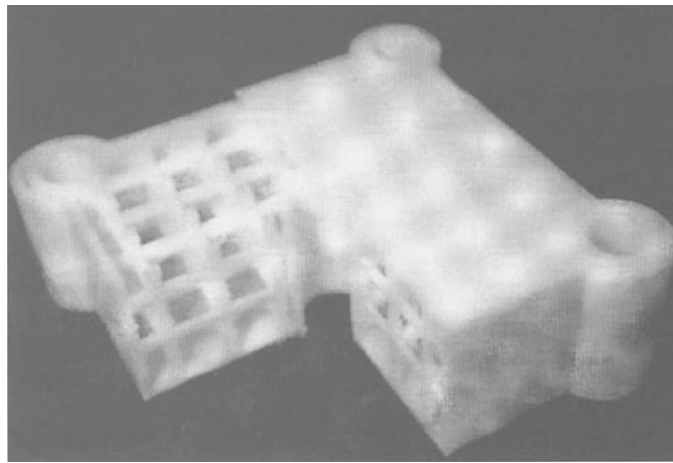


Figure 3.1. 3 RP part with internal sub-boundary octree structures [Lam, 1998]

McMains et al. [McMains, 2003] defined that build time is proportional to the amount of material deposited for the part and the support. A solid part, made by FDM, can be completed considerably fast if the part is not densely filled. Most FDM machine manufacturers, such as Stratasys®, provide their own rapid prototype post-processing software (Section 1.1.4, Chapter I) along with the machine as a user-friendly interface to select the desired printing parameters. Among other capabilities, this software allows controlling the amount of the interior material's density. As described before, less material deposited in the interior's modeled part represents a considerable reduction of the rapid prototyping process. An even-sloped modeled part, as seen in Figure 3.1.4 [McMains, 2003] represents a considerable reduction in building material and building time when the interior's fill is chosen to be sparse or low-density filled (left). However, in real practical modeled parts, this scenario is not likely to occur (areas where a part surface shows a shallow slope with respect to the build plane).

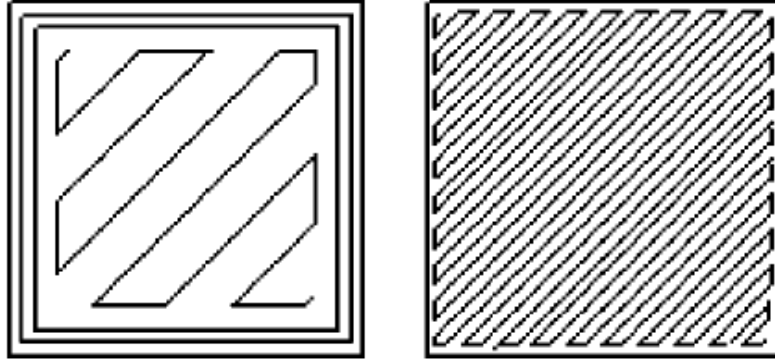


Figure 3.1. 4 Raster path optimization for the internal fill [McMains, 2003]

One of the main characteristics of FDM is enabling the production of intricate parts in less time as compared to conventional subtractive manufacturing (in terms of process planning). These parts vary in complexity due to the number of different sections, difference in wall thicknesses, non-uniform slopes, different cross sections, etc. According to McMains et al. [McMains, 2003], whenever the software intersects and part surfaces that approach the horizontal, the software will tend to fill with solid dense material on the entire slice because near the intersection with the near-horizontal faces the loose fill pattern would be evident. In some other cases, the part's morphology does not allow for differentiating the wall and the interior areas.

Their approach calculated the areas in each 2D layer that were in the thin-wall offset region where the solid fill was to be deployed rather than calculating the boundary of the 3D offset. They found that the savings in build time and material increase with the number of slices through near-horizontal faces and the volume to surface ratio. Figure 3.1.5 [McMains, 2003] depicts free form geometries fabricated with the QuickSlice® software (left), provided by Stratasys®, and with the proposed algorithm (right). Results show that the algorithm reduced the material usage as much as 2.2 to 3.7 times and enhanced the build time up to 14% to 64%.

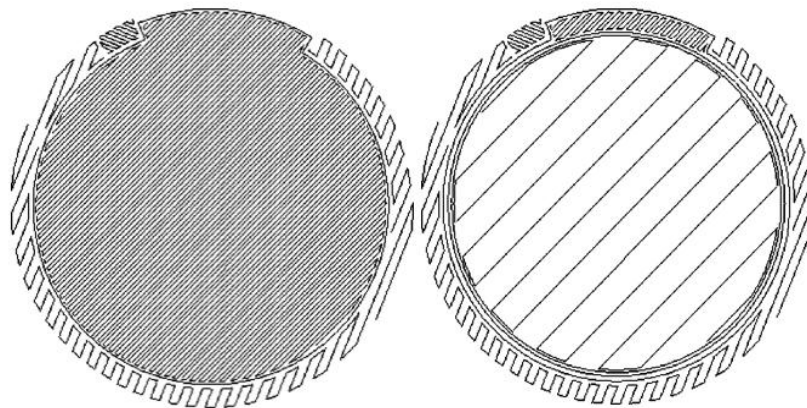


Figure 3.1. 5 Free form geometry with the optimization algorithm [McMains, 2003]

Their research intended to divide the part into a thin outer wall region (for a solid fill) and an interior region (for the loose fill). They accomplished this division by finding the exact interior offset surface in 3D and then slicing this offset surface along with the original part. This was made by offsetting algorithms and Boolean operations to approximate the true inner 3D surface. At the end, they proposed freeform models provided many complex test cases for debugging and validating their implementation. For example, Figure 3.1.6 [McMains, 2003] shows a detail of the tail region (halfway) through building the cow model where their software correctly processed a self-intersection in the input model, the resulting island, and a very thin region.

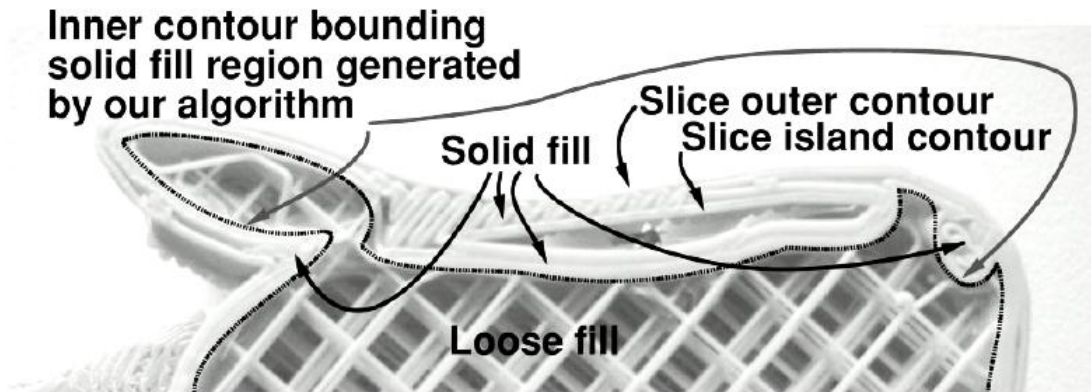


Figure 3.1. 6 ABS RP part with the free form geometry optimization algorithm [McMains, 2003]

Park [Park, 2005] describes that in order to accelerate the part building processes in rapid prototyping (RP) systems, approaches have been made to hollow a solid model by generating internal contours within parts with uniform wall thickness as depicted in Figure 3.1.7 [Park, 2005]. Figure 3.1.7 [Park, 2005] depicts the transformation process of hollowing a solid model from the (a) original solid model minus the (b) offset model (inward processing) equals to the (c) hollowed model.

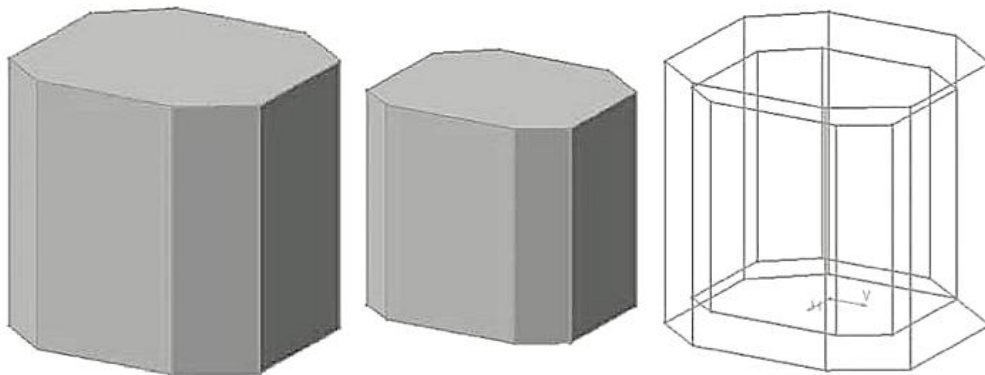


Figure 3.1. 7 Hollowing process based on the 3D surface geometry [Park, 2005]

External contours can be easily obtained by slicing the solid model and internal contours by slicing the offset surface for the uniform wall thickness. The difficulties in offsetting the model of an STL part are due to irregularities such as self-intersections, gaps, and invalid triangles. To avoid the difficulties in computing a correct offset model, Park [Park, 2005] overcomes the weakness of the conventional curve offsetting methods, by developing a method to generate internal contours that can achieve uniform wall thickness. The method is based on 2D geometric algorithms including 2D curve offsetting, which differs to other methods employing 3D geometric algorithms develops a new procedure to generate internal contours directly from the external contours. The underlying concept of the proposed algorithm is that the sum of circle swept volumes of external contours represents the offset model. While it is possible to compute an internal contour of a layer by slicing the circle swept volumes affecting the layer, it is not necessary to compute the actual circle swept volumes because the sliced curves can be generated with a simple combination of 2D geometric operations. The results indicate that the approach proposed by Park [Park, 2005] allowed to build a hollowed prototype instead of a solid part, which significantly reduces the building time and expenses in the RP material as shown in Figure 3.1.8 [Park, 2003], where the offset surface defined by the sum of circle swept volumes comprises the (a) solid model and external contours definition, the (b) external contour and circle swept volume differentiation, and the (c) the sum of volumes of all the external contours.

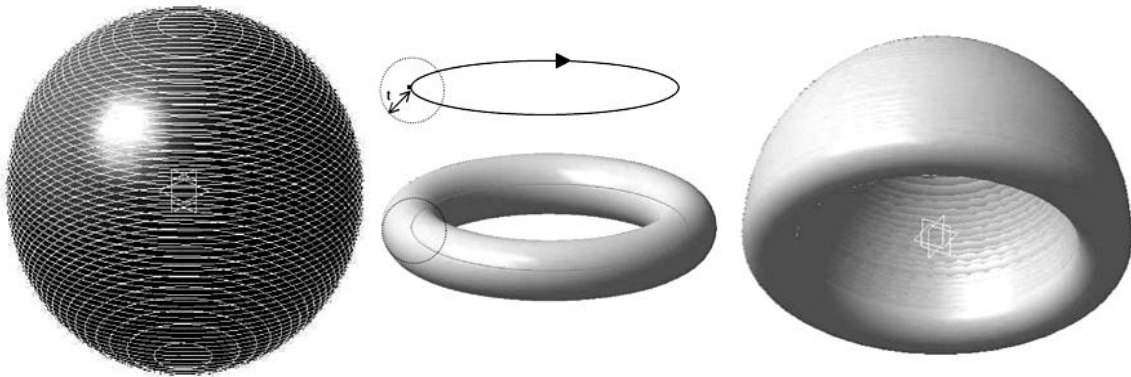


Figure 3.1. 8 Swept volume obtained based on the 3D surface geometry [Park, 2005]

Yao et al. [Yao, 2000] performed research on the investment casting technologies. They found that typical expandable patterns -usually produced by the injection of a type of wax into a mold until the required shell is obtained- are being replaced with stereolithography apparatus (SLA) thermally expandable patterns, which are quicker and more cost effective. A main challenge of these patterns is the ability to collapse into them without breaking the shell during the pattern

burnout process. The epoxy resin used in this technology does not melt like common wax. The difference of the coefficients of thermal expansion of the pattern material and the investment material (ceramic) is considerable, thus the pattern exerts high stresses on the shell; hence promoting cracks during the pattern burnout process. The cracking occurs when the shell rupture temperature is lower than both the pattern's buckling temperature and the resin's glass transition temperature. A larger web width has a larger moment of inertia. As a result, the internal web structure with a larger web width can better resist bending while a longer web link span can bend easier. As thermal expansion occurs due to temperature rise, a compressive normal force F is developed in the web's beam as shown in Figure 3.1.9 [Yao, 2000]. Likewise, the ceramic shell also expands. This force F depends on both materials' coefficients of expansion, the length of the web link, the cross-sectional area of the web's link, and the temperature gradient ΔT . Thus, a critical compressive load is inversely proportional to the square of the web link span length. Now then, it would be desirable that the epoxy web structures buckle first so that the shell wall stresses drop dramatically, keeping the shell intact. At the same time, such web structures must provide enough support to the ceramic shell.

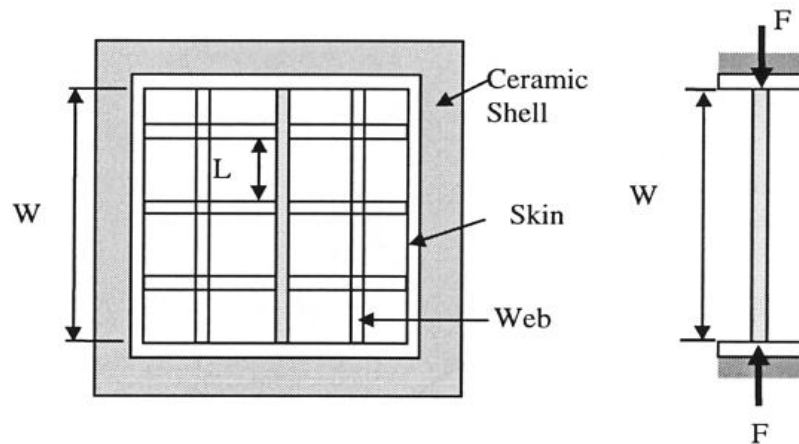


Figure 3.1. 9 Schematic of the force acting on the investment casting inner walls [Yao, 2000]

Web structures with controllable wall thicknesses and lengths are designed to control the hoop stress exerted on the ceramic shell. Modifications to the characteristics of the pattern's wall temperature will impact the thermal response on the exerted force of the web links on the ceramic shell. Having found that the yield of castings depends on the void ratio defined by the fraction of air space in the pattern, a quasi-hollow web SL pattern would collapse inwards instead of cracking the ceramic shell by expanding outwards. A triangular web structure, a square web structure, and a hexagon web structure were modeled and tested as depicted in Figure 3.1.10 [Yao, 2000]. The (a) triangular web structure consisted of a series of equilateral triangles, which

are built on the top of each other for each layer thickness with an offset so that they form equilateral triangles. The other two structures ((b) square and (c) hexagonal) were built in the same topological manner. The same area in each of the different types of web cells was kept constant. Having the same area will allow keeping the drainage rate for all the various web structures constant.

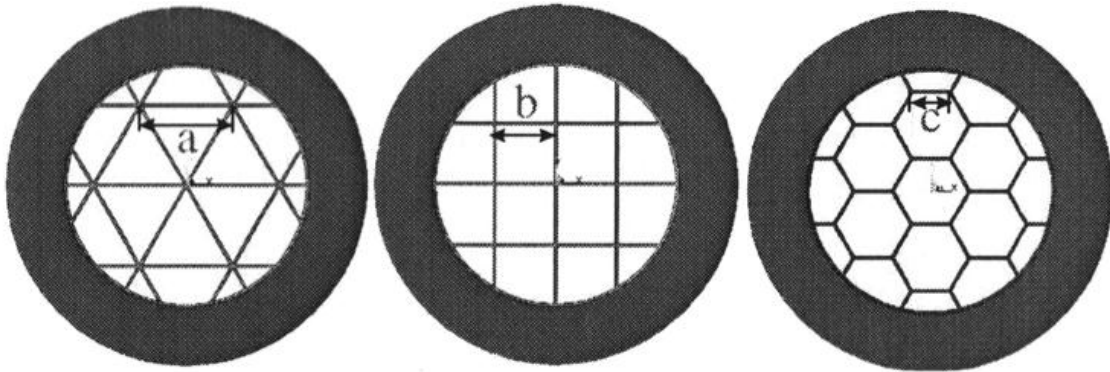


Figure 3.1. 10 Investment casting internal structures [Yao, 2000]

A finite element analysis (FEA) was carried out to determine thermally induced stresses during a pattern burnout process. They validated the FEA predictions by experimental measurements with strain gauges mounted in test parts of webbed epoxy patterns. They carried out the same procedure in three different web structures. The FEA results showed that the hexagonal structure exhibited a reduction of the maximum stresses. The triangular structure showed a 32% increase, while the square structure showed a 22% increase (Figure 3.1.11 [Yao, 2000]). The abovementioned shows that the incorporation of web structures in a predefined way (hexagonal) affects the thermal induced stresses during the burnout process in investment casting. Although many factors interact with the heat distribution within the SL quasi-hollow pattern such as transient heat, the addition of modeled web structures avoids crack propagation in the ceramic shell. There are two important factors that must be mentioned, the fact that the addition of a parametric internal structure aids in redirecting the thermal distribution of the SLA epoxy pattern and providing a better way to balance the thermal stresses; the fact that the research compared the effect of three different web structures and identified an overall better structure.

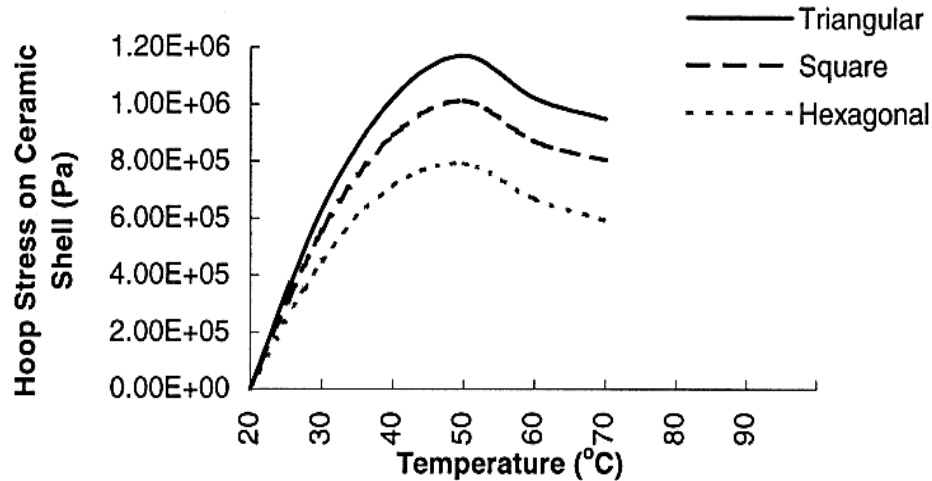


Figure 3.1. 11 Hoop stresses on the ceramic casting walls for different structures [Yao, 2000]

In a similar way, Wang et al. [Wang, 2005] developed a hybrid geometric modeling method to create CAD models of large-scale conformal cellular structures. They utilized a method of constructing models of uniform trusses patterning unit cells linearly within a CAD system. By orienting strut directions and adjusting strut sizes, the trusses can be optimized to achieve superior strength, stiffness, and weight characteristics. Their approach utilizes both solid modeling and surface modeling techniques to create tessellated models and automate the geometric modeling process of conformal truss structures. The aforementioned was accomplished by creating geometric models of conformal trusses using solid modeling and a hybrid geometric method as depicted in Figure 3.1.12 [Wang, 2005]. The first one creates complete solid models of truss structures using ACIS (a geometric modeling kernel) and generating STL models. This approach takes significant computational resources to generate the solid models since Boolean operations are required to add every single strut onto the existing truss part.

However, the second approach is a hybrid geometric modeling method, which creates the STL model for the truss structure directly, without creating a complete solid model of the entire structure. The hybrid method creates an STL model of each unit truss (a selected microstructure of truss structure) using both solid modeling and surface modeling techniques, and then simply stacks all the unit truss tessellated surface (STL) models together without complex Boolean operations to generate the STL model of the entire structure. According to Wang et al. [Wang, 2005], the ACIS faceting tool must be configured to ensure the STL vertices along the coincident circular edge are coincident. Therefore, no Boolean operation is required during stacking the STL

models of all the unit trusses. The solid modeling process was implemented with C++ and ACIS. The input is the truss topology and the output is the STL model of the entire truss structure.

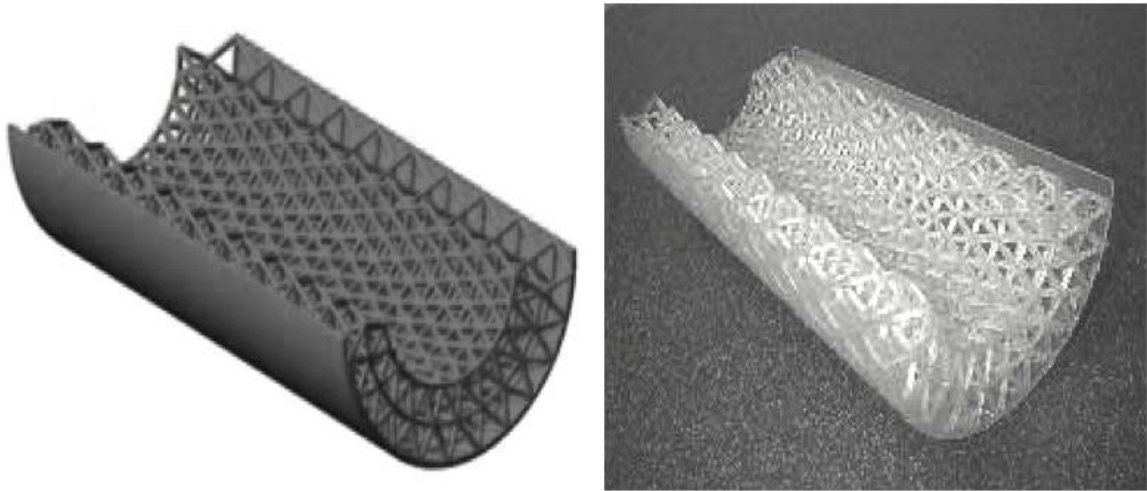


Figure 3.1. 12 Truss structural geometries before and after RP [Wang, 2005]

To accomplish the above described, Wang et al. [Wang, 2005] modeled the struts as simple shape primitives (truss primitives) repeated in certain directions from one another in terms of their size, position, and orientation. The truss consists of a central node and half-struts connected to the central node. Each strut is divided into two half-struts by its middle. The number of half-struts in a unit truss depends on the truss type and the location of the central node (sphere). A unit truss with a central node in the middle of an octet truss has 12 half-struts, while a unit cell with a central node at the boundary has 9 half-struts as depicted in Figure 3.1.13 [Wang, 2005].

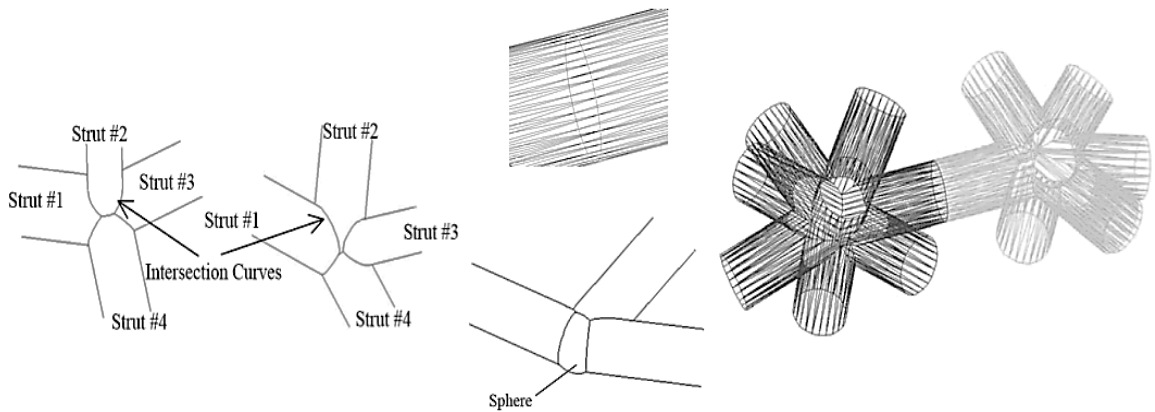


Figure 3.1. 13 Node bonding truss morphology [Wang, 2005]

The truss structures can be generated through repeating the primitives in several directions as a pattern of the truss primitives. The geometries of the joints where neighboring microstructures are

connected are complicated for a conformal truss due to the struts' sizes and orientation changes. With the unit truss, Wang et al. [Wang, 2005] constructed models with tetrahedron (tetra) geometries, which then formed the octet trusses (octahedron) as depicted in Figure 3.1.14 [Wang, 2005]. The topology of the unit truss is parameterizable and patternable. As shown in Figure 3.1.13 [Wang, 2005], unit trusses are connected at the ends of their half-struts with no overlap of their geometry. Therefore, geometric models of unit trusses can be simply stacked after positioned at the desired coordinates. There is no overlap between any two-unit trusses. The stacking process does not require any Boolean operations. Finally, the most outstanding aspect of their work is that topology of the truss structure can be generated by using a parametric modeling method; hence, the unit trusses can be patterned parametrically.

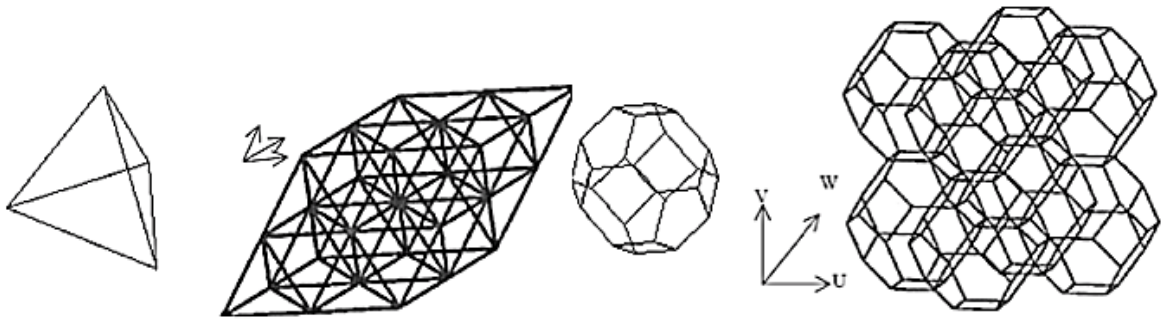


Figure 3.1. 14 Simple and complex geometrical structures obtained by truss bonding [Wang, 2005]

3.1.2 DESIGN FOR STRENGTH

It has been discussed that for said additive manufacturing processes, the manufacture of mesoscopic structures becomes feasible for meso and macro scale sizes and is more cost-effective than other manufacturing methods. These developments may enable new applications in industries such as aerospace, automotive, manufacturing, and bioengineering. The manufacturing of this type of structures allows the fabrication of parts with virtually any geometry. Parts with a variety of topologies may exhibit a number of different characteristics due to their geometries and complexities. In this regard, a part may be affected in a number of different ways when prototyped by the layered manufacturing technologies. In any case, the part's meso-structure affects both stiffness and strength by introducing anisotropy. Hence, it is necessary to have models for the RP part's material stiffness and strength as a function of the meso and macro structural parameters. Now that the efforts have concentrated on explaining several CAD and mathematical methods to obtain intricate internal designs in a variety of shapes and forms, it is

important to mention the impact of the analysis and study of such methods in the context of this research. Now then, a brief review of relevant researches that combine a unique strategy to design parts for optimizing material usage while reducing time and characterizing the mechanical properties is presented.

Galantucci et al. [Galantucci, 2008] researched on topologically optimized structures for accelerating the FDM RP process in terms of the reduction of materials consumption, manufacturing times and cost. Internal voids arranged in a specific manner were introduced into specimens and then tested according to the standard EN ISO 604. The specimens were designed using a narrow-waisted structure capable of being manufactured layer by layer without using building supports. Five kinds of FDM – PC specimens were prototyped; the first one was full and dense while the other four were created using the narrow-waisted structure. These four specimens are identifiable on the basis of two factors, namely the internal angle of the narrow waist and the width of the external shell as encompassed by Table 3.1.

Table3. 1 Schematics for the different specimens with internal voids [Galantucci, 2008]

Specimen	Internal Void Angle	Raster Width (mm)	Shell Width (mm)	Schematic
1	20°	0.98	2	
		0.41	1	
2	50°	0.98	2	
		0.41	1	

In order to study the mechanical behavior of the designed structure, a numerical simulation was performed as an approximate analysis to the compressive test. The analysis takes into account the topology of the specimens, but cannot consider the anisotropy of the layered manufactured material (polycarbonate). The numerical simulation was made using the mesh-less analysis software FieldMagic®, with a compressive strength to be equal to the tensile strength (52 MPa), the Poisson ratio equal to 0.35, the compressive elastic modulus equal to the tensile (2000 MPa), specific gravity equal to 1.2 g/cm³. Figure 3.1.15 [Galantucci, 2008] shows specimens width equal to 2 mm for the (a) 50° and (b) 20° internal void angles. For the first one (a), the failure starts at a uniform pressure load equal to 15 MPa whereas for the second one (b), the failure starts for a uniform pressure load equal to 30 MPa (Von Mises failure criterion).

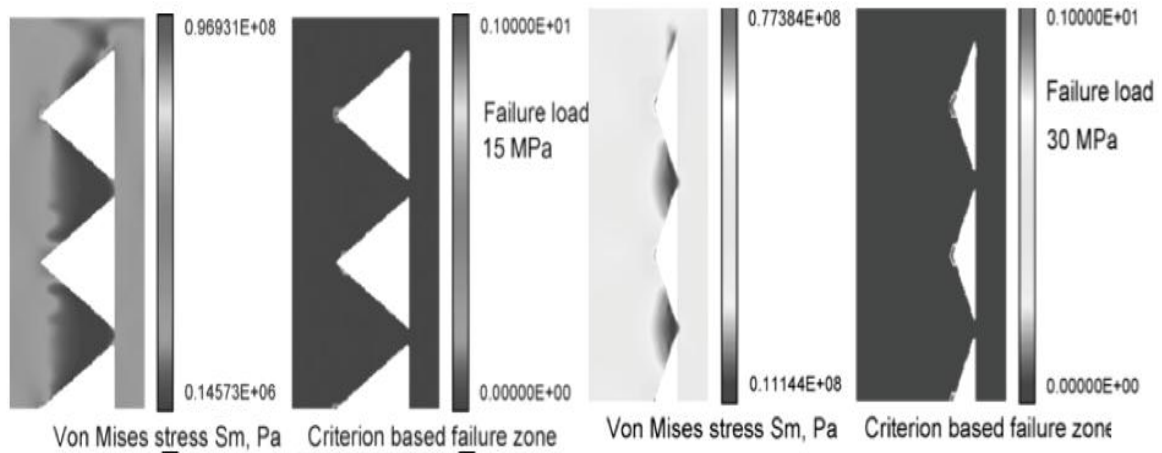


Figure 3.1. 15 Von Mises stress distribution for the specimens with internal voids [Galantucci, 2008]

According to the experimentation, necessary especially because of the anisotropy of the layered products, for the part with a raster of 1mm and a 50° void angle, the reduction of the total volume is 44% combined. For the part with a raster of 2 mm and a 20° void angle, the reduction of the total volume is 31% combined. In terms of stress, there is a reduction of maximum tolerable compressive stress of 48% combined for the 1mm raster specimen and a 32% combined for the 2 mm raster specimen as depicted in Figure 3.1.16 [Galantucci, 2008]. In terms of manufacturing time, there is a reduction of 25% in manufacturing for a 50° void angle specimen compared to a 15% in manufacturing time for a 20° void angle specimen when the raster is 1 mm. Conversely, it was observed that when the raster is 2 mm, the 50° void angle specimen's manufacturing time is just reduced 15% whereas for the 20° void angle specimen's manufacturing time is increased 13% compared to the specimen without voids.

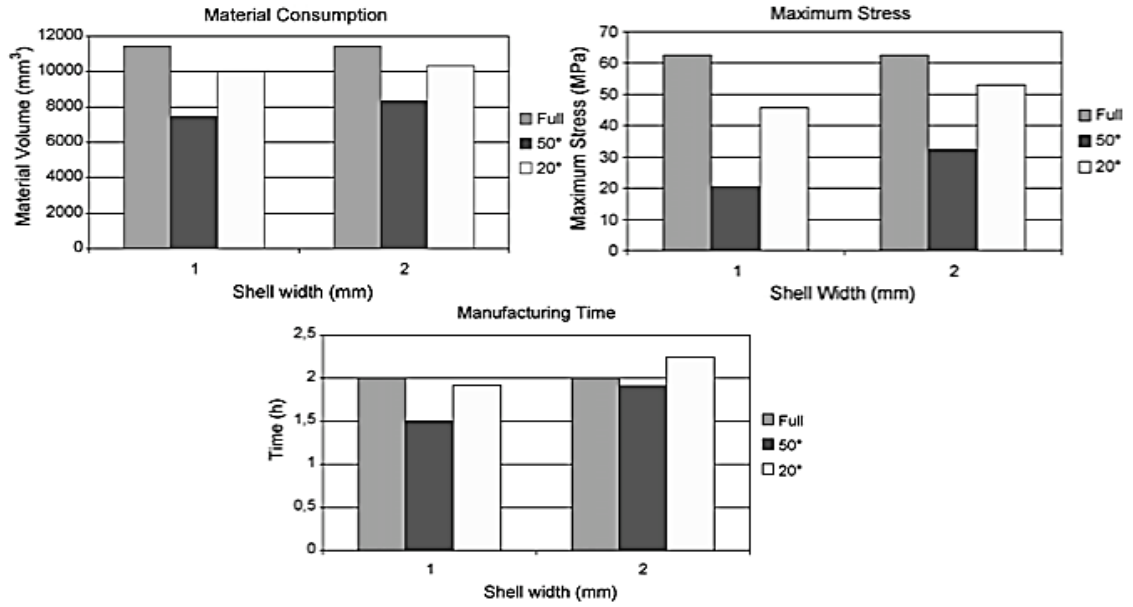


Figure 3.1. 16 Material use, maximum stresses, and build time for the void specimens [Galantucci, 2008]

Additionally, Galantucci et al. [Galantucci, 2010] utilized this approach to compare the effect of FDM-ABS large and small parts on manufacturing time, material utilization and compression strength. They refer to small parts to cylinders with a diameter of 20 mm and height of 50 mm. The large parts are referred to those parts with diameters of 140 mm and heights of 350 mm. Like in their previous work, Galantucci et al. [Galantucci, 2008] defined two different raster widths and layer sizes and defined a set of different plane angles as the angle voids; Table 3.2 comprises said parameters. Evidently, they carried out simulation analysis on the newly ABS parts. They discovered that for smaller parts, raster width is the most influential factor of the production time, whereas for compression strength, the most influential factor is the angle of the narrow-waisted structure.

Table3. 2 Strength, time, and material use values for parts in different void angles [Galantucci, 2010]

Internal Void Angle	Raster Width (mm)	Shell Width (mm)	Small Specimens			Large Specimens		
			Compression Strength (MPa)	Production Time (hours)	Material (cm ³)	Compression Strength (MPa)	Production Time (hours)	Material (cm ³)
20°	0.310	1	25.25	2.68	14.470	28.25	898.92	4819.17
		2	25.78	2.28	12.860	25.78	787.13	4261.51
42°		1	30.06	2.52	13.370	30.06	808	4378.9
		2	23.96	2.22	11.620	23.96	699.8	3798.26
0°		Full	28.25	2.68	14.470	28.25	898.92	4819.17
20°		0.980	1	37.54	1.15	14.270	37.54	267.76
	2		41.29	1.27	15.090	41.29	266.49	5048.28
42°	1		22.24	1.02	11.720	22.24	219.37	4054.83
	2		29.85	1.15	13.080	29.85	232.12	4378.28
0°	Full		49.71	1.05	16.530	49.71	286.78	5556.9

For large parts, the structure built with an angle of 20° evidences good values for compression strength and a decrease in production time ranging from 6.2 to 14.9 %. Overall, the specimen construction material is reduced by using internal structures, saving ranging from 7.6 to 29.5 % compared to the full specimen. Material reductions for large parts range from 9.13% (20° angle) to 27% (42° angle). Finally, an internal double narrow-waisted specimen, as depicted in Figure 3.1.17 [Galantucci, 2010], was fabricated obtaining a reduction of compression strength of 42.2% with a reduction of material, but with an increase in production time about 17.7% due to the complexity of the tool paths.

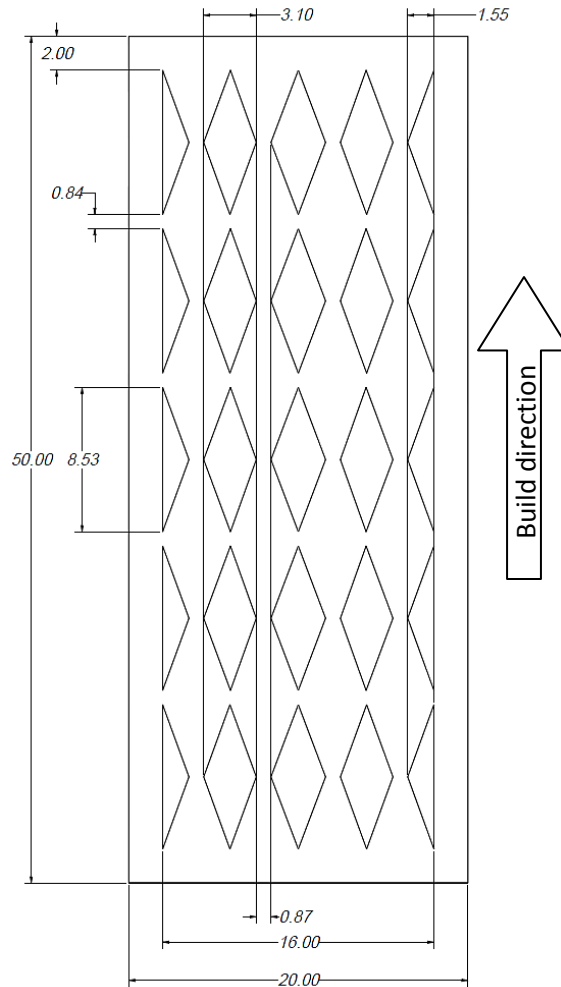


Figure 3.1. 17 Double narrow-waisted specimen
[Galantucci, 2010]

Wu [Wu, 2011] studied on the feasibility to create parts with porous-like internal structures to be used in the medical field as bionic scaffolds. Depending on the use, bionic scaffolds may be used to grow cellular tissue in different parts of the body. Wu [Wu, 2011] utilized simple units (cylinders) which structures are determined by unit space mode and size. The cylinders were arranged in a (a) $0/90^\circ$, (b) $0/60^\circ/120^\circ$ and (c) intersected. The distance of the adjacent cylinders (parameter s), the parameter f (space between layers), and the parameter d (cylinder diameter) are also represented in Figure 3.1.18 [Wu, 2011]. The cylinders in $0/60^\circ/120^\circ$ mode overlap those of the $0/90^\circ$, but form a 60° angle between layers. Thus, the cylinders in the intersected mode not only overlay in a layer, but they also do between layers.

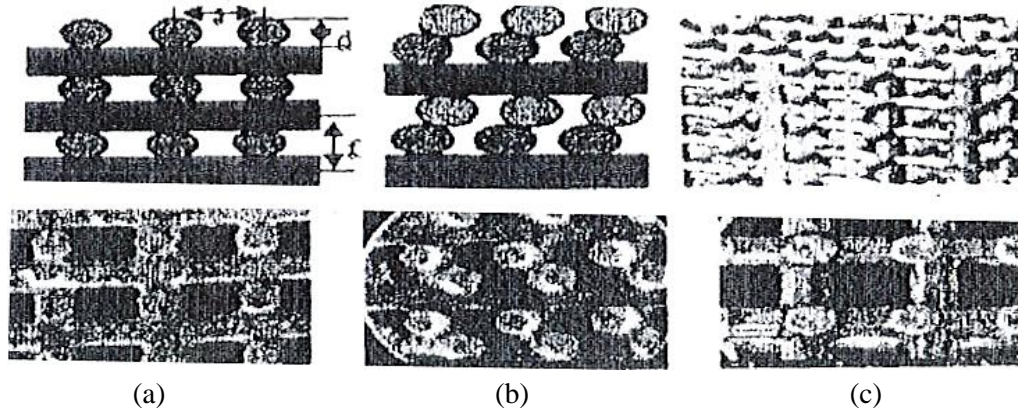


Figure 3.1.18 Cylinder orientation affecting the topology of the RP part [Wu, 2011]

A block of 18 mm length, 14 mm height, and width of 0.25 mm layer on both ends was RP in order to evaluate the mechanical properties of the test part, described in Figure 3.1.19 [Wu, 2011].

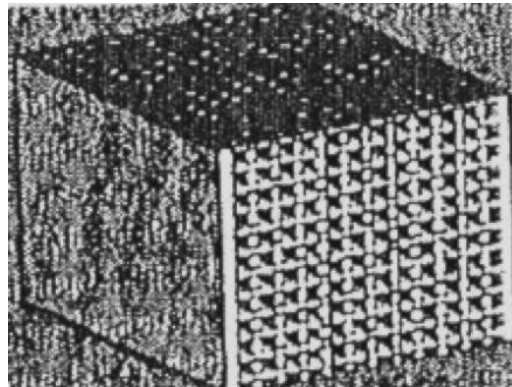


Figure 3.1.19 Compressive test part with inside porous parts [Wu, 2011]

Table 3.3 summarizes the parameters and the results captured from the experiments performed on the test samples. As it can be seen from Table 3.3, group A's vertical direction (Y) has the greatest stress equal to 3.52 MPa. The horizontal (X) direction in the 0/90° specimen exhibits a value close to the one of the (Y) direction. The horizontal (Z) direction has the least stress of about 2.56 MPa. According to results, Wu [Wu, 2011] commented that the 0/90° array specimen evidences the greatest ability to withstand the force acting along the X and Y axis, the 0/60°/120° specimen creates a 30° angle that causes an extra shear stress, and the intersected specimen allows point to point link which decreases the burden ability.

Table3. 3 Build parameters for the compressive inside porous parts [Wu, 2011]

Cylinder Array Orientation	Stress on specific Axis (MPa)			Diameter of Cylinder d (mm)	Layer space f (mm)	Neighboring distance s (mm)
	X	Y	Z			
0/90°	3.25	3.50	2.50	0.4	0.38	0.62
0/60°/120°	3.15	3.0	2.70			
Intersected	3.0	3.05	2.40			
0/90°	3.60	3.55	2.70	0.5	0.48	
0/60°/120°	3.45	3.50	3.0			
Intersected	3.35	3.0	2.45			
0/90°	3.90	3.85	3.25	0.6	0.58	
0/60°/120°	3.60	3.75	3.45			
Intersected	3.5	3.15	3.0			

El-Gizawy et al. [El-Gizawy, 2010] performed research on the characterization of the mechanical properties and internal structure of FDM processed thermoplastics. They developed an approach that uses analytical methods with non-conventional testing techniques for generating properties in order to optimize ULTEM 9085 (a flame retardant high performance thermoplastic) structures. In order to accomplish the aforementioned, El-Gizawy et al. [El-Gizawy, 2010] gathered data on the stiffness properties and images of internal structure of FDM processed samples with different raster angles and build orientations. The basis of their research was classical lamination (CLT) to determine the anisotropic stiffness matrix of the parts built by the FDM RP machine. This was intended to establish constitutive relationships of the models that could predict the internal structure (meso-structure) behavior of the ULTEM 9085 thermoplastic.

The specimens were RP using the Stratasys® FORTUS 400mc® with two build directions. One group of specimens was built along the X-Y plane whereas the second was built in the Z direction. The system was constrained to maintain the integrity of the structures by forcing the internal raster to maintain the same parameters at every layer when setting the machine on default for the ULTEM 9085 compliance. The specimens were tested under tension (ASTM D-638-03) using a MTS® System with a 5.0 kN load cell and a data acquisition system at a constant speed of 5mm/min. In order to capture strain, tri-axial strain gauges were used for measuring individual strains along the 0°, 45° and 90° directions. Also, width measurements were taken at five different locations along the longitudinal axis of the samples. In this regard, Figure 3.1.20

synthesizes the effect of laminar samples (mono filament) on the tensile properties (anisotropic stiffness) of the FDM RP part depending upon the raster orientation.

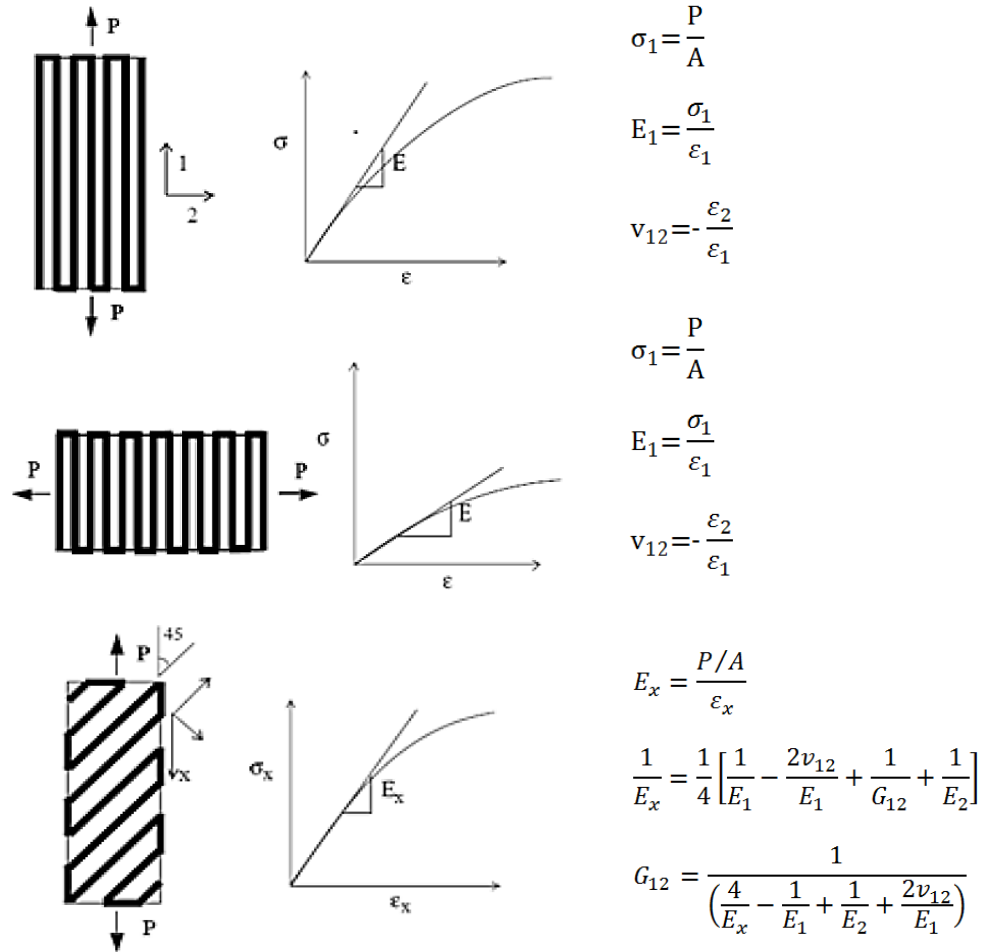


Figure 3.1. 20 Mono filament tensile stress equations [El-Gizawy, 2010]

El-Gizawy et al. [El-Gizawy, 2010] commented that due to inaccuracy of the assumption of transversely isotropic properties of layers deposited during FDM RP, they prototyped specimens in the Z direction with different raster orientations. Values were obtained from directional strain gauges (rosettes), stress-strain curves, and from data of the vertically prototyped samples. Table 3.4 [El-Gizawy, 2010] summarizes the values obtained from the processed tensile test data from specimens (X-Y plane orientation) at different raster angle orientations. These results arose from the average representing a sample size of 5 specimens for each raster orientation.

Table3. 4 Values from the tensile test at different angle orientations [El-Gizawy, 2010]

Raster Angle	Modulus of Elasticity (MPa)	Ultimate Tensile Strength (MPa)	Yield Strength (MPa)
0°	2,539.40	78.60	57.50
45°	2,424.60	56.76	3.31
90°	2,327.80	45.70	2.37

Additionally, due to the difference in the topology of the samples when RP in the Z plane orientation, Table 3.5 [El-Gizawy, 2010] comprises the computed mechanical values from the data obtained from the tensile tests for the upright specimens at different raster angle orientations. Similarly, the results arose from the average representing a sample size of 5 specimens for each raster orientation. According to El-Gizawy et al. [El-Gizawy, 2010] the results from Table 3.4 and 3.5 [El-Gizawy, 2010] reveal that strength and modulus of the materials (ULTEM 9085) built along the Z direction are lower by about 20% in average than those built in the X-Y plane.

Table3. 5 Mechanical properties of the upright specimens at different angle orientations [El-Gizawy, 2010]

Raster Angle	Modulus of Elasticity (MPa)	Ultimate Tensile Strength (MPa)	Yield Strength (MPa)
0°	2,163.50	52.00	43.80
15°	2,180.80	42.50	46.50
30°	2,154.20	50.40	47.10
45°	2,170.70	51.90	45.50
60°	2,211.40	48.90	46.40
75°	2,169.90	50.90	45.10
90°	1,991.70	54.30	43.70

Finally, El-Gizawy et al. [El-Gizawy, 2010] used classical lamina theory (CLT) to determine the anisotropic stiffness matrix for parts built by FDM. Each lamina is subjected to normal stresses σ_1 , σ_2 and σ_3 and shear stresses τ_{23} , τ_{13} and τ_{12} . These stresses are related to strains as shown in Equation 3.1, namely:

$$\begin{Bmatrix} \varepsilon_1 \\ \varepsilon_2 \\ \varepsilon_3 \\ \gamma_{23} \\ \gamma_{13} \\ \gamma_{12} \end{Bmatrix} = \begin{bmatrix} 1/E_1 & -\nu_{21}/E_2 & -\nu_{31}/E_3 & 0 & 0 & 0 \\ -\nu_{12}/E_1 & 1/E_2 & -\nu_{32}/E_3 & 0 & 0 & 0 \\ -\nu_{13}/E_1 & -\nu_{23}/E_2 & 1/E_3 & 0 & 0 & 0 \\ 0 & 0 & 0 & 1/G_{23} & 0 & 0 \\ 0 & 0 & 0 & 0 & 1/G_{13} & 0 \\ 0 & 0 & 0 & 0 & 0 & 1/G_{12} \end{bmatrix} \begin{Bmatrix} \sigma_1 \\ \sigma_2 \\ \sigma_3 \\ \tau_{23} \\ \tau_{13} \\ \tau_{12} \end{Bmatrix} \quad \text{(Equation 3.1)}$$

Where E_1 , E_2 , and E_3 are the Young's modules and the Poisson's ratios are ν_{12} , ν_{21} , ν_{13} , ν_{31} , ν_{23} , and ν_{32} and the shear modules are G_{12} , G_{13} , and G_{23} . Thus, Equation 3.1 can take the form of Equation 3.2, namely:

$$\{\varepsilon\} = [S] \{\sigma\} \quad (\text{Equation 3.2})$$

Where $[S]$ is the compliance matrix, $\{\varepsilon\}$ is the strain column vector and $\{\sigma\}$ is the stress column vector. According to El-Gizawy et al. [El-Gizawy, 2010], the assumption of plane stresses in the plane of the layer (lamina) allows for the stress components σ_3 , τ_{23} , and τ_{13} to be zero. This yields a reduced stiffness matrix described by Equation 3.3, namely:

$$\begin{Bmatrix} \sigma_x \\ \sigma_y \\ \tau_{xy} \end{Bmatrix} = \begin{bmatrix} \bar{Q}_{11} & \bar{Q}_{12} & \bar{Q}_{16} \\ \bar{Q}_{12} & \bar{Q}_{22} & \bar{Q}_{26} \\ \bar{Q}_{16} & \bar{Q}_{26} & \bar{Q}_{66} \end{bmatrix} \begin{Bmatrix} \varepsilon_x \\ \varepsilon_y \\ \gamma_{xy} \end{Bmatrix} \quad (\text{Equation 3.3})$$

Where $[Q]$ is the compliance matrix and, σ_x , σ_y , τ_{xy} are the in-plane stresses, and ε_x , ε_y , and γ_{xy} the in-plane strains.

Finally, Chen [Chen, 2006] developed a method and to generate solid models of various structures using a file format based on Extensible Markup Language (XML) to define structure configurations. The methodology developed was named universal structure generating system (USGS) in which a configuration file is used as the common interface between various structure designs. The generated models (in STL format) are to be water tight so as to be RP. As previously reviewed in Section 3.1.1, Wang et al. [Wang, 2005] presented a hybrid geometric modeling method for creating conformal cellular structures where it divided truss structures into a set of unit truss. In their research, each unit truss has one central node and semi-struts connected to the central node and the solid model of each unit truss is created and Boolean operations are performed in ACIS. Chen [Chen, 2006] utilized this same method to create structures that can be generalized in two types of dimensions, 3D and 2.5D. Regardless of its dimension, a structure can be decomposed into a set of nodes and a set of links between them. A node may be in any positions and have different strut connections, varying from one to many. Struts can have different orientations and different shapes may also be used in the struts of a structure for various purposes. There may be as many internal nodes as required based on a given approximation tolerance as depicted in Figure 3.1.21 [Chen, 2006].

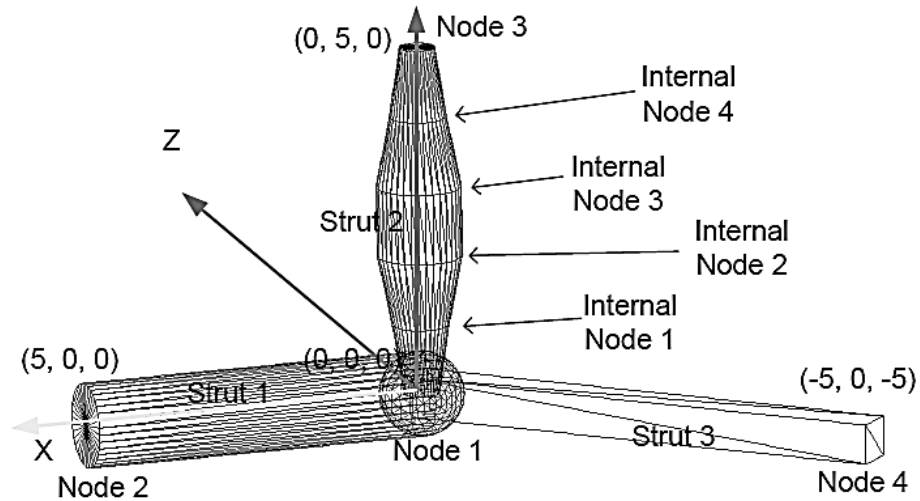


Figure 3.1. 21 Internal node approximation for different geometries [Chen, 2006]

The structure configuration design is defined in a general file format in order to create a solid model. This format is the XML that describes data in a standardized and simple manner. After a XML file is generated based on structure optimization design results, it can be input to a mesh-based structure generating system. The mesh-based structure generating system creates a node array and a strut array after reading an input structure configure file. It generates meshes for each node first and a set of planar contours is recorded as the node boundaries. Meshes of struts are then generated from pairs of these boundary contours. Finally all the meshes are combined to get the meshes of the whole structure as described in Figure 3.1.22 (a) for 3D and (b) for 2.5D [Chen, 2006].

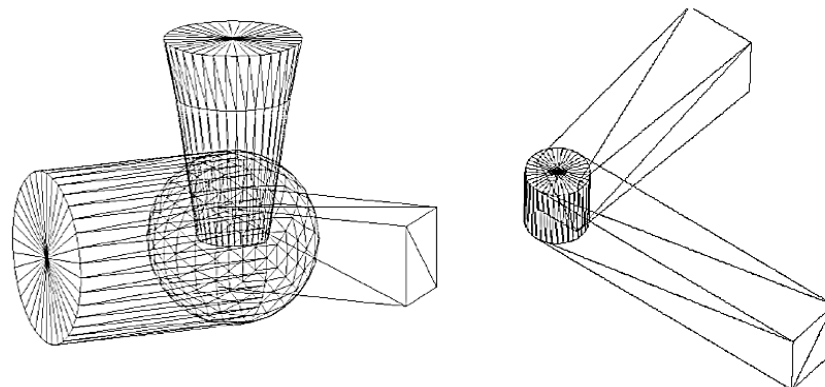


Figure 3.1. 22 Mesh approximation to different strut geometries [Chen, 2006]

A point-based method is utilized in this research to do filleting operation to input node meshes as previously described by Wang et al. 2005 [Wang, 2005]. After the meshes for all nodes and struts are generated from the offsetting and the filleting processes, they are combined into a single STL

model for the entire structure. This is shown in Figure 3.2.23 [Chen, 2006] where the meshes of nodes and struts have the same boundaries, thus generating an STL model without gaps or overlaps.

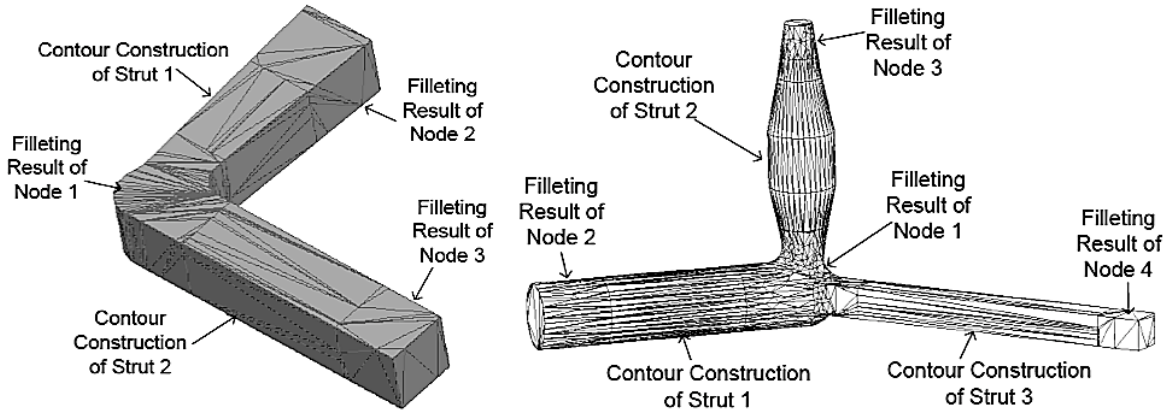


Figure 3.1. 23 Mesh refinement based on the resulting strut filleting [Chen, 2006]

Different examples were tested to evaluate the effectiveness and efficiency of the mesh-based geometric modeling method. Separate applications were developed to convert various structure designs into structure configuration files. These files were then used as inputs to the structure generating system to create STL models of the structures. In example, some STL models (built on an SLA system) were obtained from an application to convert a STL file into a structure configuration file where each vertex of a STL model is defined as a node and each edge of the model is defined as a strut. The result of this integration is shown in Figure 3.1.24 [Chen, 2006] where the final SLA RP part is obtained.

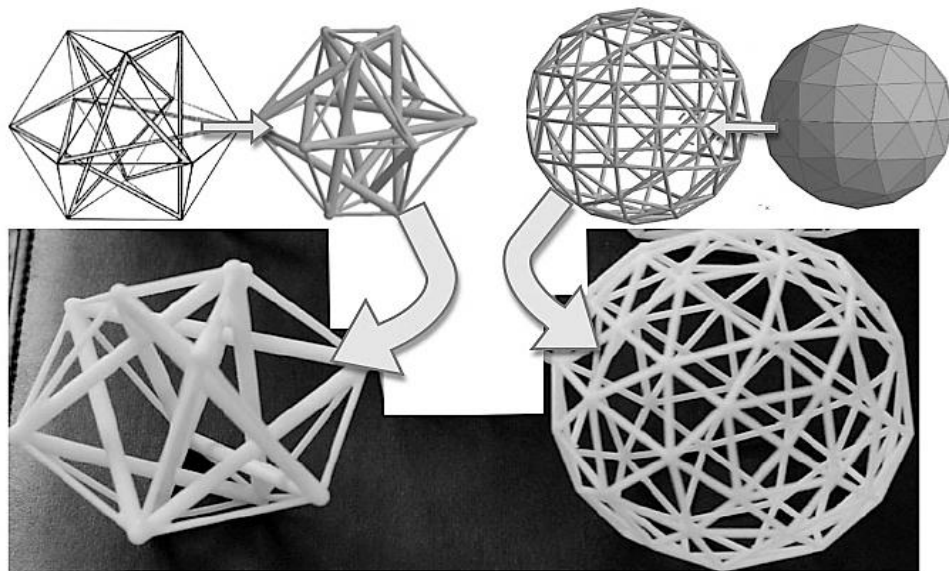


Figure 3.1. 24 SLA RP parts constructed via truss bonding [Chen, 2006]

Additionally, Chen [Chen, 2007] proposed a 3D texture mapping which uses microstructures to model internal structures for the purpose of product design and manufacturing. The basic idea of the proposed 3D texture mapping was motivated by the developments of bio-mimetic design and layer manufacturing. As disclosed by Chen [Chen, 2007], it is desirable to build parts with internal structures since less material is added, the part will have less shrinkage and warpage. In this sense, microstructures can be added to the system since it uses a general structure configuration model which can be used to define both (a) 2.5D and (b) 3D structures with different strut shapes, dimensions, and connections as represented in Figure 3.1.25 (a) and (b) [Chen, 2006].

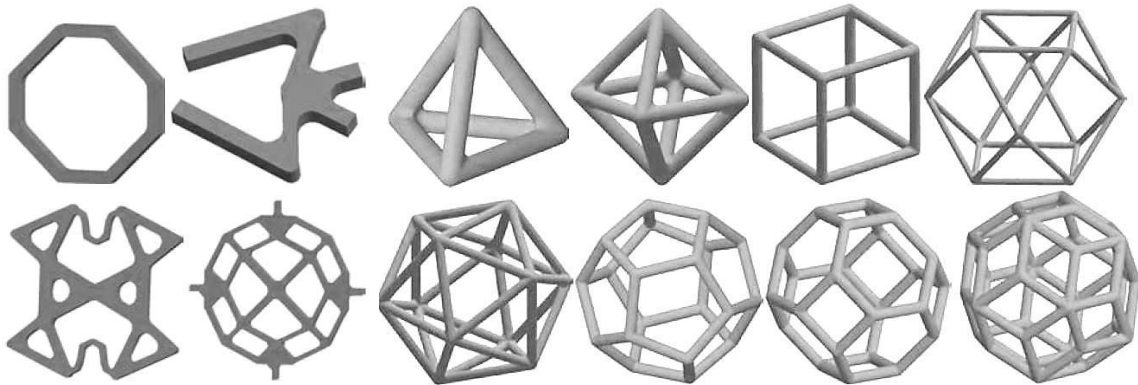


Figure 3.1. 25 2.5D and 3D SLA RP parts with the proposed truss approach [Chen, 2006]

Chen [Chen, 2007] used a universal data format (XML) for saving the microstructure definition file and load it automatically when selected as the microstructure to generate the internal structure for a given CAD model. Thus, 3D microstructures need to be mapped into a design space in order to form an internal structure. Ideally the generated internal structure should be adaptive to the outside part shape. That is to say, the synthesis of microstructures is the process of determining where to put microstructures in a design space to achieve any given design requirements. According to Chen [Chen, 2007], there are two types of approaches for the synthesis of microstructures, namely: a (a) uniform approach by using a microstructure as a pattern to duplicate in all directions to cover the design space (generally used for uniform cellular structures) and an (2) adaptive approach by using structural optimization to adapt structures based on design requirements. Similar to the adaptive approaches, Chen's [Chen, 2007] approach utilizes an internal structure based on the warped design space and on design requirements. Thus, more materials are to be concentrated in higher stress areas and less material in lower stress areas. This can be achieved by stretching the unit cells from low stress to high stress regions; so smaller sizes of microstructures are used in higher stress regions, and vice versa. This principle is similar

to space-optimized texture mapping and adaptive mesh generation. The difference is that warp space is based on design requirements such as stress distribution while texture mapping is based on image curvature and local curvedness of a surface respectively.

Consequently, their approach let the designer to change the generated structures just by modifying the warping function $f(\mathbf{V})$. Different values for various areas as a function f so that stiffer areas within the design space are expected and such, materials will be deposited accordingly. The generated (a) 2.5D and (b) 3D structures for the defined warping functions are shown in Figure 3.1.26 [Chen, 2007].

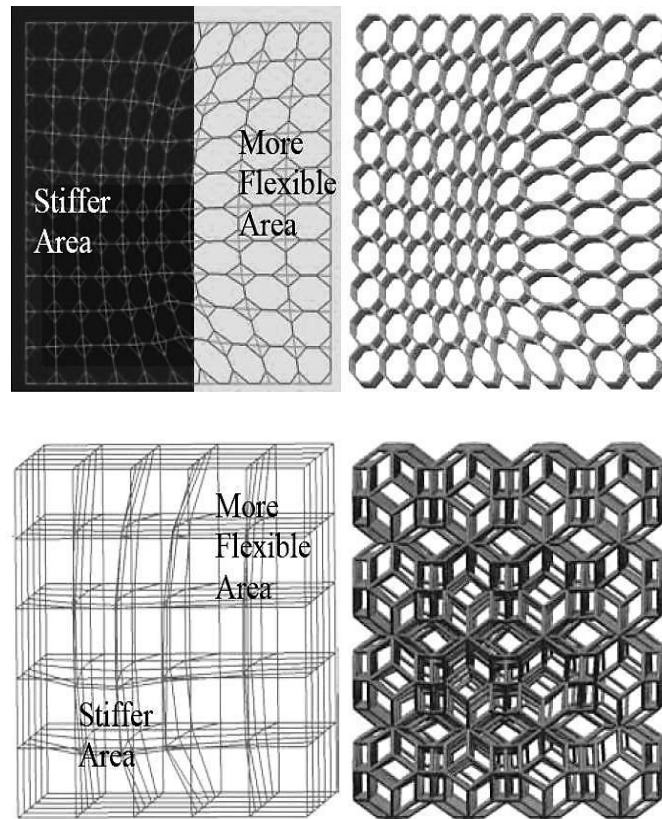


Figure 3.1. 26 2.5D and 3D structures constructed by inside geometry warping functions [Chen, 2007]

A truss structure defined in the XML file can have different strut size, shape, and connectivity. Generating a CAD model for such a structure is beyond a simple patterning operation provided in CAD software. Thus, a mesh-based geometric modeling method and the related algorithms were developed in the universal structure generation system (USGS) addressed by Chen [Chen, 2006]. They integrate this methodology into the 3D texture mapping design system for converting a structure definition file to a CAD model. At this stage, the USGS first creates an array of joints

and an array of struts based on the input structure configures. Then, it generates meshes for each joint first. In addition, a set of planar contours is recorded as the joint boundaries. Meshes of each strut are then generated from a pair of these boundary contours. Finally all the meshes are combined to get a polygonal model of the entire structure. Since meshes of a joint and all the struts that connect it have the same boundaries, the generated STL model is watertight without gaps or overlaps as shown in Figure 3.1.27 [Chen, 2007] (b) and (c).

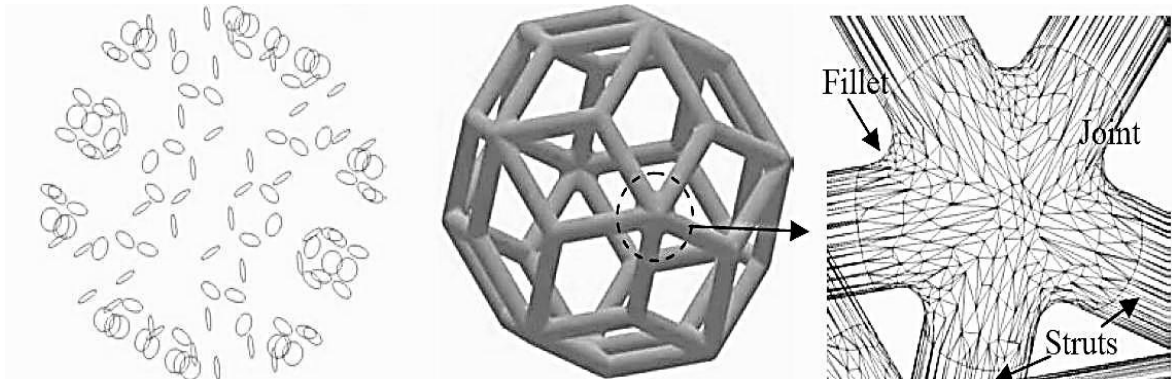


Figure 3.1. 27 Gaps and overlaps refinement at the node level [Chen, 2007]

Finally, a two-stage process is carried out in order to obtain the processed 3D models. The first stage deals with Boolean operations, which are used to combine an input CAD model \mathbf{M} with an internal structure \mathbf{S} . Figure 3.1.28 depicts an example utilizing the described method disclosed by Chen [Chen, 2007] where \mathbf{M} and \mathbf{S} are combined into a final model \mathbf{P} , where an octahedron is chosen as the microstructure for generating internal structures.

An internal shell for a cube by a distance r is generated. Then, a cube is used to clip the internal structure ($\mathbf{S} \cap \mathbf{M}$). Finally a union operation on the clipped internal structure and the shelled cube model is carried out. A sampling-based method is used after the Boolean operation on the two arbitrary polygonal models along with initial cell size to construct a uniform volumetric grid for sampling the two models. Based on the sampling results, an octree is used to refine the cells with complex shapes inside. An adaptive sampling test, in which an error-minimizing point is tested, is used to determine if it captures all the geometric objects inside the cell. After a uniform grid and an octree (explained in Section 3.1.1 of this chapter) grid are constructed, an iso-surface extracting method for reconstructing the Boolean-processed polygonal model is used. The reconstructed surfaces have the same topology as the exact surfaces, and the maximum approximation error from the exact surfaces is delimited by a user specified tolerance.

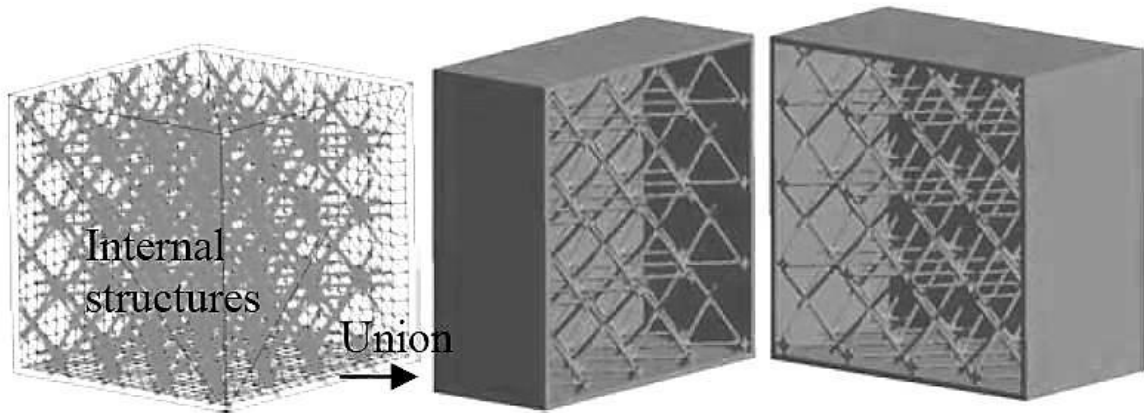


Figure 3.1. 28 Internal structures allocated inside a hollow part based on trusses and struts [Chen, 2007]

The second phase of the process is to shell the model. This operation is performed based on an operation defined by $S_r \downarrow = S \circ b_r$, which can then be combined with M to generate a shelled model. Then, a point-based method for offsetting a polygonal model by an arbitrary distance and hybrid data structure is employed. This method combines point samples, voxels, and polygonal surfaces. Each face, edge, and vertex of the original solid generates a set of offset points. Then, the user evaluates the offset points to generate a set of boundary points, which will reconstruct the offset boundary by an iso-surface extracting algorithm. Finally, a polygonal model P based on the Boolean and shelling operations can be saved as a STL file for final RP prototyping.

3.2 DISCUSSION

Now that a relevant number of approaches have been disclosed, the present section will scrutinize and identify the relevancy of such studies so as to define the orientation of the present study and help the reader to understand the merit of the present research along with the foundations for the decisions made in terms of the CAD method followed herein. The research was partitioned in two sections. Section 3.1.1 (Design for Optimization) describes the work done by Lam et al. [Lam, 1998], McMains et al. [McMains, 2003], Park [Park, 2005], Yao et al. [Yao, 2000], and Wang et al. [Wang, 2005] where, according to the author of this thesis, they centralize their studies in the optimization of CAD and mathematical methods to improve the characteristics of the functions of specific parts according to their use.

In this sense, Lam et al. [Lam, 1998] sought for the reduction of time of the RP process by extracting empty volumes from an original solid by using a recursive procedure implemented in

C++ language. The results obtained from their approach yielded FDM parts with octree internal structures that reduced the material usage and reduced the build time as well. However, due to the nature of the automatic sub-boundary octree partition approach, the characteristics of the internal structure cannot be measured in terms of volume density (length, area, volume). Therefore, the approach is limited by the general octree arrangement (cubic) defined by the external solid model. That is to say, the octree will emulate the shape of the external referencing solid body.

McMains et al. [McMains, 2003] searched for the reduction of time of the FDM process by altering the RP software in which their approach will identify the areas where a solid fill is being used and replace such areas by offsetting a certain edge portion of the external body of the model and filing the interior with the sparse support material. Their algorithm utilized offsetting and Boolean operations to approximate the inner 3D surface, which in return, proved that the build time could be reduced up to 64 % yielding lighter parts. Again, this approach automatically creates a loose fill for every outer contour without the possibility of tracing the internal topology in terms of the volume density of the interior topography.

The approach carried out by Park [Park, 2005] pursued a method to generate internal contours with uniform wall thicknesses by utilizing 2D geometric algorithms including curve offsetting. This method identifies the contour of 2D sliced areas and generates a circle swept volume representing an offset internal area, which then is added to form a cluster of external contours to form a 3D model. This hollowing approach has the capability to mimic the external contouring surface and create an internal replica, which serves as an offset surface. Evidently, this approach serves its purpose to generating a hollow body from any type of 3D geometry, which could be beneficial in terms of reducing the build material and build time in any RP process. However, as it is evident, there is no indication or capability that the proposed algorithm includes any type of internal geometry.

In their study, Yao et al. [Yao, 2000] explored a method to modify the internal topology of thermally expandable patterns with a set of different geometries. According to the internal web structure, they found that the hoop stresses on the ceramic shell reduced when utilizing an hexagonal web structure due to the better dissipation of stresses along the struts elements of SLA built collapsible patterns. This turned out to be beneficial since less residual stresses mean less crack propagation once the burn out process takes place. This approach centralized on the effects of the geometries in an external wall. As it can be identified, there is a difference in terms of stress distribution depending on the web type: the more geometrical elements (trusses) the better the stress distribution along the axial individual component axes.

Finally, Wang et al. [Wang, 2005] made a significant contribution since they came up with a method to model conformal trusses by utilizing a hybrid geometrical method by generating STL models from a primitive truss repeated in certain directions. A predefined strut is used as the basis for generating more complex 3D geometries that can be stacked together to form complete assembly truss structures. Their computational method was deployed using C++ and ACIS and incorporating it to the CAD domain. The advantage with this method is the significantly reduction in computational resources for a number “ n ” of parametrical trusses. However, the method disclosed by Wang et al. [Wang, 2005] does not comprise a detailed analysis on the volume fraction of the truss assembly within the solid model.

Section 3.1.2 (Design for Strength) describes the work done by Galantucci et al. [Galantucci, 2008 and 2010], Wu, [Wu, 2011], El-Gizawy et al. [El-Gizawy, 2010], and Chen [Chen, 2006 and 2007] where, again, they centralize their studies in the optimization of CAD and mathematical methods to enhance the mechanical properties of the modified 3D models either by incorporating new structural features or removing material to the 3D solid models.

According to Galantucci et al. [Galantucci, 2008 and 2010], internal voids with different angles can be a solution in order to reduce the material and the build time for cylindrical solid models. They performed compressive tests to the different model settings along with a finite element simulation analysis. Their results yielded that the raster width is relevant only for the manufacturing time, while it has no influence on the maximum compressive stress. On the other hand, the internal angle and the shell width are very important for these aspects. The tested specimens had a material reduction ranging from 9% to 27% for angles of 20° and 42°, respectively. The economical cost was analyzed and it was concluded that the cost depends on the production time and the material used, in which the production time depended on the machine head path length. It was observed that their approach is constrained by a similar void geometry. Due to the FDM nature, parts with steeper angles do not require support material. Hence, there is an intrinsic limitation of the angle hence the geometry of the parts the proposed approach intends.

Wu [15] describes a method to design porous parts determined by unit space array modes and sizes for parts used as bionic scaffolds. This functional approach enables to create parts with microstructures without affecting the mechanical properties of the parts. Three different raster orientations were used to create spaced-structures in which the parameters were the pore ratio and the shape. Mechanical tests were carried out to the three group parts in three different compressive loads configurations and the results demonstrated that the [0°/90°] array delivered more force when the cylindrical element is placed vertically and the load is applied axially.

However, the geometry allows a single layered array with no interconnecting structures from one layer plane to the other. As described by the researcher, this approach was carried out for mini-scaled parts.

The analytic approach by El-Gizawy, et al [El-Gizawy, 2010] considered parts with a monofilament deposition carried out layer by layer. This approach yields an important foundation for studying the stress at different orientations and the interactions between layers of FDM models. This approach does not intend to optimize in terms of strength, material usage, and build time in the CAD domain but it aims to characterize the strength, ductility, and toughness FDM-processed ULTEM 9085 parts based on the orientation of the raster angle. Formulas that relate stresses and strains were achieved and accommodated in a matrix form. According to the researchers, the decrease in strength and ductility can be attributed to thermal degradation of FDM-processed materials mechanical properties. This is caused by the polymer molecular deterioration as a result of heating. At high temperatures, components of the long chain backbone of ULTEM 9085 begin to separate (molecular scission) and react with one another resulting in reduction of strength and ductility of FDM processed ULTEM 9085 materials.

Chen [Chen, 2006 and 2007] accomplished a CAD method, for designing and modeling internal structures, where a designer can choose a microstructure based on design requirements from a microstructure library and then the system automatically generates a warped design space also based on design requirements. Combined with the selected microstructure, the internal structure is generated and defined in a XML file. The system can automatically convert the structure definition file into a CAD model that can be combined with an offset CAD model by geometric Boolean operations. Hence, a designer can select a microstructure based on specific requirements such as strength and flexibility. Microstructures can also be designed to produce unique physical properties such as non-uniform structures with stiff characteristics depending on the direction. However, the structural design based on the uniform approach is usually not optimal since the geometries are not adaptive either the outside part shape or design requirements.

3.3 RESULTS

As it can be seen from the literature, none of the research to date has proposed the incorporation of parametric internal structures within shelled bodies as proposed in the present research. Nevertheless, the approach carried out by Chen [Chen, 2006 and 2007] demonstrated that internal structures with geometrical elements could be incorporated into shelled solid bodies in a practical

and computational-lightweight fashion. However, due to the intrinsic nature of the approach due to the automatic realization, a precise volumetric density of the sum of the internal components (trusses) is not feasible to obtain. The same happens in the approaches performed by Lam et al. [Lam, 1998], McMains et al. [McMains, 2003], Park [Park, 2005], and Wang [2005] there is a commonality: there is no an exact control of the number count of elements which reflect in the lack of description of the internal volume density. Hence, it is complicated to study these internal modifications with mathematical approximations of the internal volume fraction. Therefore, major complications will arise in order to establish the relationships between material volume fraction and the mechanical characteristics of the RP parts.

Similarly, Galantucci et al. [Galantucci, 2008 and 2010], Yao et al. [Yao, 2000], and Wu [Wu, 2011] considered the volume fraction (length, height, width) of the internal elements that construct the matrix arrangements. However, in the case of Wu [Wu, 2011] and El-Gizawy et al. [El-Gizawy, 2010], the approach describes the mechanical behavior of the parts in the micro-scale. That is to say, the isotropy in the monofilament deposition of such small components does not reflect the interactions of the monofilament once deposited at any direction when being part of an individual truss, such like the truss arrangement described by Chen [Chen, 2007]. Galantucci et al. [Galantucci, 2008 and 2010] does not utilize a defined structure but voids located near the part's sidewalls. The aforementioned approach does not study the effects of different internal structures for tension and compressive loads and fails to include internal structure with parametrical characteristics into shelled bodies.

Finally, it is important to mention that it will become significantly relevant to know the internal structure volume fraction for the purpose of assigning material properties, calculating the total material usage and for subsequent analytical studies which can be performed to correlate the strength of the part with the fraction of material depending on the type of web structure organization, the level of density of the material within the shelled body, and the influence of this parameter when studying the level of significance of this parameter with other parameters such as raster orientation and part orientation. This knowledge will allow designers to reduce the fabrication costs (i.e., material and build time), without compromising the desired mechanical characteristics.

CHAPTER IV

RAPID PROTOTYPING OF PARAMETRICAL MODELS

4.1 INTRODUCTION TO 3D CAD MODELING

As described in Section 3.2 of Chapter III, there are many different modeling methods to represent geometrical 3D elements. Some of the methods employ the use of embedded geometric algorithms programmed within the internal 3D kernel structure that may be used as a library for further reference and some others as the integrator (add on) of a specific module of the 3D modeling software. In both cases, these approaches follow an iterative process that requires the programming of mathematical operations that use specific formulas that represent the spatial configuration by lines, points, and curves and the combination of all of them.

According to the scope of the present approach, such methodologies were not relevant for the reach of the study. Nevertheless, there was the necessity to design and model matrix configurations in due form. These configurations should be the basis for the internal matrix structures for further inclusion into other shapes and forms. There were some design requirements that were considered when utilizing this approach. Knowing that this approach has its own disadvantage due to the nature of the software, as described by Chen [Chen, 2006] when he mentions that geometric approaches consume considerable computational resources, the present approach presents an agile way to have modifiable structures at the designer's will.

4.1.1 METHODOLOGY

The present section corresponds to the CAD Modeling and FDM Rapid Prototyping from Figure 2.3.2 of Section 2.3 of Chapter II. Such sections represent a very important portion of the present research since they transform the idea of incorporating interchangeable matrix-type structures to hollow objects in an efficient way without affecting the material strength or at least affect it as less as possible. Similarly, the FDM RP portion represents the medullar characteristic of the present research since specific RP characteristics (pros and cons) are evident and will shape the results obtained when characterizing the material and the specimens themselves.

The approach followed to accomplish the modeling of parametrical elements utilizing commercial 3D CAD software ensures the compatibility of designing and deploying the present method in any 3D CAD software independently from the internal architecture. Therefore, future research in

this field will not be limited by CAD software or software add-on; however, it will only be limited by the nature of the material and the RP process itself. Hence, the present approach is to be carried out using any of the RP technologies described in Section 1.1.5 of Chapter I.

4.1.2 PARAMETRIC ELEMENT GENERATION

SolidWorks® from Dassault Systemes®, commercial 3D CAD software, was used to model the internal structures. There are three different types of internal structures chosen for the present research: orthogonal, hexagonal, and pyramid. These internal structures represent the basic group entities that conform more complex structures. All these group entities coincide by sharing the basic parametric element. This element is considered to be the mathematical basis from which all the parametric capabilities of further structures reside. The element is formed by a couple of simple spheres and a cylinder connecting the two end spheres and the design process is disclosed in Table 4.1 for the spheres and cylinder, respectively. This basic geometrical arrangement is also described by Wang et al. [Wang, 2005] in Section 3.1.1 of Chapter III where he suggested the use of a truss primitive consisting of a central node and two half-struts connected to the central node. The basic parametric element construction is described in Figure 4.1.1

Table 4. 1 Steps to construct the basic parametric element

Geometry	Detailed Instructions
Sphere A	1. Draw a line and assign a value of R with the line's midpoint at the origin (X, Y, Z) 2. Draw a tangent semi-circle to close the line R 3. Revolve the 2D sketch having the line R as the rotation axis
Cylinder	4. Draw a circle with diameter D (" D ": " R "/ n) with its origin at (X, Y, Z) at a perpendicular plane from the initial sketch of line R 5. Extrude the circle forward and assign a value of L (" L ": " R "* n)
Sphere B	6. Draw a line and assign the value of R with the line's midpoint at the origin of the cylindrical extrusion end 7. Revolve the 2D sketch having the line R as the rotation axis

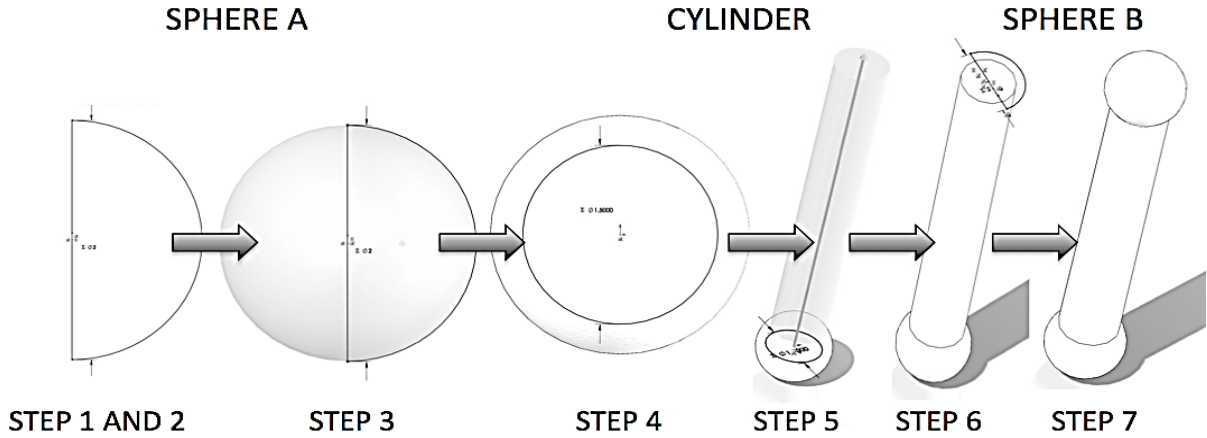


Figure 4.1. 1 Process for modeling the basic parametric element

The basic parametric element is constrained by 2D relationships and mathematical equations as shown in Figure 4.1.2. The element is modifiable simply by assigning the desired value to the “R” parameter located in the 2D sketch referred to “D1@Sketch1”. The other parameters such as “D” and “L” can be modified at any time by assigning new values to the equation “D1@Sketch1”*n located in the 2D sketch referred to “D1@Sketch2” and the equation “D1@Sketch1”*n located in the 3D feature property referred to “D1@Boss-Extrude1”, respectively. It is relevant to mention that such values n for both, **D** and **L**, are the ones that will let the quick modification of the basic parametric element size and consecutive structures.

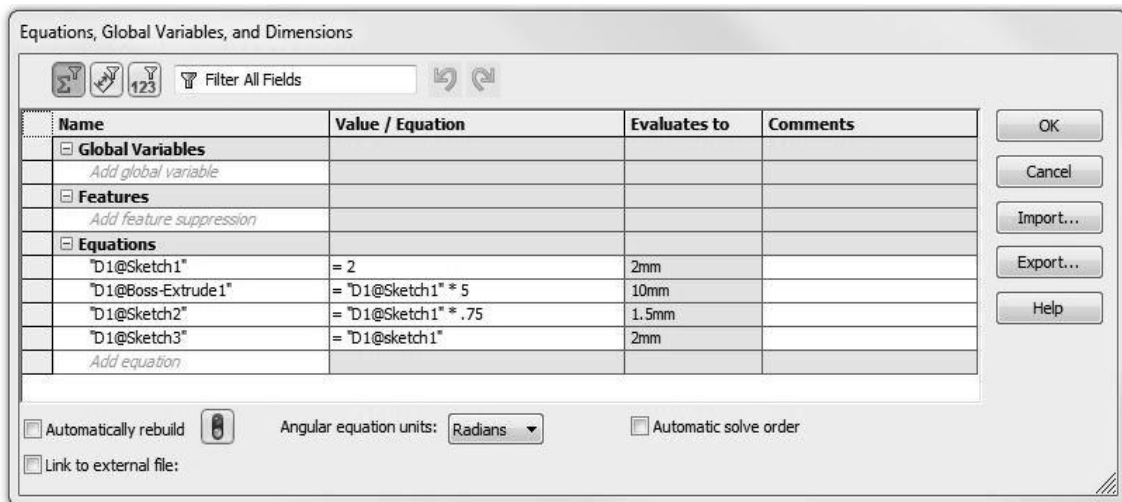
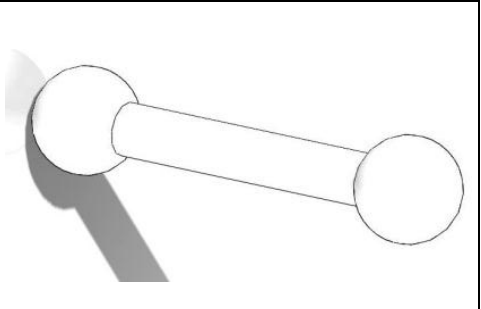
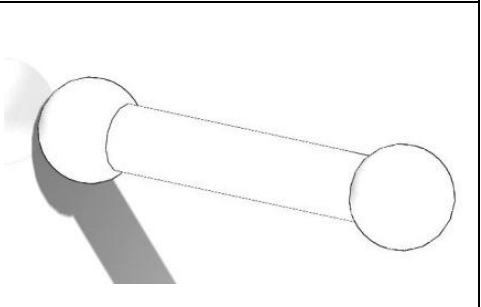


Figure 4.1. 2 SolidWorks® interface for setting up or modifying the parametric relations

4.1.3 PARAMETRIC MATRIX WEB STRUCTURES

As described before, equation “ $DI@SketchI$ ”ⁿ is determinant to establishing the configuration of the basic parametric element and the consecutive structural dependency. In the present study, two additional factors to study were chosen which represent two variants of this formula. As previously referred in Section 2.3 of Chapter II, the “*loose*” and the “*compact*” factors are described in Table 4.2. These two variants intend to describe the material usage in terms of the volume fraction occupied within the hollowed object. Evidently, the “*loose*” structure will incorporate less material, whereas the “*compact*” structure will incorporate more material. In both cases, the distance **L** between the spheres or nodes is consistent.

Table 4. 2 Dimension differences between the loose and the compact mode specimens

Basic Parametric Element Mode	R (mm)	D (mm)	L (mm)	Schematic
Loose	2	1	7	
Compact	2	1.3	7	

Once the parametric element was created, the element was incorporated to an assembly in order to design the basic geometrical entities. These entities respond to the other modifiable factor studied in the present research. Figure 4.1.3 depicts the modeling process that yielded the basic entities. In this case, Figure 4.1.3 represents the formation of the orthogonal entity. In all these entities, a 3D-level constraint was used: coincident at the nodes (spherical elements).

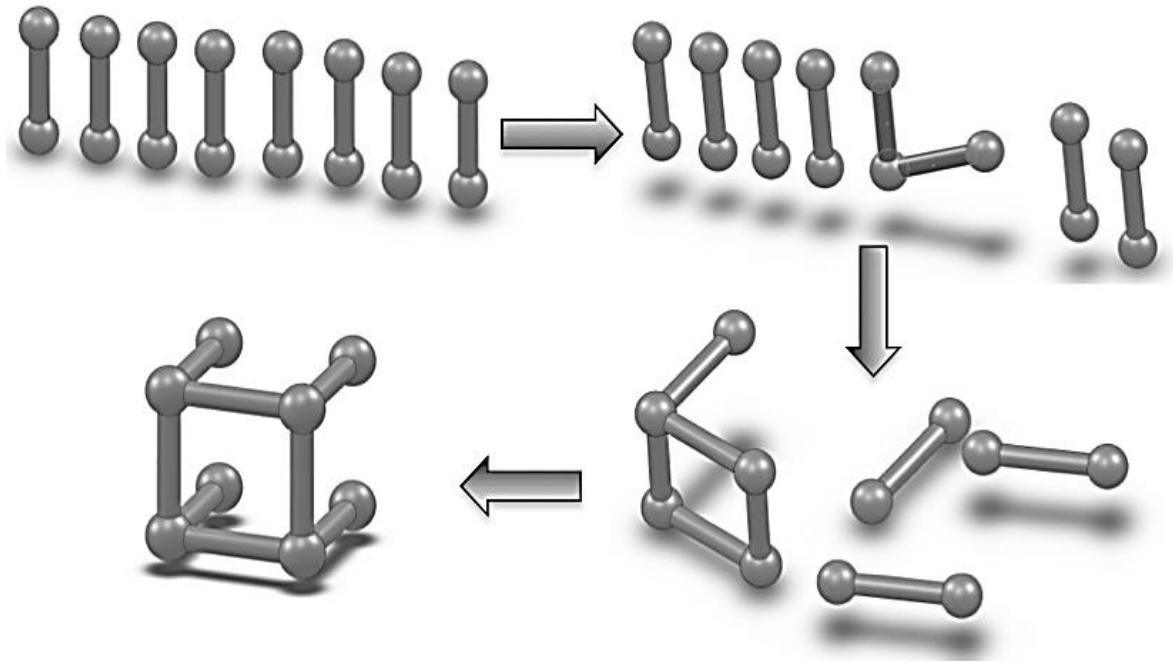


Figure 4.1. 3 Basic CAD modeling process to construct the geometrical elements

Similarly, as described in Section 2.3 of Chapter II, the “*orthogonal*”, “*hexagonal*”, and “*pyramid*” structural geometries respond to the necessity to evaluate the influence and differences exerted to the hollowed objects. The aforementioned geometries were chosen because of the difference in the intrinsic nature of themselves and to the previously researched geometries in similar approaches as described in Sections 3.1.1 and 3.1.2 of Chapter III. Table 4.3 comprises the three geometrical entities representative of the internal structure as a factor considered in the present study.

Table 4. 3 Orthogonal, hexagonal, and pyramid geometrical elements studied in the present research

Orthogonal	Hexagonal	Pyramid

Figure 4.1.4 describes the modeling process of matrix geometrical structure for the orthogonal structure. The same process was performed for the other two structures. It should be noted that for the two modes, loose and compact, the distance from center to center (spherical nodes) was kept constant. For the present research, the variation in the basic geometrical entity “*packing*” will determine the parametrical characteristics of strength and material usage. All the basic geometrical matrix structures are assembled following a constraint and relationship approach. Each of the nodes is mated together by a 3D coincident constraint, whereas the distance of the aperture between the shaft bodies of the elements is constrained by angle relationships.

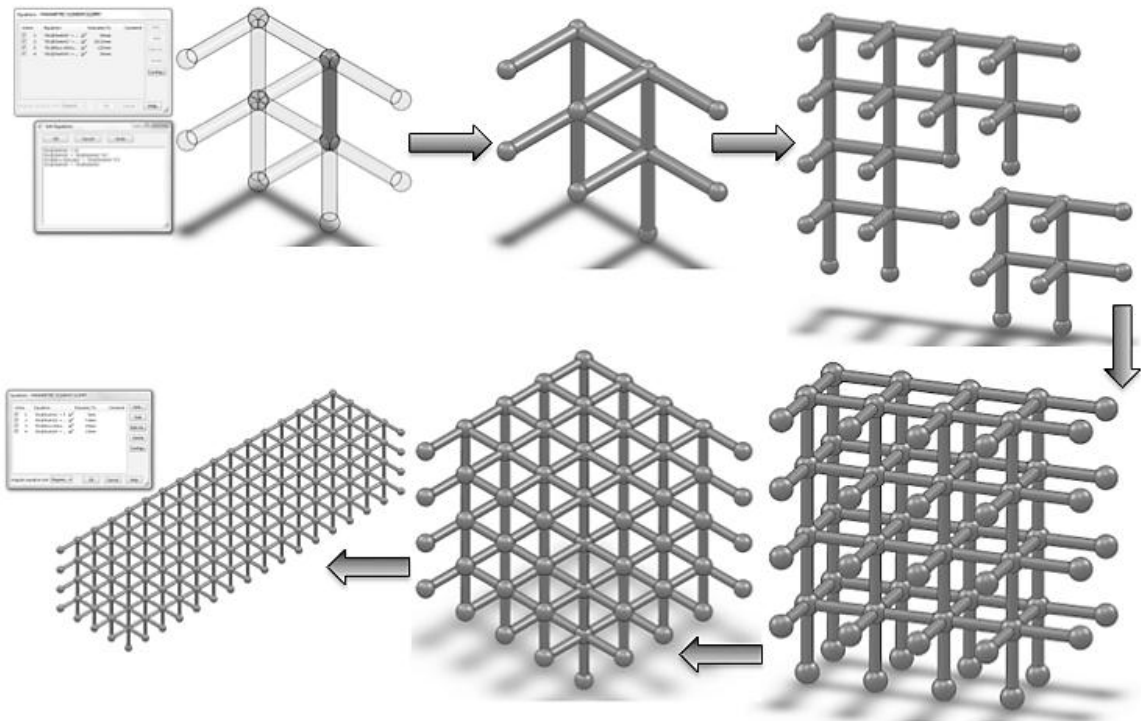


Figure 4.1. 4 CAD modeling process for assembling the parametric matrix-type structure

Each assembly comprised an “*n*” number of primitive elements with parametric capabilities. Hence, in the event of modifying any of the assembly components, all the assembly will be modified without affecting the constraints and relations at the 3D level and the entire structure will keep its integrity. This level of associativity promotes the reconfigurability of the virtual enablers proposed in the present approach.

4.1.4 INTERNAL STRUCTURE INTEGRATION

As described in Figure 4.1.4, once the basic geometrical elements are modeled, they are used to create bigger assemblies. The process is then repeated in order to obtain a general matrix structure that can be used to “fill” any previously hollowed object. Now then, in order to create test samples for tensile and compressive testing, the orthogonal, hexagonal, and pyramid matrix structures are incorporated into the hollowed tensile and compressive samples. As it is described in Sections 5.1.1 and 5.1.2 of Chapter V, ASTM standardized sample size guidelines were utilized. Consequently, such specimens were modeled and the matrix structures were integrated as described in the process of Figure 4.1.5 for the compressive specimens.

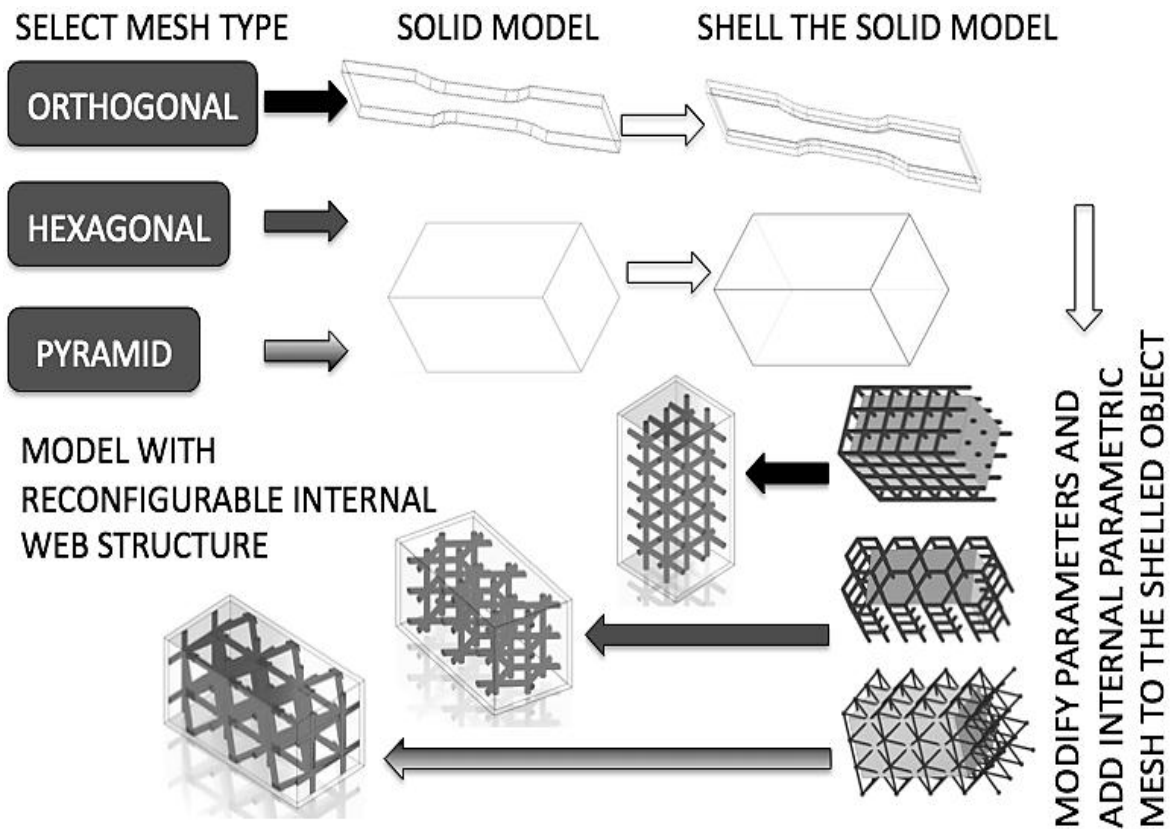


Figure 4.1. 5 CAD process flow for modeling the specimen parts with internal parametric structures

In order to create a part **P** (tensile or compressive specimens for example) with internal structures, $P = \Delta(\mathbf{M}, \mathbf{r}) \cup (\mathbf{S} \cap \mathbf{M})$, where \cap and \cup are intersection and union respectively, and $\Delta(\mathbf{M}, \mathbf{r})$ is the shelling operation of model **M** by a distance **r**, and $(\mathbf{S} \cap \mathbf{M})$ is the Boolean operation of the intersection of the structure **S** and the model **M**.

4.2 PREPARATION OF TEST SAMPLES

Following the modeling process described in Figure 4.1.5, the matrix structure for the tensile specimens is grown linearly, whereas for the compressive specimens, the matrix structure is grown cubic-wise. Figure 4.2.1 discloses the internal structures for the (a) orthogonal, (b) hexagonal, and (c) pyramid tensile specimens in a middle section cut.

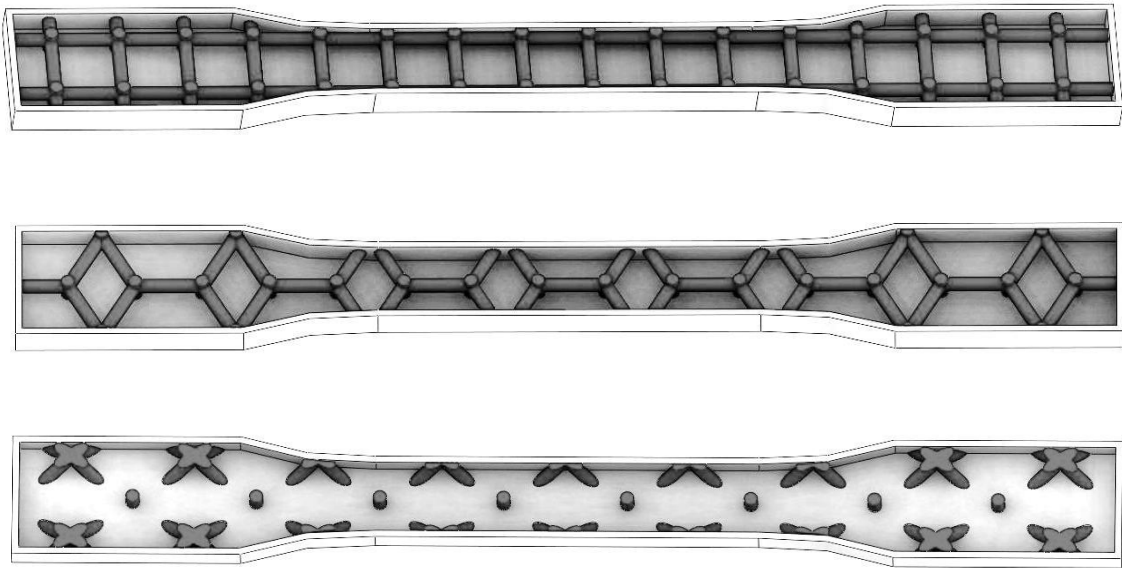
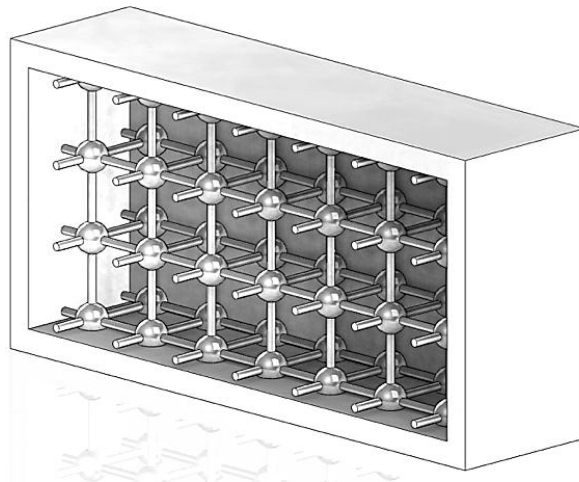


Figure 4.2. 1 CAD models for the tensile samples with different internal structures

Figure 4.2.2 illustrates the internal structures for the (a) orthogonal, (b) hexagonal, and (c) pyramid compressive specimens in a middle section cut.



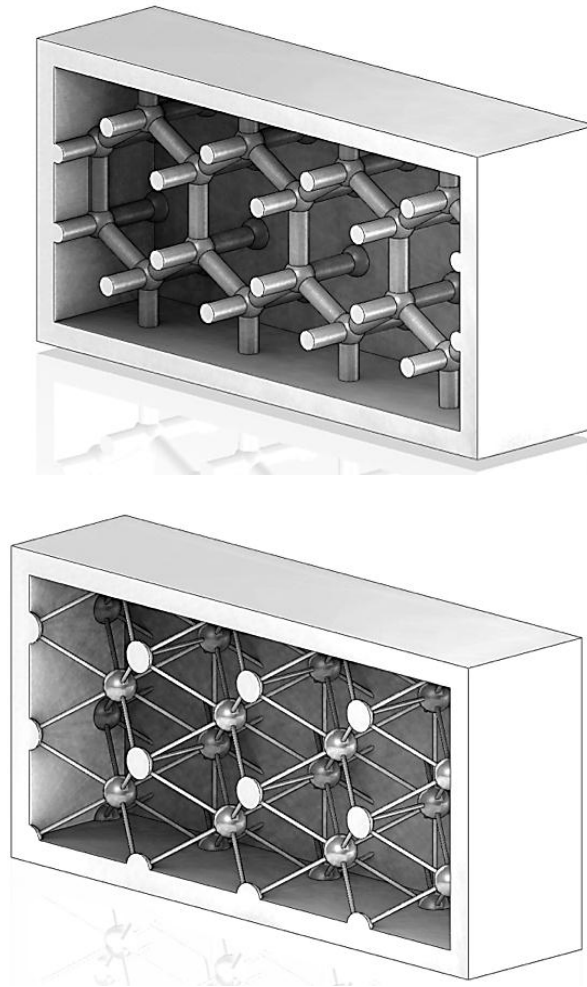


Figure 4.2. 2 CAD models for the compressive samples with different internal structures

4.3 FDM MACHINE SOFTWARE SIMULATION

Once all the necessary parts are modeled in the CAD software. The next step, as described in the process flow chart from Figure 2.3.2 in Chapter II, is to RP such parts according to the parameters established as the main criterion to be study in the present research; such parameters are encompassed by Table 4.4. Table 4.4 comprises the “*Study Parameters*” and the “*INSIGHT® Parameters*”. These second ones refer to the parameters pertaining to specific machine setting, which were kept constant for all the RP samples. It should be mentioned that the obtained CAD modeled specimen parts (16 parts for compression and 16 parts for tension) serve to perform the FEA simulation, later described in Section 5.4 of Chapter V.

Table 4. 4 Study and machine-related parameters involved in the present research

Study Parameters	Low / High	Low / High	Low / High	Low / High	Low / High
Raster Orientation	0°/90° / 45°/- 45°	0°/90° / 45°/- 45°	0°/90° / 45°/- 45°	0°/90° / 45°/- 45°	0°/90° / 45°/- 45°
Build Plane	XY / XZ	XY / XZ	XY / XZ	XY / XZ	XY / XZ
Internal Structure	Solid	Hollow	Orthogonal	Hexagonal	Pyramid
Internal Density	NA	NA	Compact/ Loose	Compact/ Loose	Compact/ Loose
INSIGHT® Parameters	General, Toolpath, and Support Values				
Part Interior Style	Solid-Normal				
Visible Surface Style	Enhanced				
Support Style	SMART				
Model Material Extrusion Tip	T16 Tip				
Support Material Extrusion Tip	T12 Tip				
Model Material	ABS-M30				
Support Material	SR20 Support				
Slice Height	0.2540 mm				
Part Fill Style	One Contour/ Rasters				
Contour Width	0.5814 mm				
Visible Surface Rasters	0.4564 mm				
Visible Surface Air Gap	0.0 mm				
Surface Max Contours	0				
Internal Rasters	0.4814 mm				
Internal Raster Air Gap	0.0 mm				

Now then, in order to evaluate and understand the interaction between the chosen parameters (Study Parameters), 32 experiments are to be performed for each set of compressive and tensile samples. Each of the 32 experiments were repeated three times, hence, a total of 96 of compressive and 96 tensile specimens were rapid prototyped. The total number of prototyped parts was 192 parts.

4.4 RESULTS

The results from the FDM RP are described in the present section. These result conform one of the two main groups of factors to study in the present research. That is to say, based on the results from the RP virtual experiments, a proper statistical analysis of the interactions between build time, model and support material use is to follow. Hence, in order to make use of such factors in an optimal manner, Table 4.5 describes the level correspondence of the 3 leading factors in the present approach.

Table 4. 5 Level descriptions and correspondence for the factors studied

Factors	Level Descriptions	Level Correspondence
Raster Angle	[-45° / 45°]	-1
	[0° / 90°]	+1
Build Plane	XY	-1
	YZ	+1
Internal Density	Loose	-1
	Compact	+1

Table 4.6 comprises the RP results provided by the INSIGHT® software. The results describe the model material use and the support material use in cm³ and the build time in minutes for all the 32 tensile specimens.

Similarly, Table 4.7 comprises the RP results provided by the INSIGHT® software. These results describe the model material use and the support material use in cm³ and the build time in minutes for all the 32 compressive specimens.

CHAPTER IV: RAPID PROTOTYPING OF PARAMETRICAL MODELS

Table 4. 6 RP software results at the moment of rapid prototyping the tensile specimens

Exp. No.	Type of Structure	Raster Angle	Build Plane	Internal Density	Model Material (cm ³)	Support Material (cm ³)	Time (min)
1	Orthogonal	-1	-1	-1	8.25	6.27	41.33
2	Orthogonal	-1	-1	1	9.31	6.25	46.66
3	Orthogonal	-1	1	-1	9.13	6.14	71.33
4	Orthogonal	-1	1	1	10.13	5.69	86.33
5	Orthogonal	1	-1	-1	8.19	6.22	41
6	Orthogonal	1	-1	1	9.27	6.19	45.33
7	Orthogonal	1	1	-1	9.07	6.06	69
8	Orthogonal	1	1	1	10.17	5.68	83.33
9	Hexagonal	-1	-1	-1	8.11	6.15	36
10	Hexagonal	-1	-1	1	8.9	6.12	41.66
11	Hexagonal	-1	1	-1	8.97	6.2	66.66
12	Hexagonal	-1	1	1	9.63	5.98	80
13	Hexagonal	1	-1	-1	8.07	6.13	35.66
14	Hexagonal	1	-1	1	8.91	6.09	39.66
15	Hexagonal	1	1	-1	8.89	6.13	65.66
16	Hexagonal	1	1	1	9.56	5.9	79
17	Pyramid	-1	-1	-1	8.19	5.85	43.66
18	Pyramid	-1	-1	1	8.81	5.64	48
19	Pyramid	-1	1	-1	9.003	6.28	61.33
20	Pyramid	-1	1	1	9.56	5.73	68.66
21	Pyramid	1	-1	-1	8.15	5.86	43
22	Pyramid	1	-1	1	8.78	5.61	48.33
23	Pyramid	1	1	-1	8.92	6.23	61.66
24	Pyramid	1	1	1	9.51	5.68	69
25	Solid	-1	-1	-	17.33	0.006	19.33
26	Solid	-1	1	-	16.33	1.72	34.33
27	Solid	1	-1	-	17.32	0.006	18.33
28	Solid	1	1	-	15.84	1.71	30.33
29	Hollow	-1	-1	-	7.87	5.3	20
30	Hollow	-1	1	-	8.7	6.19	38.66
31	Hollow	1	-1	-	7.83	5.28	19.66
32	Hollow	1	1	-	8.62	6.16	38.33

CHAPTER IV: RAPID PROTOTYPING OF PARAMETRICAL MODELS

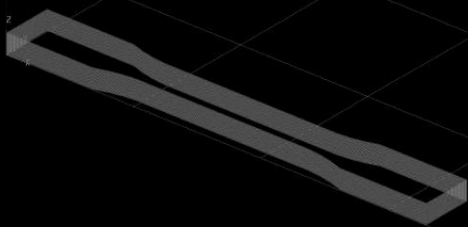
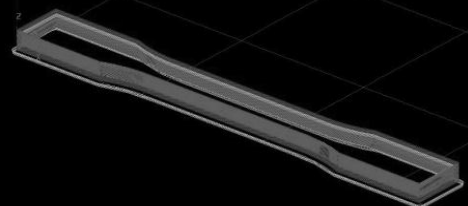
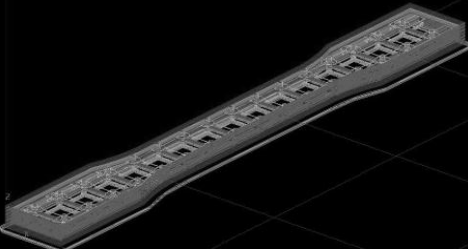
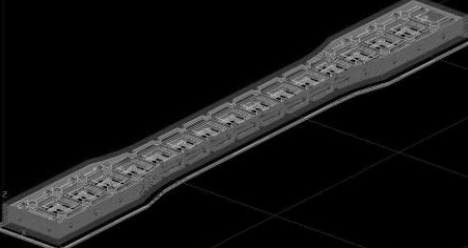
Table 4. 7 RP software results at the moment of rapid prototyping the compressive specimens

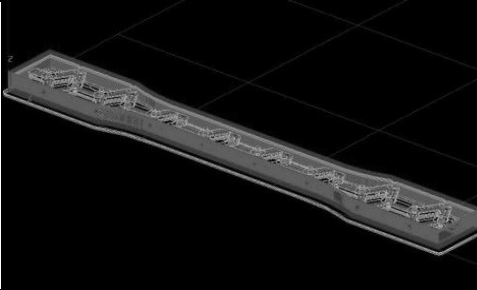
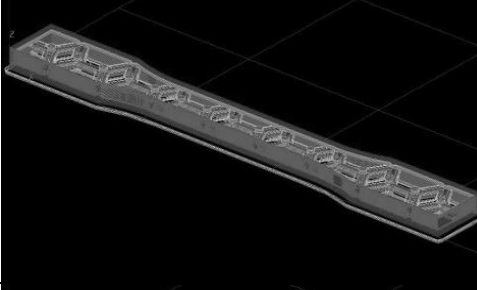
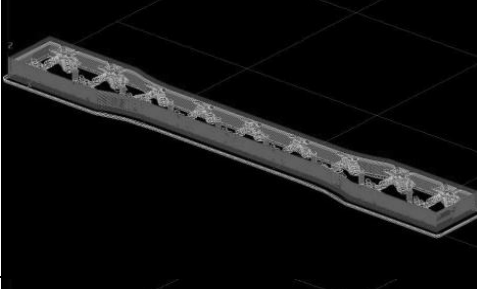
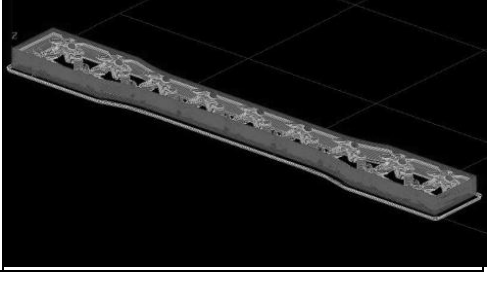
Exp. No.	Type of Structure	Raster Angle	Build Plane	Internal Density	Model Material (cm ³)	Support Material (cm ³)	Time (min)
1	Orthogonal	-1	-1	-1	1.98	3.06	24.66
2	Orthogonal	-1	-1	1	2.34	3.17	42.33
3	Orthogonal	-1	1	-1	2.76	3.99	37
4	Orthogonal	-1	1	1	2.98	4.03	57.66
5	Orthogonal	1	-1	-1	2.11	3.08	24.66
6	Orthogonal	1	-1	1	2.33	3.15	42
7	Orthogonal	1	1	-1	2.76	3.98	36.66
8	Orthogonal	1	1	1	2.97	4	57.66
9	Hexagonal	-1	-1	-1	2.06	2.92	20
10	Hexagonal	-1	-1	1	2.28	3.02	39
11	Hexagonal	-1	1	-1	2.706	4.03	38
12	Hexagonal	-1	1	1	2.91	4.17	51.33
13	Hexagonal	1	-1	-1	2.05	2.903	20.33
14	Hexagonal	1	-1	1	2.27	2.99	38.66
15	Hexagonal	1	1	-1	2.7	4.03	38
16	Hexagonal	1	1	1	2.906	4.13	50.66
17	Pyramid	-1	-1	-1	2.03	2.91	24.66
18	Pyramid	-1	-1	1	2.49	3.29	47.33
19	Pyramid	-1	1	-1	2.71	3.86	39
20	Pyramid	-1	1	1	3.15	4.35	69.33
21	Pyramid	1	-1	-1	2.01	2.91	24.66
22	Pyramid	1	-1	1	2.48	3.29	47
23	Pyramid	1	1	-1	2.706	3.86	38.66
24	Pyramid	1	1	1	3.15	4.37	69
25	Solid	-1	-1	-	5.88	0.38	9.33
26	Solid	-1	1	-	5.74	0.23	10.66
27	Solid	1	-1	-	5.78	0.38	8.66
28	Solid	1	1	-	5.67	0.23	10
29	Hollow	-1	-1	-	2.003	2.53	16.33
30	Hollow	-1	1	-	2.65	3.44	28.66
31	Hollow	1	-1	-	1.99	2.56	16
32	Hollow	1	1	-	2.65	3.43	28.66

4.4.1 LAYERED TENSILE SPECIMENS' MORPHOLOGY

It is necessary to understand the toolpaths from all the different cases depending upon the part orientation in the build chamber and the internal density depending on the internal packing. Hence, Table 4.8 and Table 4.9 comprise the graphic representation of the tensile parts corresponding to the XY plane orientation and the YZ plane orientation, respectively.

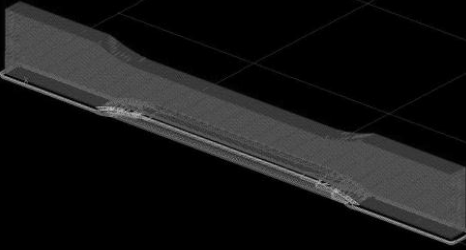
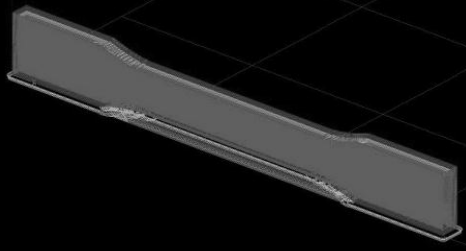
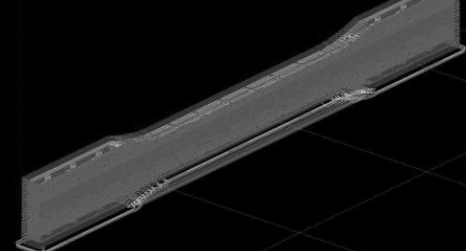
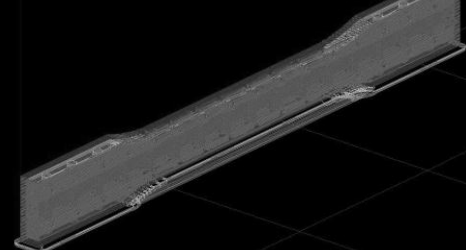
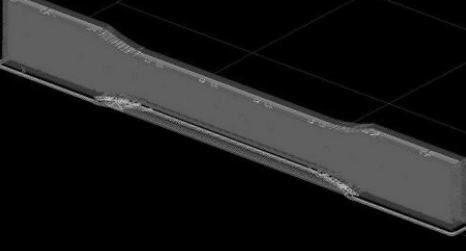
Table 4. 8 Layered tensile CAD models obtained from the RP software oriented in the XY planes

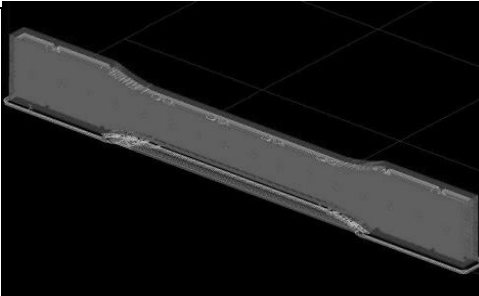
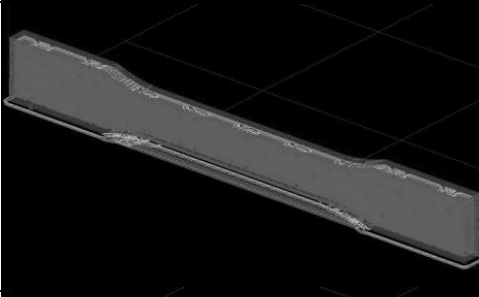
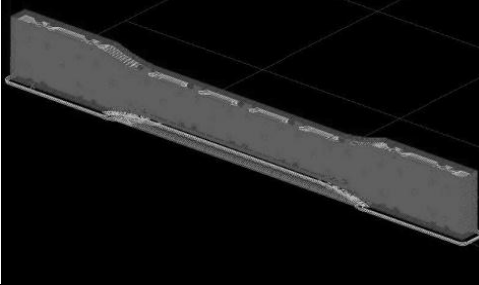
Specimen Type	Specimen Description	Schematic
Solid	NA	
Hollow	NA	
Orthogonal	Loose	
	Compact	

Hexagonal	Loose	
	Compact	
Pyramid	Loose	
	Compact	

CHAPTER IV: RAPID PROTOTYPING OF PARAMETRICAL MODELS

Table 4. 9 Layered tensile CAD models obtained from the RP software oriented in the YZ planes

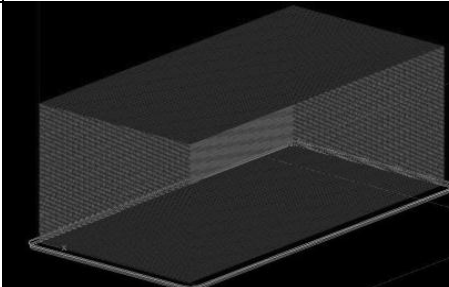
Specimen Type	Specimen Description	Schematic
Solid	NA	
Hollow	NA	
Orthogonal	Loose	
	Compact	
Hexagonal	Loose	

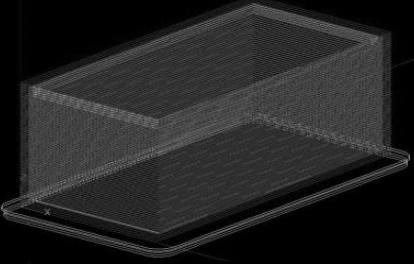
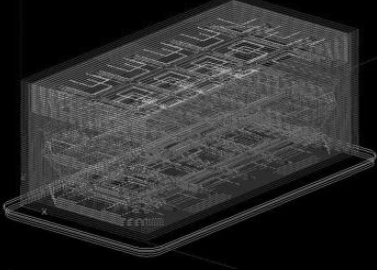
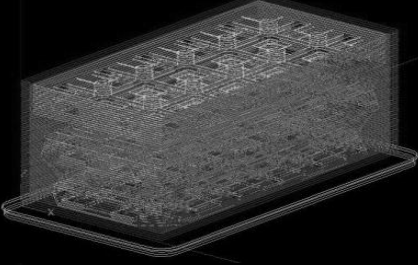
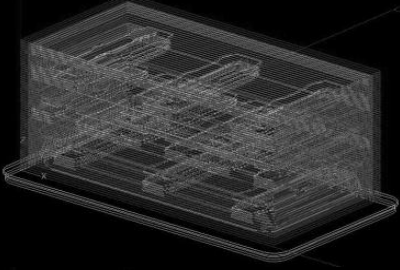
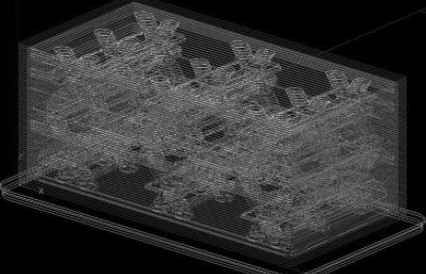
	Compact	
Pyramid	Loose	
	Compact	

4.4.2 LAYERED COMPRESSIVE SPECIMENS' MORPHOLOGY

As it was pointed out in the previous section regarding the tensile specimens' layer morphology, Table 4.10 and Table 4.11 comprise the graphic representation of the compressive parts once are layered in the RP software, which correspond to the XY plane orientation and the YZ plane orientation, respectively.

Table 4. 10 Layered compressive CAD models obtained from the RP software oriented in the XY planes

Specimen Type	Specimen Description	Schematic
Solid	NA	

Hollow	NA	
Orthogonal	Loose	
	Compact	
Hexagonal	Loose	
	Compact	

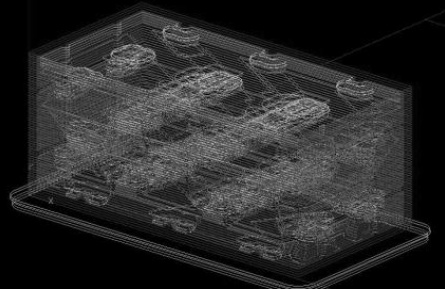
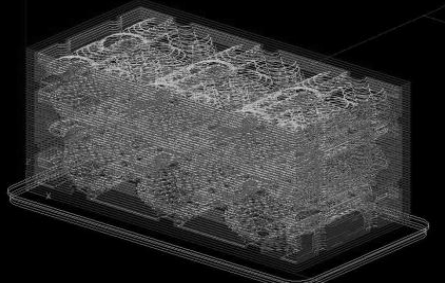
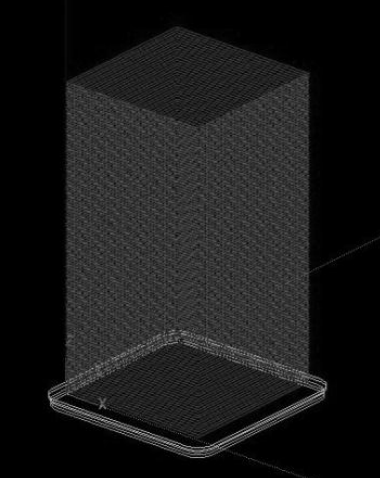
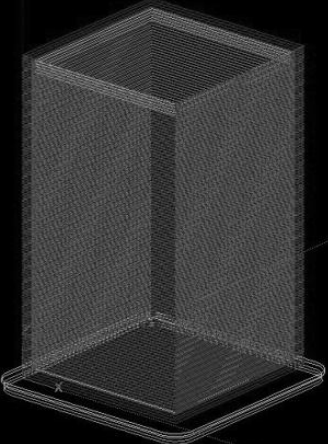
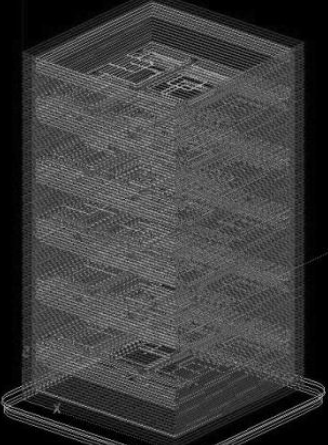
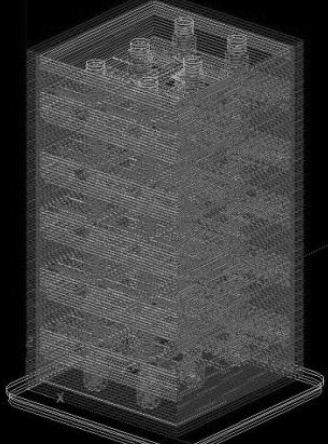
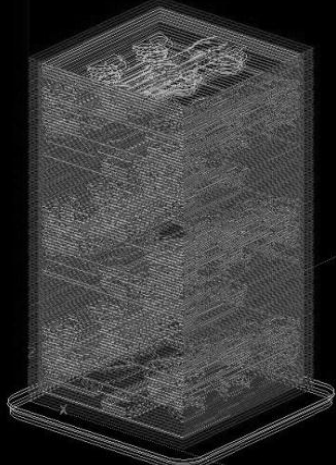
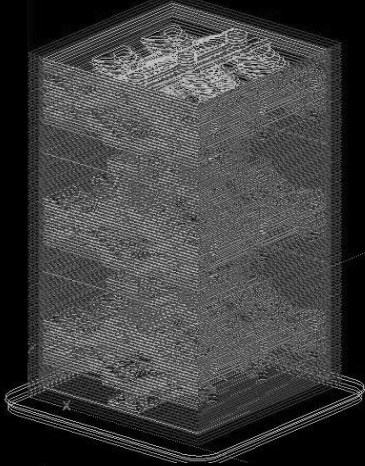
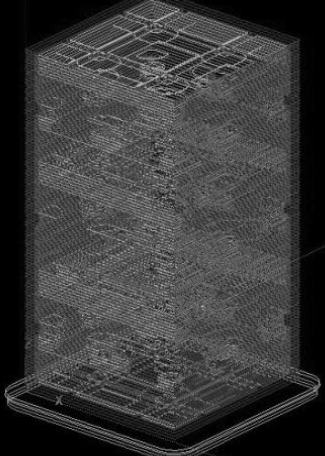
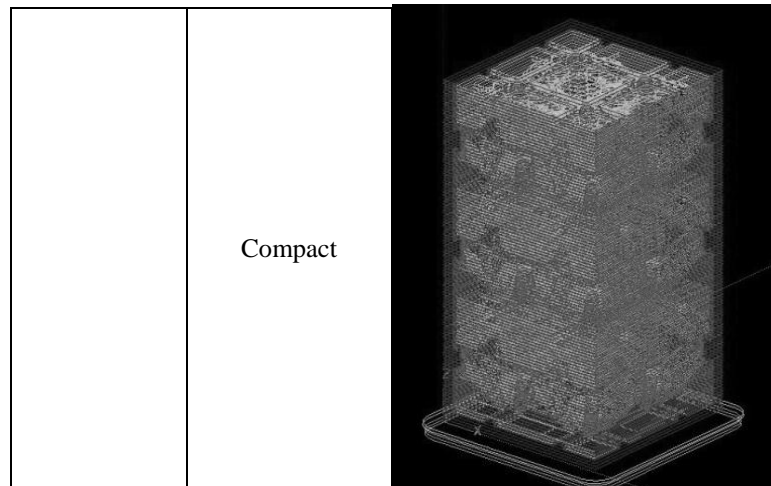
Pyramid	Loose	
	Compact	

Table 4. 11 Layered compressive CAD models obtained from the RP software oriented in the YZ planes

Specimen Type	Specimen Description	Schematic
Solid	NA	

Hollow	NA	
Orthogonal	Loose	
	Compact	

Hexagonal	Loose	
	Compact	
Pyramid	Loose	



The specimens were processed by INSIGHT® and the “*slice*” results are comprised by Tables 4.8 to 4.11. It should be noticed that the “slicing” varied depending intrinsic characteristics. For the compressive specimens, the two part orientations (XY and YZ) evidenced optimal internal matrix post processing except the internal loose structures for the hexagonal and pyramid structure types when oriented in the YZ. Due to the nature of the specimens’ geometries, the raster paths changed from one set of specimen to the other.

4.5 ANALYSIS OF VARIANCE FOR THE MATERIAL, SUPPORT, AND TIME

Analysis of Variance (ANOVA) is a cluster of statistical models in which the observed variance in a particular variable is partitioned into components attributable to different sources of variation. In its simplest form, ANOVA provides a statistical test of whether or not the means of several groups are all equal and helps to understand their interactions [Montgomery, 2009].

Regression Analysis (RA) helps to understand how the typical value of the dependent variable changes when any one of the independent variables is varied, while the other independent variables are held fixed. Regression analysis estimates the conditional expectation of the dependent variable given the independent variables. The estimation target is a function of the independent variables called the regression function from which characterization of the coefficient values is preponderant [Montgomery, 2009].

The following Sections 4.5.1 and 4.5.2 comprise the ANOVA and Regression Analysis performed on the tensile and compressive specimens once the values from the FDM RP and the physical testing are performed and this is accomplished by using SPSS Statistics® from IBM®. It is important to mention that this section will make reference to the tables and/or formulas

comprised in the Appendix of this thesis. Hence, any further reference to the subject matter herein covered should be made directly to such Appendix. That cluster of tables does not follow any particular order. Appendix comprises the ANOVA and Regression models for the tensile and the compressive specimens, respectively. Each of it comprises the load, the model material, the support material, and the time ANOVA and RA for the respective orthogonal/hexagonal/pyramid and the solid/hollow individually and respectively.

In order to understand the results from the ANOVA and the RA, it is important to make reference to Table 4.12 where the abbreviation for the variables involved in both analyses is presented.

Table 4. 12 Variable description and respective abbreviation

Variable Description	Variable Abbreviation
Structure Type	St
Raster Angle	Ra
Build Plane	Bp
Internal Density	Id
Load	Load
Time	Time
Model Material	Mm
Support Material	Sm

4.5.1 ANOVA – MATERIAL USAGE FROM VIRTUAL RP

With respect to the material use, the ANOVA for the model material and support material was performed on the tensile and compressive specimens, respectively. The variables are given a number (Table A7) in order to perform the ANOVA where Tables A8 and A40 comprise the results for the analysis where the model material is studied for the tensile and compressive specimens, respectively. Similarly, Tables A11 and A43 comprise the results for the analysis where the support material is studied for the tensile and compressive specimens, respectively. Those four tables provide the source factors or variables individually and in combinations, for example: structure type, raster angle, build plane, internal density, structure type and raster angle, raster angle and build plane, etc. Similarly, the tables provide the significance value from those source factors from the tensile and compressive specimens. This significance shows whether the variable is significant or not or if it is significantly affecting the response variable. It is important to mention that the level of significance is taken to be as 5% based on previous similar studies. If

CHAPTER IV: RAPID PROTOTYPING OF PARAMETRICAL MODELS

the value reflected from Tables A8, A40, A11, and A43 is smaller than 5%, the variable is significant; else, it is not significant.

Significant values from the tensile specimen model material are: St, Ra, Bp, Id, and St.Id.

Significant values from the compressive specimen model material are: St, Bp, Id, and St. Id.

Significant values from the tensile specimen support material are: St, Ra, Bp, Id, St.Id, St.Bp, Bp.Id, and St.Bp.Id.

Significant values from the compressive specimen support material are: St, Bp, Id, St.Bp, St.Id, and St.Bp.Id.

From said tensile analysis, it is conclusive that the structure type (St), build plane (Bp), and internal density (Id) are significant when considered independently, and structure type (St) and internal density (Id) are significant when considered jointly.

From said compressive analysis, it is conclusive that the build plane (Bp) and internal density (Id) are the two most significant variables affecting the load when they interact with other variables together and when they are considered independently.

From said tensile analysis, it is conclusive that the structure type (St) and internal density (Id) are significant when considered independently, and structure type (St) is significant when considered with other variables.

From said compressive analysis, it is conclusive that the build plane (Bp) and internal density (Id) are the two most significant variables affecting the load when they interact with other variables together and when they are considered independently.

Once the ANOVA has been accomplished, sufficient elements are gathered in order to proceed to carry out the Regression Analysis. It should be pointed out that the ANOVA estimates the coefficients for different levels of variables, whereas the RA and its regression function combine all the levels; hence, one coefficient for each independent variable is obtained. Therefore, the RA serves to obtain a model equation that relates all the variables involved in both, tension and compression, specimens.

Tables A10 and A42 comprise the variables and the coefficients from all the variables involved in the prediction of the tensile and the compressive model material use, respectively. The generated equations are shown herein below, namely:

CHAPTER IV: RAPID PROTOTYPING OF PARAMETRICAL MODELS

$$\begin{aligned}
 Mm(Tensile) = & 9.303 - 0.163St - 0.011Ra + 0.452Bp + 0.630Id - 0.005St.Ra - 0.026St.Bp \\
 & - 0.115St.Id + 0.013Ra.Bp + 0.019Ra.Id - 0.011Bp.Id - 0.009St.Ra.Bp \\
 & - 0.005St.Ra.Id - 0.004St.Bp.Id + 0.01Ra.Bp.Id - 0.004St.Ra.Bp.Id
 \end{aligned}$$

(Equation 4.1)

$$\begin{aligned}
 Mm(Compressive) = & 2.473 + 0.031St + 0.02Ra + 0.333Bp + 0.053Id - 0.009St.Ra + 0.05St.Id - \\
 & 0.023Ra.Bp - 0.026Ra.Id - 0.022Bp.Id + 0.01St.Ra.Bp + 0.01St.Ra.Id + 0.006St.Bp.Id + \\
 & 0.022Ra.Bp.Id - 0.008St.Ra.Bp.Id
 \end{aligned}$$

(Equation 4.2)

Tables A13 and A45 comprise the variables and the coefficients from all the variables involved in the prediction of the tensile and the compressive support material use, respectively. The generated equations are shown herein below, namely:

$$\begin{aligned}
 Sm(Tensile) = & 6.206 - 0.101St - 0.032Ra - 0.318Bp - 0.038Id - 0.005St.Ra + 0.145St.Bp \\
 & - 0.043St.Id + 0.006Ra.Bp + 0.013Ra.Id - 0.092Bp.Id - 0.006St.Ra.Bp \\
 & - 0.006St.Ra.Id + 0.009St.Bp.Id + 0.01Ra.Bp.Id - 0.0024St.Ra.Bp.Id
 \end{aligned}$$

(Equation 4.3)

$$\begin{aligned}
 Sm(Compressive) = & 3.515 + 0.024St - 0.012Ra + 0.442Bp - 0.089Id + 0.004St.Ra + \\
 & 0.031St.Bp + 0.095St.Id - 0.008Ra.Bp - 0.014Ra.Id - 0.038Bp.Id + 0.004St.Ra.Bp + \\
 & 0.005St.Ra.Id + 0.022St.Bp.Id + 0.001Ra.Bp.Id
 \end{aligned}$$

(Equation 4.4)

Additionally, the model material for the hollow/solid tensile and compressive specimens was analyzed separately. Tables A24 and A50 comprise the significant values for such tensile and compressive specimens.

Significant values from the tensile specimen model material are: St.

Significant values from the compressive specimen model material are: St, Bp, and St. Bp.

Similarly, Tables A26 and A52 comprise the RA model for the tensile and compressive specimens respectively. The generated equations are shown herein below, namely:

$$Mm(Tensile) = 12.48 + 4.225St - 0.077Ra - 0.108Bp - 0.047St.Ra - 0.512St.Bp - 0.065Ra.Bp$$

(Equation 4.5)

$$\begin{aligned}
 Mm(Compressive) \\
 = & 4.045 + 1.722St - 0.023Ra + 0.132Bp - 0.02St.Ra - 0.195St.Bp + 0.005Ra.Bp
 \end{aligned}$$

(Equation 4.6)

Finally, the support material for the hollow/solid tensile and compressive specimens was analyzed separately. Tables A27 and A53 comprise the significant values for such tensile and compressive specimens.

Significant values from the tensile specimen model material are obtained from Table A29, namely: St, Ra, Bp, and St.Bp.

Significant values from the compressive specimen model material are: St, Bp, and St. Bp.

Similarly, Tables A29 and A55 comprise the RA model for the tensile and compressive specimens respectively. The generated equations are shown herein below, namely:

$$Sm(Tensile) = 3.297 - 2.436St - 0.008Ra + 0.649Bp + 0.005St.Ra + 0.206St.Bp - 0.003Ra.Bp$$

(Equation 4.7)

$$Sm(Compressive) = 1.648 - 1.342St + 0.003Ra + 0.185Bp - 0.003St.Ra - 0.26St.Bp - 0.005Ra.Bp$$

(Equation 4.8)

4.5.2 ANOVA – BUILD TIME FROM VIRTUAL RP

Similarly, with respect to the building characteristics, the ANOVA for the build time was performed on the solid and hollow tensile and compressive specimens, respectively. The data resulted from the 32 samples; each with 3 experiments, respectively.

Table A14 comprises the results from the ANOVA build time for the tensile specimens. Said table provides the source factors or variables individually and in combinations, for example: structure type, raster angle, build plane, internal density, structure type and raster angle, raster angle and build plane, etc. Similarly, the table provides the significance value from said source factors from the tensile and compressive specimens.

Significant values from said table are: St, Ra, Bp, Id, St.Id, St.Bp, Bp.Id, and St.Bp.Id.

Table A16 comprises the variables and the coefficients from all the variables involved in the prediction of the build time. The generated equation is shown herein below, namely:

$$Time(Tensile) = 62.261 - 2.542St - 1.374Ra + 21.904Bp + 5.984Id + 0.458St.Ra - 3.626St.Bp - 0.916St.Id - 0.681Ra.Bp - 0.431Ra.Id + 3.571Bp.Id + 0.292St.Ra.Bp + 0.167St.Ra.Id - 0.917St.Bp.Id + 0.206Ra.Bp.Id - 0.082St.Ra.Bp.Id$$

(Equation 4.9)

Results from the substitution of the respective limiting values for the corresponding factor level value yields the tension load and the compression deformation values, accordingly. Reference to Table A2 should be done for substituting the variables' values.

Table A46 comprises the results from the ANOVA build time for the compressive specimens. Said table provides the source factors or variables individually and in combinations, for example: structure type, raster angle, build plane, internal density, structure type and raster angle, raster angle and build plane, etc. Similarly, the table provides the significance value from said source factors from the tensile and compressive specimens.

Significant values from said table are: St, Bp, Id, St.Bp, St.Id, Bp.Id and St.Bp.Id.

Table A48 comprises the variables and the coefficients from all the variables involved in the prediction of the build time. The generated equation is shown herein below, namely:

$$\begin{aligned} \text{Time (Compressive)} = & 36.134 + 2.313St - 0.057Ra + 5.693Bp + 6.61Id - 0.021St.Ra + \\ & 1.063St.Bp + 1.813St.Id - 0.028Ra.Id - 0.669Bp.Id - 0.021St.Ra.Bp - 0.021St.Ra.Id + \\ & 0.563St.Bp.Id + 0.083Ra.Bp.Id - 0.021St.Ra.Bp.Id \end{aligned} \quad (\text{Equation 4.10})$$

Results from the substitution of the respective limiting values for the corresponding factor level value yields the tension load and the compression deformation values, accordingly. Reference to Table A2 should be done for substituting variables' values.

Table A30 comprises the results from the ANOVA build time for the hollow/solid tensile specimens. Said table provides the source factors or variables individually and in combinations, for example: structure type, raster angle, build plane, internal density, structure type and raster angle, raster angle and build plane, etc. Similarly, the table provides the significance value from said source factors from the tensile and compressive specimens.

Significant values from said table are: Bp.

Table A32 comprises the variables and the coefficients from all the variables involved in the prediction of the build time. The generated equation is shown herein below, namely:

$$\begin{aligned} \text{Time(Tensile)} = & 27.371 - 1.791St + 8.041Bp - 0.709Ra - 0.541St.Ra - 1.291St.Bp - \\ & 0.374Ra.Bp \end{aligned} \quad (\text{Equation 4.11})$$

Results from the substitution of the respective limiting values for the corresponding factor level value yields the tension load and the compression deformation values, accordingly. Reference to Table A2 should be done for substituting variables' values.

Table A56 comprises the results from the ANOVA build time for the hollow/solid compressive specimens. Said table provides the source factors or variables individually and in combinations, for example: structure type, raster angle, build plane, internal density, structure type and raster angle, raster angle and build plane, etc. Similarly, the table provides the significance value from said source factors from the tensile and compressive specimens.

Significant values from said table are: St, Bp, and St.Bp.

Table A58 comprises the variables and the coefficients from all the variables involved in the prediction of the build time. The generated equation is shown herein below, namely:

$$\begin{aligned} \text{Time (Compressive)} = 16.038 - 6.375St - 0.207Ra + 3.458Bp - 0.125St.Ra - 2.79St.Bp + \\ 0.042Ra.Bp \end{aligned} \quad (\text{Equation 4.12})$$

Results from the substitution of the respective limiting values for the corresponding factor level value yields the tension load and the compression deformation values, accordingly. Reference to Table A2, in the Appendix, should be done for substituting variables' values.

Finally, a simplified approach was performed once the main or most relevant parameters were chosen. This simplified versions of the equations herein presented will serve as a hands-on tool in order to obtain the model material, the support material, and the build time values for all the types of specimens and all the types of structures with the variety of internal densities and particular location in the building envelope. These results are presented in Table 6.5 in Chapter VI of this thesis.

CHAPTER V

CHARACTERIZATION OF THE MECHANICAL BEHAVIOR OF FDM PARTS

EXPERIMENTAL INVESTIGATION

5.1 INTRODUCTION

Once the parts with enhanced capabilities (internal topologic arrangement) have been modeled, it is necessary to test those parts built by the FDM Stratasys® FORTUS 400mc® as described in Chapter IV in order to assess the mechanical strength of a finalized 3D model. For this reason, tests are to be carried out so as to understand the mechanical properties of the FDM ABS thermoplastic that could allow the proper characterization and statistical analysis of the experimental approach. Likewise, the results obtained from the physical tests will be of relevancy when performing the FEA simulation since the 3D simulation will be fed by values obtained from data from the experiments.

As previously described in Section 2.1.3 of Chapter II, meso-structure affects the mechanical properties of the FDM ABS material. Furthermore, it has been observed that the mechanical strength is influenced by the part orientation since the fiber-to-fiber bonding affects the strength and the material degradation when the air gap controls the quality of the material at high stress values.

In this regard, mechanical testing is used to determine a material property or a set of properties. The most common tests performed on materials are uniaxial tension test, compression test, impact toughness test, flexure test, hardness tests, and creep tests [Kridli, 2006]. The following Sections 5.1.1 thru 5.3 will explain the process carried out to obtaining the data necessary to appraise the mechanical properties later discussed in Section 5.5 of this chapter. Now then, as previously discussed in Chapter I, the following research focuses on the characterization of FDM parts build with ABS for tension and compression where Section 5.4 of this chapter encompasses the FEA simulation of such specimens.

Finally, Sections 5.5 and 5.6 comprise a comparison with the results from the physical experiments and a statistical analysis of the interactions and relevance of the parameters involved in defining the mechanical characteristics of the type of specimen, respectively.

5.1.1 TENSILE STRENGTH

Tensile strength is a material's ability to withstand an axial load and the tension test is one of the most commonly used tests to evaluate material response to static and quasi-static loading. The test is performed, usually, with the aid of a testing machine, a load cell, and a displacement transducer. Load and grip displacement data are obtained from the load cell and displacement transducer readings, respectively. However, an extensometer, mounted on the specimen gage section, yields more accurate data. Testing procedures and parameters, as well as specimen size, can be obtained from the American Society for Testing and Materials (ASTM). The Standard Test Method for Tensile Properties of Plastics - ASTM D-638-10 is used to determine the tensile properties of unreinforced and reinforced plastics in the form of standard dumbbell-shaped test specimens when tested under defined conditions of pretreatment, temperature, humidity, and testing machine speed. The data obtained from the testing helps to calculate the proportional limit, the elastic stress limit, the yield stress, and the ultimate yield stress. Figure 5.1.1 [ASTM D-638, 2010] depicts the geometry of a “dog-bone” specimen according to Type I, II, III, and IV of this standard.

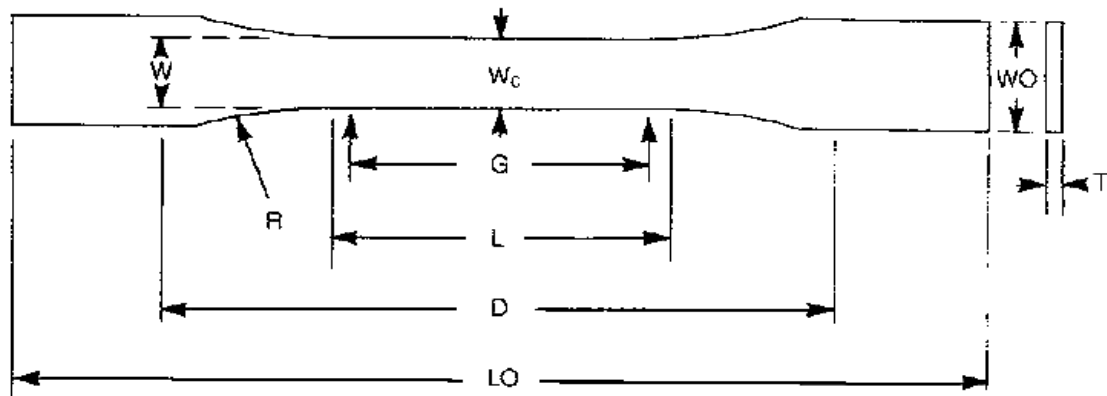


Figure 5.1. 1 ASTM D-638 Type I specimen characteristics [ASTM]

The dimensions for the chosen specimens are encompassed in Table 5.1.

Table 5. 1 ASTM D-638 Type I specimen dimensions [ASTM]

Width of narrow section	Length of narrow section	Width overall	Length overall	Gage length	Distance between grips	Radius of fillet
W	L	WO	LO	G	D	R
13 mm	57 mm	19 mm	165 mm	50 mm	115 mm	76 mm

5.1.2 COMPRESSIVE STRENGTH

Compressive stress is the compressive force divided by cross-sectional area, measured in psi or MPa. It is usually assumed that the compressive strength of a plastic material is equal to its tensile strength. However, the ultimate compressive strength of thermoplastic materials is often greater than the ultimate tensile strength. Thus, most plastics can withstand more compressive surface pressure than tensile load [Tres, 2006].

Compressive properties are useful when a material is used under conditions similar to those in which the test is made. This type of test is useful for materials that fail by shattering under load and is similar in concept to tensile and flexural tests except the deformation mode is compressive rather than stretching. Thus, this test is useful for determining permanent deformation for thermoplastic elastomers and yields compressive properties that include: modulus of elasticity, yield stress, and compressive strength. Nevertheless, the most useful property obtained from this test is compressive strength. Table 5.2 encompasses a description of the aforementioned relevant properties obtained from the compression test.

Table 5. 2 Compressive properties and respective description

Compressive Property	Description
Compressive Strength	It is the maximum load the sample carries divided by the cross sectional area of the sample. It is expressed in MPa or psi.
Compressive Yield Strength	It is obtained by dividing the load at yield by the cross sectional area of the sample. These values are reported in MPa or psi.
Modulus of Elasticity	It is calculated by drawing a tangent line to the linear portion of load-deformation curve, selecting any point on the tangent line and dividing by the strain at that point. Modulus is reported in GPa or psi.

Similar to tensile testing, the testing procedures and parameters, as well as specimen size, can be obtained from the American Society for Testing and Materials (ASTM). The Standard Test Method for Compressive Properties of Rigid Plastics - ASTM D-695 is used to determine the aforementioned compressive properties of unreinforced and reinforced rigid plastics, including high-modulus composites, when loaded in compression at relatively low uniform rates of straining or loading. Now then, a variant from that method, the ASTM D-695-10 was used in the present research since the geometry of the standard specimen allows the proposed approach allowing internal structures within the specimen. Figure 5.1.2 depicts the possible geometries according to the ASTM standard.

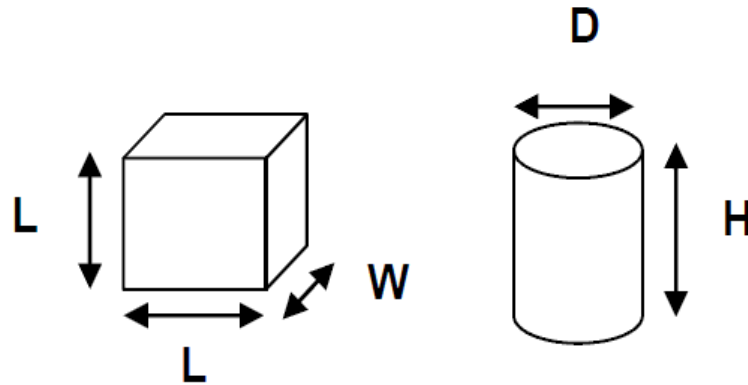


Figure 5.1. 2 ASTM D-695 cylinder and rectangle specimen characteristics [ASTM]

The dimensions for the standard specimens are encompassed in Table 5.3.

Table 5. 3 ASTM D-695 specimens dimensions [ASTM]

Block			Cylinder	
Length	Height	Width	Diameter	Height
L	L	W	D	H
12.7 mm	12.7 mm	25.4 mm	12.7 mm	25.4 mm

5.2 THE BEHAVIOR OF THERMOPLASTICS

According to Persson et al. [Persson, 2004], many polymers that undergo loading above the yield stress stretch uniformly for a few percent and then, instead of breaking, they fail by forming a neck. The neck does not continue shrinking until the specimen fails. Instead, the material in the neck stretches only to a “*natural draw ratio*” which is a function of temperature and specimen processing, beyond which the material in the neck stops stretching and new material at the neck shoulders necks down. The neck then propagates until it spans the full gage length of the specimen, a process called drawing. Figure 5.2.1 [Roylance, 1996] depicts the strain-stress curve for polyamide thermoplastic where the necking and drawing phenomena are present.

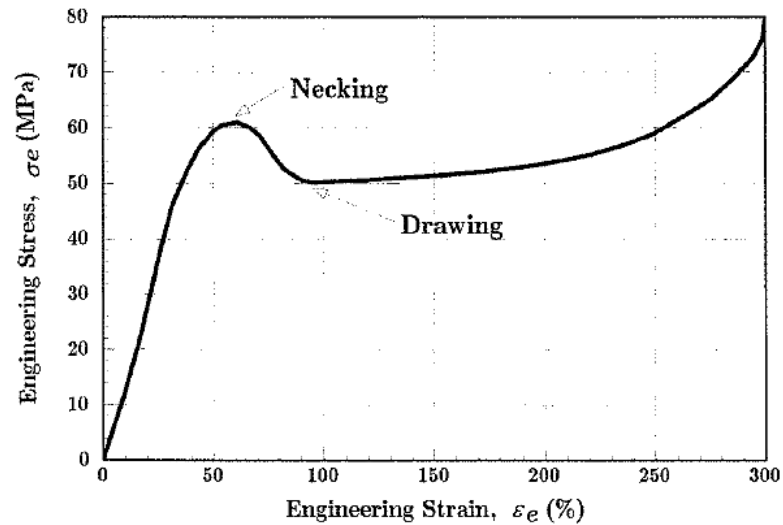


Figure 5.2. 1 Engineering stress-strain diagram for common thermoplastics [Roylance, 1996]

Necking is a geometrical behavior, which typically starts before the softening on the engineering stress-strain curve. Furthermore strain will change the softening process into a hardening process until failure. Nevertheless, not all polymers are able to exhibit drawing, this occurs when the necking process produces a strengthened microstructure whose breaking load is greater than that needed to induce necking in the untransformed material just outside the neck. Figure 5.2.2 [Roylance, 1996] depicts this phenomenon when polyethylene is stretched.

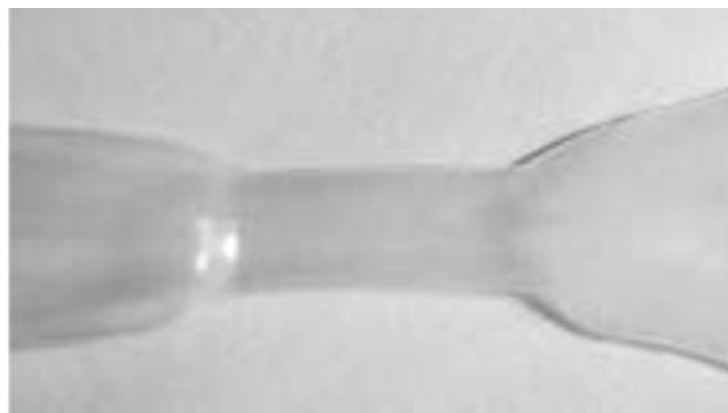


Figure 5.2. 2 Tensile specimen evidencing necking behavior [Roylance, 1996]

Another feature of thermoplastic materials is that they show a different behavior when they are subjected to compression compared to tension. Usually, the response in tension is significantly

stiffer than the response in compression. When looking at polycarbonate (PC), which is a component of PC-ABS, an evident difference is observable in Figure 5.2.3 [Persson, 2004].

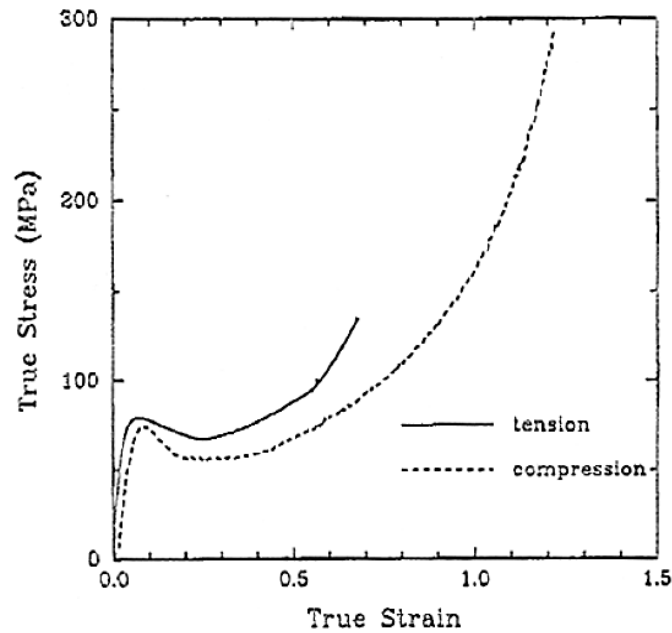


Figure 5.2. 3 Difference of the mechanical behavior for tension and compression [Persson, 2004]

Therefore, the following sections explain the subject matter pertaining to the tensile and compressive mechanical behavior encountered during and after the physical test which will provide meaningful results when performing the mechanical simulation.

5.2.1 THE STRAIN-STRESS CURVE

The load-displacement data is converted into stress and strain data in order to obtain the material properties. Stress is the load bearing capacity of a material normalized per unit area. Stress can be of two types: normal and shear. Normal stress results from an applied load that is perpendicular to the material surface whereas shear stress results from a load applied parallel to the surface [Kridli, 2012]. Figure 5.2.4 [Tres, 2006] depicts the stress-strain diagram for plastic materials and is a representation for the engineering (a) stress and engineering (b) strain equations herein below, respectively:

$$\sigma_e = \frac{P}{A_0}, \quad \epsilon_e = \frac{\delta}{L_0} \quad (\text{Equation 5.1})$$

The stress σ_e is plotted against the strain ϵ_e , an engineering stress-strain curve such as the one depicted in Figure 5.2.4.

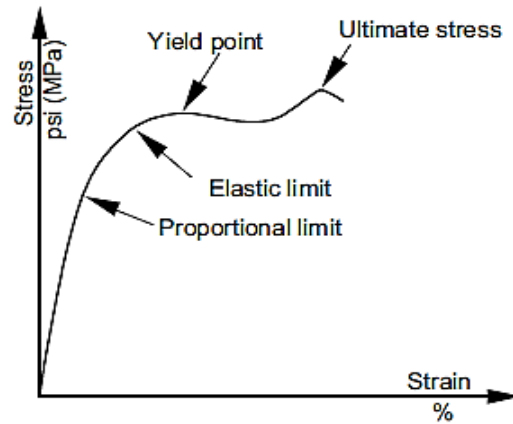


Figure 5.2. 4 Stress-strain diagram for plastic materials [Tres, 2006]

Upon applying a tensile load, the specimen stretches uniformly until the onset of necking. Accordingly, the width and thickness compress. The initial volume of the material in the gage section is assumed to remain constant during plastic deformation and equal to the final volume of material in the gage section [Kridli, 2006]. Similarly, when a compressive load is applied to the specimen, the equation is the same as Equation 5.1, but the force is compressive.

The stress-strain curve in compression is similar to the tensile stress/strain diagram, except the values of stresses in the compression test are greater for the corresponding elongation levels. This is because it takes much more compressive stress than tensile stress to deform a plastic. The aforementioned is evident in Figure 5.2.3 [Persson, 2004] where a stress-strain curve for polycarbonate is shown.

5.2.2 TRUE STRAIN-STRESS

The true stress, σ_{true} , represents the actual stress in the material based on the instantaneous cross-sectional area. Since the instantaneous width and thickness are not readily available, the true stress is usually calculated using engineering stress and engineering strain with the assumption that the volume of material in the gage section of the test specimen remains constant. Thus, the true stress is calculated according to Equation 5.2 [Kridli, 2012].

$$\sigma_{true} = \frac{P}{A} = \sigma_{eng} (1 + \epsilon_{eng}) \quad (\text{Equation 5.2})$$

The true strain, ϵ_{true} , represents the change in length based on the instantaneous length. It is calculated as the natural logarithm of the ratio of instantaneous length divided by the initial length, as shown in Equation 5.3 [Kridli, 2006]. The equation also shows that the true strain can be calculated using the engineering strain.

$$\epsilon_{true} = \int_{l_0}^l \frac{dl}{l} = \ln\left(\frac{l}{l_0}\right) = \ln\left(\frac{A_0}{A}\right) = \ln(1 + \epsilon_{eng}) \quad (\text{Equation 5.3})$$

Figure 5.2.5 [Roylance, 1996] shows a comparison of the engineering and the true stress-strain curves for copper. The arrow indicates the position on the “true” curve of the ultimate tensile stress on the respective true and engineering curves [Roylance, 1996].

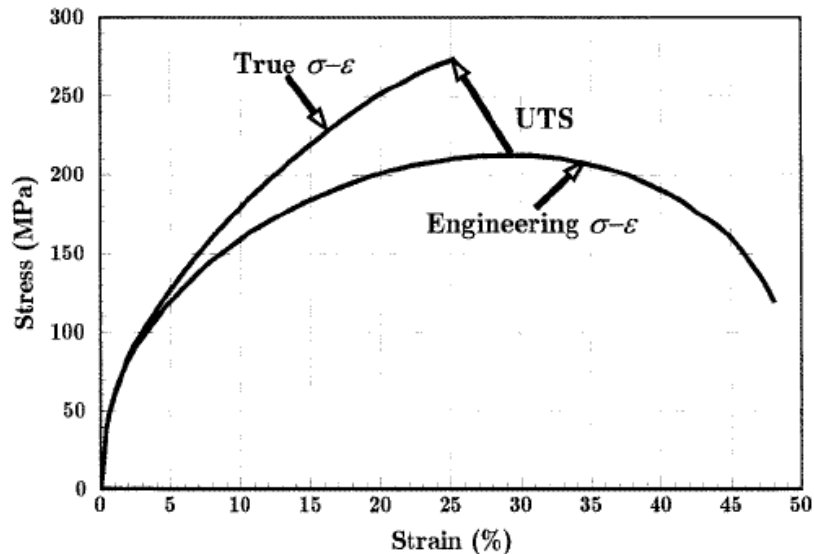


Figure 5.2. 5 Engineering stress-strain and true stress-strain diagrams [Roylance, 1996]

5.3 MATERIAL TESTING

This section will describe the methodology followed in order to carry out the tensile and compressive tests. The tensile and compressive tests will verify the results obtained from the simulations performed in the FEA model. Once the parts were prototyped and post processed, the parts were labeled and the machine was calibrated according to the respective mechanical test. Figure 5.3.1 depicts the tensile/compressive machine setup at the time of the mechanical tests.



Figure 5.3. 1 Tinius Olsen® tensile/compressive equipment setup

5.3.1 THE TENSILE TEST

5.3.1.1 TEST PREPARATION

A specimen as depicted in Figure 5.1.1 is placed in a TINIUS-OLSEN® machine in a tensile testing array. Both ends of the specimen are clamped into the machine's jaws. One end of the tensile specimen is pulled while the other remains static. Load and displacement values are automatically gathered and stored in the array's PC. Figure 5.3.2 depicts the machine array setup at the moment of the experiment.

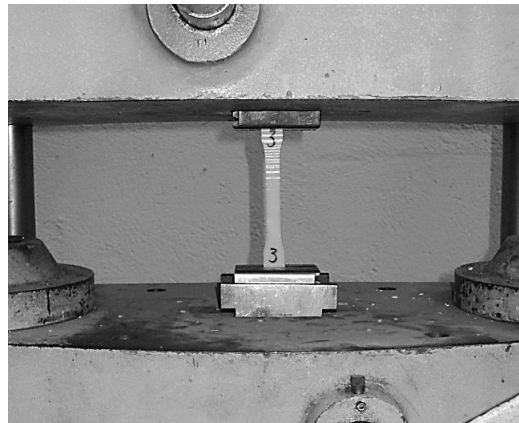


Figure 5.3. 2 Tensile test setup while testing

CHAPTER V: CHARACTERIZATION OF THE MECHANICAL BEHAVIOR OF FDM PARTS - EXPERIMENTAL INVESTIGATION

The axial load is applied to the specimen when the machine pulls the ends of the specimen bar in opposite directions at a slow and constant rate of speed. A 0.2 in. per minute (5 mm/min) pulling speed is used to approximate the material's behavior in a hand assembly operation as depicted in Figure 5.3.3 [Tres, 2006] where F is the applied tensile force, L is the initial specimen's length and ΔL is the change in length after the applying the load F to the specimen.

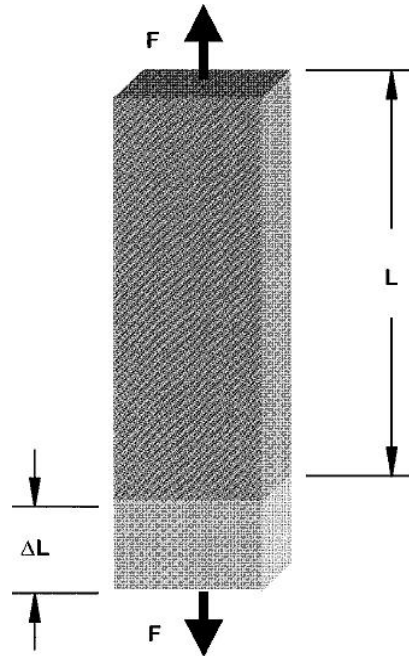


Figure 5.3. 3 Force effect in the a tensile specimen [Tres, 2006]

5.3.1.2 TESTING PROCEDURE

As the pulling progresses, the specimen bar elongates at a uniform rate that is proportionate to the rate at which the load or pulling force increases. The load, divided by the cross-sectional area of the specimen, represents the unit stress resistance of the plastic material to the pulling or tensile force [Tres, 2006].

5.3.1.3 RESULTS OF THE TENSILE TESTS

A total of 3 tests per experiment type were carried out with data taken every one (1) second. This was intended to ensure repeatability in the results for the tensile tests. Table 5.4 summarizes the values obtained from such physical experiments where the values represent the average from this set of experiments for each sample type.

CHAPTER V: CHARACTERIZATION OF THE MECHANICAL
BEHAVIOR OF FDM PARTS - EXPERIMENTAL INVESTIGATION

Table 5. 4 Load values obtained from the physical tensile testing (3 samples per exp. = 96 reps.)

Experiment No.	Type of Structure	Raster Angle	Build Plane	Internal Density	Max Load (N)	Deformation (%)
1	Orthogonal	-1	-1	-1	1209	1.67
2	Orthogonal	-1	-1	1	1356	1.71
3	Orthogonal	-1	1	-1	1628	1.92
4	Orthogonal	-1	1	1	1527	1.70
5	Orthogonal	1	-1	-1	1208	1.3
6	Orthogonal	1	-1	1	1199	1.03
7	Orthogonal	1	1	-1	1448	1.70
8	Orthogonal	1	1	1	1655	2.46
9	Hexagonal	-1	-1	-1	1307	1.78
10	Hexagonal	-1	-1	1	1268	1.74
11	Hexagonal	-1	1	-1	1573	2.21
12	Hexagonal	-1	1	1	1451	2.07
13	Hexagonal	1	-1	-1	1278	2.07
14	Hexagonal	1	-1	1	1162	1.47
15	Hexagonal	1	1	-1	1411	1.91
16	Hexagonal	1	1	1	1435	1.91
17	Pyramid	-1	-1	-1	1278	1.37
18	Pyramid	-1	-1	1	1255	1.57
19	Pyramid	-1	1	-1	1477	1.63
20	Pyramid	-1	1	1	1428	1.49
21	Pyramid	1	-1	-1	1364	1.89
22	Pyramid	1	-1	1	1332	1.52
23	Pyramid	1	1	-1	1442	1.85
24	Pyramid	1	1	1	1492	2.13
25	Solid	-1	-1	-	2954	3.23
26	Solid	-1	1	-	2844	2.64
27	Solid	1	-1	-	3023	3.54
28	Solid	1	1	-	2620	3.18
29	Hollow	-1	-1	-	1450	2.08
30	Hollow	-1	1	-	1941	2.99
31	Hollow	1	-1	-	1557	1.88
32	Hollow	1	1	-	1811	3.65

5.3.2 THE COMPRESSION TEST

Compression tests provide information about the mechanical properties of rigid plastics, including high modulus composites, when loaded in compression at low rates of straining and loading. However, there are advantages and disadvantages of the process, which are shown in Table 5.5.

Table 5. 5 Advantages and disadvantages of compression testing

Advantages of compressive testing	Disadvantages of compressive testing
Flexibility in sample configuration	Results are dependent on test conditions and sample configuration
Useful for brittle materials experiencing load	Sample preparation can affect results
Standardize test for high strength composites	Data will experience some scatter, therefore multiple test are required

5.3.2.1 TEST PREPARATION

The compressive test is similar to that of tensile properties. A test specimen is compressed to rupture between two parallel platens. The test specimen adopted in this research was the cube type as depicted in Figure 5.1.2. Figure 5.3.4 depicts TINIUS-OLSEN® machine in a compressive testing array. The specimen is simply located between the two parallel platens while the top platen is brought down at a constant rate while the lower platen remains static. Load and displacement values are automatically gathered and stored in the array's PC.

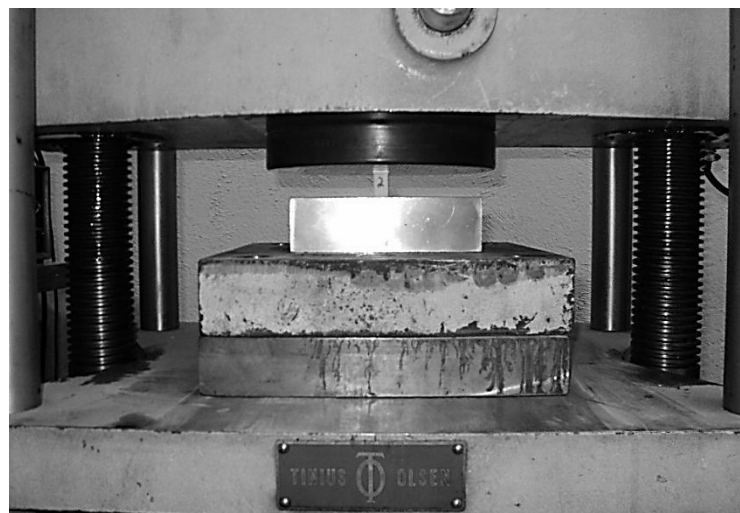


Figure 5.3. 4 Compressive test setup while testing

CHAPTER V: CHARACTERIZATION OF THE MECHANICAL BEHAVIOR OF FDM PARTS - EXPERIMENTAL INVESTIGATION

The load is applied to the specimen from two directions in axial opposition at a rate of 0.05 in. per minute (1.3mm/min). The ultimate compressive strength is measured when the specimen fails by crushing as depicted in Figure 5.3.5 [Tres, 2006] where P is the compressive load applied to the specimen, L is the initial height of the specimen and ΔL is the dimensional change in length.

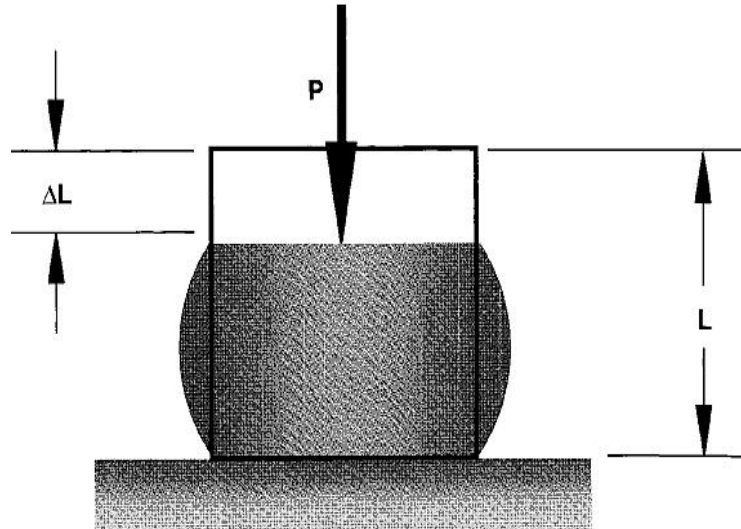


Figure 5.3. 5 Load effect in a compressive specimen [Tres, 2006]

5.3.2.2 TESTING PROCEDURE

A stress/strain diagram is developed during the test, and values are obtained for the four distinct regions: the proportional region, the elastic region, the yield region, and the ultimate (or breakage) region. As the pushing progresses, the specimen cube compresses at a uniform rate that is proportionate to the rate at which the load or pushing force increases. The structural analysis of thermoplastic parts is more complex when the material is in compression. Failure develops under the influence of a bending moment that increases as the deflection increases. A plastic part's geometric shape is a significant factor in its capacity to withstand compressive loads [Tres, 2006].

5.3.2.3 RESULTS OF THE COMPRESSIVE TESTS

A total of 3 tests per experiment type were carried out. This was intended to ensure repeatability in the results for the compressive tests. Table 5.6 summarizes the values obtained from such physical experiments where the values represent the average from that set of experiments for each sample type.

CHAPTER V: CHARACTERIZATION OF THE MECHANICAL
BEHAVIOR OF FDM PARTS - EXPERIMENTAL INVESTIGATION

Table 5. 6 Load values obtained from the physical compressive testing (3 samples per exp. = 96 reps.)

Experiment No.	Type of Structure	Raster Angle	Build Plane	Internal Density	Max Load (N)	Deformation (%)
1	Orthogonal	-1	-1	-1	1734	11.46
2	Orthogonal	-1	-1	1	2670	13.54
3	Orthogonal	-1	1	-1	2006	6.96
4	Orthogonal	-1	1	1	2611	9.47
5	Orthogonal	1	-1	-1	1943	8.96
6	Orthogonal	1	-1	1	2520	11.94
7	Orthogonal	1	1	-1	1878	7.91
8	Orthogonal	1	1	1	2434	10.80
9	Hexagonal	-1	-1	-1	1846	9.09
10	Hexagonal	-1	-1	1	2041	10.97
11	Hexagonal	-1	1	-1	1505	8.21
12	Hexagonal	-1	1	1	1612	10.86
13	Hexagonal	1	-1	-1	1917	8.90
14	Hexagonal	1	-1	1	2077	10.06
15	Hexagonal	1	1	-1	1378	6.75
16	Hexagonal	1	1	1	1398	8.63
17	Pyramid	-1	-1	-1	1442	7.13
18	Pyramid	-1	-1	1	2053	11.09
19	Pyramid	-1	1	-1	1573	6.60
20	Pyramid	-1	1	1	2058	11.96
21	Pyramid	1	-1	-1	1364	5.74
22	Pyramid	1	-1	1	2003	9.18
23	Pyramid	1	1	-1	1613	6.75
24	Pyramid	1	1	1	1960	12.85
25	Solid	-1	-1	-	19100*	143.50
26	Solid	-1	1	-	19204*	134.88
27	Solid	1	-1	-	19288*	164.43
28	Solid	1	1	-	19380*	138.32
29	Hollow	-1	-1	-	1416	7.34
30	Hollow	-1	1	-	1400	6.86
31	Hollow	1	-1	-	1151	4.05
32	Hollow	1	1	-	1491	6.92

*End values were taken approximately close to 19,000 N

5.4 SIMULATION OF THE MECHANICAL BEHAVIOR OF THE INTERNALLY MODIFIED STRUCTURES

Material models are mathematical descriptions of the material behavior at specific situations. Finite Element Analysis (FEA) simulation provides a better understanding of the mechanical behavior when the parts are tested under tension and compression, respectively. Several parameters are needed in order to perform the material model in computer aided engineering (CAE) software. Hence, experimental data is needed. This data is obtained from the data of the material provided by the FDM supplier and input in Abaqus/CAE®. Abaqus/CAE® is a commercial finite element method (FEM) tool that model and analyze mechanical components and assemblies (pre-processing) and visualizes the finite element analysis result.

Section 5.4.1 revises specific approaches that researchers have carried out in the realm of thermoplastics such as ABS and PC. Sections 5.4.2 thru Sections 5.4.5 comprise the complete description of the element type, mesh, loads and boundary conditions, the input data, and graphical results from the simulations.

5.4.1 BACKGROUND

There have been some researchers that have dug into the finite element analysis of thermoplastic materials. In this regard, Thomas et al. [Thomas, 2000] analyzed the fracture strength developed between FDM extruded roads in terms of the wetting and thermally driven diffusion bonding processes. As mentioned before, strength depends on the fiber-to-fiber bond quality. For a monofilament, road-to-road interface data are obtained from a heat transfer analysis and used to develop model predictions based on reptation theory for the inter-diffusion of long-chain polymer molecules. Fracture toughness data on FD-ABS plastic specimens is used to quantify the model. In this approach, Thomas et al. [Thomas, 2000] combined analytical-computational-experimental study of the fiber-to-fiber interface strength of FD-ABS plastic materials as depicted in Figure 5.4.1 [Thomas, 2000]. The model is used to make interface toughness estimates for process variable settings of possible interest. According to the researchers, results show that most of the fracture strength develops during the surface wetting stage of bonding and that slower cooling rates during solidification promote stronger bonding between the roads.

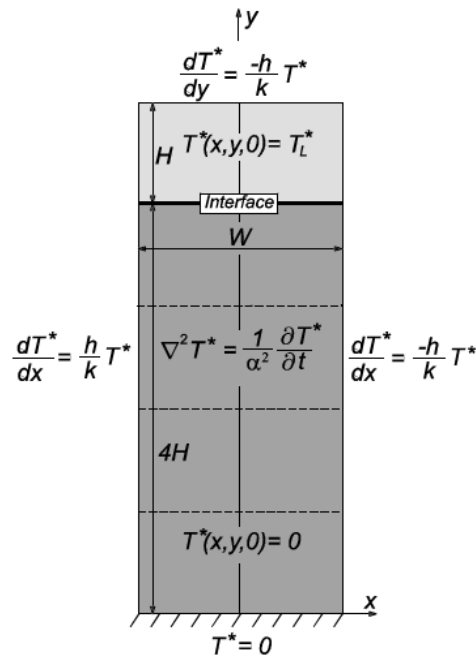


Figure 5.4. 1 Fiber-to-fiber interface strength model [Thomas, 2000]

As stated by Arriaga et al. [Arriaga, 2006], the use of calculation codes based on the finite element method in the design phase of any industrial product, usually, results in cost reduction compared to the trial-and-error testing to build physical prototypes. Similarly, the general use of CAE software permits solving the loading conditions, provides the visualization, and entices the interpretation of the generated results.

Persson et al. [Persson, 2004] utilized FEA simulation to recreate the effect of PC-ABS samples under large deformations. For this purpose, they adopted ANSYS® for large strain rates with a visco-plastic model named the Perzyna model. This model requires identification of two parameters γ (material viscosity) and \mathbf{m} (strain rate hardening) to describe the visco-plastic behavior. This model describes the softening behavior accurately at an arbitrary loading rate. Figure 5.4.2 [Persson, 2004] shows real tensile tests made in a tensile test machine, at different strain rates, compared with simulations of tensile tests made in ANSYS with the visco-plastic model; where the solid line represents the real test whereas the dotted line represents the simulation results.

CHAPTER V: CHARACTERIZATION OF THE MECHANICAL BEHAVIOR OF FDM PARTS - EXPERIMENTAL INVESTIGATION

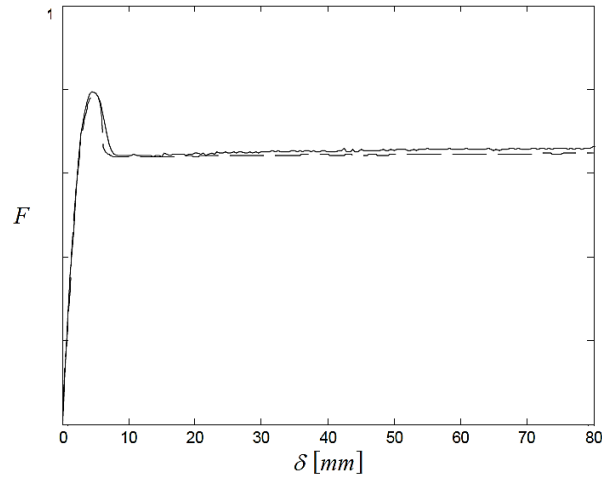


Figure 5.4. 2 Load and displacement of physical and simulation experiments [Persson, 2004]

Arriaga et al. [Arriaga, 2006] adopted ANSYS® as the FEA solver in order to validate the results from the model of the uniaxial tensile test. The model ought to be simple in the sense of low computational costs for a number of different variations in tensile testing deformation ratios. Once a force-displacement curve of the experimental test is obtained, the model is to be considered as valid for the number of test representing the uniaxial tensile mode. Before obtaining a consisting model, Arriaga et al. [Arriaga, 2006] sought to adopt a related Von Mises yielding criterion, to evaluate different friction coefficients between the plastic part (specimen) and the metallic parts (gripping claws of the tensile machine), to use different element types such as 3D solid or shell-type elements, and to use different solution characteristics such as the selection of a correct number of sub-steps. Fig 5.4.3 [Arriaga, 2006] shows the reproduction of the necking effect simulation of the tensile test specimen.

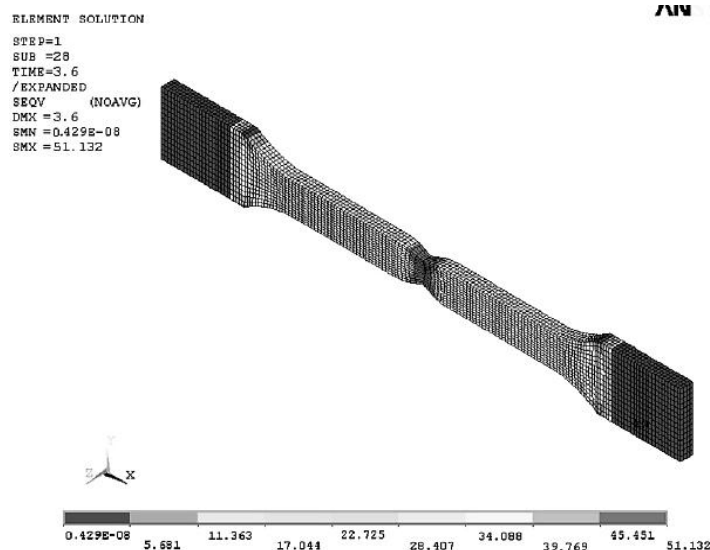
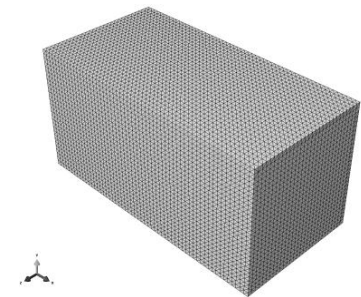
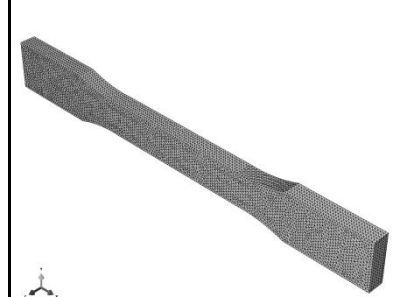


Figure 5.4. 3 Necking FEA simulation of a tensile specimen via ANSYS® [Arriaga, 2006]

5.4.2 ELEMENT TYPE AND MESH

The simulated model of the tensile and compressive specimens represents the real specimens as tested in the physical experiments. In this sense, Table 5.7 summarizes the Abaqus/CAE® FEA simulation parameters for each of the specimen types.

Table 5. 7 Abaqus/CAE® FEA simulation parameters, mechanical properties, and mesh schematics

Specimen Type	Tensile	Compressive
Mesh Size	3D Solids – Tetrahedral	3D Solids – Tetrahedral
No. of Approx. Elements	180,000	846,000
Order Type	1st Order	1st Order
Element Type	CD34- 4 NODE Linear Tetrahedron	CD34- 4 NODE Linear Tetrahedron
Simulation Type	Implicit Simulation	Implicit Simulation
Material Density	1050 g/m ³	1050 g/m ³
Modulus of Elasticity	2.55 GPa	2.55 GPa
Poisson Ratio	0.4	0.4
Linearity of Simulation	Non-Linear General Static Simulation	Non-Linear General Static Simulation
Yield Stress	25 MPa	25 MPa
Specimen Schematic		

5.4.3 BOUNDARY CONDITIONS

The boundary conditions refer to the location of the displacement constraints for both, the tension and compression, specimens. As depicted in Figure 5.4.4, the (a) compressive specimen was constrained on the bottom end, emulating the physical testing conditions. This condition prevent the 3D modeled part to move in X and Y axes. By this means, the specimen will only be allowed to move freely in the Z-axis. Similarly, Figure 5.4.4 depicts the (b) tensile specimen, which was constrained on the top end, emulating the physical testing conditions. Same arrangement prevented from rotation and translation in all directions except the allowed axial direction.

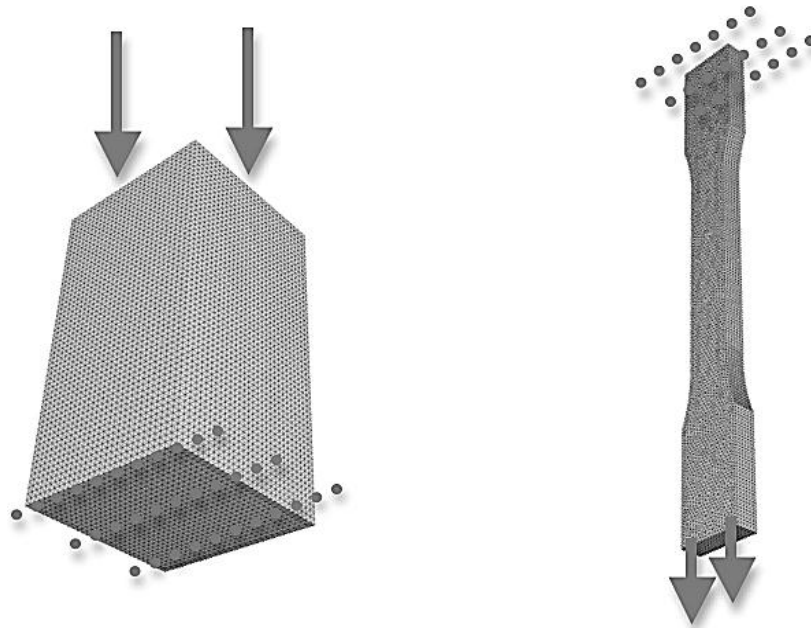


Figure 5.4. 4 Constraints location for the compressive and tensile specimens

5.4.4 INPUT DATA

Usually the input data is given in terms of engineering stress and engineering strain. In large strain analysis, generally stress-strain input is provided in terms of true stress and true strain. In small strain applications, the area reduction effect is insignificant and it will therefore not affect the accuracy of the simulation results. Since the cross-sectional area of each of the specimens, except in the solid case, does not remain constant along the axial length of each of the specimens, load values become the relevant parameter/result out from both, physical and virtual, tests.

In order to carry out the FEA, input data must be provided to the system. In this case, input data was obtained from the results obtained from the physical experiments in tension. Particularly, the average load and displacement was gathered from all the solid specimens where the cross-sectional area along the axial orientation is constant and a quasi-isotropic condition is assumed. Figure 5.4.5 shows the true stress vs. true strain for the average values from the solid tensile samples. As it can be seen, there is a linear relationship between the stress and strain of the tested part. Based on these results and on the behavior of the tensile parts in the physical experiments, the simulation was carried within the elastic region of the material since the specimens shown brittle behavior.

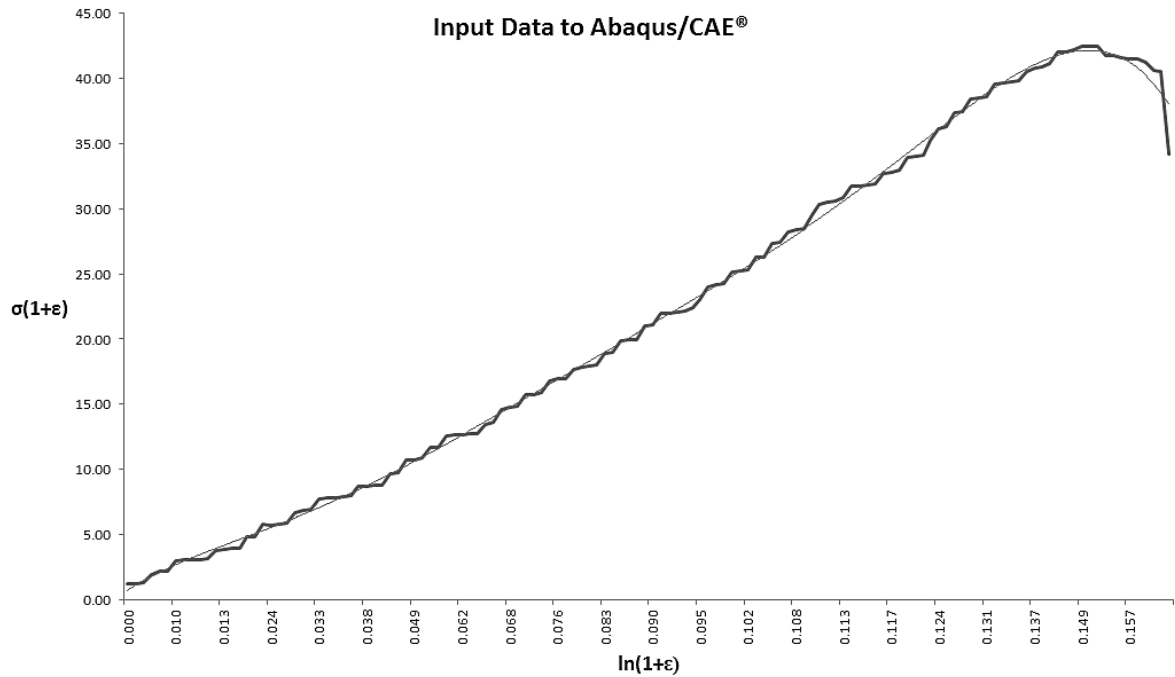


Figure 5.4. 5 True stress-strain diagram from the average solid tensile specimens tests

Based on the tensile and compressive standards (ASTM), respective load rates were used as the simulation conditions in the CAE simulation software. This was performed in order to emulate the physical testing conditions to the virtual boundary conditions as close as possible.

5.4.5 RESULTS

Results from the FEA simulation are presented in this section in the form of (a) comparative graph between sets of specimens and (b) schematics from the sets of specimen for both, tension and compressions, Abaqus/CAE® simulation.

Figure 5.4.6 shows a graph of the tensile load against the displacement of both, solid and hollow, tensile specimens. It is evident the difference in load withstood from the solid specimen to the hollow specimen.

Solid vs Hollow Tensile Specimen

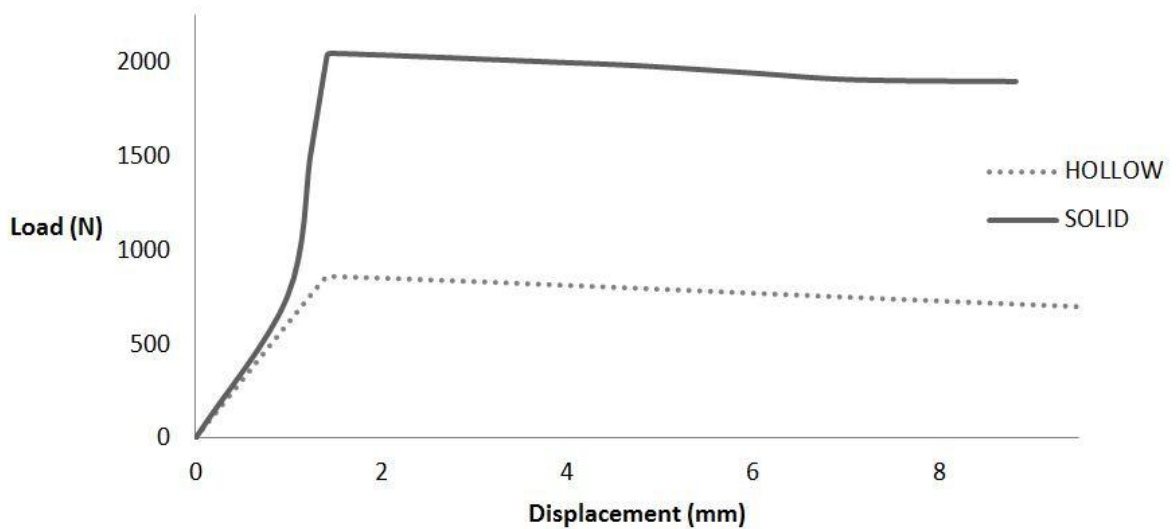

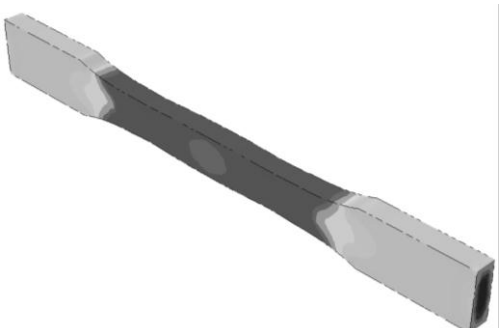


Figure 5.4. 6 Load and displacement diagram for the solid and hollow tensile specimens

Similarly, Table 5.8 describes, graphically, the tensile testing result and the necking behavior experienced by the hollow and solid tensile samples. According to the simulation, there are two necking sites along the specimens for both, solid and hollow. However, in a physical test scenario, this only occurs in one site: the site that begins to fracture and propagate the fiber rupture.

Table 5. 8 FEA simulation of the solid/hollow specimens' deformation and stress distribution

	Specimen Deformation	Specimen Stress
Solid		

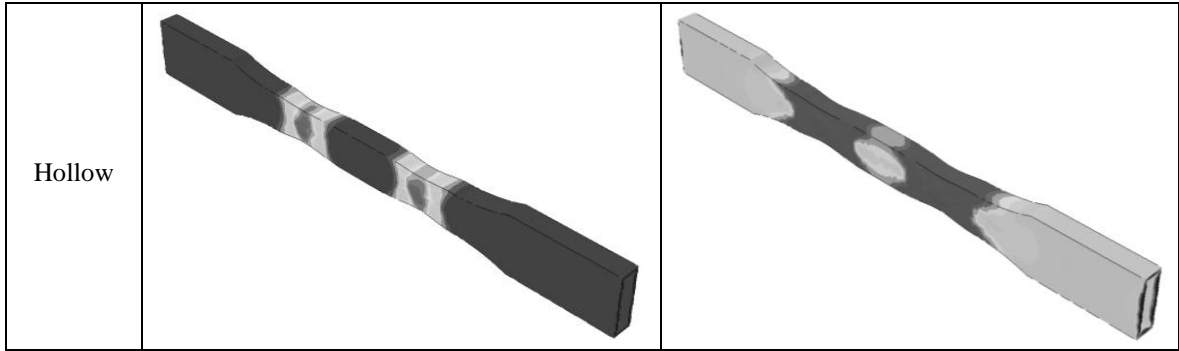


Figure 5.4.8 shows a graph of the tensile load against the displacement of both, loose and compact, orthogonal tensile specimens. There is a slight difference between the compact and loose specimens. Evidently, the load withstood from this pair of tensile specimens is much lower than the solid tensile specimen; however, both yield higher load values compared to that of the hollow tensile specimen.

Loose vs Compact Orthogonal Tensile Specimen

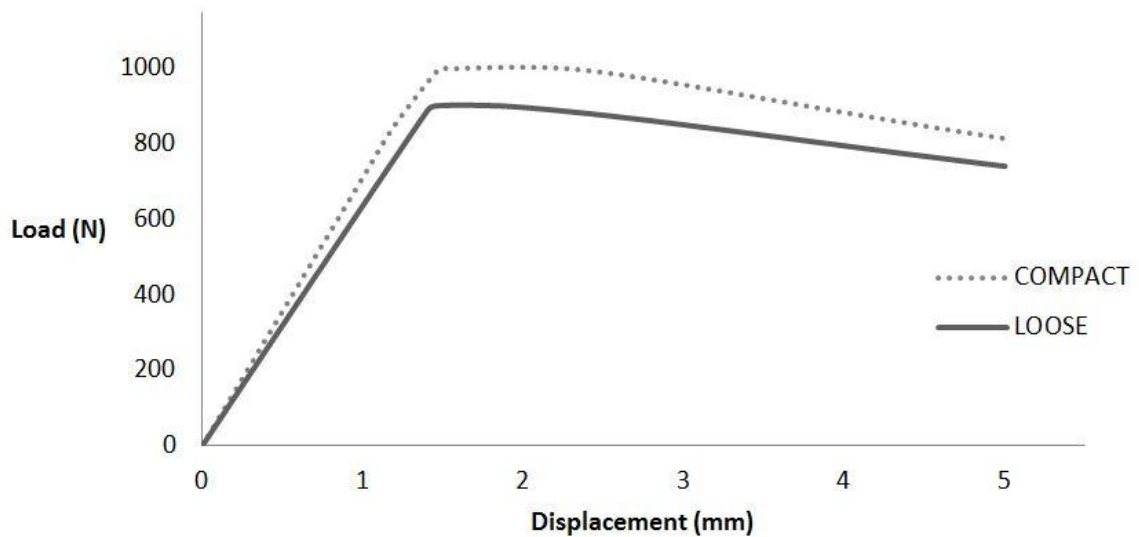


Figure 5.4. 7 Load and displacement diagram for the loose and compact orthogonal tensile specimens

Similarly, Table 5.9 describes, graphically, the tensile testing result experienced by the orthogonal loose and orthogonal compact tensile samples. Table 5.9 comprises the simulation of the rupture location of the internal structure arrangement. As it can be seen, both loose and compact specimens fail in the middle of the tensile sample.

Table 5. 9 FEA simulation of the loose/compact orthogonal specimens' deformation


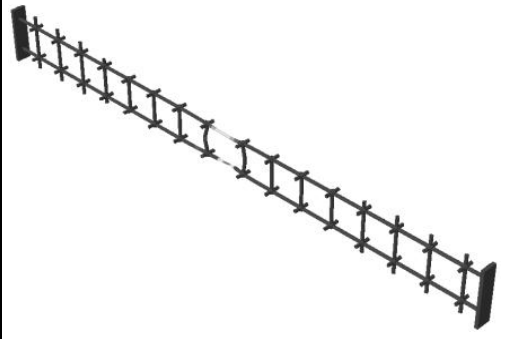

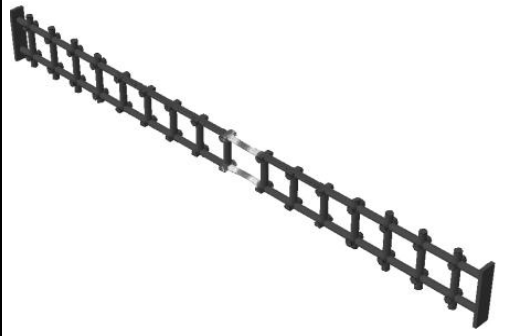
	Tensile Specimen	Specimen's Internal Structure
Loose		
Compact		

Figure 5.4.8 shows a graph of the tensile load against the displacement of both, loose and compact, hexagonal tensile specimens. In this case, there is a very small difference between the loads withstood from the compact to the loose specimen. Evidently, the load withstood from this pair of tensile specimens is much lower than the solid tensile specimen; again, both yield higher load values compared to that of the hollow tensile specimen.

Loose vs Compact Hexagonal Tensile Specimen

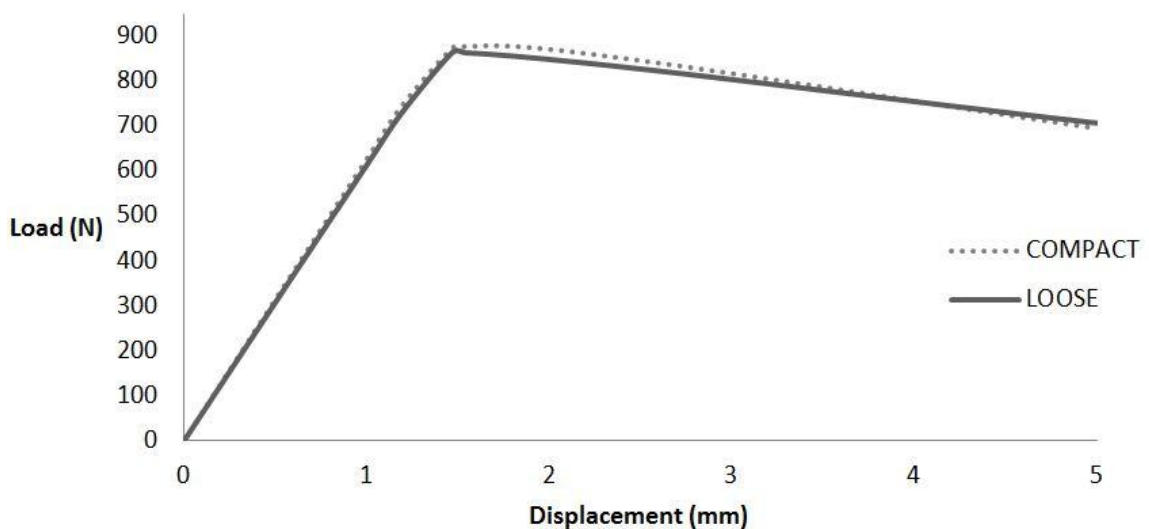


Figure 5.4. 8 Load and displacement diagram for the loose and compact hexagonal tensile specimens

CHAPTER V: CHARACTERIZATION OF THE MECHANICAL BEHAVIOR OF FDM PARTS - EXPERIMENTAL INVESTIGATION

Table 5.10 describes, graphically, the tensile testing result experienced by the hexagonal loose and hexagonal compact tensile samples. Table 5.10 comprises the simulation of the rupture location of the internal structure arrangement. As it can be seen, both loose and compact specimens do not fail in the middle of the tensile sample as compared to the orthogonal set of specimens.

Table 5. 10 FEA simulation of the loose/compact hexagonal specimens' deformation


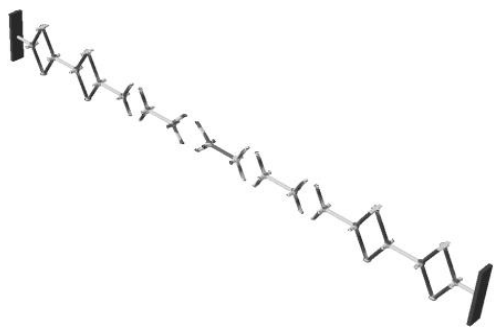


	Tensile Specimen	Specimen's Internal Structure
Loose		
Compact		

Figure 5.4.9 shows a graph of the compressive load against the displacement of both, solid and hollow, compressive specimens. It is evident the vast difference in load withstood from the solid specimen to the hollow specimen.

Solid vs Hollow Compressive Specimen

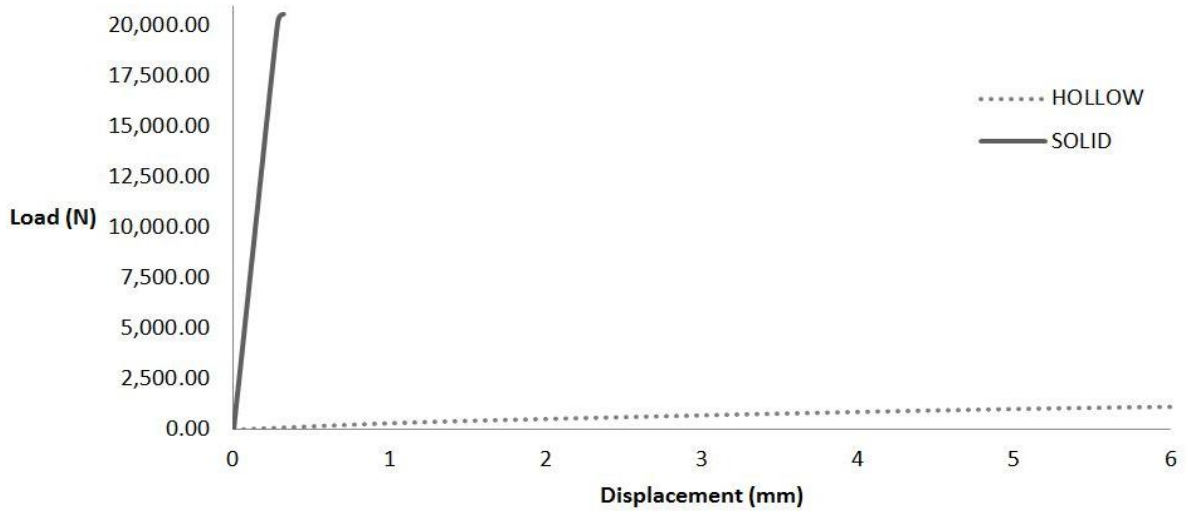


Figure 5.4. 9 Load and displacement diagram for the solid and hollow compressive specimens

Table 5.11 describes, graphically, the compressive testing result and the buckling behavior experienced by the hollow and solid compressive samples. According to the simulation, the solid specimen behaved differently from the hollow specimen in the sense that the solid specimen did not evidence a significant deformation when loaded under the same conditions of that of the hollow specimen. However, in a physical test scenario, a reduction ΔL , identified as the dimensional change in length referred in Section 5.3.2.1 of this chapter, of more than the original specimen length was observed for the same upper load value.

Table 5. 11 FEA simulation of the solid/hollow specimens’ deformation and stress distribution

	Specimen Deformation	Specimen Stress
Solid		

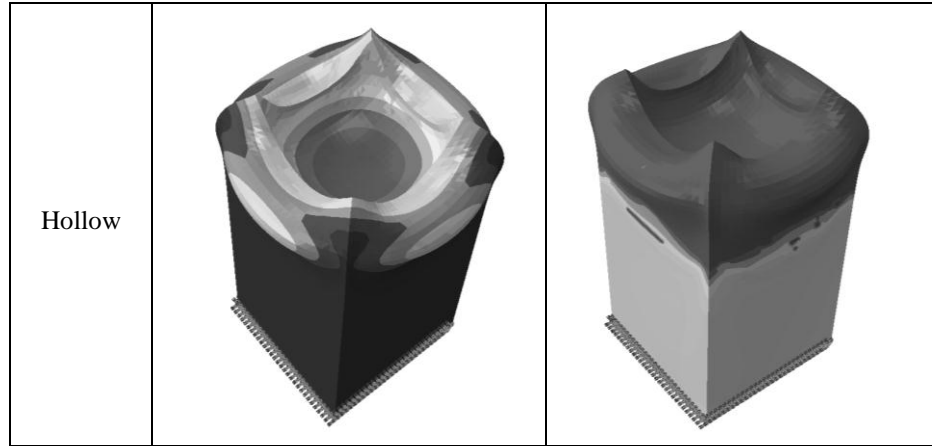


Figure 5.4.10 shows a graph of the compressive load against the displacement of both, loose and compact, orthogonal compressive specimens. There is a considerable difference between the compact and loose specimens from that type. Evidently, the load withstood from this pair of compressive specimens is not comparable to the solid compressive specimen; however, the compact specimen exhibited higher load allowance than the hollow specimen, but the loose specimen exhibited less load allowance than the hollow specimen.

Loose vs Compact Orthogonal Compressive Specimen

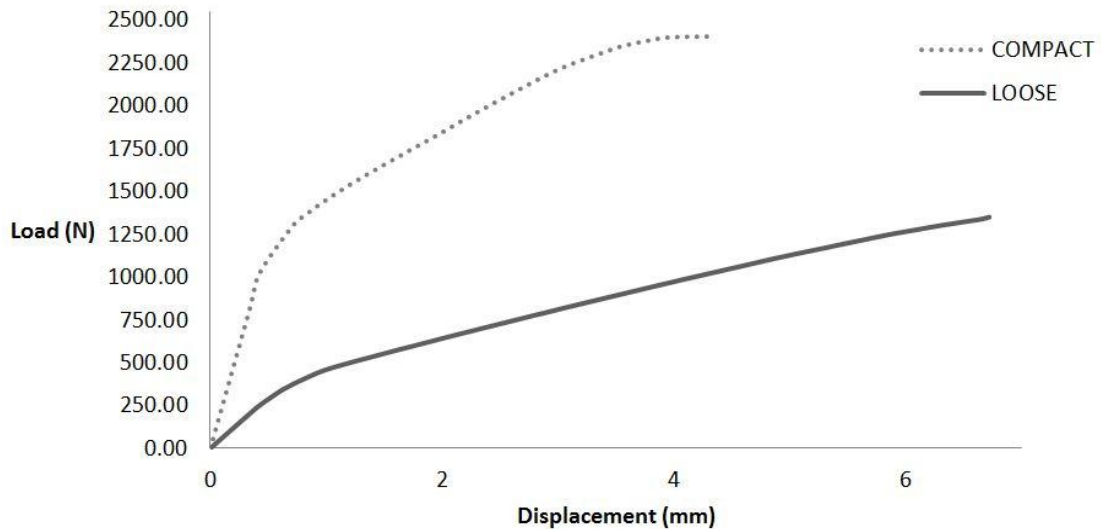


Figure 5.4. 10 Load and displacement diagram for the loose and compact orthogonal compressive specimens

CHAPTER V: CHARACTERIZATION OF THE MECHANICAL BEHAVIOR OF FDM PARTS - EXPERIMENTAL INVESTIGATION

Table 5.12 describes, graphically, the compressive testing result experienced by the orthogonal loose and orthogonal compact compressive samples. Table 5.12 comprises the simulation of the sample deformation and the internal structure stress concentration. As it can be seen from both, the loose and compact orthogonal structures, knurls are formed in the upper ends, respectively.

Table 5. 12 FEA simulation of the loose/compact orthogonal specimens' deformation and stress

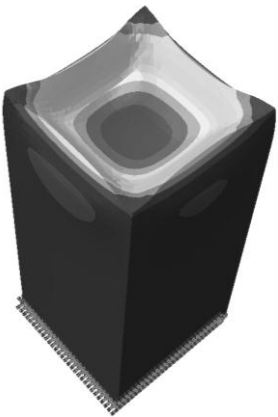
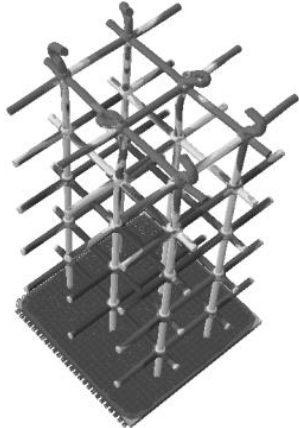
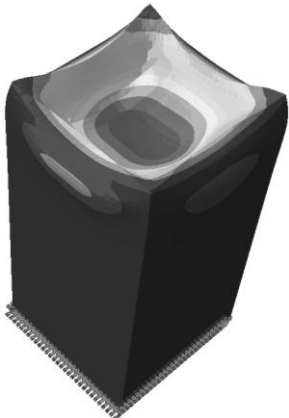
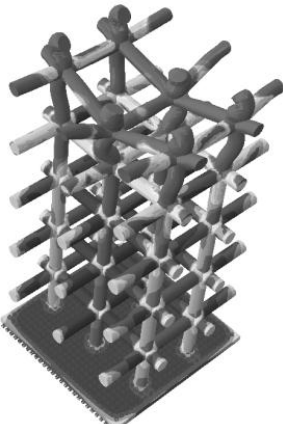
	Specimen Deformation	Specimen's Internal Structure
Loose		
Compact		

Figure 5.4.11 shows a graph of the compressive load against the displacement of both, loose and compact, hexagonal compressive specimens. In this case, there is a slight difference between the pair of loads withstood from one specimen to the other. Evidently, the load withstood from this pair of compressive specimens is much lower than the solid compressive specimen; similarly, both show lower load values compared to that of the hollow compressive specimen.

Loose vs Compact Hexagonal Compressive Specimen

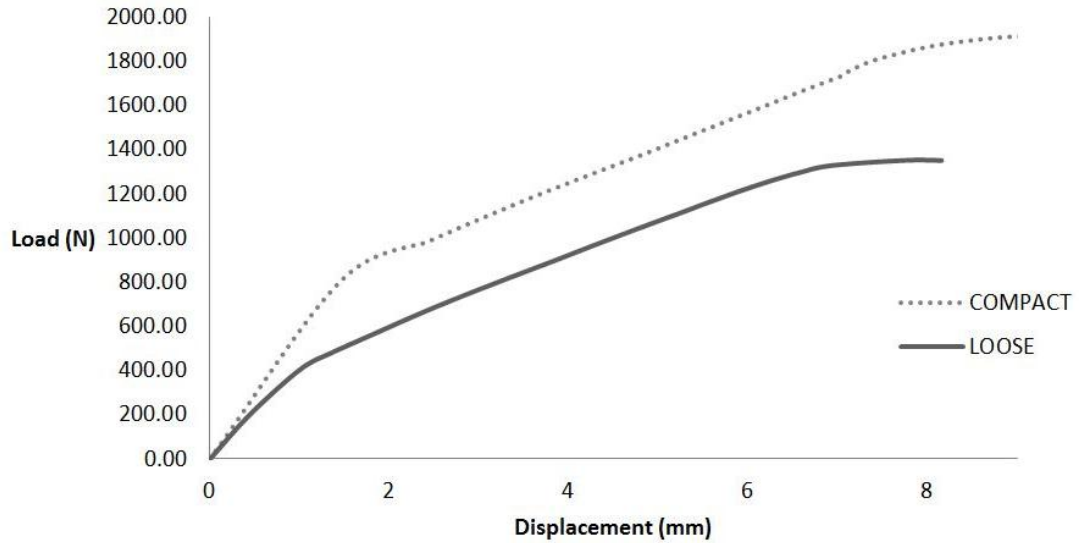

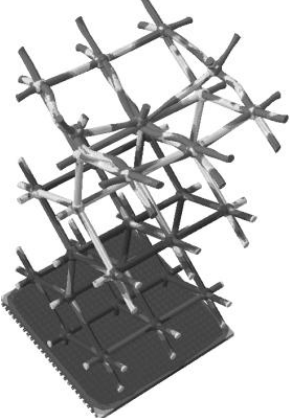


Figure 5.4. 11 Load and displacement diagram for the loose and compact hexagonal compressive specimens

Table 5.13 describes, graphically, the compressive testing result experienced by the hexagonal loose and hexagonal compact compressive samples. Table 5.13 comprises the simulation of the sample deformation and the internal structure stress concentration. As it can be seen from both, the loose and compact orthogonal structures, exhibit a similar structural behavior with no apparent knurls formed in the contacting upper ends, respectively.

Table 5. 13 FEA simulation of the loose/compact hexagonal specimens' deformation and stress

	Specimen Deformation	Specimen's Internal Structure
Loose		

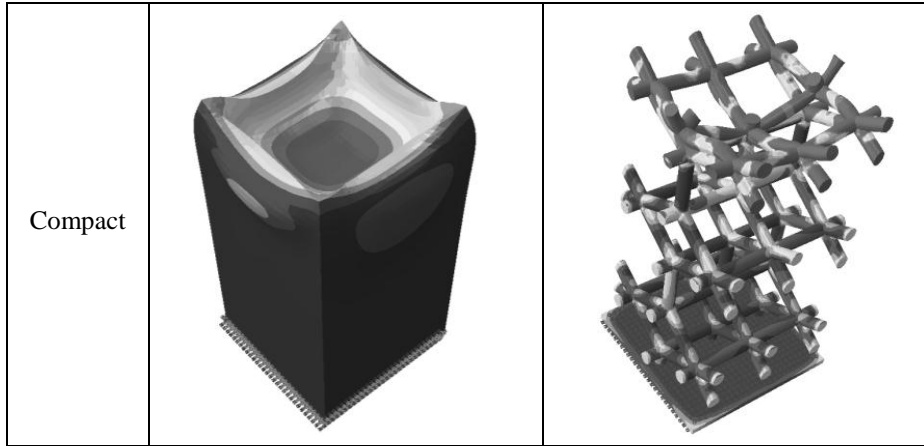


Figure 5.4.12 shows a graph of the compressive load against the displacement of both, loose and compact, pyramid compressive specimens. In this case, there is a considerable difference between the loads withstood from the compact to the loose specimen. Evidently, the load withstood from this pair of compressive specimens is much lower than the solid compressive specimen. The compact pyramid evidenced higher admissible load than the hollow specimen, but the pyramid loose specimen did not.

Loose vs Compact Pyramid Compressive Specimen

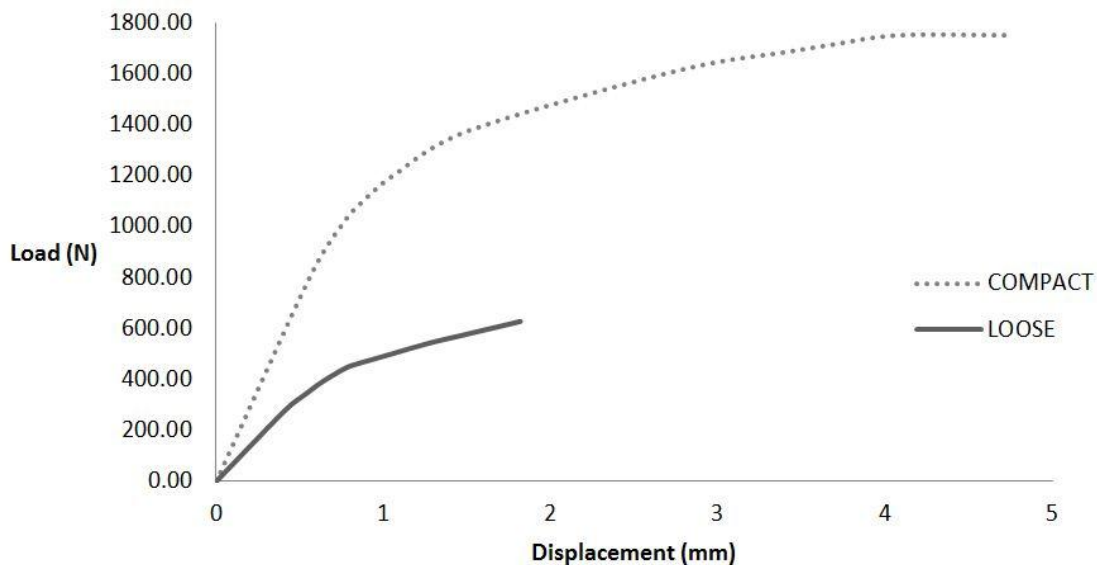


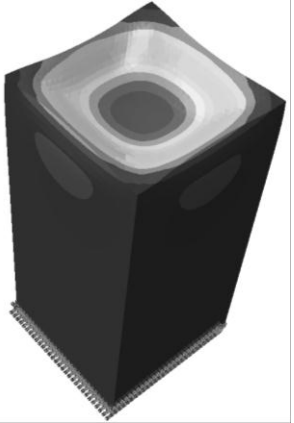

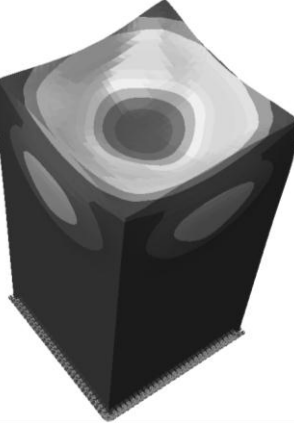
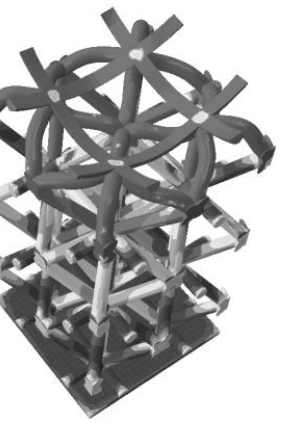
Figure 5.4. 12 Load and displacement diagram for the loose and compact pyramid compressive specimens

Similarly, Table 5.14 describes, graphically, the tensile testing result experienced by the pyramid loose and pyramid compact compressive samples. Table 5.13 shows the simulation of the structural behavior of the pyramid internal structures. Both exhibited a similar behavior with a

CHAPTER V: CHARACTERIZATION OF THE MECHANICAL BEHAVIOR OF FDM PARTS - EXPERIMENTAL INVESTIGATION

deformation in the upper end that, apparently, did not disturb the mid and lower structural zones, respectively.

Table 5. 14 FEA simulation of the loose/compact pyramid specimens' deformation and stress

	Specimen Deformation	Specimen's Internal Structure
Loose		
Compact		

Results from the physical tests showed that the machine failed to add up more load once the compressive specimens were initially broken. In other word, one the compressive machine did not experience any relevant opposite force, the load count stopped. Not in the case of the displacement which was lowering at the designated rate. In the case of the solid compressive specimen, a plastic behavior was observed when physically testing; therefore, a maximum load reading of 19,000 N was chosen to be the top limit.

5.5 ANALYSIS OF VARIANCE FOR THE MECHANICAL PROPERTIES

The following Sections 5.5.1 and 5.5.2 comprise the ANOVA and Regression Analysis performed on the tensile and compressive specimens once the values from the FDM RP and the

CHAPTER V: CHARACTERIZATION OF THE MECHANICAL BEHAVIOR OF FDM PARTS - EXPERIMENTAL INVESTIGATION

physical testing are performed and this is accomplished by using SPSS Statistics® from IBM®. It is important to mention that this section will make reference to the tables and/or formulas comprised in the Appendix of this thesis. Hence, any further reference to the subject matter herein covered should be made directly to such Appendix. The cluster of tables does not follow any particular order. Appendix comprises the ANOVA and Regression models for the tensile and the compressive specimens, respectively. Each of it comprises the load, the model material, the support material, and the time ANOVA and RA for the respective orthogonal/hexagonal/pyramid and the solid/hollow individually and respectively.

In order to understand the results from the ANOVA and the RA, it is important to make reference to Table 5.15 where the abbreviation for the variables involved in both analyses is presented.

Table 5. 15 Variable description and corresponding abbreviation

Variable Description	Variable Abbreviation
Structure Type	St
Raster Angle	Ra
Build Plane	Bp
Internal Density	Id
Load	L
Time	T
Model Material	Mm
Support Material	Sm
Orthogonal	St ₁
Hexagonal	St ₂
Pyramid	St ₃

5.5.1 ANOVA – MECHANICAL PROPERTIES – INTERNAL STRUCTURES

With respect to the mechanical properties, the ANOVA for the load was performed on the tensile and compressive specimens, respectively. Tables A1 and A33 encompass the load data for the tensile and compressive specimens, respectively. The data resulted from the 32 samples for the tensile and 24 for the compressive; each with 3 experiments, respectively. The variables are given a number (Table A2 and A34) in order to perform the ANOVA where Tables A3 and A35 comprise the results from said analysis. Said two tables provide the source factors or variables individually and in combinations, for example: structure type, raster angle, build plane, internal density, structure type and raster angle, raster angle and build plane, etc. Similarly, the tables provide the significance value from said source factors from the tensile and compressive specimens. This significance shows whether the variable is significant or not or if it is

CHAPTER V: CHARACTERIZATION OF THE MECHANICAL
BEHAVIOR OF FDM PARTS - EXPERIMENTAL INVESTIGATION

significantly affecting the response variable. It is important to mention that the level of significance is taken to be as 5% based on previous similar studies. Now then, if the value reflected from said Table A3 and A5 is smaller than 5%, the variable is significant; else, it is not significant.

Significant values from said two tables are: Bp, St.Ra, St.Bp, St.Id, Ra.Bp.Id, and St.Ra.Bp.Id for the tensile and St, Ra, Bp, Id, St.Bp, St.Id, Ra.Id, Ra.Bp, Ra.Id, Bp.Id, St.Ra.Bp, and St.Ra.Bp.Id.

From said tensile analysis, it is conclusive that the structure type (St) is significantly affecting the load when it interacts with other variables and that build plane (Bp) is significant when considered independently, and structure type (St) and build plane (Bp) are significant when considered jointly. From said compressive analysis, it is conclusive that the build plane (Bp) and internal density (Id) are the two most significant variables affecting the load when they interact with other variables together and when they are considered independently.

Once the ANOVA has been accomplished, sufficient elements are gathered in order to proceed to carry out the Regression Analysis. It should be pointed out that the ANOVA estimates the coefficients for different levels of variables, whereas the RA and its regression function combine all the levels; hence, one coefficient for each independent variable is obtained. Therefore, the RA serves to obtain a model equation that relates all the variables involved in both, tension and compression, specimens.

Tables A6 and A36 comprise the variables and the coefficients from all the variables involved in the prediction of the tensile and the compressive load, respectively. The generated equations are shown herein below, namely:

$$\begin{aligned} \text{Load (Tensile)} = & 1405.361 - 12St - 66.583Ra + 201.361Bp + 32.278I + 27St.Ra - 44St.Bp \\ & - 16.792St.Id + 24.417Ra.Bp + 23.111Ra.Id - 10.278Bp.Id - 13.083St.Ra.Bp \\ & - 5.708St.Ra.Id + 7.458St.Bp.Id + 79.889Ra.Bp.Id - 24.042St.Ra.Bp.Id \end{aligned}$$

(Equation 5.4)

$$\begin{aligned} \text{Load (Compressive)} = & 2367.986 - 233.167St - 35.181Ra - 101.292Bp + 292.208Id + 3.750St.Ra \\ & + 17.583St.Bp - 36.958St.Id - 85.069Ra.Bp - 63.958Ra.Id - 33.181Bp.Id \\ & + 27.083St.Ra.Bp + 18.625St.Ra.Id - 4.208St.Bp.Id + 63.264Ra.Bp.Id \\ & - 29.708St.Ra.Bp.Id \end{aligned}$$

(Equation 5.5)

Results from the substitution of the respective limiting values for the corresponding factor level value yields the tension and compression load values, accordingly. Reference to Tables A7 and A39 should be done for substituting variables' values.

5.5.2 ANOVA – MECHANICAL PROPERTIES – SOLID AND HOLLOW

Since the load values from the solid and hollow specimens in both, tension and compression experiments vary extensively; an independent model was performed.

Similarly, with respect to the mechanical properties, the ANOVA for the load was performed on the solid and hollow tensile and compressive specimens, respectively. Table A17 encompasses the load data for the tensile specimens. Table A59 encompasses the deformation data from the compressive specimens. The data resulted from the 32 samples; each with 3 experiments, respectively. The variables are given a number (Table A18 and A49) in order to perform the ANOVA where Table A19 comprises the results from said analysis. Said table provides the source factors or variables individually and in combinations, for example: structure type, raster angle, build plane, internal density, structure type and raster angle, raster angle and build plane, etc. Similarly, the table provides the significance value from said source factors from the tensile and compressive specimens.

Significant values from said table are: St, St.Bp, and Ra.Bp.

From said tensile analysis, it is conclusive that the structure type (St) is significantly affecting the load when it interacts with other variables and that build plane (Bp) is significant when considered with the structure type (St) and the raster angle (Ra).

Now then, for the solid and hollow compressive specimens, a special consideration was made. Since the compressive load could be high enough not to present any interaction with any of the parameters chosen since such may affect the range of the values, instead, deformation was subjected to study. In this case, the ANOVA presented in Table A62 yielded that Ra, Bp, and Ra.Bp are significant values.

Tables A22 and A65 comprise the variables and the coefficients from all the variables involved in the prediction of the tensile load and the compressive deformation, respectively. The generated equations are shown herein below, namely:

CHAPTER V: CHARACTERIZATION OF THE MECHANICAL BEHAVIOR OF FDM PARTS - EXPERIMENTAL INVESTIGATION

$$\begin{aligned} \text{Load(Tensile)} = & 2274.708 + 585.208St - 22.458Ra + 29.292Bp - 16.292St.Ra - 157.542St.Bp \\ & - 66.208Ra.Bp - 7.042St.Ra.Bp \end{aligned}$$

(Equation 5.6)

$$\text{Deformation(Compressive)} = 145.282 + 6.095Ra - 8.682Bp - 4.372Ra.Bp$$

(Equation 5.7)

Results from the substitution of the respective limiting values for the corresponding factor level value yields the tension load and the compression deformation values, accordingly. Reference to Tables A18 and A49 should be done for substituting variables' values.

Similarly as carried out in Chapter IV, a simplified approach was performed once the main or most relevant parameters were chosen. This simplified versions of the equations herein presented will serve as a hands-on tool in order to obtain the load values for all the types of specimens and all the types of structures with the variety of internal densities and particular location in the building envelope. These results are presented in Table 6.5 in Chapter VI of this thesis.

5.6 CASE STUDY: PLASTIC BOTTLE BLOW MOLD

In order to validate the merit of the present approach, it is necessary to provide a real case scenario situation where the novel method of including an inner structure benefits the overall total build time while reducing tooling expenses. For this reason, a blow molding application was selected in order to evaluate the effect of the incorporation of internal parametric structures into a hollowed component without affecting the intrinsic part rigidity with the aim of reducing the material use.

5.6.1 INTRODUCTION

Blow molding is a manufacturing process that makes hollow plastic parts such as beverage containers used for the high volume production of soda bottles and milk jugs. These types of containers evolve very rapidly and need to be manufactured accordingly; unfortunately, the current prototype development process continues to be slow and costly. Therefore, replacing machined tooling with FDM molds will provide quality blow molded prototypes that could be made in few days. These parts offer proof of design and validation of manufacturing parameters.

In this sense, blow molding is a process in which air pressure inflates heated plastic in a mold cavity. It is used for the production of hollow plastic parts with thin walls, such as beverage bottles. Since molding pressures are much lower than those for injection molding, blow molding is also ideal for large plastic tubs and containers.

5.6.2 DESIGN PROCESS

It is said that the design of blow molds and the specification of process parameters combine science, art, and skill. A small change in the pinch-off or vent design, or a slight change to die temperature or blow pressure, can dramatically affect the molding results. To validate these parameters and accelerate design approval, prototype tooling is needed. However, machined prototype tooling is both costly and time consuming.

When FDM is used to construct blow molds, the lead-time for prototype parts is reduced from weeks to some days. In addition, the cost for RP manufacturing is comparability less than that of machined tools. According to Sciortino [Sciortino, 2007], FDM tooling will cost one-third to one-half that of a prototype aluminum tool. The FDM process is unique in its use of thermoplastics, and it is this feature that provides the benefits of rapid tooling for blow molding. Polycarbonate, which is one of the FDM materials, can withstand both the temperature and pressure of blow molding.

Figure 5.6.1 describes the design process that led to the fabrication of a blow mold with internal parametric we-like structures. The process starts with a new bottle design (a) - made out of Polyethylene terephthalate (PET) - that is going to the marketed shortly and a group of engineers need to perform a number of tests to the bottle. Hence, an inexpensive and fast way to obtain a vast number of bottles is to develop a blow mold. Once the bottle has been designed, the next step is to create a solid mold model as depicted in Figure 5.6.1 (b). The (c) modified blow mold is obtained by incorporating the internal structures (orthogonal type) as previously described in the procedure of Chapter IV, Section 4.1.1: Methodology. The final step is to export the generated CAD model into the STL format for rapid prototyping. The (d) RP software model is obtained when the RP software slices the 3D model (as described in Section 1.1.4 of Chapter I) and yields the total amount of support material, build material, and time as described in the next section of this chapter.

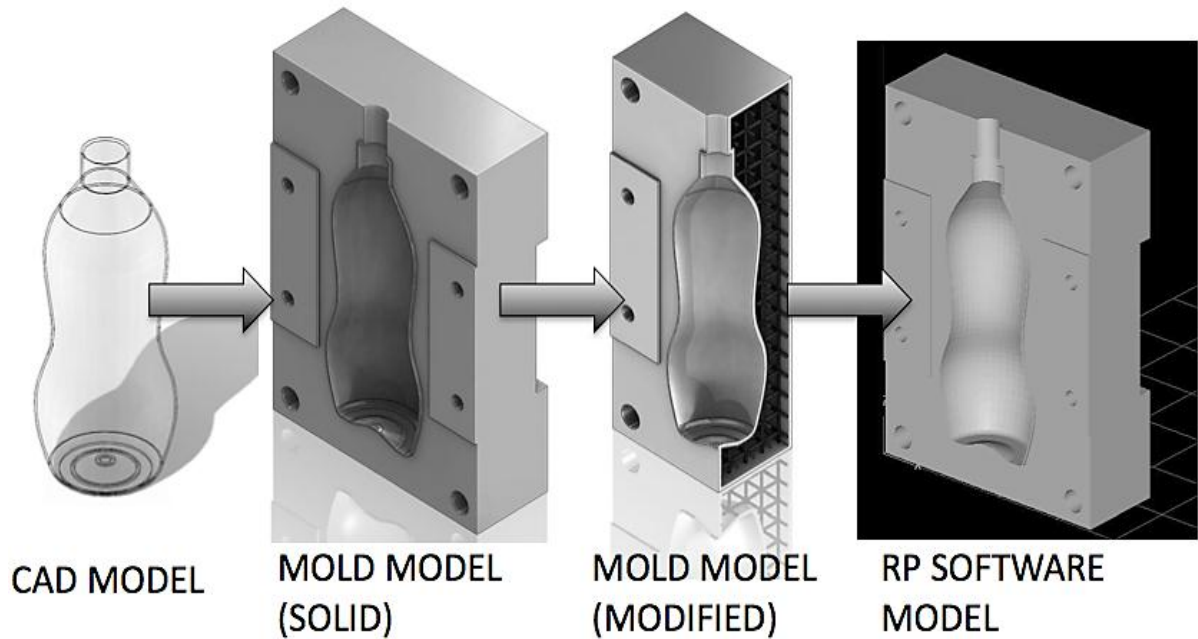


Figure 5.6. 1 Plastic bottle blow mold design process

5.6.3 RESULTS

With FDM blow molds, prototype bottles and containers are produced quickly and affordably. The near-production quality of the molded parts expedites product and process analysis and customer design approval. Unlike other prototype tooling methods, FDM requires only minor modifications to standard tool design and molding parameters. Thus, any prototype blow-molding project can use FDM tools without radical changes to conventional practices. Shop efficiency is maximized with the simple, unattended operation of an FDM machine.

Table 5.16 presents the values for the material, material support, and the build time for a blow mold under the specified specifications described in Figure 5.6.2 (a) and (b). It should be noted that the part represents a real size blow mold; however, a bigger blow mold size is also possible. This capability is subjected to the size restriction of the build chamber. In this case the FDM Stratasys® FORTUS 400mc®, the build chamber is 16 x 14 x 16 in.

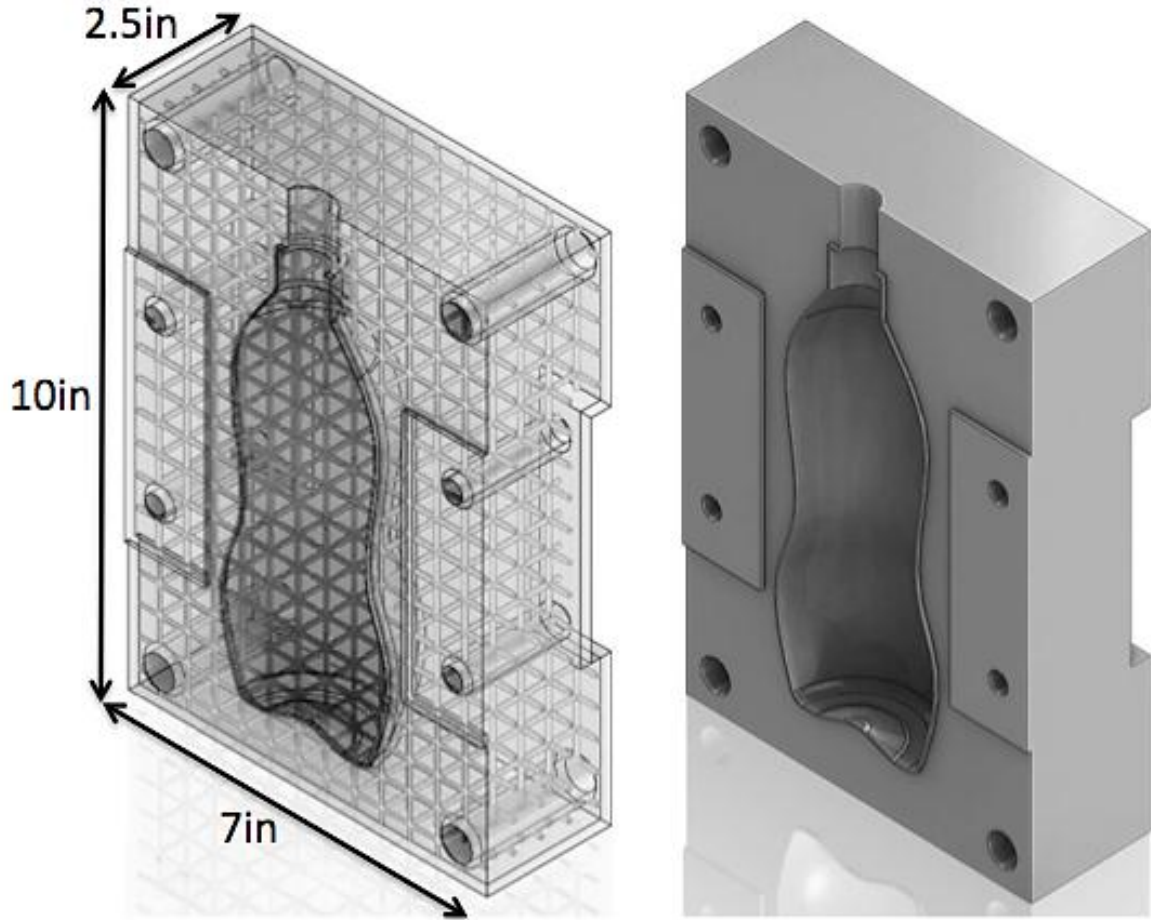


Figure 5.6. 2 Internally enhanced hollowed blow mold half and solid blow mold half

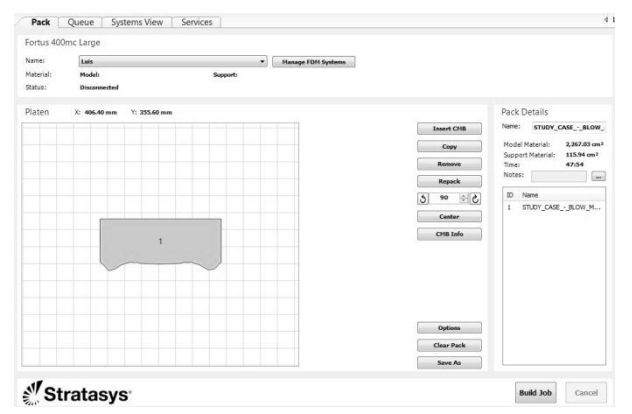
Table 5.16 compares the parts as described in Figure 5.6.2 (a) and (b), where (a) corresponds to the internally modified hollow blow mold and (b) corresponds to the solid blow mold.

Now then, it is evident the significance difference from one blow mold to the other in terms of model material since the solid blow mold allocates 4.25 times more material than the hollow (structure-wise modified) blow mold. In terms of support material, the gain of support material of the modified blow mold with respect to the solid blow mold was about 3.7 times. Lastly, the time addition of the modified hollow blow mold compared to the solid blow mold was just about 7% more.

It should be addressed that the RP was performed at full scale using the same parameters for both blow mold such as: raster angle, part build orientation, layer thickness, support layer thickness, and other parameters.

CHAPTER V: CHARACTERIZATION OF THE MECHANICAL BEHAVIOR OF FDM PARTS - EXPERIMENTAL INVESTIGATION

Table 5. 16 Comparison between the internally enhanced blow mold half and the solid blow mold half

Blow Mold Type	Model Material (cm³)	Support Material (cm³)	Build Time (hr:min)	Schematic
(a)	536.96	432.26	52:34	
(b)	2,267.03	120.94	49:54	

Finally, neglecting the price for the modeling bases for ABS-M30 (as described by the manufacturer), Table 5.17 encompasses the potential expenditures if these two blow mold halves were to be RP in the FDM Stratasys® FORTUS 400mc®. As it can be seen, there is a slight price reduction when utilizing the modified blow mold approach. However, it should be taken into consideration that the internal packing of the orthogonal matrix structure was chosen as dense. Therefore, if a looser internal matrix structure is chosen, the potential savings may be increased.

Table 5. 17 Potential savings when adopting the internally modified blow mold

Blow Mold Type	Material (cm³)	Unit Price of Model Material (ABS-M30) in USD	Unit Price of Support Material (ABS-M30) in USD	Hourly Rate of RP Machine in USD	Total Price in USD
(a)	Model → 536.96	Canisters of 1,512.52 cm³ each		\$75.00	Model=\$131 Material=\$91 Time=\$3900 \$ 4,122.00
	Support → 432.26 Hours → 52.34				
(b)	Model → 2,267.03 Support → 120.94 Hours → 49.52	\$370.00	\$320.00		Model=\$554 Material=\$25 Time=\$3675 \$ 4,254.00

CHAPTER VI

DISCUSSION

6.1 DISCUSSION AND COMPARISON

Section 6.1 includes the overall results from the present study and is divided into four main parts. The first part summarizes the findings gathered from the FDM RP process for both tensile and compressive specimens. The second part discloses the findings observed from the physical experiments performed to the modeled tensile and compressive specimens. The third part encompasses the results from the FEA simulations for both, tensile and compressive, specimens. It also comprises the range of the data gathered from the tensile and compressive physical experiments and a comparison with the FEA results. The fourth and final part compares all the results from parts one to three and provides a general and specific discussion on the validity of the FEA model that gives an answer to the thesis statement of the present study.

Section 6.2 presents the statistical refinement arose from the Analysis of Variance (ANOVA) that yields a simplification from the model presented in the Regression Analysis (RA) comprised in Section 4.5 of Chapter IV for the material, support material, and build time and in Section 5.5 of Chapter V for the mechanical properties (allowed load) for the tensile and compressive specimens, respectively.

6.1.1 FDM RP RESULTS

In order to better understand the results presented in this and in the following sections, it is convenient to present Table 6.1. Said Table 6.1 comprises the full description of each of the experiments in a convenient manner. It should be noted that the following Table 6.1 applies for both, the tensile and compressive, specimens.

Table 6.1 Experiment number and complete description for tensile and compressive specimens

Exp. No.	Description	Exp. No.	Description
1	Orthogonal, -45/45, XY, Loose	17	Pyramid, -45/45, XY, Loose
2	Orthogonal, -45/45, XY, Compact	18	Pyramid, -45/45, XY, Compact
3	Orthogonal, -45/45, YZ, Loose	19	Pyramid, -45/45, YZ, Loose
4	Orthogonal, -45/45, YZ, Compact	20	Pyramid, -45/45, YZ, Compact
5	Orthogonal, 0/90, XY, Loose	21	Pyramid, 0/90, XY, Loose
6	Orthogonal, 0/90, XY, Compact	22	Pyramid, 0/90, XY, Compact
7	Orthogonal, 0/90, YZ, Loose	23	Pyramid, 0/90, YZ, Loose
8	Orthogonal, 0/90, YZ, Compact	24	Pyramid, 0/90, YZ, Compact
9	Hexagonal, -45/45, XY, Loose	25	Solid, -45/45, XY
10	Hexagonal, -45/45, XY, Compact	26	Solid, -45/45, YZ
11	Hexagonal, -45/45, YZ, Loose	27	Solid, 0/90, XY
12	Hexagonal, -45/45, YZ, Compact	28	Solid, 0/90, YZ
13	Hexagonal, 0/90, XY, Loose	29	Hollow, -45/45, XY
14	Hexagonal, 0/90, XY, Compact	30	Hollow, -45/45, YZ
15	Hexagonal, 0/90, YZ, Loose	31	Hollow, 0/90, XY
16	Hexagonal, 0/90, YZ, Compact	32	Hollow, 0/90, YZ

Results from the FDM RP are described by the graphs of Figures 6.1.1 and Figures 6.1.2 for the tensile and compressive specimens, respectively. Figure 6.1.1 depicts a graph that relates the model and support material with the build time for the tensile experiments 1 to 32. Evidently, specimens 25, 26, 27, and 28 consume more model material (more than 15cm^3) and less support material (less than 2cm^3) and utilize less build time (no more than 0.5 hours). Conversely, specimens 29, 30, 31, and 32 consume less model material (less than 8.5cm^3) and more support material (less than 6.5cm^3) and utilize more build time (no more than 0.68 hours).

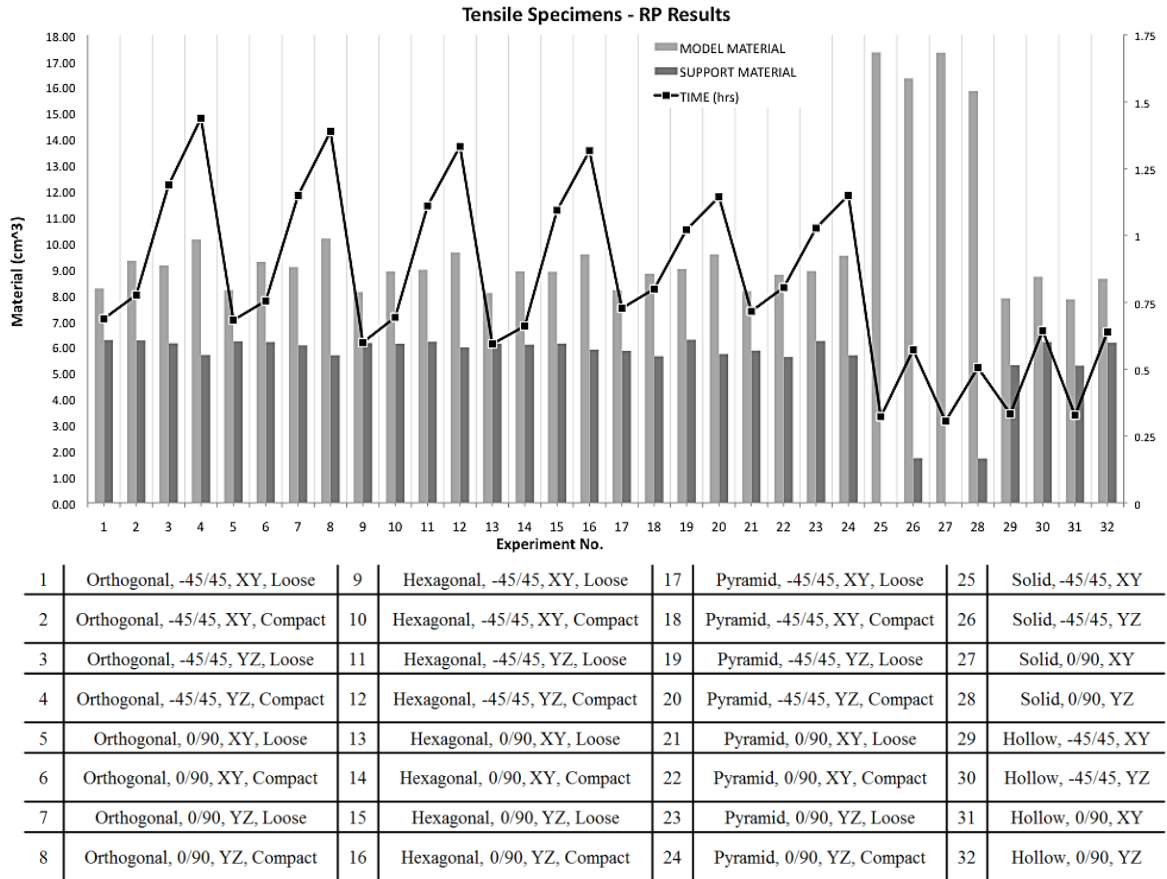


Figure 6.1.1: Material use results for the tensile specimens

Figure 6.1.2 depicts a graph that relates the model and support material with the build time for the compressive experiments 1 to 32. Evidently, specimens 25, 26, 27, and 28 consume more model material (more than 5.5cm^3) and less support material (less than 0.5cm^3) and utilize less build time (no more than .5 hours). Conversely, specimens 29, 30, 31, and 32 consume less model material (less than 2.85cm^3) and more support material (less than 3.5cm^3) and utilize more build time (no more than 0.5 hours).

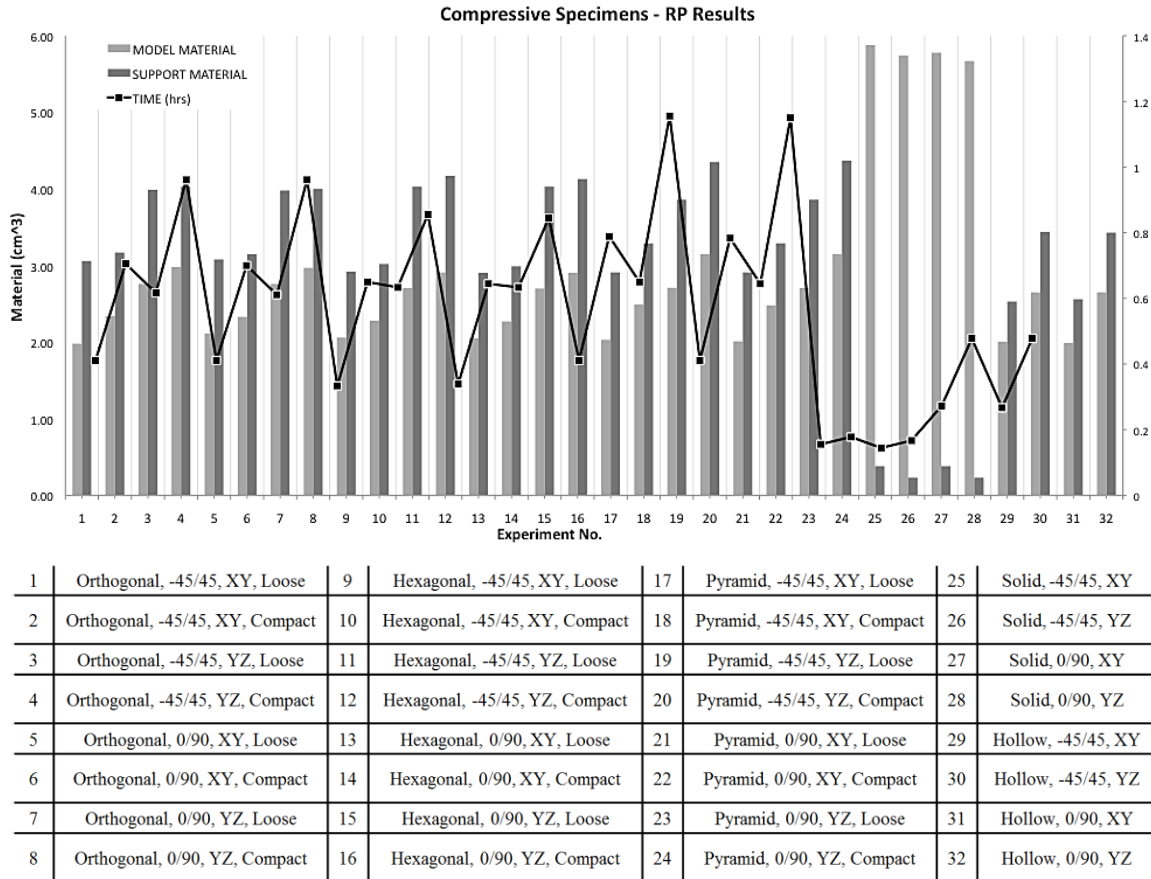
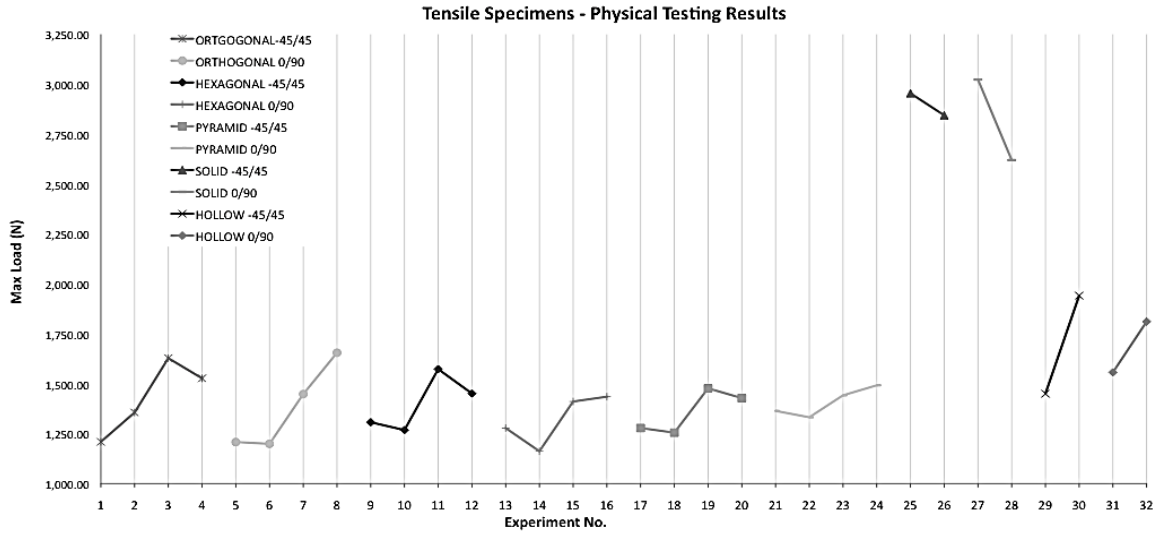


Figure 6.1.2: Material use results for the compressive specimens

6.1.2 PHYSICAL TESTING RESULTS

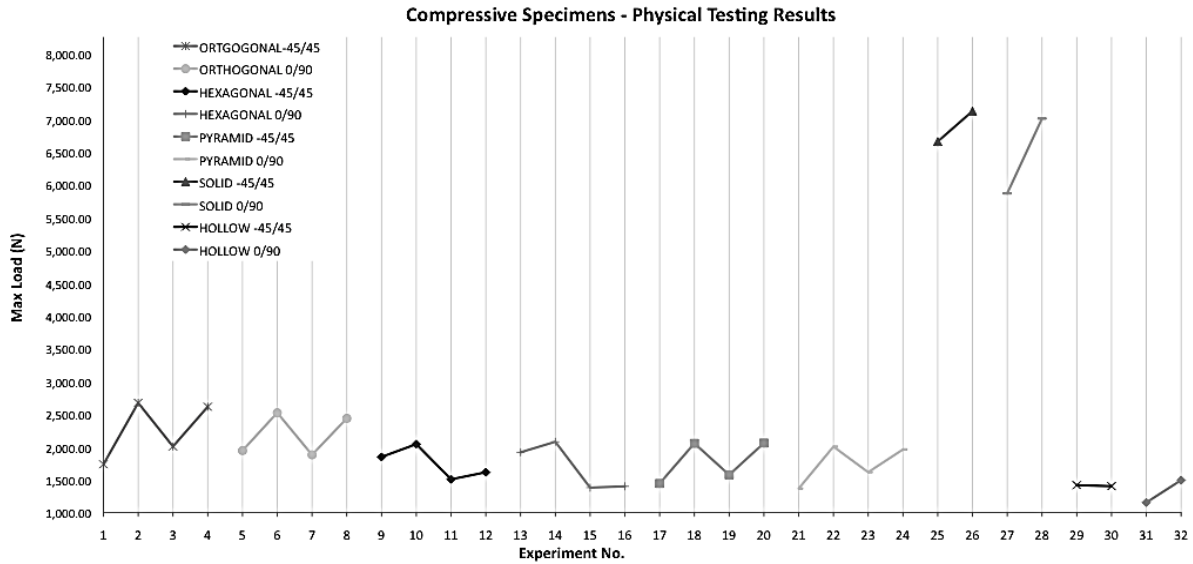
Results from the tensile tests are described by the graphs of Figures 6.1.3 and Figures 6.1.4 for the tensile and compressive specimens, respectively. Figure 6.1.3 depicts a graph that displays the maximum tensile load upon the type of structure inside the specimen for the tensile experiments 1 to 32. Evidently, specimens 25, 26, 27, and 28 allow more tensile load (ranges vary from 2,750 N to 3,000 N approximately). Surprisingly, specimens 29, 30, 31, and 32 allow more tensile load (ranges vary from 1, 500 N to 2,000 N approximately) than other tensile specimens with internal structures.



1	Orthogonal, -45/45, XY, Loose	9	Hexagonal, -45/45, XY, Loose	17	Pyramid, -45/45, XY, Loose	25	Solid, -45/45, XY
2	Orthogonal, -45/45, XY, Compact	10	Hexagonal, -45/45, XY, Compact	18	Pyramid, -45/45, XY, Compact	26	Solid, -45/45, YZ
3	Orthogonal, -45/45, YZ, Loose	11	Hexagonal, -45/45, YZ, Loose	19	Pyramid, -45/45, YZ, Loose	27	Solid, 0/90, XY
4	Orthogonal, -45/45, YZ, Compact	12	Hexagonal, -45/45, YZ, Compact	20	Pyramid, -45/45, YZ, Compact	28	Solid, 0/90, YZ
5	Orthogonal, 0/90, XY, Loose	13	Hexagonal, 0/90, XY, Loose	21	Pyramid, 0/90, XY, Loose	29	Hollow, -45/45, XY
6	Orthogonal, 0/90, XY, Compact	14	Hexagonal, 0/90, XY, Compact	22	Pyramid, 0/90, XY, Compact	30	Hollow, -45/45, YZ
7	Orthogonal, 0/90, YZ, Loose	15	Hexagonal, 0/90, YZ, Loose	23	Pyramid, 0/90, YZ, Loose	31	Hollow, 0/90, XY
8	Orthogonal, 0/90, YZ, Compact	16	Hexagonal, 0/90, YZ, Compact	24	Pyramid, 0/90, YZ, Compact	32	Hollow, 0/90, YZ

Figure 6.1.3: Maximum load results for the tensile specimens

Figure 6.1.4 depicts a graph that displays the maximum compressive load upon the type of structure inside the specimen for the compressive experiments 1 to 32. Evidently, specimens 25, 26, 27, and 28 allow more compressive load (ranges vary from 6,000 N to 7,000 N approximately). As expected, specimens 29, 30, 31, and 32 exhibited less compressive load (ranges vary from 1, 100 N to 1,500 N approximately) than other compressive specimens with internal structures.



1	Orthogonal, -45/45, XY, Loose	9	Hexagonal, -45/45, XY, Loose	17	Pyramid, -45/45, XY, Loose	25	Solid, -45/45, XY
2	Orthogonal, -45/45, XY, Compact	10	Hexagonal, -45/45, XY, Compact	18	Pyramid, -45/45, XY, Compact	26	Solid, -45/45, YZ
3	Orthogonal, -45/45, YZ, Loose	11	Hexagonal, -45/45, YZ, Loose	19	Pyramid, -45/45, YZ, Loose	27	Solid, 0/90, XY
4	Orthogonal, -45/45, YZ, Compact	12	Hexagonal, -45/45, YZ, Compact	20	Pyramid, -45/45, YZ, Compact	28	Solid, 0/90, YZ
5	Orthogonal, 0/90, XY, Loose	13	Hexagonal, 0/90, XY, Loose	21	Pyramid, 0/90, XY, Loose	29	Hollow, -45/45, XY
6	Orthogonal, 0/90, XY, Compact	14	Hexagonal, 0/90, XY, Compact	22	Pyramid, 0/90, XY, Compact	30	Hollow, -45/45, YZ
7	Orthogonal, 0/90, YZ, Loose	15	Hexagonal, 0/90, YZ, Loose	23	Pyramid, 0/90, YZ, Loose	31	Hollow, 0/90, XY
8	Orthogonal, 0/90, YZ, Compact	16	Hexagonal, 0/90, YZ, Compact	24	Pyramid, 0/90, YZ, Compact	32	Hollow, 0/90, YZ

Figure 6.1.4: Maximum load results for the compressive specimens

6.1.3 FEA SIMULATION RESULTS

Results from the FEA simulations are described by the graphs of Figures 6.1.5 to Figures 6.1.8 for the tensile and compressive specimens, respectively. Figure 6.1.5 depicts a graph that displays the behavior of the tensile specimen for the solid, hollow, orthogonal compact, orthogonal loose, hexagonal compact and hexagonal loose specimens. As it can be seen, the solid specimen describes the higher load while the hollow specimen describes the lower load allowance. Now then, it is important to mention that, for all the specimens, the displacement range, when the tensile load reaches its maximum, varies from 1.25 to 1.65 mm. These results indicate that for the loading rate utilized in the present research, the tensile specimens may behave in a brittle manner. The overall behavior of the aforementioned graph concurs with the behavior of the stress-strain graphs referred before by the literature presented in this thesis.

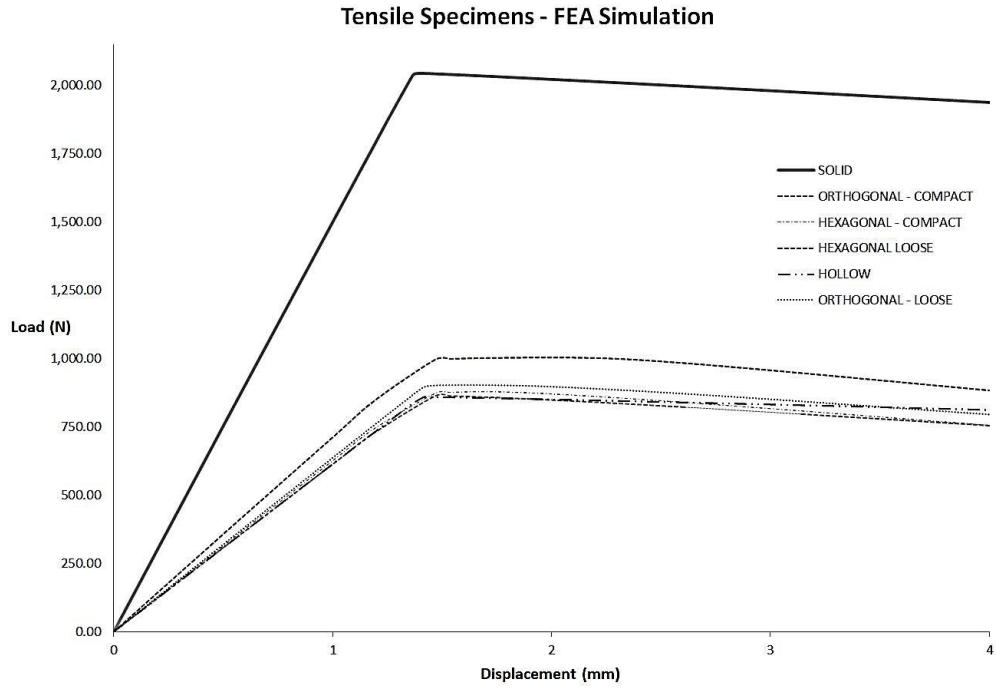


Figure 6.1.5: Mechanical behavior of the tensile specimens from the FEA simulation

Figure 6.1.6 shows the tensile specimens with a lower tensile load allowance. All the specimens tend to behave in a similar way; however, the orthogonal compact specimen exhibited a higher load allowance of 1,000 N approximately, while the orthogonal loose specimen exhibited the second higher load allowance (900N).

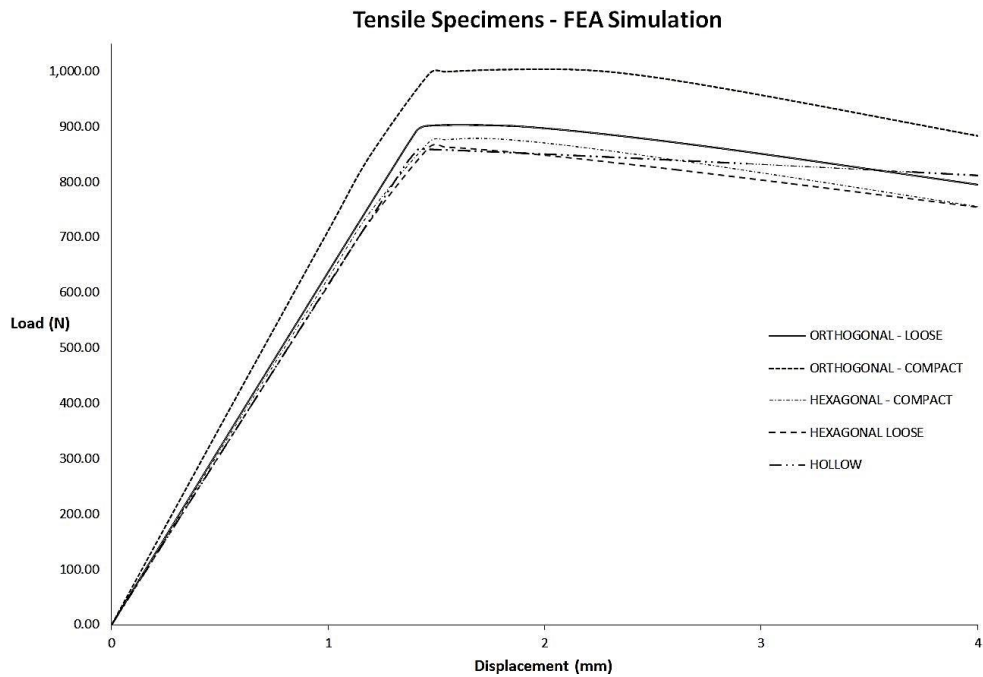


Figure 6.1.6: Detail of the behavior of specific tensile specimens from the FEA simulation

Figure 6.1.7 depicts a graph that displays the behavior of the compressive specimen for the solid, hollow, orthogonal compact, orthogonal loose, hexagonal compact, orthogonal loose, pyramid compact, and pyramid loose specimens. As it can be seen, the solid specimen describes the higher load while the pyramid compact specimen describes the lower load allowance. Now then, it is important to mention that, except for the solid specimen, the displacement range, when the compressive load reaches its maximum (2,500N), varies from 4 to 8 mm. These results indicate that for the loading rate utilized in the present research, the compressive specimens may behave in a perfectly plastic manner, but the solid specimen which maximum deformation was about 0.5mm with a load of more than 20,000N. The overall behavior of the aforementioned graph concurs with the behavior of the stress-strain graphs referred before by the literature presented in this thesis.

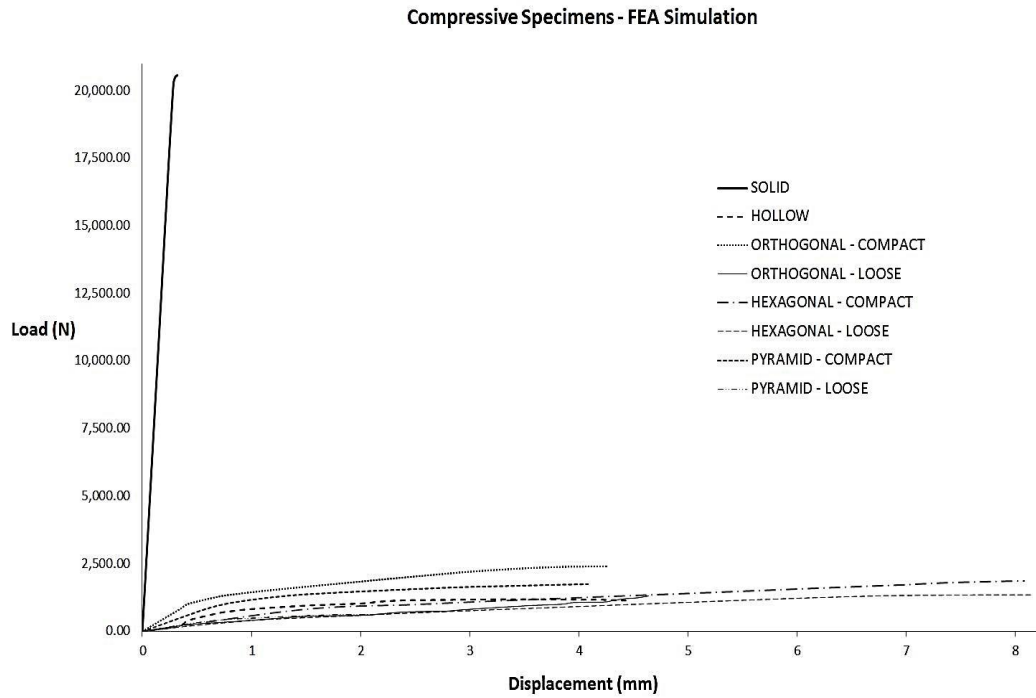


Figure 6.1.7: Mechanical behavior of the compressive specimens from the FEA simulation

Figure 6.1.8 shows the compressive specimens with a lower compressive load allowance. All the specimens tend to behave in a similar way; however, the orthogonal compact specimen exhibited a higher load allowance of 2,350N approximately, while the pyramid compact specimen exhibited the second higher load allowance of approximately 1,600N. Now then, all the other samples with a loose mode internal structure such as: orthogonal, hexagonal, and pyramid exhibited the lower compressive load allowance. Surprisingly, the hollow specimen was not ranked as the lowest load allowance type of specimen based on the FEA results.

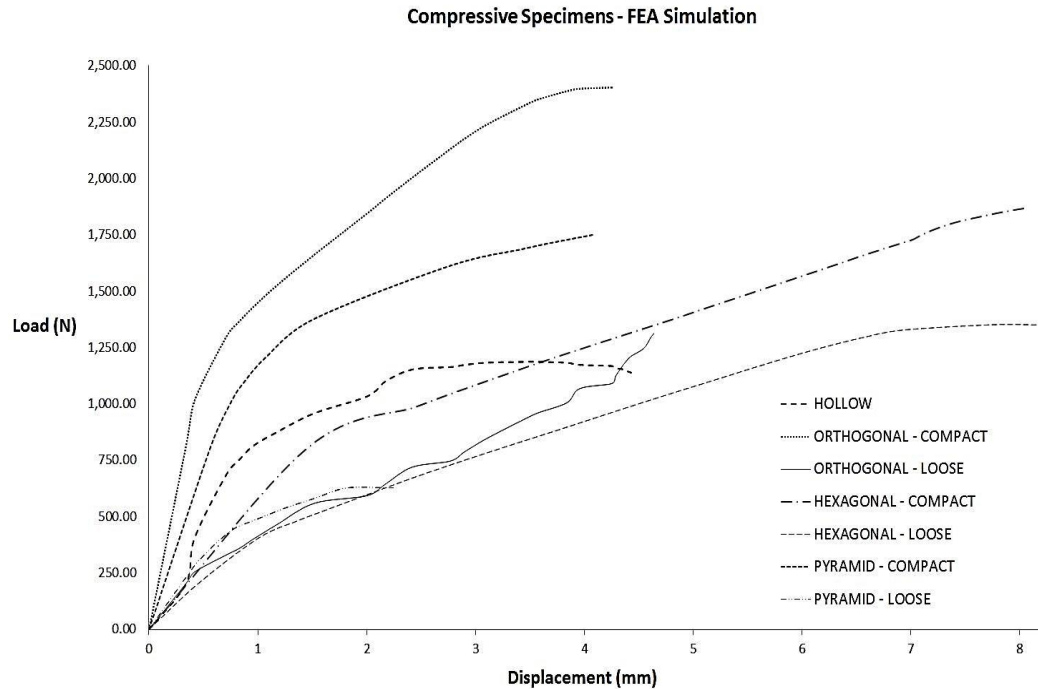


Figure 6.1.8: Detail of the behavior of specific compressive specimens from the FEA simulation

6.1.4 COMPARISON OF RESULTS

The following comprises comparisons between different types of experiments, in example: FEA and physical and RP and physical. These comparisons serve to provide a better understanding of the interactions between what was expected in a virtual environment and what was obtained in a physical scenario.

Firstly, Figures 6.1.9 and 6.1.10 describe the similitude between the FEA and the physical testing results for the tension and compression specimens, respectively. Values from the FEA simulation were picked as the deformation approached the rupture value of the experimental tensile specimens for each of the structure cases. Similarly, FEA simulation values were selected as the deformation approached the maximum allowable value from the universal testing machine for each of the structure cases. As shown in Figure 6.1.9, the behavior of the average of the 3 repetitions of tensile samples for the physical testing is very similar to the behavior of the FEA simulation for the same type of samples. The difference in the range values as depicted in Figure 6.1.11 resides in the internal topography of the sample itself. That is to say, the FEA simulation did not consider the effect of the support material or the effect of the interaction between the model material and the support material at the interface level. Other factors such as the control of

the loading rate when physically testing the part and the assumption of a linear elastic material in the FEA model may have shifted the FEA values lower. Similarly, Figure 6.1.10 depicts the behavior of the average of the 3 repetition of compressive samples for the physical testing and FEA simulations for the specific sample type. In this case, the range values of the physical experiments fail within the values of the FEA simulation as depicted in Figure 6.1.12. This result indicates that for compression only, the FEA simulation is accurate and truly represents the physical experiments performed to the compressive samples when all the FEA emulate the experimental testing conditions.

Therefore, it can be concluded that for both experiments, tensile and compressive, the FEA simulation represents fairly accurate the physical behavior of both sets of experiments. For this reason, it can be assumed that the FEA simulation will provide a reliable estimation of the tensile and compressive loads and respective deformation for parts with similar characteristics as the ones simulated in this CAE software. Nevertheless, further studies that better represent the tensile specimen experimental testing are desired.

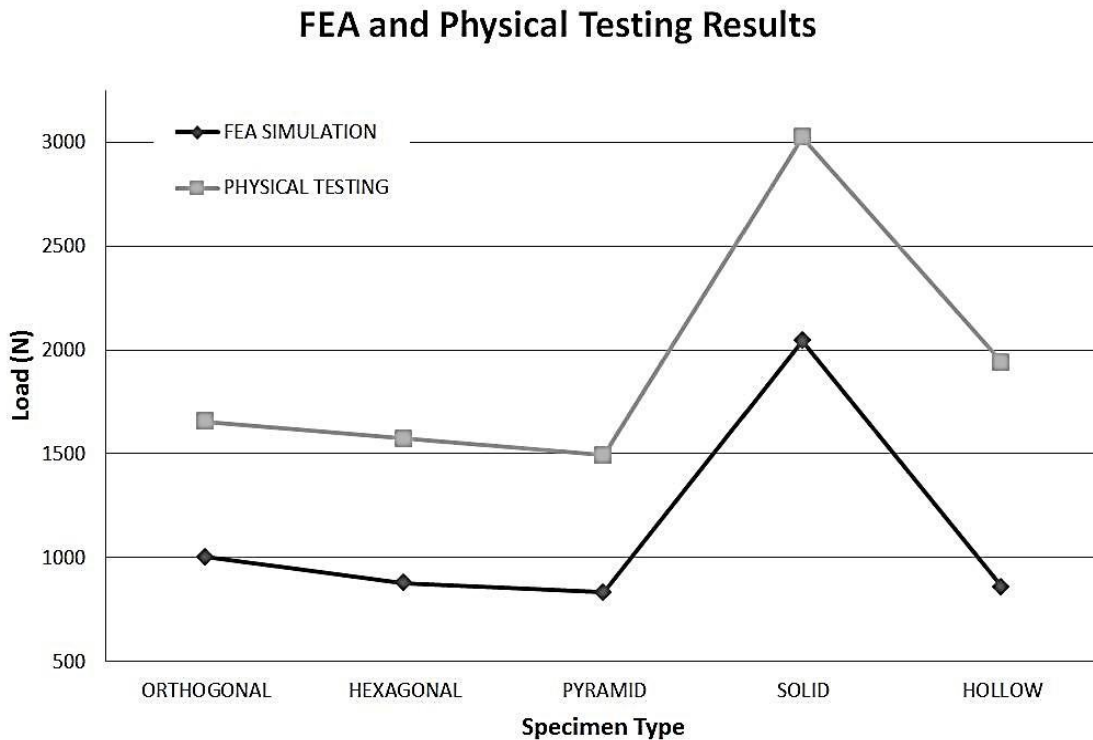


Figure 6.1.9: Similitude between the FEA and physical tensile testing

FEA and Physical Testing Results

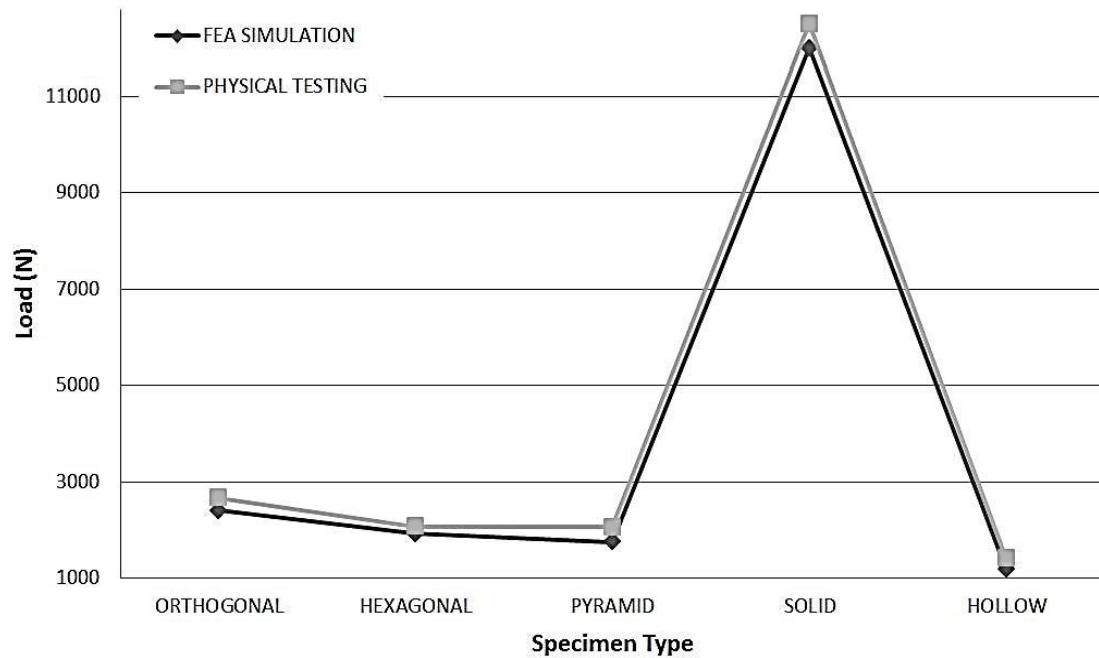
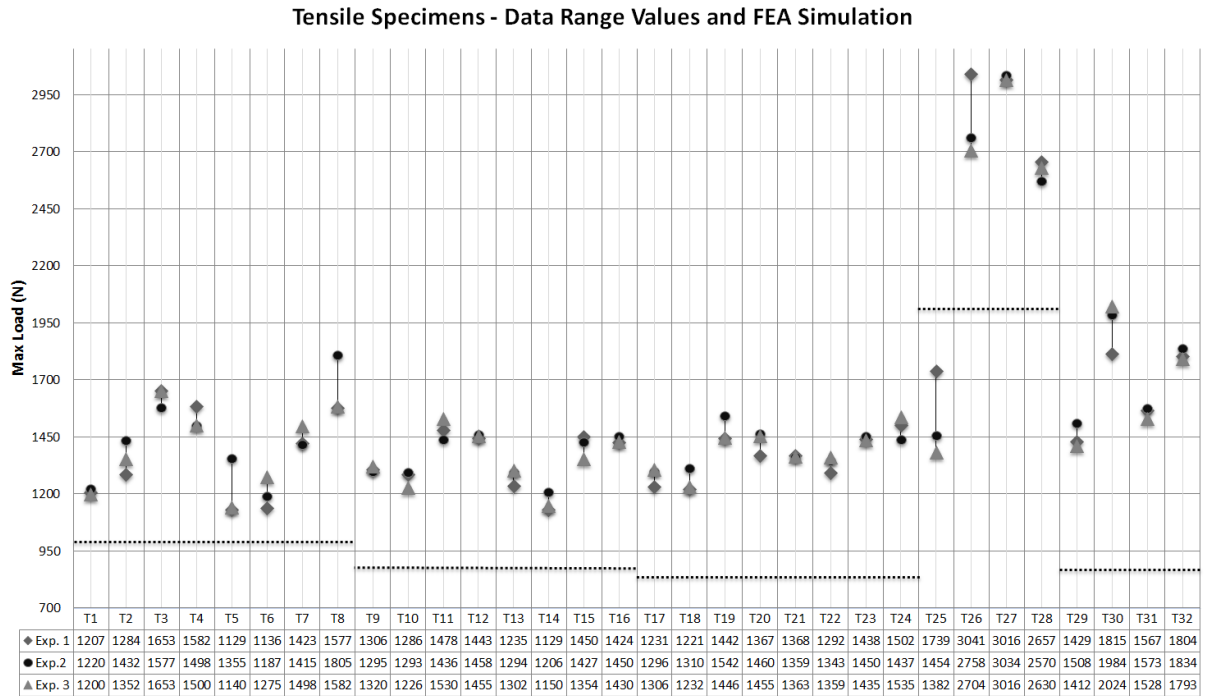


Figure 6.1.10: Similitude between the FEA and physical compressive testing

Figure 6.1.11 shows the values of all the tensile samples tested in the testing machine. As it can be seen, the ranges within the sample type are very coherent. There are no appreciable differences from the high and low value. Tensile specimens 5, 8, 25, 26, and 30 exhibit the greatest differences, however, the difference in values vary from 200 to 300 N; else, the range difference is negligible. Hence, it can be said that there is no indication that more than one repetition is needed in order to obtain reasonable results. Similarly, Figure 6.1.11 depicts 4 dotted lines embedded within the chart area. Those dotted lines represent the value of the FEA simulation for the same deformation. It should be addressed that parameters such as build plane orientation and raster angle were not considered in the FEA simulation. It is evident that the effects of such parameters are not reflected in Figure 6.1.11. However, a further exploration into the FEA simulation techniques may bring a closer approximation of such parameters in a later research.



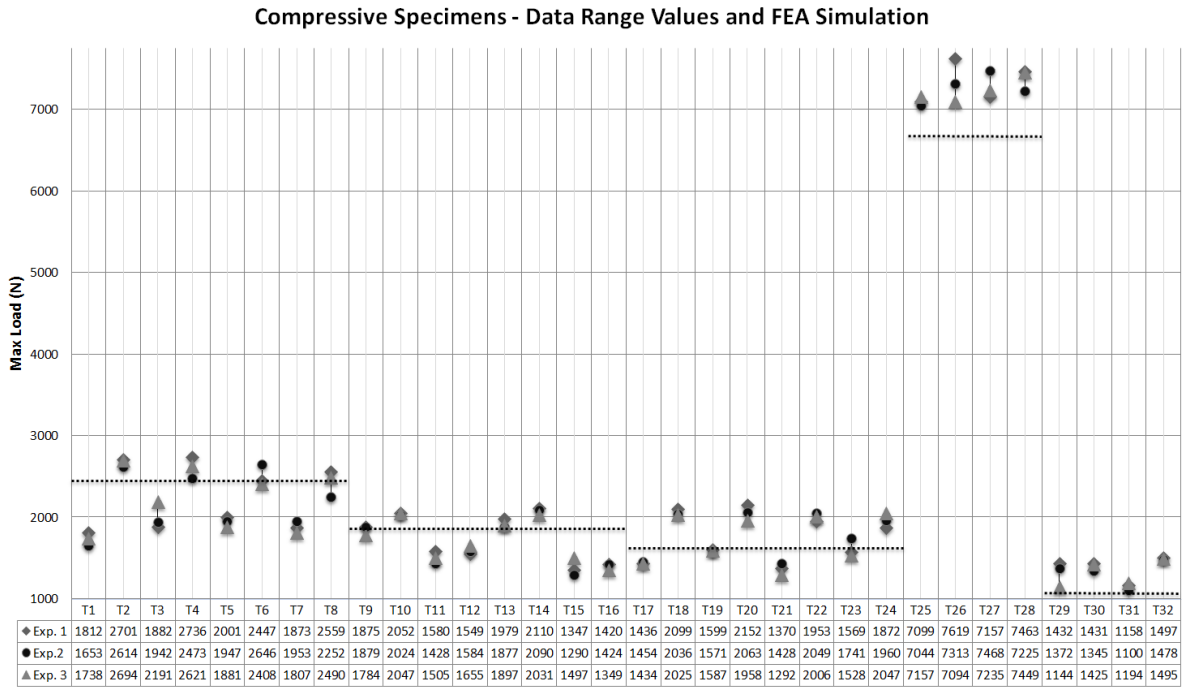
Sample Type and Respective Experiment No.

1	Orthogonal, -45/45, XY, Loose	9	Hexagonal, -45/45, XY, Loose	17	Pyramid, -45/45, XY, Loose	25	Solid, -45/45, XY
2	Orthogonal, -45/45, XY, Compact	10	Hexagonal, -45/45, XY, Compact	18	Pyramid, -45/45, XY, Compact	26	Solid, -45/45, YZ
3	Orthogonal, -45/45, YZ, Loose	11	Hexagonal, -45/45, YZ, Loose	19	Pyramid, -45/45, YZ, Loose	27	Solid, 0/90, XY
4	Orthogonal, -45/45, YZ, Compact	12	Hexagonal, -45/45, YZ, Compact	20	Pyramid, -45/45, YZ, Compact	28	Solid, 0/90, YZ
5	Orthogonal, 0/90, XY, Loose	13	Hexagonal, 0/90, XY, Loose	21	Pyramid, 0/90, XY, Loose	29	Hollow, -45/45, XY
6	Orthogonal, 0/90, XY, Compact	14	Hexagonal, 0/90, XY, Compact	22	Pyramid, 0/90, XY, Compact	30	Hollow, -45/45, YZ
7	Orthogonal, 0/90, YZ, Loose	15	Hexagonal, 0/90, YZ, Loose	23	Pyramid, 0/90, YZ, Loose	31	Hollow, 0/90, XY
8	Orthogonal, 0/90, YZ, Compact	16	Hexagonal, 0/90, YZ, Compact	24	Pyramid, 0/90, YZ, Compact	32	Hollow, 0/90, YZ

Figure 6.1.11: Data range values from the physical tests for the tensile specimens

In a similar way, Figure 6.1.12 brings on the compressive counterpart all the samples tested in the testing machine. As it can be seen, the ranges within the sample type are very coherent as well. There less appreciable differences from the high and low value compared to the tensile specimens. Compressive specimens 8, 26, and 29 exhibit the greatest differences, however, the difference in values vary from 300 to 600 N; else, the range difference is negligible. It should be addressed that the load values for the compressive samples were much higher than the ones for the tensile specimens. Proportionally, the difference between the low and the high value is lower than the difference of the tensile type. Hence, based on these results, there is no indication that more than one repetition is needed in order to obtain reasonable results and in the light of reducing the material use at this stage of the process. Similarly, Figure 6.1.12 depicts 4 dotted lines embedded within the chart area. Those dotted lines represent the value of the FEA

simulation for the same deformation. It should be noted that parameters such as build plane orientation and raster angle were not considered in the FEA simulation also. It is evident that the effects of such parameters are not reflected in Figure 6.1.12. However, a further exploration into the FEA simulation techniques may bring a closer approximation of such parameters in a later research.



Sample Type and Respective Experiment No.

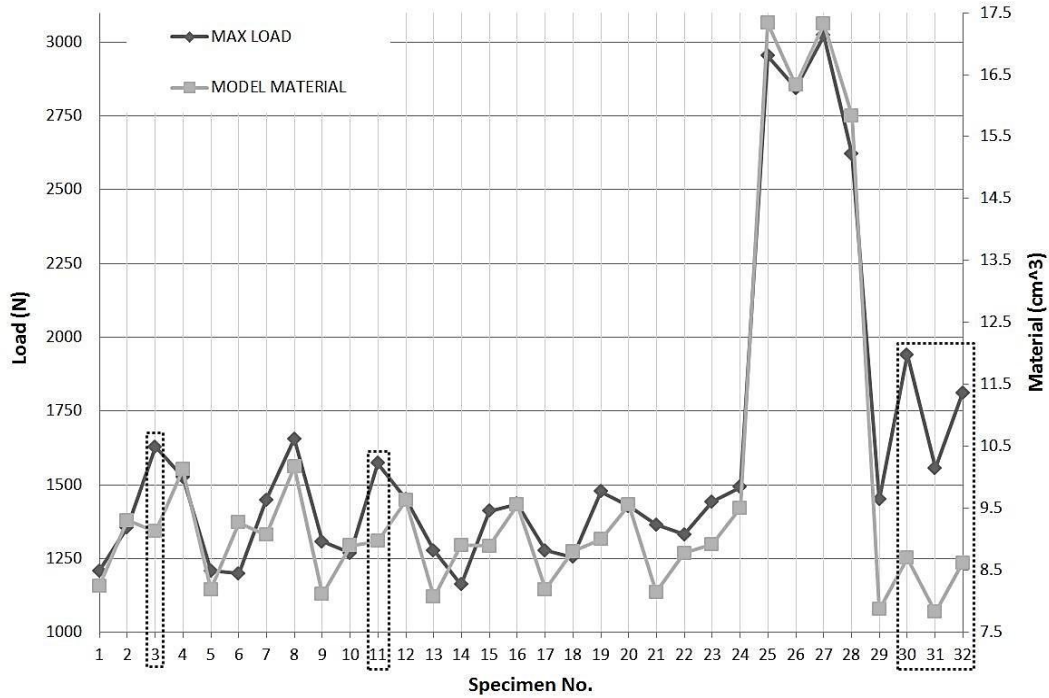
1	Orthogonal, -45/45, XY, Loose	9	Hexagonal, -45/45, XY, Loose	17	Pyramid, -45/45, XY, Loose	25	Solid, -45/45, XY
2	Orthogonal, -45/45, XY, Compact	10	Hexagonal, -45/45, XY, Compact	18	Pyramid, -45/45, XY, Compact	26	Solid, -45/45, YZ
3	Orthogonal, -45/45, YZ, Loose	11	Hexagonal, -45/45, YZ, Loose	19	Pyramid, -45/45, YZ, Loose	27	Solid, 0/90, XY
4	Orthogonal, -45/45, YZ, Compact	12	Hexagonal, -45/45, YZ, Compact	20	Pyramid, -45/45, YZ, Compact	28	Solid, 0/90, YZ
5	Orthogonal, 0/90, XY, Loose	13	Hexagonal, 0/90, XY, Loose	21	Pyramid, 0/90, XY, Loose	29	Hollow, -45/45, XY
6	Orthogonal, 0/90, XY, Compact	14	Hexagonal, 0/90, XY, Compact	22	Pyramid, 0/90, XY, Compact	30	Hollow, -45/45, YZ
7	Orthogonal, 0/90, YZ, Loose	15	Hexagonal, 0/90, YZ, Loose	23	Pyramid, 0/90, YZ, Loose	31	Hollow, 0/90, XY
8	Orthogonal, 0/90, YZ, Compact	16	Hexagonal, 0/90, YZ, Compact	24	Pyramid, 0/90, YZ, Compact	32	Hollow, 0/90, YZ

Figure 6.1.12: Data range values from the physical tests for the compressive specimens

Secondly, Figures 6.1.13 and 6.1.14 depict the physical load and the model material comparison for the tensile and compressive specimens, respectively. Figure 6.1.13 shows that specimens 3, 11, 30, 31, and 32 yield the best maximum load-model material balance. Surprisingly, specimens 30, 31 and 32, (hollow specimens) exhibit the second higher load allowance after the solid

specimens. If the main selection criterion is chosen to be model material, then hollow specimens 30(Hollow, -45/45, YZ), 31(Hollow, 0/90, XY), and 32(Hollow, 0/90, YZ) followed by specimens 3(Orthogonal, -45/45, YZ, Loose), and 11(Hexagonal, -45/45, YZ, Loose) are the best specimens.

Load and Model Material for Tensile Specimens

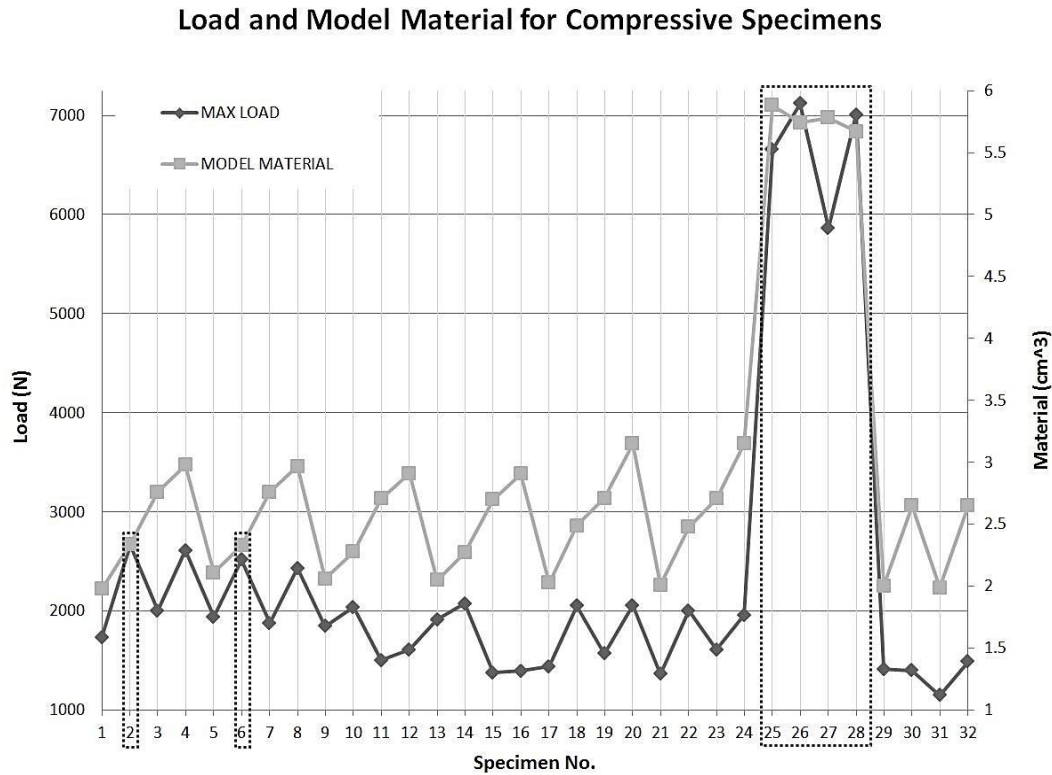


1	Orthogonal, -45/45, XY, Loose	9	Hexagonal, -45/45, XY, Loose	17	Pyramid, -45/45, XY, Loose	25	Solid, -45/45, XY
2	Orthogonal, -45/45, XY, Compact	10	Hexagonal, -45/45, XY, Compact	18	Pyramid, -45/45, XY, Compact	26	Solid, -45/45, YZ
3	Orthogonal, -45/45, YZ, Loose	11	Hexagonal, -45/45, YZ, Loose	19	Pyramid, -45/45, YZ, Loose	27	Solid, 0/90, XY
4	Orthogonal, -45/45, YZ, Compact	12	Hexagonal, -45/45, YZ, Compact	20	Pyramid, -45/45, YZ, Compact	28	Solid, 0/90, YZ
5	Orthogonal, 0/90, XY, Loose	13	Hexagonal, 0/90, XY, Loose	21	Pyramid, 0/90, XY, Loose	29	Hollow, -45/45, XY
6	Orthogonal, 0/90, XY, Compact	14	Hexagonal, 0/90, XY, Compact	22	Pyramid, 0/90, XY, Compact	30	Hollow, -45/45, YZ
7	Orthogonal, 0/90, YZ, Loose	15	Hexagonal, 0/90, YZ, Loose	23	Pyramid, 0/90, YZ, Loose	31	Hollow, 0/90, XY
8	Orthogonal, 0/90, YZ, Compact	16	Hexagonal, 0/90, YZ, Compact	24	Pyramid, 0/90, YZ, Compact	32	Hollow, 0/90, YZ

Figure 6.1.13: Physical load and model material comparison for all the tensile specimens

Figure 6.1.14 shows that 2 and 6 yield the best maximum load-model material balance. Evidently, specimens 25, 26, 27 and 28, (solid specimens) exhibit the higher load allowance. Now then, if the main selection criterion is chosen to be model material, then solid specimens 25(Solid, -45/45, XY), 26(Solid, -45/45, YZ), 27(Solid, 0/90, XY) and 28(Solid, 0/90, YZ) followed by specimens

2(Orthogonal, -45/45, XY, Compact), and 6(Orthogonal, 0/90, XY, Compact) will be the best specimens.

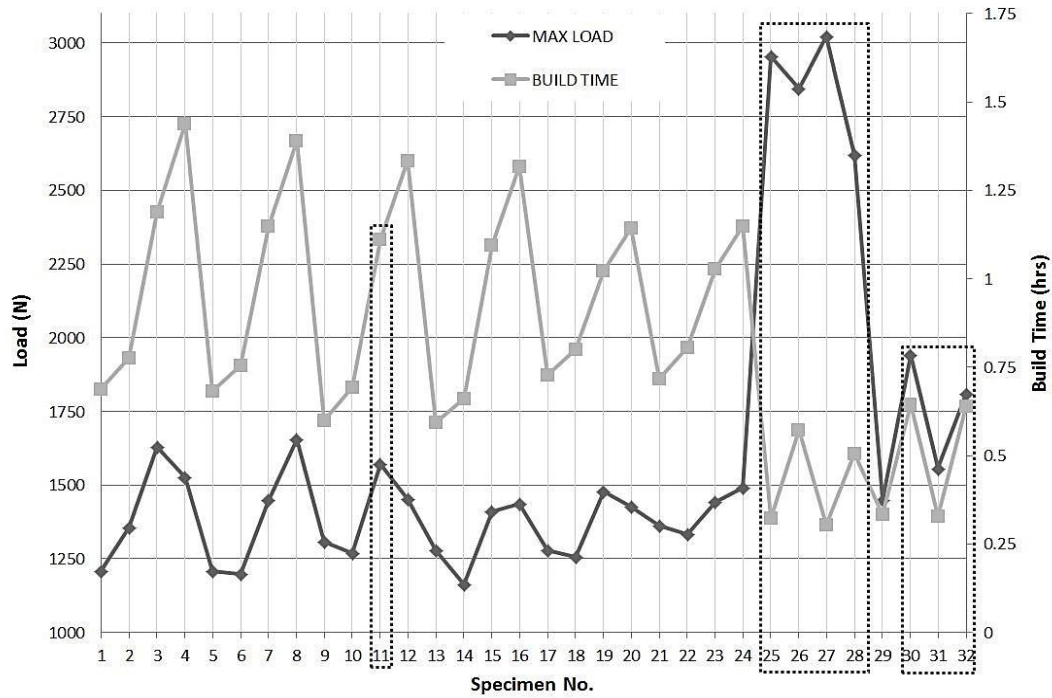


1	Orthogonal, -45/45, XY, Loose	9	Hexagonal, -45/45, XY, Loose	17	Pyramid, -45/45, XY, Loose	25	Solid, -45/45, XY
2	Orthogonal, -45/45, XY, Compact	10	Hexagonal, -45/45, XY, Compact	18	Pyramid, -45/45, XY, Compact	26	Solid, -45/45, YZ
3	Orthogonal, -45/45, YZ, Loose	11	Hexagonal, -45/45, YZ, Loose	19	Pyramid, -45/45, YZ, Loose	27	Solid, 0/90, XY
4	Orthogonal, -45/45, YZ, Compact	12	Hexagonal, -45/45, YZ, Compact	20	Pyramid, -45/45, YZ, Compact	28	Solid, 0/90, YZ
5	Orthogonal, 0/90, XY, Loose	13	Hexagonal, 0/90, XY, Loose	21	Pyramid, 0/90, XY, Loose	29	Hollow, -45/45, XY
6	Orthogonal, 0/90, XY, Compact	14	Hexagonal, 0/90, XY, Compact	22	Pyramid, 0/90, XY, Compact	30	Hollow, -45/45, YZ
7	Orthogonal, 0/90, YZ, Loose	15	Hexagonal, 0/90, YZ, Loose	23	Pyramid, 0/90, YZ, Loose	31	Hollow, 0/90, XY
8	Orthogonal, 0/90, YZ, Compact	16	Hexagonal, 0/90, YZ, Compact	24	Pyramid, 0/90, YZ, Compact	32	Hollow, 0/90, YZ

Figure 6.1.14: Physical load and model material comparison for all the compressive specimens

Thirdly, Figures 6.1.15 and 6.1.16 depict the physical load and the build time comparison for the tensile and compressive specimens, respectively. Figure 6.1.15 shows that specimens 11, 30, 31, and 32 yield the best maximum load-build time balance. Surprisingly, specimens 30, 31 and 32, (hollow specimens) exhibit the second higher load allowance after the solid specimens. If the main selection criterion is chosen to be build time, then hollow specimens 30(Hollow, -45/45, YZ), 31(Hollow, 0/90, XY), and 32(Hollow, 0/90, YZ) followed by specimen 11(Hexagonal, -45/45, YZ, Loose) will be the preferred ones.

Load and Build Time for Tensile Specimens

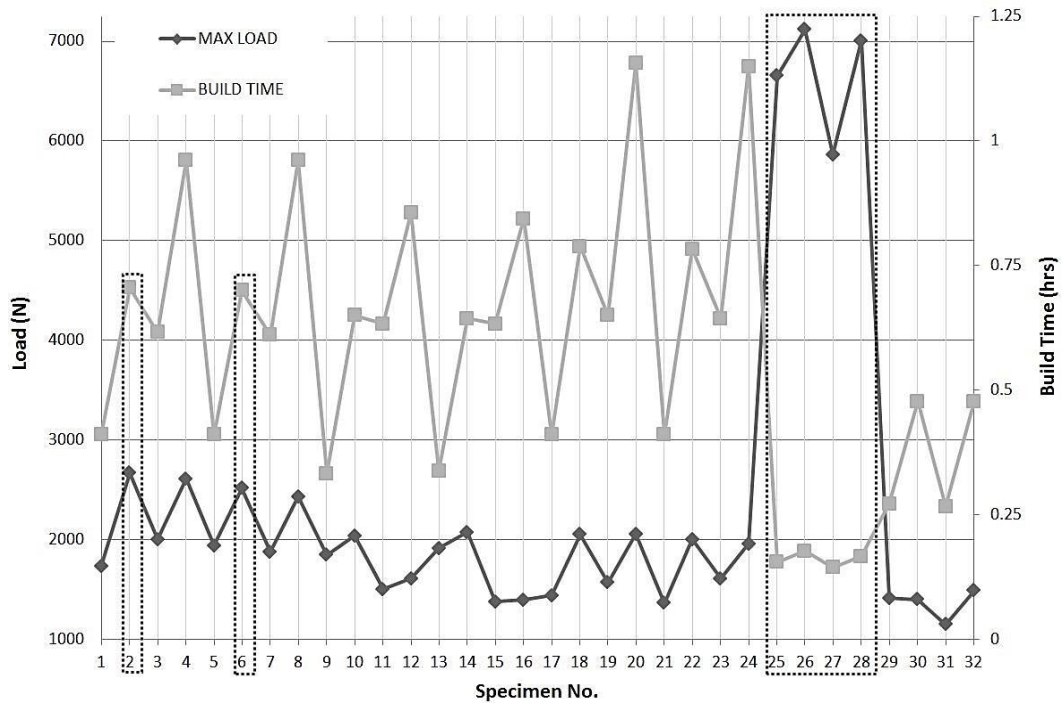


1	Orthogonal, -45/45, XY, Loose	9	Hexagonal, -45/45, XY, Loose	17	Pyramid, -45/45, XY, Loose	25	Solid, -45/45, XY
2	Orthogonal, -45/45, XY, Compact	10	Hexagonal, -45/45, XY, Compact	18	Pyramid, -45/45, XY, Compact	26	Solid, -45/45, YZ
3	Orthogonal, -45/45, YZ, Loose	11	Hexagonal, -45/45, YZ, Loose	19	Pyramid, -45/45, YZ, Loose	27	Solid, 0/90, XY
4	Orthogonal, -45/45, YZ, Compact	12	Hexagonal, -45/45, YZ, Compact	20	Pyramid, -45/45, YZ, Compact	28	Solid, 0/90, YZ
5	Orthogonal, 0/90, XY, Loose	13	Hexagonal, 0/90, XY, Loose	21	Pyramid, 0/90, XY, Loose	29	Hollow, -45/45, XY
6	Orthogonal, 0/90, XY, Compact	14	Hexagonal, 0/90, XY, Compact	22	Pyramid, 0/90, XY, Compact	30	Hollow, -45/45, YZ
7	Orthogonal, 0/90, YZ, Loose	15	Hexagonal, 0/90, YZ, Loose	23	Pyramid, 0/90, YZ, Loose	31	Hollow, 0/90, XY
8	Orthogonal, 0/90, YZ, Compact	16	Hexagonal, 0/90, YZ, Compact	24	Pyramid, 0/90, YZ, Compact	32	Hollow, 0/90, YZ

Figure 6.1.15: Physical load and build time comparison for all the tensile specimens

Figure 6.1.16 shows that specimens 2, 6, 25, 26, 27, and 28 yield the best maximum load-build time balance. Evidently, specimens 25, 26, 27 and 28, (solid specimens) exhibit the higher load allowance. Now then, if the main selection criterion is chosen to be build time, then solid specimens 25(Solid, -45/45, XY), 26(Solid, -45/45, YZ), 27(Solid, 0/90, XY) and 28(Solid, 0/90, YZ) followed by specimens 2(Orthogonal, -45/45, XY, Compact), and 6(Orthogonal, 0/90, XY, Compact) will be the best specimens.

Load and Build Time for Compressive Specimens



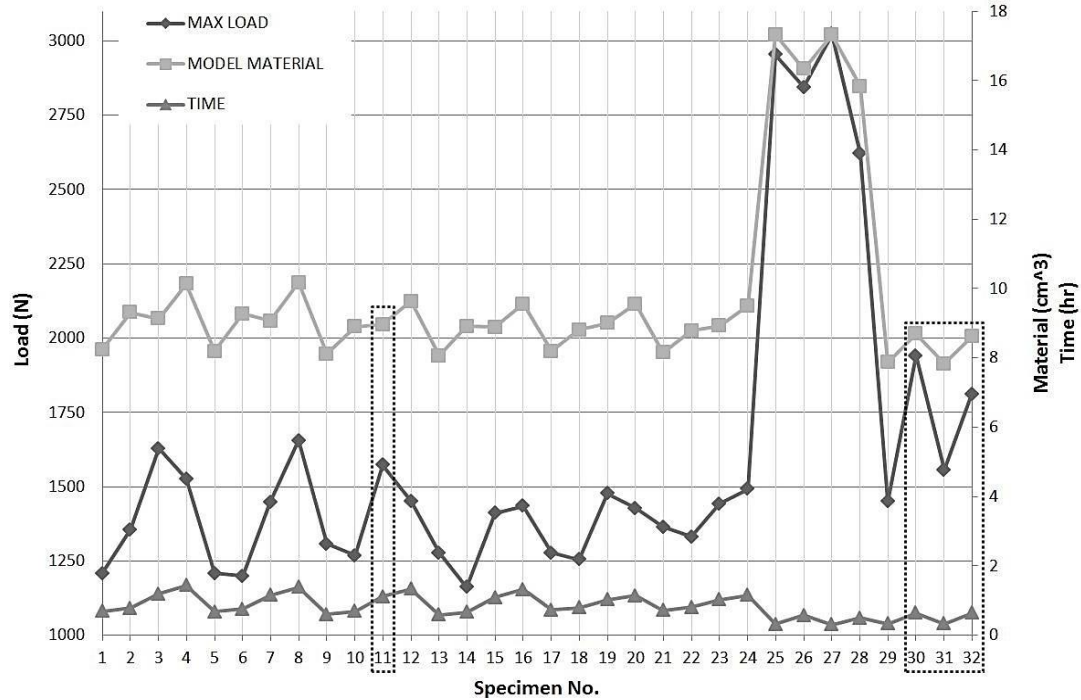
1	Orthogonal, -45/45, XY, Loose	9	Hexagonal, -45/45, XY, Loose	17	Pyramid, -45/45, XY, Loose	25	Solid, -45/45, XY
2	Orthogonal, -45/45, XY, Compact	10	Hexagonal, -45/45, XY, Compact	18	Pyramid, -45/45, XY, Compact	26	Solid, -45/45, YZ
3	Orthogonal, -45/45, YZ, Loose	11	Hexagonal, -45/45, YZ, Loose	19	Pyramid, -45/45, YZ, Loose	27	Solid, 0/90, XY
4	Orthogonal, -45/45, YZ, Compact	12	Hexagonal, -45/45, YZ, Compact	20	Pyramid, -45/45, YZ, Compact	28	Solid, 0/90, YZ
5	Orthogonal, 0/90, XY, Loose	13	Hexagonal, 0/90, XY, Loose	21	Pyramid, 0/90, XY, Loose	29	Hollow, -45/45, XY
6	Orthogonal, 0/90, XY, Compact	14	Hexagonal, 0/90, XY, Compact	22	Pyramid, 0/90, XY, Compact	30	Hollow, -45/45, YZ
7	Orthogonal, 0/90, YZ, Loose	15	Hexagonal, 0/90, YZ, Loose	23	Pyramid, 0/90, YZ, Loose	31	Hollow, 0/90, XY
8	Orthogonal, 0/90, YZ, Compact	16	Hexagonal, 0/90, YZ, Compact	24	Pyramid, 0/90, YZ, Compact	32	Hollow, 0/90, YZ

Figure 6.1.16: Physical load and build time comparison for all the compressive specimens

Finally, Figures 6.1.17 and 6.1.18 depict the physical load, model material, and the build time comparison for the tensile and compressive specimens, respectively. Said Figure 6.1.17 depicts that tensile specimens 11(Hexagonal, -45/45, YZ, Loose), 30(Hollow, -45/45, YZ), 31(Hollow, 0/90, XY), and 32(Hollow, 0/90, YZ) are the ones that provide the best results for all the variables that satisfy the best maximum load-less model material-less build time criterion.

Similarly, said Figure 6.1.18 depicts that compressive specimens 2(Orthogonal, -45/45, XY, Compact) and 6(Orthogonal, 0/90, XY, Compact) are the ones that provide the best results for all the variables that satisfy the best maximum load-less model material-less build time criterion.

Load, Time, and Model Material for Tensile Specimens



1	Orthogonal, -45/45, XY, Loose	9	Hexagonal, -45/45, XY, Loose	17	Pyramid, -45/45, XY, Loose	25	Solid, -45/45, XY
2	Orthogonal, -45/45, XY, Compact	10	Hexagonal, -45/45, XY, Compact	18	Pyramid, -45/45, XY, Compact	26	Solid, -45/45, YZ
3	Orthogonal, -45/45, YZ, Loose	11	Hexagonal, -45/45, YZ, Loose	19	Pyramid, -45/45, YZ, Loose	27	Solid, 0/90, XY
4	Orthogonal, -45/45, YZ, Compact	12	Hexagonal, -45/45, YZ, Compact	20	Pyramid, -45/45, YZ, Compact	28	Solid, 0/90, YZ
5	Orthogonal, 0/90, XY, Loose	13	Hexagonal, 0/90, XY, Loose	21	Pyramid, 0/90, XY, Loose	29	Hollow, -45/45, XY
6	Orthogonal, 0/90, XY, Compact	14	Hexagonal, 0/90, XY, Compact	22	Pyramid, 0/90, XY, Compact	30	Hollow, -45/45, YZ
7	Orthogonal, 0/90, YZ, Loose	15	Hexagonal, 0/90, YZ, Loose	23	Pyramid, 0/90, YZ, Loose	31	Hollow, 0/90, XY
8	Orthogonal, 0/90, YZ, Compact	16	Hexagonal, 0/90, YZ, Compact	24	Pyramid, 0/90, YZ, Compact	32	Hollow, 0/90, YZ

Figure 6.1.17: Physical load, model material, and build time comparison for all the tensile specimens

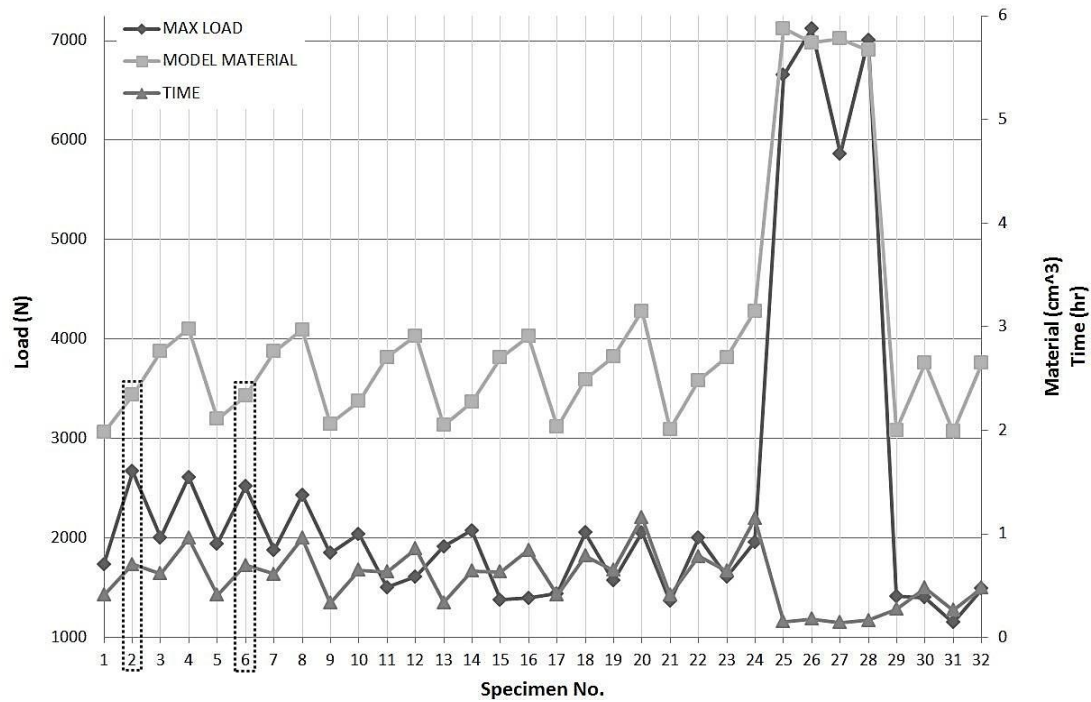
Results from Figure 6.1.17 are better explained when the Material-Load ratio (M/L) is obtained.

Table 6.2 shows that specimens 30, 32, and 31 yielded the best Material-Load relationship.

Table 6.2 Material/Load Ratio x 100 for tensile specimens

Specimen No.	1	2	3	4	5	6	7	8	9	10	11	12	13	14	15	16
Ratio	.68	.69	.56	.66	.68	.77	.63	.61	.62	.70	.57	.66	.63	.77	.63	.67
Specimen No.	17	18	19	20	21	22	23	24	25	26	27	28	29	30	31	32
Ratio	.64	.70	.61	.67	.60	.66	.62	.64	.59	.57	.57	.60	.54	.45	.50	.48

Load, Time, and Model Material for Compressive Specimens



1	Orthogonal, -45/45, XY, Loose	9	Hexagonal, -45/45, XY, Loose	17	Pyramid, -45/45, XY, Loose	25	Solid, -45/45, XY
2	Orthogonal, -45/45, XY, Compact	10	Hexagonal, -45/45, XY, Compact	18	Pyramid, -45/45, XY, Compact	26	Solid, -45/45, YZ
3	Orthogonal, -45/45, YZ, Loose	11	Hexagonal, -45/45, YZ, Loose	19	Pyramid, -45/45, YZ, Loose	27	Solid, 0/90, XY
4	Orthogonal, -45/45, YZ, Compact	12	Hexagonal, -45/45, YZ, Compact	20	Pyramid, -45/45, YZ, Compact	28	Solid, 0/90, YZ
5	Orthogonal, 0/90, XY, Loose	13	Hexagonal, 0/90, XY, Loose	21	Pyramid, 0/90, XY, Loose	29	Hollow, -45/45, XY
6	Orthogonal, 0/90, XY, Compact	14	Hexagonal, 0/90, XY, Compact	22	Pyramid, 0/90, XY, Compact	30	Hollow, -45/45, YZ
7	Orthogonal, 0/90, YZ, Loose	15	Hexagonal, 0/90, YZ, Loose	23	Pyramid, 0/90, YZ, Loose	31	Hollow, 0/90, XY
8	Orthogonal, 0/90, YZ, Compact	16	Hexagonal, 0/90, YZ, Compact	24	Pyramid, 0/90, YZ, Compact	32	Hollow, 0/90, YZ

Figure 6.1.18: Physical load, model material, and build time comparison for all the compressive specimens

Similarly, Table 6.3 shows that specimens 26, 28, and 25 yielded the best Material-Load relationship.

Table 6.3 Material/Load Ratio x 100 for compressive specimens

Specimen No.	1	2	3	4	5	6	7	8	9	10	11	12	13	14	15	16
Ratio	.11	.09	.14	.11	.11	.09	.15	.12	.11	.11	.18	.18	.11	.11	.20	.21
Specimen No.	17	18	19	20	21	22	23	24	25	26	27	28	29	30	31	32
Ratio	.14	.12	.17	.15	.15	.12	.17	.16	.09	.08	.10	.08	.14	.19	.17	.18

It is important to mention that the ratios of the tensile and compressive specimens do not take into consideration the desire of economize material while reducing the build time. The decision of selecting one or the other in a later stage will depend on the designer's will and this will be influenced by the level of safety the selected specimen type yields.

Important results yielded from this investigation and gathered along the realization of this thesis are presented herein below as a bulleted list form, namely:

- RP layering plays a primary role in terms of allocating the model and support material
- The material behaved in a brittle way and no evident necking behavior was observed
- The more complex the part, the more time spent in the FDM RP machine
- No clear indication of distortion when RP with the FDM FORTUS 400mc®
- Up to 4.25 times the increase of material when RP in a solid fill mode for massive parts
- Raster orientation does not affect significantly the allowed tensile load
- Build plane location significantly affects the tensile load
- Internal structures within tensile samples did not evidence significant improvement
- Tensile hollow samples shown the best maximum load, build time, and material use balance
- Hexagonal-loose tensile sample located in the YZ plane with a raster angle of $-45^{\circ}/45^{\circ}$ exhibited the second best maximum load, build time, and material use balance
- Raster orientation does not affect significantly the allowed compressive load
- XY orientation plane provides the best load allowance for compressive specimens
- Orthogonal-compact compressive sample located in the XY plane with a raster of $-45^{\circ}/45^{\circ}$ exhibited the best maximum load, build time, and material use balance
- Orthogonal-compact compressive sample located in the XY plane with a raster of $0^{\circ}/90^{\circ}$ exhibited the second best maximum load, build time, and material use balance

6.2 STATISTICAL RESULTS REFINEMENT

Section 4.5 in Chapter IV and Section 5.5 in Chapter V disclosed the necessity to incorporate to the body of the thesis a more refined model that can be used in a realistic scenario so that it serves as a predictive tool and eases the prediction of the tensile and compressive load for the different types of internal structures that were subject of study in the present research.

As previously described, substitution of the equation must be done by using the values of the “*Between-Subject Factors*” tables in the Appendix for the respective value label. For example, if the tensile load for the orthogonal structure type is to be predicted, the value of **Bp** can be either -

1 for an XY orientation and 1 for a YZ orientation; the value of **Ra** can be either -1 for a -45°/45° orientation and 1 for a 0°/90° orientation; and a value of **Id** of -1 for a “*loose*” packing and a value of 1 for a “*compact*” packing. Similarly, for **St**, three values can be chosen, namely: 1 for “*orthogonal*”, 2 for “*hexagonal*” and 3 for “*pyramid*”.

Table 6.4 Summary of the RA models for the orthogonal, hexagonal, and pyramid structures and load

Response Variable	Structure type	Model including significant factors	Model R ²
Tensile Load	Orthogonal	Load = 1403.667 + 160.583Bp + 57.917Ra. Bp. Id	0.82
	Hexagonal	Load = 1360.75 – 39.417Ra + 106.917Bp – 31.333Id	0.79
	Pyramid	Load = 1379.667 + 27.833Ra + 72.583Bp	0.82
Compressive Load	Orthogonal	Load = 2224.625 + 334.292Id – 51.042Ra. Id	0.88
	Hexagonal	Load = 1722.042 – 29.125Ra – 248.625Bp + 60.208Id – 55.958Ra. Bp – 28.458Bp. Id	0.96
	Pyramid	Load = 1758.292 + 42.708Bp + 260.375Id – 52.375Bp. Id	0.94

Table 6.5 comprise the most significant factors based on the ANOVA as comprised in Chapter IV and Chapter V for the tensile and compressive specimens on material, support material, build time, and load. As described by Table 6.5, the R² value for the compressive load does not describe the interaction of the parameters in determining the load. This may be due to the need for the determination of additional factors that may interact with the proposed variables. For the other R² values, the interactions of the parameters reflect accurately the parameters of study in the present research. Thus, a consistent model is obtained from the equations of Table 6.4 where the R² values range from 0.79 to 0.96 and the equations of Table 6.5 where the R² values range from 0.76 to 0.98.

Table 6.5 General model of the main interactions from the RA for the tested specimens

Test	Response variable	Model including significant factors	Model R ²
Tensile	Load	Load = 1381.361 + 201.361Bp - 1.536St. Ra - 44St. Bp - 2.958St. Id + 79.889Ra. Bp. Id - 24.042St. Ra. Bp. Id	0.76
	Model Material	Mm = 9.303 - 0.163St - 0.021Ra + 0.4Bp + 0.630Id - 0.115St. Id	0.98
	Support Material	Sm = 6.206 - 0.101St - 0.022Ra - 0.318Bp - 0.038Id + 0.145St. Bp - 0.043St. Id - 0.092Bp. Id + 0.009St. Bp. Id	0.88
	Time	Time = 62.261 - 2.542St - 0.458Ra + 21.904Bp + 5.984Id - 0.916St. Id + 3.571Bp. Id - 3.626St. Bp - 0.917St. Bp. Id	0.98
Compressive	Load	Load = 2367.986 - 233.167St - 27.681Ra - 101.292Bp + 292.208Id + 17.583St. Bp - 36.958St. Id - 85.069Ra. Bp - 26.708Ra. Id - 41.597Bp. Id + 27.083St. Ra. Bp - 2.595St. Ra. Bp. Id	0.65
	Model Material	Mm = 2.473 + 0.031St + 0.332Bp + 0.053Id + 0.05St. Id	0.98
	Support Material	Sm = 3.515 + 0.024St + 0.442Bp - 0.089Id + 0.031St. Bp + 0.095St. Id + 0.006St. Bp. Id	0.99
	Time	Time = 36.134 + 2.313St + 5.693Bp + 6.61Id + 1.063St. Bp + 1.813St. Id - 0.669Bp. Id + 0.563St. Bp. Id	0.94

CHAPTER VII

CONCLUDING REMARKS AND FUTURE WORK

7.1 CONCLUSIONS

Fundamental conclusions arose from the present study. The most important conclusion is that the present FEA simulation truly represents the physical experiments performed on the compressive samples. In a lower extent, the FEA simulation is a competitive representation of the physical experiments performed on the tensile samples. However, more research and a better FEA approximation are to be carried out in order to better calibrate the FEA parameters and boundary conditions. Regardless of the assumption of elastic behavior, the compressive specimens behaved as if no buckling was present. Thus, there is no need for deepening the study into the non-linear representation. Also, based on the data gathered from the results, there is no need for a large number of samples since load values remain within a relatively small range.

The tensile specimens did not behave according to the literature in the sense that the ABS plastic did not exhibit plastic characteristics such as necking that is characteristic of this type of plastics. Moreover, the thermoplastic material exhibited a brittle behavior that can be approached as being located in the linear elastic region. Further study of composite materials and the interactions at the boundaries is to be performed and characterize to understand the effect of the internal topology of the samples. This leads to a further study that deals with heat deposition characterization which is inherently related to distortion.

The machine settings affect considerably the output such as quality, reliability and mechanical characteristics of the RP part. In this sense, the research performed by Villalpando et al. (Villalpando, 2010), which is the basis of the present thesis, demonstrated a different set of results when the prototyped parts exhibited distortion. Also, the tensile testing showed that the samples with internal structures exhibited higher load values than that of the solid specimen. This indicates that the machine RP software and the quality of the machine itself play an important role in the results obtained. Hence, it can be assumed that reliability of the material characterization is strictly dependent not only of the RP technology, but the model/year of the machine from the same type of technology.

The statistical method is not the best way to predict the real behavior of the tested parts. It was observed that for the model material, support material, and build time, more data needs to be collected. Nevertheless, the statistical analysis provides a fair insight of what is to be expected. Thus, it is recommendable to start with the statistical analysis and move forward to the FEA simulation once a full understanding of the real affecting values is acquired.

Considerable savings in terms of model material can be achieved with the proposed method. However, in terms of monetary resources, the difference from a solid model to a hollowed/modified model is not yet significant. However, further research on large-scale parts is to be done in order to reduce the internal complexity of the part which affects the build time.

The present approach has the potential of obtaining better results when the support material is eliminated. Thus, the further treatment of the anisotropic part as a composite thermoplastic may be simplified to an isotropic material. Consequently, reducing the level of complexity will predict better and more accurate results.

7.2 RECOMMENDATIONS

The following section encompasses the recommendations when replicating the present study either partially or completely. If the researcher opts for using the present methodology in order to develop a new one, this section also comprises specific suggestions that could be of great help once the researchers submerges into the relatively novel rapid prototyping ocean of possibilities. Initially, in terms of CAD and 3D modeling, the researcher might modify the internal density by modifying the thickness of the primitive cylinder and primitive spheres of the basic parametric element. Also, the researcher may want to alter the internal density by modifying the length of the basic parametric element. Then, the researcher may like to refine the STL size. Now then, in terms of FDM rapid prototyping, the researcher is suggested to keep track of any change in the RP software change and duplicate the machine specific parameters in order to avoid flaws of not constraining all the involved parameters. Then, the researcher would like to verify the toolpath before printing the part in order to adopt the one that best fits the specific layer topology. Then, the researcher is exhorted to utilize a thin sharp knife in order to remove the samples from the disposable substrate tray. Now then, in terms of the FEA simulation, the researcher is encouraged to vary the load and the loading rate on the tensile and compressive specimens in order to observe the deformation and stress distribution along the tested sample parts. Then, the researcher is advised to consider the specimens as brittle and not a material with high-elongation capabilities as

it was described in the present research. Now then, in terms of physical testing, the researcher is urged to utilize an extensometer (specially, for the tensile specimens) since better and more accurate displacement data is obtained from it. Generally, it is highly recommended to utilize a more modern universal tensile machine UTM.

7.3 FUTURE WORK

Lastly, with regards to broadening the scope of this research, the following is suggested to the researcher, namely:

- To design and adopt a different geometrical entity such as a tetrahedron, dodecahedron, or any other 2D or 3D geometry and characterize their effects on the tensile and compressive specimens in terms of load, material use, and build time.
- To rapid prototype the tensile and compressive specimens in a different FDM material such as PC or ULTEM 9085®, when possible, in order to understand and characterize the influence of the internal structures with these materials.
- To FEA simulate and/or physically test parts exceeding the tensile and compressive dimensions (such as the plastic bottle blow mold from Chapter V).
- To consider testing the tensile and compressive samples in other mechanical tests such as torsion, impact, etc.
- To FEA simulate different types of mechanical tests such as flexure bending and/or torsion on the tensile samples and with the same material as discloses in the present thesis.
- To substitute and evaluate the RA model formulas and compare the results with the results obtained from the physical test results and FDM rapid prototyping results in order to validate the ANOVA and regression analysis.
- To perform the methodology proposed in this thesis for a different additive manufacturing technology such as SLA.
- To perform the methodology proposed in this thesis for a different additive manufacturing technology such as SLS.
- To propose and study a FEA analytical method to characterize the strength of the internal structures based on the geometry and selected parameters such as **R**, **L**, and **D**.
- To study the effects of heat distribution of parts with internal structures when being built by FDM.

CHAPTER VII: CONCLUDING REMARKS AND FUTURE WORK

- To obtain SEM micrographs for all the tensile and compressive samples in order to assess fracture sites based on the internal topography and determine stress concentrators.

The aforementioned possibilities open a wider scope for research. However, the abovementioned suggestions may not be taken as individual efforts, but a combination of two or more. In any case, results obtained from these research branches are considered as experimental and novel due to the uniqueness in nature of the studied subject matter.

REFERENCES

- Agarwala, M.K., Jamalabad, V.R., Langrana, N.A., Safari, A., Whalen, P.J., Danforth, S.C., 1996. Structural quality of parts processed by fused deposition. *Rapid Prototyping Journal*. Vol. 2, No. 4, pp.4-19.
- Ahn, S.H, Montero, M., Odell, D., Roundy, S., Wright, P. K., 2002. Anisotropic material properties of fused deposition modeling. *ABS Rapid Prototyping*. Vol. 8, No. 4, pp. 248–257.
- Anitha, R., Arunachalam, S., Padhakrishnan, P., 2001. Critical parameters influencing the quality of prototypes in fused deposition modeling. *Journal of Materials Processing Technology*. Vol. 118, pp. 385-388.
- ASTM D638-10 Standard Test Method for Tensile Properties of Plastics. *ASTM International*. 2012.
- ASTM D695-10 Standard Test Method for Compressive Properties of Rigid Plastics. *ASTM International*. 2012.
- Arriaga, A., Lazkano, J.M., Pagaldai, R., Zaldua, A.M., Hernandez, R., Atxurra, R., Chrysostomou, A., 2006. Finite-element analysis of quasi-static characterization tests in thermoplastic materials: Experimental and numerical analysis results correlation with ANSYS. *Polymer Testing*. Vol. 26, pp. 284–305.
- Bak, D., 2003. Rapid Prototyping or rapid production? 3D printing process move industry towards the latter. *Assembly Automation*, Vol. 23, Iss: 4, pp. 340-345.
- Bakar, N.S.A., Alkahari, M.R., Boejang, H., 2010. Analysis on fused deposition modeling performance. *Journal of Zhejiang University-SCIENCE A (Applied Physics & Engineering)*. Vol. 11, No. 12, pp. 972-977.
- Bertoldi M., Yardimci M. A., Pistor C. M., GUYeri S. I., Sala G. 1998. Mechanical Characterization of Parts Processed via Fused Deposition. *Proc. 9th Solid Freeform Fabr. Symp., The University of Texas at Austin, Austin, TX*, Vol. 9, pp. 557-565.
- Chaturvedi, V., 2009. Parametric optimization of fused deposition modeling using response surface methodology. *Thesis, Department of Mechanical Engineering, National Institute of Technology Rourkela*.
- Chen, Y., 2007. 3D texture mapping for rapid manufacturing. *Computer-Aided Design & Applications*, Vol. 4, No. 6, pp 761-771.
- Chen, Y., 2006. A mesh-based geometric modeling method for general structures. *Proceedings of DETC'06 2006 ASME Design Engineering Technical Conferences and Computers and Information in Engineering Conference Philadelphia, Pennsylvania*, September 10-13, pp. 1-13.
- Chockalingam, K., Jawahar, N., Ramanathan, K.N., Banerjee, P.S., 2006. Optimization of stereolithography process parameters for part strength using design of experiments. *International Journal of Advanced Manufacturing Technology*. Vol. 29, pp. 79-88.

- El-Gizawy, A., Cardona, J., Graybill, B., 2010. An integrated approach for characterization of properties and mesostructure of fused deposition modeling ULTEM 9085 products. *International SAMPE Symposium and Exhibition (Proceedings), SAMPE 2010 Conference and Exhibition "New Materials and Processes for a New Economy"*. May, 2010.
- Es-Said, O.S., Foyos, J., Noorani, R., Mendelson, M., Marloth, R., Pregger, B.A., 2000. Effect of Layer Orientation on Mechanical Properties of Rapid Prototyped Samples. *Materials and Manufacturing Processes*. Vol. 15, No.1, pp. 107-122.
- Fodran E., Koch M., Menon, U., 1996, SFF Symposium Proc., Austin, TX, pp. 419-442.
- Galantucci, L.M., Lavecchia, F., Percoco, G., 2008. Study of compression properties of topologically optimized FDM made structured parts. *CIRP Annals - Manufacturing Technology*. Vol. 57, pp. 243–246.
- Galantucci, L.M., Lavecchia, F., Percoco, G., 2010. Internal structure optimization for fused deposition modeling ABS parts. *Innovative Developments in Design and Manufacturing - Advanced Research in Virtual and Rapid Prototyping, 4th International Conference on Advanced Research in Virtual and Physical Prototyping*, pp. 435-440.
- Gebhardt, A., 2003. *Rapid Prototyping*. ISBN: 978-1569902813. Hanser Gardner Publications. Chapter 2, pp. 30-74.
- Gu, P., Li, L., 2002. Fabrication of Biomedical Prototypes with Locally Controlled Properties Using FDM. *CIRP Annals - Manufacturing Technology*. Vol. 51, No. 1, pp. 181–184.
- Kridli, G.T., 2006. “Material Properties and Characterization,” *Rapid Prototyping Handbook* Edited by A. Kamrani, Springer Publishing.
- Lam, T.W., Yu, K.M., Cheung, K.M. Li, C.L., 1998. Octree reinforces thin shell objects rapid prototyping by fused deposition modeling. *International Journal of Advanced Manufacturing Technology*, Vol. 33, pp.631-636.
- Lee, B.H., Abdullah, J., Khan, Z.A., 2005. Optimization of rapid prototyping parameters for production of flexible ABS object. *Journal of Materials Processing Technology*. Vol. 169, pp. 54–61.
- Levy, G. N., Schindel, R., Kruth, J.P., 2003. Rapid manufacturing and rapid tooling with layer manufacturing (LM) technologies, state of the art and future perspectives. *CIRP Annals - Manufacturing Technology*. Vol. 52, No. 2, pp. 589–609.
- McMains, S., Smith, J., Se´quinThin, C., 2003. Wall Calculation for Layered Manufacturing. *Journal of Computing and Information Science in Engineering*. Vol. 3, pp. 210-218.
- Montero, M., Roundy, S., Odell, D., Ahn, S.H., Wright, P.K., 2001. Material Characterization of Fused Deposition Modeling (FDM) ABS by Designed Experiments. *Proceedings of Rapid Prototyping & Manufacturing Conference*. May 15-17, Cincinnati, OH, USA.
- Montgomery, Douglas C, 2009. *Design and Analysis of Experiments (7th Edition)*. John Wiley & Sons.

- Pande, S., Kumar, S., 2008. A generative process planning system for parts produced by rapid prototyping. *International Journal of Production Research*. Vol. 46, No. 22, pp. 6431-6460.
- Pandey, P.M., Venkata, N.R., Dhande, S.G., 2007. Part deposition orientation studies in layered manufacturing. *Journal of Materials Processing Technology*. Vol. 185, pp. 125–131.
- Park, S., 2005. Hollowing objects with uniform wall thickness. *CAD Computer Aided Design*, Vol. 37, No. 4, pp. 451-460.
- Persson, H., Ådán, K., 2004. Modeling and experimental studies of PC/ABS at large deformations. *Thesis, Division of Solid Mechanics, Lund University*.
- Rodríguez, J.F., Thomas, J.P., Renaud, J.E., 1999. Mechanical behavior of acrylonitrile butadiene styrene (ABS) fused deposition materials. *Experimental Investigation Rapid Prototyping Journal*. Vol. 7, No. 3, pp. 148-158.
- Rodríguez, J.F., Thomas, J.P., Renaud, J.E., 2003. Design of Fused-Deposition ABS Components for Stiffness and Strength. *Journal of Mechanical Design*. Vol. 125, pp. 545-551.
- Roylance, D., 1996. *Mechanics of Materials*, John Wiley & Sons, New York.
- Santos, D.M.C., Pertence, A.E.M., Camposa, H.B. and Cetlin, P.R., 2005. The development of 3D models through rapid prototyping concepts. *Journal of Materials Processing Technology*. Vol. 169, pp. 1–4.
- Saravanan, M., 2010. Investigation of thermal stress development by layer manufacturing on fused deposition modeling parts. *International Journal of Enterprise Network Management 2010*. Vol. 4, No. 2, pp. 183-200.
- Sood, A.K., Ohdar, R.K., Mahapatra, S.S., 2009. Parametric appraisal of fused deposition modeling process using the grey Taguchi method. *Proceedings of the Institution of Mechanical Engineers, Part B: J. Engineering Manufacture*. Vol. 224, pp. 136-145.
- Sood, A.K., Ohdar, R.K., Mahapatra, S.S., 2010. Mahapatra Parametric appraisal of mechanical property of fused deposition modeling processed parts. *Materials and Design*. Vol. 31, pp. 287–295.
- Sciortino, S., 2007. Extrusion blow molding with FDM. Stratasys Inc. U.S.
- Sun, Q., Rizvi, G.M., Bellehumeur, C.T., Gu, P., 2008. Effect of processing conditions on the bonding quality of FDM polymer filaments. *Rapid Prototyping Journal*. Vol.14, No. 2, pp. 72–80.
- Thomas, J.P., Rodriguez, J., 2000. Modeling the fracture strength between fused-deposition extruded roads. *11th Solid Freeform Fabrication Symposium Proceedings, Austin, TX*.
- Too, M.H., Leong, K.F., Chua, C.K., Du, Z.H., Yang, S.F., Cheah, C.M., Ho, S.L., 2002. Investigation of 3D Non-Random Porous Structures by Fused Deposition Modeling. *International Journal of Advanced Manufacturing Technology*. Vol. 19, pp. 217–223.
- Tres, P.A., 2006. *Designing Plastic Parts for Assembly*. 6th Ed. Hanser Gardner Publications Inc., U.S.

- Urbanic, J. ElMaraghy, W., Rohrauer, G., 2003. Generation of associative rapid prototyping tool paths from a solid model. *International Workshop on Advanced Manufacturing and Integrated Systems*. 17 pgs.
- Urbanic, J., Hedrick, R., 2004. Developing a virtual model for the fused deposition rapid prototyping process. *Intelligent Manufacturing Systems (IMS) Centre*. University of Windsor, pp. 1 -7.
- Villalpando, L. and Urbanic, J. (2010) "Parametric Internal Matrix Structures for Components Built by Fused Deposition Modeling", *Proceedings of the 4th International Conference on Changeable, Agile, Reconfigurable and Virtual Production (CARV2011)*, Montreal, Canada, October 2-5.
- Wang, H., Chen, Y., Rosen, D.W. 2005. A Hybrid Geometric Modeling Method for Large Scale Conformal Cellular Structures. *Proceeding of ASME Computers and Information in Engineering Conference, Long Beach, CA*. Sept 24-28, pp. 1-13.
- Wu, M.L., 2011. CAD design and mechanical test on inside porous parts. *Advanced Materials Research - Manufacturing Process Technology*, Vol. 189-193, pp. 2224-2227.
- Yao, W.L., Ming, U., Leu, C., 2000. Analysis and design of internal web structure of laser stereolithography patterns for investment casting. *Materials and Design*. Vol. 21, pp. 101-109.
- Zhang, Y., Chou, K., 2008. A parametric study of part distortions in fused deposition modeling using three-dimensional finite element. *Proceedings of the Institution of Mechanical Engineers. Part B: J. Engineering Manufacture*. Vol. 222, pp. 959-967.

**APPENDIX
ANALYSIS OF VARIANCE**

Tensile Specimens

Dependent Variable: Load

Data:

TENSILE TEST							
Exp. NO.	Type of Structure	Raster Angle	Build Plane	Internal Density	Load		
					Spc1	Spc2	Spc3
1	Orthogonal	-1	-1	-1	1207	1220	1200
2	Orthogonal	-1	-1	1	1284	1432	1352
3	Orthogonal	-1	1	-1	1653	1577	1653
4	Orthogonal	-1	1	1	1582	1498	1500
5	Orthogonal	1	-1	-1	1129	1355	1140
6	Orthogonal	1	-1	1	1136	1187	1275
7	Orthogonal	1	1	-1	1423	1423	1498
8	Orthogonal	1	1	1	1577	1805	1582
9	Hexagonal	-1	-1	-1	1306	1295	1320
10	Hexagonal	-1	-1	1	1286	1293	1226
11	Hexagonal	-1	1	-1	1753	1436	1530
12	Hexagonal	-1	1	1	1444	1458	1455
13	Hexagonal	1	-1	-1	1236	1294	1303
14	Hexagonal	1	-1	1	1130	1206	1151
15	Hexagonal	1	1	-1	1450	1428	1354
16	Hexagonal	1	1	1	1424	1450	1430
17	Pyramid	-1	-1	-1	1231	1296	1307
18	Pyramid	-1	-1	1	1221	1310	1233
19	Pyramid	-1	1	-1	1443	1452	1446
20	Pyramid	-1	1	1	1368	1460	1455
21	Pyramid	1	-1	-1	1368	1360	1364
22	Pyramid	1	-1	1	1292	1343	1360
23	Pyramid	1	1	-1	1439	1451	1436
24	Pyramid	1	1	1	1503	1438	1536
25	Solid	-1	-1	-	2901	3010	2950
26	Solid	-1	1		3042	2785	2704
27	Solid	1	-1		3016	3035	3017
28	Solid	1	1		2657	2571	2631
29	Hollow	-1	-1		1429	1508	1412
30	Hollow	-1	1		1816	1984	2025
31	Hollow	1	-1		1565	1574	1528
32	Hollow	1	1		1805	1835	1793

Table A1.

Between-Subjects Factors

Variable	Value Label		N
Structure_type	1:	Orthogonal	24
	2:	Hexagonal	24
	3:	Pyramid	24
Raster_angle	-1:	-45/45	36
	1:	0/90	36
Build_plane	-1:	XY	36
	1:	YZ	36
Internal_density	-1:	loose	36
	1:	compact	36

Table A2.

ANOVA

Source	Type III Sum of Squares	df	Mean Square	F	Sig.
Corrected Model	1.287E6	23	55943.534	14.281	.000
Intercept	1.374E8	1	1.374E8	35072.165	.000
Structure_type	22205.444	2	11102.722	2.834	.069
Raster_angle	11400.500	1	11400.500	2.910	.094
Build_plane	925253.389	1	925253.389	236.198	.000
Internal_density	122.722	1	122.722	.031	.860
Structure_type * Raster_angle	60913.000	2	30456.500	7.775	.001
Structure_type * Build_plane	94423.111	2	47211.556	12.052	.000
Structure_type * Internal_density	45994.111	2	22997.056	5.871	.005
Raster_angle * Build_plane	220.500	1	220.500	.056	.813
Raster_angle * Internal_density	9846.722	1	9846.722	2.514	.119
Build_plane * Internal_density	1549.389	1	1549.389	.396	.532
Structure_type * Raster_angle * Build_plane	8745.333	2	4372.667	1.116	.336
Structure_type * Raster_angle * Internal_density	1931.444	2	965.722	.247	.782
Structure_type * Build_plane * Internal_density	2900.111	2	1450.056	.370	.693
Raster_angle * Build_plane * Internal_density	72834.722	1	72834.722	18.593	.000
Structure_type * Raster_angle * Build_plane * Internal_density	28360.778	2	14180.389	3.620	.034
Error	188029.333	48	3917.278		
Total	1.389E8	72			
Corrected Total	1474730.611	71			

Table A3.

Parameter Estimates

Parameter	B	Std. Error	t	Sig.	95% Confidence Interval	
					Lower Bound	Upper Bound
Intercept	1492.333	36.135	41.299	.000	1419.678	1564.988
[Structure_type=1]	162.333	51.103	3.177	.003	59.584	265.083
[Structure_type=2]	-57.667	51.103	-1.128	.265	-160.416	45.083
[Raster_angle=-1]	-64.667	51.103	-1.265	.212	-167.416	38.083
[Build_plane=-1]	-160.667	51.103	-3.144	.003	-263.416	-57.917
[Internal_density=-1]	-50.333	51.103	-.985	.330	-153.083	52.416
[Structure_type=1] * [Raster_angle=-1]	-63.333	72.271	-.876	.385	-208.643	81.976
[Structure_type=2] * [Raster_angle=-1]	82.333	72.271	1.139	.260	-62.976	227.643
[Structure_type=1] * [Build_plane=-1]	-294.667	72.271	-4.077	.000	-439.976	-149.357
[Structure_type=2] * [Build_plane=-1]	-111.667	72.271	-1.545	.129	-256.976	33.643
[Structure_type=1] * [Internal_density=-1]	-156.333	72.271	-2.163	.036	-301.643	-11.024
[Structure_type=2] * [Internal_density=-1]	26.333	72.271	.364	.717	-118.976	171.643
[Raster_angle=-1] * [Build_plane=-1]	-12.333	72.271	-.171	.865	-157.643	132.976
[Raster_angle=-1] * [Internal_density=-1]	69.667	72.271	.964	.340	-75.643	214.976
[Build_plane=-1] * [Internal_density=-1]	82.667	72.271	1.144	.258	-62.643	227.976
[Structure_type=1] * [Raster_angle=-1] * [Build_plane=-1]	297.000	102.206	2.906	.006	91.501	502.499
[Structure_type=2] * [Raster_angle=-1] * [Build_plane=-1]	100.667	102.206	.985	.330	-104.832	306.166
[Structure_type=1] * [Raster_angle=-1] * [Internal_density=-1]	238.000	102.206	2.329	.024	32.501	443.499
[Structure_type=2] * [Raster_angle=-1] * [Internal_density=-1]	75.000	102.206	.734	.467	-130.499	280.499
[Structure_type=1] * [Build_plane=-1] * [Internal_density=-1]	132.667	102.206	1.298	.200	-72.832	338.166
[Structure_type=2] * [Build_plane=-1] * [Internal_density=-1]	56.667	102.206	.554	.582	-148.832	262.166
[Raster_angle=-1] * [Build_plane=-1] * [Internal_density=-1]	-78.667	102.206	-.770	.445	-284.166	126.832
[Structure_type=1] * [Raster_angle=-1] * [Build_plane=-1] * [Internal_density=-1]	-384.667	144.541	-2.661	.011	-675.286	-94.047
[Structure_type=2] * [Raster_angle=-1] * [Build_plane=-1] * [Internal_density=-1]	-142.667	144.541	-.987	.329	-433.286	147.953

Table A4.

Regression

Model summary:

R	R Square	Adjusted R Square	Std. Error of the Estimate	Change Statistics				
				R Square Change	F Change	df1	df2	Sig. F Change
.906 ^a	.820	.772	68.783	.820	17.047	15	56	.000

Table A5.

Coefficients:

Model	Unstandardized Coefficients		Standardized Coefficients	t	Sig.
	B	Std. Error	Beta		
(Constant)	1405.361	21.447		65.528	.000
Structure_type	-12.000	9.928	-.068	-1.209	.232
Raster_angle	-66.583	21.447	-.465	-3.105	.003
Build_plane	201.361	21.447	1.407	9.389	.000
Internal_density	32.278	21.447	.226	1.505	.138
structure_raster	27.000	9.928	.408	2.720	.009
structure_build	-44.000	9.928	-.664	-4.432	.000
structure_internal	-16.792	9.928	-.253	-1.691	.096
raster_build	24.417	21.447	.171	1.138	.260
raster_internal	23.111	21.447	.161	1.078	.286
build_internal	-10.278	21.447	-.072	-.479	.634
str_ras_bui	-13.083	9.928	-.197	-1.318	.193
str_ras_int	-5.708	9.928	-.086	-.575	.568
str_bui_int	7.458	9.928	.113	.751	.456
ras_bui_int	79.889	21.447	.558	3.725	.000
str_ras_bui_int	-24.042	9.928	-.363	-2.422	.019

Table A6.

Between-Subjects Factors:

Variable	Value Label		N
Structure_type	1:	Orthogonal	8
	2:	Hexagonal	8
	3:	Pyramid	8
Raster_angle	-1:	-45/45	12
	1:	0/90	12
Build_plane	-1:	XY	12
	1:	YZ	12
Internal_density	-1:	loose	12
	1:	compact	12

Table A7.

Dependent Variable: Model Material

ANOVA

Source	Type III Sum of Squares	df	Mean Square	F	Sig.
Corrected Model	8.485 ^a	21	.404	897.866	.001
Intercept	1934.651	1	1934.651	4299225.037	.000
Structure_type	.539	2	.269	598.370	.002
Raster_angle	.010	1	.010	23.148	.041
Build_plane	3.840	1	3.840	8533.333	.000
Internal_density	3.840	1	3.840	8533.333	.000
Structure_type * Internal_density	.222	2	.111	247.111	.004
Structure_type * Raster_angle	.000	2	.000	.481	.675
Structure_type * Build_plane	.015	2	.007	16.333	.058
Raster_angle * Build_plane	.000	1	.000	.926	.437
Raster_angle * Internal_density	.002	1	.002	4.481	.168
Build_plane * Internal_density	.008	1	.008	17.926	.052
Structure_type * Raster_angle * Build_plane	.003	2	.001	2.926	.255
Structure_type * Raster_angle * Internal_density	.000	2	.000	.481	.675
Structure_type * Build_plane * Internal_density	.005	2	.002	5.148	.163
Raster_angle * Build_plane * Internal_density	.000	1	.000	.333	.622
Error	.001	2	.000		
Total	1943.137	24			
Corrected Total	8.486	23			

Table A8.

Regression

Model summary:

R	R Square	Adjusted R Square	Std. Error of the Estimate	Change Statistics				
				R Square Change	F Change	df1	df2	Sig. F Change
.992 ^a	.984	.954	.13089	.984	32.485	15	8	.000

Table A9.

Coefficients:

Model	Unstandardized Coefficients		Standardized Coefficients	t	Sig.
	B	Std. Error	Beta		
(Constant)	9.303	.071		131.606	.000
Structure_type	-.163	.033	-.223	-4.966	.001
Raster_angle	-.011	.071	-.018	-.153	.882

Build_plane	.452	.071	.761	6.401	.000
Internal_density	.630	.071	1.060	8.912	.000
structure_raster	-.005	.033	-.018	-.153	.882
structure_build	-.026	.033	-.095	-.802	.446
structure_internal	-.115	.033	-.418	-3.514	.008
raster_build	.013	.071	.022	.189	.855
raster_internal	.019	.071	.032	.271	.793
build_internal	-.011	.071	-.018	-.153	.882
str_ras_bui	-.009	.033	-.032	-.267	.796
str_ras_int	-.005	.033	-.018	-.153	.882
str_bui_int	-.004	.033	-.014	-.115	.912
ras_bui_int	.010	.071	.017	.141	.891
str_ras_bui_int	-.004	.033	-.014	-.115	.912

Table A10.

Dependent Variable: Support Material

ANOVA

Source	Type III Sum of Squares	df	Mean Square	F	Sig.
Corrected Model	1.201 ^a	21	.057	285.841	.003
Intercept	864.960	1	864.960	4324801.333	.000
Structure_type	.249	2	.125	622.583	.002
Raster_angle	.011	1	.011	56.333	.017
Build_plane	.019	1	.019	96.333	.010
Internal_density	.365	1	.365	1825.333	.001
Structure_type * Internal_density	.070	2	.035	174.333	.006
Structure_type * Raster_angle	.001	2	.000	1.333	.429
Structure_type * Build_plane	.337	2	.168	842.333	.001
Raster_angle * Build_plane	.001	1	.001	5.333	.147
Raster_angle * Internal_density	.000	1	.000	.000	1.000
Build_plane * Internal_density	.135	1	.135	675.000	.001
Structure_type * Raster_angle * Build_plane	.001	2	.001	2.583	.279
Structure_type * Raster_angle * Internal_density	.001	2	.000	1.750	.364
Structure_type * Build_plane * Internal_density	.010	2	.005	25.750	.037
Raster_angle * Build_plane * Internal_density	.001	1	.001	3.000	.225
Error	.000	2	.000		
Total	866.161	24			
Corrected Total	1.201	23			

Table A11.

Regression

Model summary:

R	R Square	Adjusted R Square	Std. Error of the Estimate	Change Statistics				
				R Square Change	F Change	df1	df2	Sig. F Change
.942 ^a	.886	.674	.13056	.886	4.164	15	8	.024

Table A12.

Coefficients:

Model	Unstandardized Coefficients		Standardized Coefficients	t	Sig.
	B	Std. Error	Beta		
(Constant)	6.206	.071		88.013	.000
Structure_type	-.101	.033	-.370	-3.102	.015
Raster_angle	-.032	.071	-.142	-.449	.665
Build_plane	-.318	.071	-1.423	-4.515	.002
Internal_density	-.038	.071	-.171	-.544	.601
structure_raster	.005	.033	.048	.153	.882
structure_build	.145	.033	1.400	4.442	.002
structure_internal	-.043	.033	-.410	-1.302	.229
raster_build	.006	.071	.026	.083	.936
raster_internal	.013	.071	.056	.177	.864
build_internal	-.092	.071	-.414	-1.312	.226
str_ras_bui	-.006	.033	-.060	-.191	.853
str_ras_int	-.006	.033	-.060	-.191	.853
str_bui_int	.009	.033	.085	.268	.795
ras_bui_int	.010	.071	.045	.142	.891
	-.002	.033	-.024	-.077	.941

Table A13.

Dependent Variable: Time

ANOVA

Source	Type III Sum of Squares	df	Mean Square	F	Sig.
Corrected Model	6110.574 ^a	21	290.980	1335.970	.001
Intercept	78461.253	1	78461.253	360237.611	.000
Structure_type	135.637	2	67.818	311.373	.003
Raster_angle	5.033	1	5.033	23.106	.041
Build_plane	5152.991	1	5152.991	23658.827	.000
Internal_density	413.921	1	413.921	1900.428	.001
Structure_type * Internal_density	15.235	2	7.618	34.975	.028
Structure_type * Raster_angle	3.444	2	1.722	7.906	.112
Structure_type * Build_plane	293.931	2	146.966	674.761	.001
Raster_angle * Build_plane	.226	1	.226	1.039	.415
Raster_angle * Internal_density	.226	1	.226	1.039	.415
Build_plane * Internal_density	72.419	1	72.419	332.496	.003
Structure_type * Raster_angle * Build_plane	1.597	2	.798	3.666	.214
Structure_type * Raster_angle * Internal_density	.592	2	.296	1.359	.424
Structure_type * Build_plane * Internal_density	15.280	2	7.640	35.077	.028
Raster_angle * Build_plane * Internal_density	.043	1	.043	.195	.702
Error	.436	2	.218		
Total	84572.263	24			
Corrected Total	6111.010	23			

Table A14.

Regression

Model summary:

R	R Square	Adjusted R Square	Std. Error of the Estimate	Change Statistics				
				R Square Change	F Change	df1	df2	Sig. F Change
.990 ^a	.980	.943	3.87802	.980	26.556	15	8	.000

Table A15.

Coefficients:

Model	Unstandardized Coefficients		Standardized Coefficients	t	Sig.
	B	Std. Error	Beta		
(Constant)	62.261	2.094		29.728	.000
Structure_type	-2.542	.970	-.130	-2.622	.031
Raster_angle	-1.374	2.094	-.086	-.656	.530
Build_plane	21.904	2.094	1.373	10.459	.000
Internal_density	5.984	2.094	.375	2.857	.021
structure_raster	.458	.970	.062	.473	.649
structure_build	-3.626	.970	-.491	-3.740	.006
structure_internal	-.916	.970	-.124	-.944	.373
raster_build	-.681	2.094	-.043	-.325	.753
raster_internal	-.431	2.094	-.027	-.206	.842
build_internal	3.571	2.094	.224	1.705	.127
str_ras_bui	.292	.970	.040	.301	.771
str_ras_int	.167	.970	.023	.172	.868
str_bui_int	-.917	.970	-.124	-.946	.372
ras_bui_int	.206	2.094	.013	.098	.924
str_ras_bui_int	-.082	.970	-.011	-.084	.935

Table A16.

Solid/Hollow

Dependent Variable: Load

Data:

TENSILE TEST						
Exp. NO.	Type of Structure	Raster Angle	Build Plane	Load		
				Spc1	Spc2	Spc3
25	Solid	-1	-1	2901	3010	2950
26	Solid	-1	1	3042	2785	2704
27	Solid	1	-1	3016	3035	3017
28	Solid	1	1	2657	2571	2631
29	Hollow	-1	-1	1429	1508	1412
30	Hollow	-1	1	1816	1984	2025
31	Hollow	1	-1	1565	1574	1528
32	Hollow	1	1	1805	1835	1793

Table A17.

Between-Subjects Factors:

Variable	Value Label		N
Structure_type	-1:	hollow	12
	1:	Solid	12
Rater_angel	-1:	-45/45	12
	1:	0/90	12
Build_plane	-1:	XY	12
	1:	YZ	12

Table A18

ANOVA

Source	Type III Sum of Squares	df	Mean Square	F	Sig.
Corrected Model	8.960E6	7	1280054.042	196.428	.000
Intercept	1.242E8	1	1.242E8	19056.238	.000
Structure_type	8219251.042	1	8219251.042	1261.266	.000
Rater_angel	12105.042	1	12105.042	1.858	.192
Build_plane	20592.042	1	20592.042	3.160	.094
Structure_type * Rater_angel	6370.042	1	6370.042	.978	.338
Structure_type * Build_plane	595665.042	1	595665.042	91.406	.000
Rater_angel * Build_plane	105205.042	1	105205.042	16.144	.001
Structure_type * Rater_angel * Build_plane	1190.042	1	1190.042	.183	.675
Error	104266.667	16	6516.667		
Total	1.332E8	24			
Corrected Total	9064644.958	23			

Table A19.

Parameter Estimates:

Parameter	B	Std. Error	t	Sig.	95% Confidence Interval	
					Lower Bound	Upper Bound
Intercept	2619.667	46.607	56.207	.000	2520.864	2718.469
[Structure_type=-1]	-808.667	65.912	-12.269	.000	-948.395	-668.939
[Rater_angel=-1]	224.000	65.912	3.398	.004	84.272	363.728
[Build_plane=-1]	403.000	65.912	6.114	.000	263.272	542.728
[Structure_type=-1] * [Rater_angel=-1]	-93.333	93.214	-1.001	.332	-290.939	104.272
[Structure_type=-1] * [Build_plane=-1]	-658.333	93.214	-7.063	.000	-855.939	-460.728
[Rater_angel=-1] * [Build_plane=-1]	-293.000	93.214	-3.143	.006	-490.605	-95.395
[Structure_type=-1] * [Rater_angel=-1] * [Build_plane=-1]	56.333	131.825	.427	.675	-223.123	335.789

Table A20.

Regression

Model summary:

R	R Square	Adjusted R Square	Std. Error of the Estimate	Change Statistics				
				R Square Change	F Change	df1	df2	Sig. F Change
.994 ^a	.988	.983	80.726	.988	196.428	7	16	.000

Table A21.

Coefficients:

Model	Unstandardized Coefficients		Standardized Coefficients	t	Sig.
	B	Std. Error	Beta		
(Constant)	2274.708	16.478		138.044	.000
Structure_type	585.208	16.478	.952	35.514	.000
Rater_angel	-22.458	16.478	-.037	-1.363	.192
Build_plane	29.292	16.478	.048	1.778	.094
str_ras	-16.292	16.478	-.027	-.989	.338
Str_bui	-157.542	16.478	-.256	-9.561	.000
Ras_bui	-66.208	16.478	-.108	-4.018	.001
Str_ras_bui	-7.042	16.478	-.011	-.427	.675

Table A22.

Dependent Variable: Model Material

Between-Subjects Factors

Variable	Value Label		N
Structure_type	-1	hollow	4
	1	Solid	4
Rater_angel	-1	-45/45	4
	1	0/90	4
Build_plane	-1	XY	4
	1	YZ	4

Table A23.

ANOVA

Source	Type III Sum of Squares	df	Mean Square	F	Sig.
Corrected Model	145.099	6	24.183	999.302	.024
Intercept	1246.003	1	1246.003	51487.736	.003
Structure_type	142.805	1	142.805	5901.033	.008
Rater_angel	.048	1	.048	1.986	.393
Build_plane	.092	1	.092	3.820	.301
Structure_type * Rater_angel	.018	1	.018	.746	.546
Structure_type * Build_plane	2.101	1	2.101	86.829	.068
Rater_angel * Build_plane	.034	1	.034	1.397	.447
Error	.024	1	.024		
Total	1391.126	8			
Corrected Total	145.123	7			

Table A24.

Regression

Model Summary:

R	R Square	Adjusted R Square	Std. Error of the Estimate	Change Statistics				
				R Square Change	F Change	df1	df2	Sig. F Change
1.000	1.000	.999	.15556	1.000	999.302	6	1	.024

Table A25.

Coefficients:

Model	Unstandardized Coefficients		Standardized Coefficients	t	Sig.
	B	Std. Error	Beta		
(Constant)	12.480	.055		226.909	.003
Structure_type	4.225	.055	.992	76.818	.008
Rater_angel	-.077	.055	-.018	-1.409	.393
Build_plane	-.108	.055	-.025	-1.955	.301
str_ras	-.047	.055	-.011	-.864	.546
Str_bui	-.512	.055	-.120	-9.318	.068
Ras_bui	-.065	.055	-.015	-1.182	.447

Table A26.

Dependent Variable: Support Material

ANOVA

Source	Type III Sum of Squares	df	Mean Square	F	Sig.
Corrected Model	51.177	6	8.530		
Intercept	86.935	1	86.935		
Structure_type	47.473	1	47.473		
Rater_angel	.000	1	.000		
Build_plane	3.364	1	3.364		
Structure_type * Rater_angel	.000	1	.000		
Structure_type * Build_plane	.339	1	.339		
Rater_angel * Build_plane	5.000E-5	1	5.000E-5		
Error	.000	1	.000		
Total	138.113	8			
Corrected Total	51.177	7			

Table A27.

Regression

Model Summary:

R	R Square	Adjusted R Square	Std. Error of the Estimate	Change Statistics				
				R Square Change	F Change	df1	df2	Sig. F Change
1.000	1.000	1.000	.00000	1.000	.	6	1	.

Table A28.

Coefficients:

Model	Unstandardized Coefficients		Standardized Coefficients	t	Sig.
	B	Std. Error	Beta		
(Constant)	3.297	.000		2.555E8	.000
Structure_type	-2.436	.000	-.963	-1.888E8	.000
Rater_angel	-.008	.000	-.003	-581308.269	.000
Build_plane	.649	.000	.256	5.026E7	.000
str_ras	.005	.000	.002	387538.846	.000
Str_bui	.206	.000	.081	1.597E7	.000
Ras_bui	-.003	.000	.000	-193769.423	.000

Table A29.

Dependent Variable: Time

ANOVA

Source	Type III Sum of Squares	df	Mean Square	F	Sig.
Corrected Model	563.781	6	93.963	82.969	.084
Intercept	5993.483	1	5993.483	5292.200	.009
Structure_type	25.669	1	25.669	22.665	.132
Rater_angel	4.019	1	4.019	3.548	.311
Build_plane	517.294	1	517.294	456.766	.030
Structure_type * Rater_angel	2.344	1	2.344	2.069	.387
Structure_type * Build_plane	13.339	1	13.339	11.778	.181
Rater_angel * Build_plane	1.118	1	1.118	.987	.502
Error	1.133	1	1.133		
Total	6558.396	8			
Corrected Total	564.913	7			

Table A30.

Regression

Model Summary:

R	R Square	Adjusted R Square	Std. Error of the Estimate	Change Statistics				
				R Square Change	F Change	df1	df2	Sig. F Change
.999	.998	.986	1.06420	.998	82.969	6	1	.084

Table A31.

Coefficients:

Model	Unstandardized Coefficients		Standardized Coefficients	t	Sig.
	B	Std. Error	Beta		
(Constant)	27.371	.376		72.748	.009
Structure_type	-1.791	.376	-.213	-4.761	.132
Build_plane	8.041	.376	.957	21.372	.030
Str_bui	-1.291	.376	-.154	-3.432	.181
Rater_angel	-.709	.376	-.084	-1.884	.311
str_ras	-.541	.376	-.064	-1.439	.387
Ras_bui	-.374	.376	-.044	-.993	.502

Table A32.

Compressive Specimens

Dependent Variable: Load

Data:

Compressive Test							
Exp. NO.	Type of Structure	Raster Angle	Build Plane	Internal Density	Load		
					Spc1	Spc2	Spc3
1	Orthogonal	-1	-1	-1	1812	1653	1738
2	Orthogonal	-1	-1	1	2701	2615	2695
3	Orthogonal	-1	1	-1	1883	1943	2191
4	Orthogonal	-1	1	1	2737	2474	2622
5	Orthogonal	1	-1	-1	2001	1947	1882
6	Orthogonal	1	-1	1	2477	2675	2409
7	Orthogonal	1	1	-1	1874	1953	1807
8	Orthogonal	1	1	1	2559	2253	2490
9	Hexagonal	-1	-1	-1	1876	1879	1784
10	Hexagonal	-1	-1	1	2052	2024	2048
11	Hexagonal	-1	1	-1	1581	1429	1505
12	Hexagonal	-1	1	1	1595	1585	1656
13	Hexagonal	1	-1	-1	1979	1877	1897
14	Hexagonal	1	-1	1	2110	2090	2032
15	Hexagonal	1	1	-1	1347	1291	1497
16	Hexagonal	1	1	1	1420	1425	1350
17	Pyramid	-1	-1	-1	1436	1454	1435
18	Pyramid	-1	-1	1	2099	2036	2025
19	Pyramid	-1	1	-1	1560	1572	1587
20	Pyramid	-1	1	1	2152	2063	1959
21	Pyramid	1	-1	-1	1370	1429	1293
22	Pyramid	1	-1	1	1954	2049	2007
23	Pyramid	1	1	-1	1569	1741	1529
24	Pyramid	1	1	1	1872	1961	2047

Table A33.

Between-Subjects Factors

Variable	Value Label		N
Structure_type	1:	Orthogonal	24
	2:	Hexagonal	24
	3:	Pyramid	24
Raster_angle	-1:	-45/45	36
	1:	0/90	36
Build_plane	-1:	XY	36
	1:	YZ	36
Internal_density	-1:	loose	36
	1:	compact	36

Table A34.

ANOVA

Source	Type III Sum of Squares	df	Mean Square	F	Sig.
Corrected Model	1.013E7	23	440428.217	61.107	.000
Intercept	2.604E8	1	2.604E8	36125.272	.000
Structure_type	3770966.778	2	1885483.389	261.601	.000
Raster_angle	55167.347	1	55167.347	7.654	.008
Build_plane	314821.125	1	314821.125	43.680	.000
Internal_density	3430890.125	1	3430890.125	476.018	.000
Structure_type * Raster_angle	750.111	2	375.056	.052	.949
Structure_type * Build_plane	1213865.333	2	606932.667	84.209	.000
Structure_type * Internal_density	965216.333	2	482608.167	66.959	.000
Raster_angle * Build_plane	68758.681	1	68758.681	9.540	.003
Raster_angle * Internal_density	51360.125	1	51360.125	7.126	.010
Build_plane * Internal_density	124583.681	1	124583.681	17.285	.000
Structure_type * Raster_angle * Build_plane	57808.444	2	28904.222	4.010	.025
Structure_type * Raster_angle * Internal_density	21343.000	2	10671.500	1.481	.238
Structure_type * Build_plane * Internal_density	7064.778	2	3532.389	.490	.616
Raster_angle * Build_plane * Internal_density	1065.681	1	1065.681	.148	.702
Structure_type * Raster_angle * Build_plane * Internal_density	46187.444	2	23093.722	3.204	.049
Error	345959.333	48	7207.486		
Total	2.708E8	72			
Corrected Total	1.048E7	71			

Table A35.

Parameter Estimates:

Parameter	B	Std. Error	t	Sig.	90% Confidence Interval	
					Lower Bound	Upper Bound
Intercept	1960.00	49.015	39.988	.000	1877.79	2042.210
[Structure_type=1]	474.000	69.318	6.838	.000	357.738	590.262
[Structure_type=2]	-561.667	69.318	-8.103	.000	-677.929	-445.405
[Raster_angle=-1]	98.000	69.318	1.414	.164	-18.262	214.262
[Build_plane=-1]	43.333	69.318	.625	.535	-72.929	159.595
[Internal_density=-1]	-347.000	69.318	-5.006	.000	-463.262	-230.738
[Structure_type=1] * [Raster_angle=-1]	79.000	98.031	.806	.424	-85.419	243.419
[Structure_type=2] * [Raster_angle=-1]	115.667	98.031	1.180	.244	-48.752	280.086
[Structure_type=1] * [Build_plane=-1]	43.000	98.031	.439	.663	-121.419	207.419
[Structure_type=2] * [Build_plane=-1]	635.667	98.031	6.484	.000	471.248	800.086
[Structure_type=1] * [Internal_density=-1]	-209.000	98.031	-2.132	.038	-373.419	-44.581
[Structure_type=2] * [Internal_density=-1]	327.000	98.031	3.336	.002	162.581	491.419
[Raster_angle=-1] * [Build_plane=-1]	-48.000	98.031	-.490	.627	-212.419	116.419
[Raster_angle=-1] * [Internal_density=-1]	-138.000	98.031	-1.408	.166	-302.419	26.419
[Build_plane=-1] * [Internal_density=-1]	-292.333	98.031	-2.982	.004	-456.752	-127.914
[Structure_type=1] * [Raster_angle=-1] * [Build_plane=-1]	21.000	138.636	.151	.880	-211.524	253.524
[Structure_type=2] * [Raster_angle=-1] * [Build_plane=-1]	-201.667	138.636	-1.455	.152	-434.190	30.857
[Structure_type=1] * [Raster_angle=-1] * [Internal_density=-1]	88.667	138.636	.640	.525	-143.857	321.190
[Structure_type=2] * [Raster_angle=-1] * [Internal_density=-1]	51.000	138.636	.368	.715	-181.524	283.524
[Structure_type=1] * [Build_plane=-1] * [Internal_density=-1]	271.333	138.636	1.957	.056	38.810	503.857
[Structure_type=2] * [Build_plane=-1] * [Internal_density=-1]	152.667	138.636	1.101	.276	-79.857	385.190
[Raster_angle=-1] * [Build_plane=-1] * [Internal_density=-1]	165.667	138.636	1.195	.238	-66.857	398.190
[Structure_type=1] * [Raster_angle=-1] * [Build_plane=-1] * [Internal_density=-1]	-475.333	196.061	-2.424	.019	-804.172	-146.495
[Structure_type=2] * [Raster_angle=-1] * [Build_plane=-1] * [Internal_density=-1]	-114.000	196.061	-.581	.564	-442.838	214.838

Table A36.

Regression

Model Summary:

R	R Square	Adjusted R Square	Std. Error of the Estimate	Change Statistics				
				R Square Change	F Change	df1	df2	Sig. F Change
.808	.652	.559	255.070	.652	7.001	15	56	.000

Table A37.

Coefficients:

Model	Unstandardized Coefficients		Standardized Coefficients	t	Sig.
	B	Std. Error	Beta		
(Constant)	2367.986	79.532		29.774	.000
Structure_type	-233.167	36.816	-.499	-6.333	.000
Raster_angle	-35.181	79.532	-.092	-.442	.660
Build_plane	-101.292	79.532	-.266	-1.274	.208
Internal_density	292.208	79.532	.766	3.674	.001
structure_raster	3.750	36.816	.021	.102	.919
structure_build	17.583	36.816	.100	.478	.635
structure_internal	-36.958	36.816	-.209	-1.004	.320
raster_build	-85.069	79.532	-.223	-1.070	.289
raster_internal	-63.958	79.532	-.168	-.804	.425
build_internal	-33.181	79.532	-.087	-.417	.678
str_ras_bui	27.083	36.816	.153	.736	.465
str_ras_int	18.625	36.816	.105	.506	.615
str_bui_int	-4.208	36.816	-.024	-.114	.909
ras_bui_int	63.264	79.532	.166	.795	.430
str_ras_bui_int	-29.708	36.816	-.168	-.807	.423

Table A38.

Between-Subjects Factors

Variable	Value Label		N
Structure_type	1:	Orthogonal	8
	2:	Hexagonal	8
	3:	Pyramid	8
Raster_angle	-1:	-45/45	12
	1:	0/90	12
Build_plane	-1:	XY	12
	1:	YZ	12
Internal_density	-1:	loose	12
	1:	compact	12

Table A39.

Dependent Variable: Model Material

ANOVA

Source	Type III Sum of Squares	df	Mean Square	F	Sig.
Corrected Model	3.339	21	.159	218.380	.005
Intercept	154.219	1	154.219	211839.643	.000
Structure_type	.045	2	.022	30.891	.031
Raster_angle	8.817E-5	1	8.817E-5	.121	.761
Build_plane	2.652	1	2.652	3642.885	.000
Internal_density	.562	1	.562	772.566	.001
Structure_type * Raster_angle	.002	2	.001	1.155	.464
Structure_type * Build_plane	.002	2	.001	1.221	.450
Structure_type * Internal_density	.067	2	.033	45.825	.021
Raster_angle * Build_plane	.000	1	.000	.506	.551
Raster_angle * Internal_density	.001	1	.001	1.028	.417
Structure_type * Raster_angle * Build_plane	.002	2	.001	1.265	.442
Build_plane * Internal_density	.002	1	.002	2.923	.229
Structure_type * Raster_angle * Internal_density	.002	2	.001	1.435	.411
Structure_type * Build_plane * Internal_density	.001	2	.001	.729	.578
Raster_angle * Build_plane * Internal_density	.001	1	.001	.909	.441
Error	.001	2	.001		
Total	157.559	24			
Corrected Total	3.340	23			

Table A40.

Regression

Model Summary:

R	R Square	Adjusted R Square	Std. Error of the Estimate
.991	.982	.949	.08624

Table A41.

Coefficients:

Model	Unstandardized Coefficients		Standardized Coefficients	t	Sig.
	B	Std. Error	Beta		
(Constant)	2.473	.047		53.096	.000
Structure_type	.031	.022	.068	1.438	.188
Raster_angle	.020	.047	.053	.428	.680
Build_plane	.333	.047	.892	7.148	.000
Internal_density	.053	.047	.141	1.129	.292
structure_raster	-.009	.022	-.052	-.417	.687
structure_build	.000	.022	-.001	-.012	.991
structure_internal	.050	.022	.291	2.331	.048
raster_build	-.023	.047	-.063	-.503	.629
raster_internal	-.026	.047	-.070	-.560	.591
build_internal	-.022	.047	-.060	-.481	.643
str_ras_bui	.010	.022	.056	.452	.663
str_ras_int	.010	.022	.059	.475	.647
str_bui_int	.006	.022	.038	.301	.771
ras_bui_int	.022	.047	.060	.478	.646
str_ras_bui_int	-.008	.022	-.049	-.394	.704

Table A42.

Dependent Variable: Support Material

ANOVA

Source	Type III Sum of Squares	df	Mean Square	F	Sig.
Corrected Model	6.624	21	.315	3426.837	.000
Intercept	304.544	1	304.544	3308761.000	.000
Structure_type	.026	2	.013	143.571	.007
Raster_angle	.000	1	.000	5.183	.151
Build_plane	6.107	1	6.107	66355.568	.000
Internal_density	.245	1	.245	2666.514	.000
Structure_type * Raster_angle	.001	2	.000	3.906	.204
Structure_type * Build_plane	.061	2	.030	330.769	.003
Structure_type * Internal_density	.172	2	.086	933.060	.001
Raster_angle * Build_plane	7.042E-6	1	7.042E-6	.077	.808
Raster_angle * Internal_density	.000	1	.000	3.915	.186
Structure_type * Raster_angle * Build_plane	.000	2	.000	1.353	.425
Build_plane * Internal_density	.001	1	.001	13.549	.067
Structure_type * Raster_angle * Internal_density	.000	2	.000	2.666	.273
Structure_type * Build_plane * Internal_density	.008	2	.004	44.024	.022
Raster_angle * Build_plane * Internal_density	7.042E-6	1	7.042E-6	.077	.808
Error	.000	2	9.204E-5		
Total	311.168	24			
Corrected Total	6.624	23			

Table A43.

Regression

Model Summary:

R	R Square	Adjusted R Square	Std. Error of the Estimate
.993	.986	.961	.10655

Table A44.

Coefficients:

Model	Unstandardized Coefficients		Standardized Coefficients	t	Sig.
	B	Std. Error	Beta		
(Constant)	3.515	.058		61.078	.000
Structure_type	.024	.027	.037	.892	.399
Raster_angle	-.012	.058	-.023	-.208	.841
Build_plane	.442	.058	.841	7.680	.000
Internal_density	-.089	.058	-.169	-1.544	.161
structure_raster	.004	.027	.015	.141	.892
structure_build	.031	.027	.129	1.173	.274
structure_internal	.095	.027	.391	3.566	.007
raster_build	-.008	.058	-.015	-.140	.892
raster_internal	-.014	.058	-.026	-.241	.816
build_internal	-.038	.058	-.072	-.657	.530
str_ras_bui	.004	.027	.015	.141	.892
str_ras_int	.005	.027	.021	.188	.856
str_bui_int	.022	.027	.093	.845	.423
ras_bui_int	.001	.058	.001	.009	.993
str_ras_bui_int	2.780E-17	.027	.000	.000	1.000

Table A45.

Dependent Variable: Time

ANOVA

Source	Type III Sum of Squares	df	Mean Square	F	Sig.
Corrected Model	4427.175 ^a	21	210.818	15027.111	.000
Intercept	39873.878	1	39873.878	2842212.838	.000
Structure_type	255.523	2	127.762	9106.858	.000
Raster_angle	.230	1	.230	16.402	.056
Build_plane	1467.501	1	1467.501	104603.590	.000
Internal_density	2514.740	1	2514.740	179250.813	.000
Structure_type * Raster_angle	.009	2	.004	.314	.761
Structure_type * Build_plane	19.309	2	9.655	688.186	.001
Structure_type * Internal_density	117.257	2	58.629	4179.050	.000
Raster_angle * Build_plane	.043	1	.043	3.030	.224
Raster_angle * Internal_density	.113	1	.113	8.086	.105
Structure_type * Raster_angle * Build_plane	.026	2	.013	.941	.515
Build_plane * Internal_density	5.014	1	5.014	357.413	.003
Structure_type * Raster_angle * Internal_density	.124	2	.062	4.413	.185
Structure_type * Build_plane * Internal_density	47.243	2	23.621	1683.725	.001
Raster_angle * Build_plane * Internal_density	.043	1	.043	3.030	.224
Error	.028	2	.014		
Total	44301.081	24			
Corrected Total	4427.203	23			

Table A46.

Regression

Model Summary:

R	R Square	Adjusted R Square	Std. Error of the Estimate
.968 ^a	.937	.819	5.89626

Table A47.

Coefficients:

Model	Unstandardized Coefficients		Standardized Coefficients	t	Sig.
	B	Std. Error	Beta		
(Constant)	36.134	3.184		11.347	.000
Structure_type	2.313	1.474	.139	1.569	.155
Raster_angle	-.057	3.184	-.004	-.018	.986
Build_plane	5.693	3.184	.419	1.788	.112
Internal_density	6.610	3.184	.487	2.076	.072
structure_raster	-.021	1.474	-.003	-.014	.989
structure_build	1.063	1.474	.169	.721	.491
structure_internal	1.813	1.474	.288	1.230	.254
raster_build	.000	3.184	.000	.000	1.000
raster_internal	-.028	3.184	-.002	-.009	.993
build_internal	-.669	3.184	-.049	-.210	.839
str_ras_bui	-.021	1.474	-.003	-.014	.989
str_ras_int	-.021	1.474	-.003	-.014	.989
str_bui_int	.563	1.474	.090	.382	.712
ras_bui_int	.083	3.184	.006	.026	.980
str_ras_bui_int	-.021	1.474	-.003	-.014	.989

Table A48.

Solid/Hollow

Between-Subjects Factors

Variable	Value Label		N
Structure_type	-1	hollow	4
	1	Solid	4
Rater_angel	-1	-45/45	4
	1	0/90	4
Build_plane	-1	XY	4
	1	YZ	4

Table A49.

Dependent Variable: Model Material

ANOVA

Source	Type III Sum of Squares	df	Mean Square	F	Sig.
Corrected Model	24.176	6	4.029	111538.186	.002
Intercept	130.920	1	130.920	3624096.087	.000
Structure_type	23.726	1	23.726	656767.228	.001
Rater_angel	.004	1	.004	115.879	.059
Build_plane	.140	1	.140	3865.913	.010
Structure_type * Rater_angel	.003	1	.003	85.291	.069
Structure_type * Build_plane	.303	1	.303	8388.405	.007
Rater_angel * Build_plane	.000	1	.000	6.398	.240
Error	3.612E-5	1	3.612E-5		
Total	155.096	8			
Corrected Total	24.176	7			

Table A50.

Regression

Model Summary:

R	R Square	Adjusted R Square	Std. Error of the Estimate
1.000 ^a	1.000	1.000	.00601

Table A51.

Coefficients^a

Model	Unstandardized Coefficients		Standardized Coefficients	t	Sig.
	B	Std. Error	Beta		
(Constant)	4.045	.002		1903.706	.000
Structure_type	1.722	.002	.991	810.412	.001
Rater_angel	-.023	.002	-.013	-10.765	.059
Build_plane	.132	.002	.076	62.176	.010
str_ras	-.020	.002	-.011	-9.235	.069
Str_bui	-.195	.002	-.112	-91.588	.007
Ras_bui	.005	.002	.003	2.529	.240

Table A52.

Dependent Variable: Support Material

ANOVA

Source	Type III Sum of Squares	df	Mean Square	F	Sig.
Corrected Model	15.233	6	2.539	12694.458	.007
Intercept	21.714	1	21.714	108570.250	.002
Structure_type	14.418	1	14.418	72092.250	.002
Rater_angel	5.000E-5	1	5.000E-5	.250	.705
Build_plane	.274	1	.274	1369.000	.017
Structure_type * Rater_angel	5.000E-5	1	5.000E-5	.250	.705
Structure_type * Build_plane	.541	1	.541	2704.000	.012
Rater_angel * Build_plane	.000	1	.000	1.000	.500
Error	.000	1	.000		
Total	36.948	8			
Corrected Total	15.234	7			

Table A53.

Regression

Model Summary:

R	R Square	Adjusted R Square	Std. Error of the Estimate
1.000	1.000	1.000	.01414

Table A54.

Coefficients:

Model	Unstandardized Coefficients		Standardized Coefficients	t	Sig.
	B	Std. Error	Beta		
(Constant)	1.648	.005		329.500	.002
Structure_type	-1.342	.005	-.973	-268.500	.002
Rater_angel	.003	.005	.002	.500	.705
Build_plane	.185	.005	.134	37.000	.017
str_ras	-.003	.005	-.002	-.500	.705
Str_bui	-.260	.005	-.188	-52.000	.012
Ras_bui	-.005	.005	-.004	-1.000	.500

Table A55.

Dependent Variable: Time

ANOVA

Source	Type III Sum of Squares	df	Mean Square	F	Sig.
Corrected Model	483.516	6	80.586	6295.783	.010
Intercept	2057.611	1	2057.611	160750.879	.002
Structure_type	325.125	1	325.125	25400.391	.004
Rater_angel	.344	1	.344	26.910	.121
Build_plane	95.634	1	95.634	7471.441	.007
Structure_type * Rater_angel	.125	1	.125	9.766	.197
Structure_type * Build_plane	62.273	1	62.273	4865.063	.009
Rater_angel * Build_plane	.014	1	.014	1.129	.481
Error	.013	1	.013		
Total	2541.140	8			
Corrected Total	483.529	7			

Table A56.

Regression

Model Summary:

R	R Square	Adjusted R Square	Std. Error of the Estimate
1.000	1.000	1.000	.11314

Table A57.

Coefficients:

Model	Unstandardized Coefficients		Standardized Coefficients	t	Sig.
	B	Std. Error	Beta		
(Constant)	16.038	.040		400.937	.002
Structure_type	-6.375	.040	-.820	-159.375	.004
Rater_angel	-.207	.040	-.027	-5.187	.121
Build_plane	3.458	.040	.445	86.437	.007
str_ras	-.125	.040	-.016	-3.125	.197
Str_bui	-2.790	.040	-.359	-69.750	.009
Ras_bui	.042	.040	.005	1.062	.481

Table A58.

Only Solid

Dependent Variable: Deformation

Data:

Compressive Test						
Exp. NO.	Type of Structure	Raster Angle	Build Plane	Deformation		
				Spc1	Spc2	Spc3
25	Solid	-1	-1	139.81%	142.77%	147.91%
26	Solid	-1	1	136.84%	133.92%	133.87%
27	Solid	1	-1	163.99%	164.05%	165.25%
28	Solid	1	1	137.07%	137.81%	140.09%

Table A59.

Between-Subjects Factors

Variable	Value Label		N
Raster_angel	-1:	-45/45	6
	1:	0/90	6
Build_plane	-1:	XY	6
	1:	YZ	6

Table A60.

Descriptive Statistics:

Raster_angel	Build_plane	Mean	Std. Deviation	N
-45/45	XY	143.4967	4.09860	3
	YZ	134.8767	1.70048	3
	Total	139.1867	5.49248	6
0/90	XY	164.4300	.71077	3
	YZ	138.3233	1.57408	3
	Total	151.3767	14.34087	6
Total	XY	153.9633	11.76362	6
	YZ	136.6000	2.38990	6
	Total	145.2817	12.15404	12

Table A61.

ANOVA

Source	Type III Sum of Squares	df	Mean Square	F	Sig.
Corrected Model	1579.582	3	526.527	92.890	.000
Intercept	253281.152	1	253281.152	44683.992	.000
Raster_angel	445.788	1	445.788	78.646	.000
Build_plane	904.456	1	904.456	159.565	.000
Raster_angel * Build_plane	229.338	1	229.338	40.460	.000
Error	45.346	8	5.668		
Total	254906.080	12			
Corrected Total	1624.928	11			

Table A62.

Parameter Estimates:

Parameter	B	Std. Error	t	Sig.	95% Confidence Interval	
					Lower Bound	Upper Bound
Intercept	138.323	1.375	100.631	.000	135.154	141.493
[Raster_angel=-1]	-3.447	1.944	-1.773	.114	-7.929	1.036
[Build_plane=-1]	26.107	1.944	13.430	.000	21.624	30.589
[Raster_angel=-1] * [Build_plane=-1]	-17.487	2.749	-6.361	.000	-23.826	-11.147

Table A63.

Regression

Model Summary:

R	R Square	Adjusted R Square	Std. Error of the Estimate	Change Statistics				
				R Square Change	F Change	df1	df2	Sig. F Change
.986	.972	.962	2.38081	.972	92.890	3	8	.000

Table A64.

Coefficients:

Model	Unstandardized Coefficients		Standardized Coefficients	t	Sig.
	B	Std. Error	Beta		
(Constant)	145.282	.687		211.386	.000
Rater_angel	6.095	.687	.524	8.868	.000
Build_plane	-8.682	.687	-.746	-12.632	.000
Ras_bui	-4.372	.687	-.376	-6.361	.000

Table A65.

VITA AUCTORIS

NAME Luis Fernando Villalpando Rosas

PLACE OF BIRTH Mexico

YEAR OF BIRTH 1984

EDUCATION Western Kentucky University, Bowling Green, KY, U.S.
Bachelor of Science Diploma (Mechanical Engineering)

University of Windsor, Windsor, ON, Canada
Master in Engineering (Mechanical, Materials, Automotive)